2007-04-19

Biomass and Coal Fly Ash in Concrete: Strength, Durability, Microstructure, Quantitative Kinetics of Pozzolanic Reaction and Alkali Silica Reaction Investigations.

Shuangzhen Wang

Brigham Young University - Provo

BIOMASS AND COAL FLY ASH IN CONCRETE: STRENGTH,

DURABILITY, MICROSTRUCTURE, QUANTITATIVE

KINETICS OF POZZOLANIC REACTION AND

ALKALI SILICA REACTION INVESTIGATIONS

by

Shuangzhen Wang

A dissertation submitted to the faculty of

Brigham Young University

in partial fulfillment of the requirements for the degree of

Doctor of Philosophy

Department of Chemical Engineering

Brigham Young University

August 2007

BRIGHAM YOUNG UNIVERSITY

GRADUATE COMMITTEE APPROVAL

of a dissertation submitted by

Shuangzhen Wang

This dissertation/thesis has been read by each member of the following graduate committee and by majority vote has been found to be satisfactory.

_____   _____
Date   Larry Baxter, Chair

_____   _____
Date   Merrill W. Beckstead

_____   _____
Date   Fernando S. Fonseca

_____   _____
Date   Calvin H. Bartholomew

_____   _____
Date   William C. Hecker

BRIGHAM YOUNG UNIVERSITY

As chair of the candidate's graduate committee, I have read the dissertation of Shuangzhen Wang in its final form and have found that (1) its format, citations, and bibliographical style are consistent and acceptable and fulfill university and department style requirements; (2) its illustrative materials including figures, tables, and charts are in place; and (3) the final manuscript is satisfactory to the graduate committee and is ready for submission to the university library.

_____   _____
Date   Larry Baxter
                                                          Chair, Graduate Committee

Accepted for the Department

                                                      _____
                                                      W. Vincent Wilding
                                                      Dept. Chair, Chemical Engineering

Accepted for the College

                                                      _____
                                                      Alan R. Parkinson
                                                      Dean, Ira A. Fulton College of Engineering
                                                      and Technology

ABSTRACT

BIOMASS AND COAL FLY ASH IN CONCRETE: STRENGTH,

DURABILITY, MICROSTRUCTURE, QUANTITATIVE

KINETICS OF POZZOLANIC REACTION AND

ALKALI SILICA REACTION INVESTIGATIONS

Shuangzhen Wang

Department of Chemical Engineering

Doctor of Philosophy

Biomass represents an important sustainable energy resource, with biomass-coal cofiring representing among the most effective and cost efficient CO_2 reduction strategies. Fly ash generated during coal combustion represents a technically advantageous, inexpensive, and environmentally beneficial admixture in concrete production, partially replacing cement. However, strict interpretation of American Society of Testing and Materials (ASTM) and American Concrete Institute (ACI) standards prohibits use of fly ashes from any source other than coal in concrete production; therefore, fly ash from biomass coal cofiring is excluded from use in concrete.

This dissertation discusses biomass impacts on concrete properties through experiments conducted on several combinations of blended and pure biomass fly ash in

concrete mixtures to determine the effects on freshly mixed concrete, strength and durability of hardened concrete, and implication for long-term material properties. The results show that the performance of biomass and blended biomass-coal fly ash is comparable to that of traditional (neat) coal fly ash. Pozzolanic reactions occur simultaneously but not necessarily proportionally to strength development. Mixtures of biomass and coal fly ash in all proportions mitigate alkali-silica-reaction-based (ASR-based) expansion in concrete. Biomass-specific results indicate that biomass-containing fly ash samples can generate 3-6 times the strength of some neat coal fly ash samples in terms of pozzolanic reactions and that biomass-containing fly ash samples have better or comparable ASR mitigation performance relative to neat coal fly ash. Biomass fly ash applications in concrete production involve pozzolanic, cementitious, and ASR reactions in combination with mixture compositions and preparation techniques to dictate ultimate properties. In these practical applications, biomass fly ash demonstrates no consistent improvement or deprecation of concrete properties relative to coal fly ash. Quantitative pozzolanic reaction mechanism and kinetic analyses indicate biomass and coal fly ashes exhibit comparable reaction rates and react by similar mechanisms.

The general conclusion from the experiments is that biomass-containing fly ash, when used in concrete, performs comparable to or better than similar neat coal fly ash preparations in most respects; Substantial efforts were made to ensure samples represent typical commercial samples. Therefore, there exists no reason to exclude biomass from cofiring applications on the basis of fly ash performance in concrete and the related standards should be revised.

ACKNOWLEDGEMENTS

Dr. Baxter has mentored me to enter the fly ash and concrete world; he has also spent a long time on polishing my reports and papers, which stimulated me to be a good writer in English. I really appreciate his academic support and financial generosity for this project.

My wife, Xiaochun, has taken care of my daughter and all the housework. She has also offered so much love for me and our daughter, which is the driving force of my PhD accomplishments.

Maggie, our lovely daughter, was born during the process of my PhD project. She is a smile producer of our family. She helps me to work persistently and progressively on the project, although she never says that way.

Thanks for all the undergraduates, Emilio Llamozas, Amber Miller, Sharon Bragonje and Justin Tullis, who have worked hard on this project and are great team workers.

Thanks for David Tingey, research professor of Geology Department at BYU, who helped with the pore solution analysis and other instrumental analysis.

Thanks for David Anderson, lab director of Civil Engineering Department at BYU, who generously offered high quality technical support through the whole process.

TABLE OF CONTENTS

LIST OF FIGURES

xxvi

LIST OF TABLES

1. Introduction

The inorganic fraction of coal produces ash during combustion. The ash eventually accumulates in the furnace bottom, in one or several hoppers located between the furnace exit and the cleanup system, and in the particulate removal system (bag house or electrostatic precipitator). The ash stream from the cleanup system is fly ash and typically represents the largest fraction of the total ash (70-80% by weight) produced during pulverized coal combustion. Fly ash also has the smallest particle size and is more homogeneous than the other ash effluent streams. It has long been established that fly ash represents a potential cement partial substitute in concrete production. As early as in the 2nd century, the ancient Romans built the Pantheon, with a dome of 141 feet, as shown in Figure 1-1, using volcanic ash and hydrated lime. Hungry Horse Dam, shown in Figure 1-2, was constructed in 1948 using fly-ash-augmented concrete and was the fourth largest dam in the world at that time. Different parts of the dam have different fly ash to (fly ash + cement) ratio, ranging from 24-32 wt%; the total weight of cement plus fly ash is as much as 275,000 metric tons (Helmuth 1987). These applications demonstrate how fly-ash-based or –augmented concrete finds application in some of the most demanding and famous concrete applications in the world.

Figure 1-1 Interior of the Pantheon (Mindness, Young et al. 2002)

Figure 1-2 Hungry Horse Dam built with fly ash concrete in Montana, USA
(http://www.usbr.gov/dataweb/dams/mt00565.htm)

Concrete strength development proceeds through cementitious reactions that involve hydration of calcium silicates. These cementitious reactions involve several calcium silicate species, with tri-calcium silicate providing the main and a reasonably representative reactant. Tri-calcium silicate reacts approximately as indicated in Equation (1-1).

$$2Ca_3SiO_5 + 7H_2O \rightarrow 3CaO \cdot 2SiO_2 \cdot 4H_2O + 3Ca(OH)_2 \qquad (1\text{-}1)$$
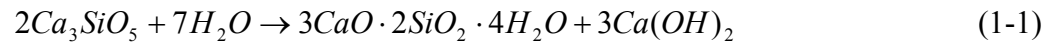
Concrete strength arises primarily from hydration of calcium silicates and their formation into long chains of materials, with the by-product, calcium hydroxide, contributing little or no strength. The chains of calcium silicate do not represent polymers in the technical sense (there is no consistently repeating mer), but they behave much like polymers in many senses, adding substantial strength to the final material. When fly ash partially replaces cement, the calcium hydroxide produced in the cementitious reactions reacts in the presence of water with amorphous and reactive silica or silicates in the fly ash to form compounds similar to those from the cement hydration. These hydroxide-derived calcium silicates add additional strength to the concrete. These calcium-hydroxide-consuming reactions are called pozzolanic reactions and a typical example appears in Equation (1-2).

$$3Ca(OH)_2 + 2SiO_2 + H_2O \rightarrow 3CaO \cdot 2SiO_2 \cdot 4H_2O \qquad (1\text{-}2)$$
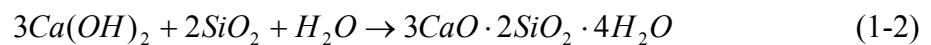
Pozzolanic reactions proceed more slowly than cementitious reactions, so their contribution to concrete strength is not noticeable in the short term, say, within one week.

Furthermore, fly ash (especially low-lime fly ash) normally depresses expansion from the alkali silica reaction (ASR). The deleterious ASRs are much slower (commonly occur over decades) than either the cementitious or pozzolanic reactions and represent reactions between alkali released mainly from cement hydration and silica from the reactive aggregate. Such reactions can increase volume, leading to cracks and eventually concrete failure. Representative ASR reactions appear in Equations (1-3) and (1-4).

$$4SiO_2 + 2NaOH = Na_2Si_4O_9 + H_2O \qquad\qquad (1\text{-}3)$$

$$SiO_2 + 2NaOH = Na_2SiO_3 + H_2O \qquad\qquad (1\text{-}4)$$
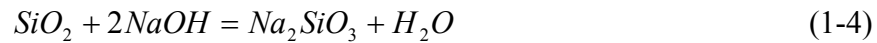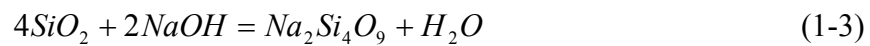
Although many international and national organizations provide written guidelines for fly ash addition in concrete production, all of them correlate closely with those of ASTM International (ASTM). Therefore, the discussion presented here centers on ASTM nomenclature. ASTM C 618 divides fly ash for potential and appropriate use in concrete into two general categories, designated Class C and Class F. Class C is a superset of Class F fly ash and is distinguished by the sum of the mass fractions of three elements, expressed as oxides (SiO_2, Al_2O_3, and Fe_2O_3) exceeding 50%. This sum exceeds 75% in Class F fly ash. Functionally, subbituminous coal generally produces Class C material and bituminous coal generally produces Class F.

Substitution of fly ash for cement not only improves the ultimate properties of concrete through the pozzolanic reaction and suppression of the ASR, as reviewed above; but also a) improves sustainability through improved resource utilization (when compared to land filling or otherwise disposing of fly ash and by avoiding energy utilization associated with cement production); b) improves concrete handling, through

4

reduction in weight and viscosity; and c) improves power generation cost by converting a financial liability to an asset. Strict interpretation of the ASTM standard, however, precludes the use of any fly ash not derived from coal (ASTM-C618 1999). The fraction of fly ash that qualifies for use in concrete under this strict interpretation is rapidly declining due to issues such as co-firing materials with coal, injecting a variety of materials for emissions control, and similar activities at power plants. More specifically, exclusion of fly ash derived from coal-biomass cofiring in concrete production represents a potentially substantial barrier to implementing this otherwise efficient and affordable production of renewable energy.

2. Literature Review

2.1 General Description

The objective of this project is to investigate the technical performance of fly ash derived from biomass co-fired with coal in relation to concrete properties and the chemical or physical mechanisms responsible for property development in such fly-ash-laden concrete. Specifically, performance comparisons will be conducted for concrete made with cement only (control group) and fly ash cement mixes using Class C, Class F, and various mixtures of Class C and Class F coal fly ashes with biomass fly ash. In addition, the chemical and physical properties of fly ash in concrete, including the rates of pozzolanic reaction, will be investigated and quantified. Finally, kinetic parameters for the pozzolanic reactions will be identified based on controlled, laboratory experiments and performances of those fly ashes in depressing the ASR expansion will be explored based on ASTM standard tests.

The ultimate objective of the work is to evaluate the exclusion of biomass-coal cofired fly ash in concrete production and to provide a performance-based rather than process-based database for evaluating fly ash utilization in concrete.

This project includes three parts: 1) analysis of concrete properties through existing ASTM concrete performance standards; 2) quantitative investigation of pozzolanic reaction rates and mechanisms; and 3) investigation of ASR mitigation by fly

ash. In the first part, concrete mix design, fresh concrete properties, hardened concrete properties (compression and flexure strength, resistance to freeze-thaw cycle and permeability), and microscopic study of pozzolanic reactions and other concrete features form the basis of the investigation. In the second part, quantitative kinetics of pozzolanic reaction as well as the strength build up (fly ash and hydrated lime only, no cement) provide mechanistic and rate parameters for pozzolanic reactions from all forms of concrete. In the final part, ASR expansion and its mitigation by both coal- and biomass-derived fly ash as well as pore solution compositions help to investigate the underlying chemical mechanisms of ASRs. Extreme pressures (up to 650 MPa) force water from cured concrete to provide information on pore solution chemistry. The remainder of this discussion summarizes the existing literature and background for each of these topics.

2.2 Cement and Concrete Production

2.2.1 History of Cement and Concrete

Assyrian and Babylonian empires used clay as cement in concrete production. Egyptians used hydrated calcium salts (lime and gypsum) for cement. However, the first structural applications of materials that reasonably represent modern Portland cement share the same roots as most of western culture. Both the ancient Greeks and Romans produced hydraulic limes, mixing certain volcanic ash and water, which had a reasonable strength and was resistant to water. The best volcanic ash was at the village Pozzuoli, near Mount Vesuvius, from the Bay of Naples, which was named Pozzolana by the ancient Romans. This word is also the origin of Pozzolans that refer to the materials having cement-forming properties and those either 1) naturally occurring, such as volcanic ash and burned clay or 2) man-made, such as coal fly ash, blast furnace slag and

silica fume. One example of the pozzolans used by the ancient Romans was in construction of Pantheon, shown in Figure 1-1.

The pioneering work for numerous modern cement inventions occurred in 1756 at the hands of John Smeaton, who rebuilt the Eddy Stone Lighthouse in England. He conducted dozens of tests to determine the right sources of lime to mix with pozzolans, and the best lime was a calcined lime from a limestone containing significant amounts of clay materials.

Modern cement production was initiated by L. J. Vicat in 1813. He prepared the primary modern cement by calcining synthetic mixtures of limestone and clay.

In 1824, the Englishman Joeseph Aspdin patented the production of the modern cement as Portland cement. He mixed the natural limestone and clay and ground them to powder, then added water to produce slurry. The slurry was calcined in a furnace similar to a lime kiln to decompose carbonates and release carbon dioxide. The product was then finally ground to powder. The powder was named Portland cement after the Portland stone, which was of high quality and durability and found in Dorset, England. From that time, the name Portland cement was kept to refer to modern cement although production procedures as well as raw materials have drastically changed.

Modern Portland cement is produced from burning pulverized limestone and clay at a temperature as high as 1350 ˚C. Pure quartz is not used for cement production because it is relatively inert compared to clay and it leads to high energy consumption in both pulverizing and burning processes. The burning process begins with calcination of limestone and then clinker formation. The cement clinker is milled and the mixture of clinker with gypsum is called Portland cement.

2.2.2 Components of Modern Cement

Concrete production represents a classical civil engineering topic and most of the literature comes from civil engineering communities. A set of composition abbreviations universally accepted and used by civil engineers appears in Table 2-1, which is also used in the remainder of this dissertation. The disadvantages of such abbreviations include that they lack stoichiometric balancing and mechanistic rigor. However, all materials (coarse aggregate, sand, cement, fly ash, and even the water) in concrete occur naturally and have significant composition variation. One view of the civil engineering community is that balancing chemical equations, as is the custom in chemical engineering and chemistry, presumes a more detailed knowledge of component composition than is justified. Furthermore, the often low-level impurities in natural materials impact reaction rates and properties relative to reagent-grade materials, making the classical chemical descriptions that imply pure materials misleading. Without arguing the merits of different nomenclatures, this dissertation uses the classical civil engineering nomenclature to be consistent with the community most likely to be interested in these results.

Table 2-1 Abbreviations of cement components in civil engineering field

abbreviations	C	S	A	F	M	K	N	$\bar{S}$	$\bar{C}$	H
oxides	CaO	SiO_2	Al_2O3	Fe_2O_3	MgO	K_2O	Na_2O	SO_3	CO_2	H_2O

Principal reactive components of cement come from kiln clinkers, which contain four main components: alite (C_3S), belite (C_2S), tetracalcium aluminoferrite (C_4AF) and tricalcium aluminate (C_3A). Alite and belite are the main silicates and account for the most concrete strength. Both of these compounds contain small amounts of foreign ions

such as Na, Mg, and K. Gypsum ($CaSO_4 \cdot 2H_2O$) slows C_3A hydration rates, thus reducing

concrete's flash setting. The final mixture of clinker and gypsum is called cement. C_3S

usually represents more than 50% (by weight) of Portland cement and C_2S represents

approximately 10-20%. Portland cement is classified into five major types for different

applications (Table 2-2) (Mindness, Young et al. 2002). Different cement type has

different compressive strength (1 day) and heat release (7 day) due to composition and

fineness differences, which is the guidance for their various applications.

Table 2-2 Classifications of Portland cement
(Mindness, Young et al. 2002)

(Weight %)		I	II	III	IV	V
C_3S		55	55	55	42	55
C_2S		18	19	17	32	22
C_3A		10	6	10	4	4
C_4AF		8	11	8	15	12
$C\bar{S}H_2$		6	5	6	4	4
Fineness (Blain m^2/Kg)		365	375	550	340	380
Compressive strength 1-day	MPa	15	14	24	4	12
	Lb/in^2	2200	2000	3500	600	1750
Release heat of hydration (7 days, J/g)		350	265	370	235	310

2.2.3 Cement Hydration

C_3S hydrates exothermically (see Table 2-2 for range of heats of hydration). The

approximate stoichiometric reaction appears in Equation (2-1):

$$2C_3S + 11H \rightarrow C_3S_2H_8 + 3CH \qquad (2\text{-}1)$$

C$_3$S hydrates rapidly relative to the other cement components and is primarily responsible for the initial concrete setting (reaction over a few hours). Approximately 80% of the C$_3$S hydration occurs within three months.

The hydration of C$_2$S resembles that of C$_3$S except that it proceeds much more slowly. The approximate stoichiometric C$_2$S hydration is given in Equation (2-2):

$$2C_2S + 9H \rightarrow C_3S_2H_8 + CH \qquad (2\text{-}2)$$

Laboratory synthesized C$_3$S and C$_2$S (Shebl and Helmy 1985) exhibit less reactivity than alite and belite from real cement, respectively; presumably because ionic impurities in the components of alite and belite make them more reactive (Hewlett 1998).

C-S-H exhibits a degenerated layered structure much like clay. The ideal model has two main layers: a calcium silicate sheet and a second layer that includes additional calcium ions and water molecules. The two layers form laminae. However, the actual C-S-H introduces different pore sizes and the layers can intertwine. Such a model partially explains how C-S-H gel accounts for concrete strength buildup.

C-S-H gel morphology evolves with time as follows: a) a fibrous material initially forms with fiber lengths of up to 2 μm; b) a honeycomb or reticular network also forms at early stages; c) homogeneous grains up to 300 nm in diameter, packed in old cement paste; d) featherless and amorphous gel persists, even in old cement paste (Diamond 1976). The Ca to Si molar ratio in C-S-H gel varies over n a wide range, but the normal

range is between 0.8-2.2, with an average of 1.5. Figure 2-1 presents SEM pictures with the four main morphologies of C-S-H gels (Taylor 1997), a) through d).

C_3S and C_2S hydration also produces CH as by-product, which often shows a laminated morphology as illustrated by circled stuff in Figure 2-2 (Taylor 1997; Mindness, Young et al. 2002).

2.2.4 Concrete Mixing and Fresh Concrete Properties

ASTM C 192 describes procedures that promote homogeneous concrete mixing (ASTM-C192/192M-98 1998). In addition to these mix procedures, two commonly measured and important characteristics of freshly mixed concrete are slump and air content. Slump is among the most widely used tests of workability and is measured as the difference in height of a concrete specimen before and after a truncated conical mold is removed (ASTM-C143/C143M-98 1998). Several techniques measure air entrainment, which provides fracture resistance during freeze-thaw cycles (Mindness, Young et al. 2002). Small air bubbles in cement paste avoid otherwise serious freezing damage since they can drastically lower the freezing temperature of water thermodynamically; e.g., water in pores of 3.5-nm does not freeze until -20 ºC (Mindness, Young et al. 2002).

By contrast, big air bubbles, such as entrapped air and air in natural aggregate voids, are not as effective as small bubbles in reducing damage from freezing and thawing. Ideally, about 8 % of the paste volume should be entrained air, although for practical reasons most test procedures do not distinguish between entrapped or entrained air. Although the entrained air should be reported as a paste basis, in reality, most standard tests report it rather on concrete mix.
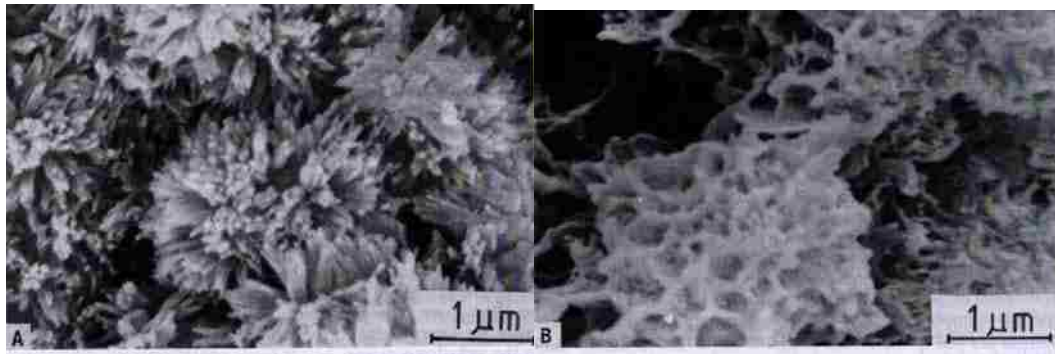
a)   b)
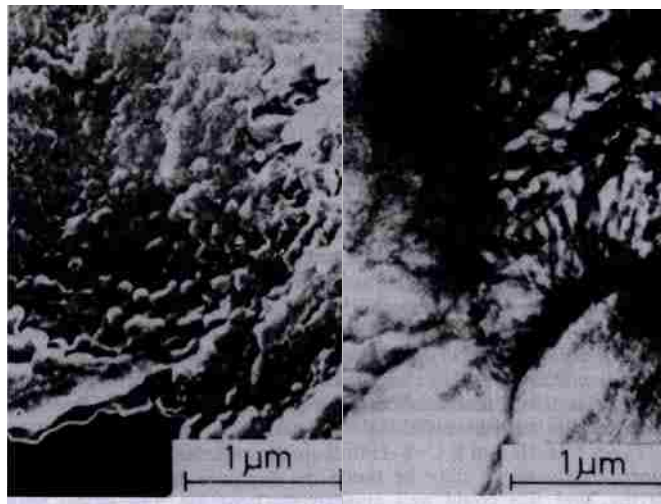
c)   d)

Figure 2-1 Morphology of C-S-H (Diamond 1976)
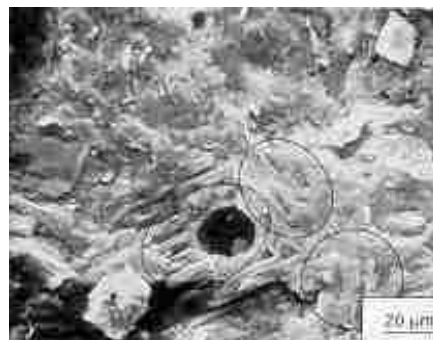
Figure 2-2 Laminated CH (Mindness, Young et al. 2002)

In addition to slump and air content, setting time is also an important characteristic of fresh concrete. Setting is the term used to describe the onset of rigidity of fresh concrete. Setting describes the fresh concrete's transitional state from fluidity to rigidity, and precedes and differs from hardening. Setting time is measured by needle penetration resistance according to ASTM C 403.

2.2.5 Hardened Concrete Properties: Strength and Durability

2.2.5.1 Cylinder Compression

Compression tests measure compressive strength of concrete. Samples in cylindrical molds (4 in diameter X 8 in height) cure in a fog room with 100% humidity at a fixed temperature (ASTM-C192/192M-98 1998). The two sample ends are sulfur-capped to form a smooth surface orthogonal to the axial surface. A compression machine stresses the sample to its failure load and the variation of this result as a function of curing time provides a measure of concrete strength (ASTM-C617 1998).

2.2.5.2 Beam Flexure Tests

Concrete tensile strength is difficult for direct measurement because secondary stresses are introduced by gripping mechanisms. Beam flexure represents a commonly used alternative measure of tensile strength. Prismatic beams, typically 6 x 6 x 20 inches, provide samples for the test. The modulus of rupture R, which is an alternative measurement of the tensile strength, is then calculated as in Equation (2-3) (ASTM-C293 1994). P is the maximum applied load, L is the span length (length of beam), b and d are beam width and depth, respectively, and a is the average distance between fracture point and the nearest support.

$$R = \begin{cases} \dfrac{PL}{bd^2} & \text{for rupture in middle third of beam} \\ \dfrac{3Pa}{bd^2} & \text{for rupture within 5\% of span lenght of middle third of beam} \end{cases} \qquad (2\text{-}3)$$

The beam flexure test overestimates the actual tensile strength of the beam by about 50% but is physically more representative of actual concrete application and failure tests than a true tensile strength test; therefore, the modulus of rupture is a common and useful measure of concrete performance.

2.2.5.3 Freeze–Thaw Resistance

Many climates result in concrete exposure to periodic freezing and thawing, creating the potential for rapid degradation or failure. Typical freezing and thawing procedures involve immersing concrete samples in water and varying the temperature from -17.8 ˚C to 4.4 ˚C for up to 300 cycles (ASTM-C666 1997). As discussed before, more sub-micron air bubbles lower the freezing temperature of water in the concrete, thus increasing the resistance to freezing-thawing damage. Sample weight loss provides one measure of durability with a high rate of weight loss indicating poor durability. Vibration modes of the sample also indicate structural fracturing. Entrainment of enough small air bubbles imbues concrete with resistance to such freezing and thawing degradation, as is shown in Table 2-3 (Woods 1968). Durability factor is a measurement of durability of concrete, and is computed according to ASTM standard (ASTM-C666 1997). The calculation of durability factor is listed in Equations (2-4) and (2-5). The higher the durability factor, the better the concrete durability; the maximum durability factor is 1. Therefore, submicron air bubbles greater than 4% of concrete volume can improve the concrete durability, as shown in Table 2-3.

Table 2-3 Effect of air content on durability factor

Air content (%)	Durability factor (%) by ASTM C 666
< 3	< 80
>4	> 85

$$Pc = (n_1^2 / n^2) \times 100 \tag{2-4}$$

Where:

Pc = relative dynamic modulus of elasticity, after c cycles of freezing and thawing , percent;

n = fundamental transverse frequency at 0 cycles of freezing and thawing, and

n1 = fundamental transverse frequency after c cycles of freezing and thawing.

Durability Factor:

$$DF = PN / M \tag{2-5}$$

Where:

DF = durability factor of the test specimen;

P = relative dynamic modulus of elasticity at N cycles, %

N = number of cycles at which P reaches the specified minimum value for discontinuing the test or the specified number of cycles at which the exposure is to be terminated, whichever is less, and

M = specified number of cycles at which the exposure is to be terminated.

2.2.5.4 Rapid Chloride Permeability Test

Permeability measures transfer rates of ions within concrete and is an important concrete property. Low chloride permeability in concrete delays ionic and moisture transfer and prevents chemical erosion or attack in chemically severe environments. Permeability decreases as water/cement ratio decreases and as tortuosity increases. The rapid chloride ion permeability test determines the permeability of concrete samples. At two months, a 60V voltage is applied to a standard size (4 in diameter X 2 in thickness) concrete specimen, and the total charge passed by chloride ion during an interval of six hours represents the chloride permeability (ASTM-C1202 1997). By increasing the replacement ratio or curing periods, fly ash can reduce the chloride permeability (Ball and Carroll 1999). There exist at least two reasons for such an increase (Aldridge 1982): (a) fly ash improves the distribution of pore size and shape, and (b) fly ash promotes C-S-H formation leading to chloride ion adsorption and diffusion path blocking. Rapid chloride ion permeability is classified by the amount of passed charges as given in Table 2-4.

2.3 Chemistry of Pozzolanic Reaction

Pozzolanic reactions refer to the reactions between pozzolans materials and calcium hydroxide, which produce similar products to those of cement hydration. Old cement appeared two thousand years ago, which was made by the ancient Romans mixing volcanic ash and hydrated limes. The best ash was near a village called Pozzuoli around the bay of Naples and that is where the name Pozzolans comes from. Pozzolans, whether naturally available or produced from industrial process, have similar properties.

Table 2-4 Classification of rapid chloride ion permeability (ASTM-C1202 1997)

Charges Passed (coulombs)	Chloride Ion Permeability
> 4,000	High
2,000 – 4,000	Moderate
1,000 – 2,000	Low
100 – 1,000	Very Low
< 100	Negligible

2.3.1 Properties of Coal Fly Ash

2.3.1.1 Generation and Classification of Coal Fly Ash

Coal fly ash is produced from utility boilers burning pulverized coal. The coal particles are typically about 50 micron in diameter (typically 75% less than 74 microns). The ash captured from utility boilers with electrostatic precipitators or a bag house is called fly ash and the ash collected at the bottom of the boiler is called bottom ash. Fly ash is more homogeneous and has a much smaller particle size than bottom ash.

ASTM standard (ASTM-C618 1999) classifies coal ash into Class C and Class F, based on the chemical and physical properties. The ash requirements of the chemical properties appear in Table 2-5. Properties of coal fly ash depend strongly on the coal properties as well as the combustion conditions.

Items	Class C	Class F
$(SiO_2 + Al_2O_3 + Fe_2O_3)$ wt% $\geq$	50.0	70.0
SO_3 wt% $\leq$	5.0	5.0
Moisture content wt% $\geq$	3.0	3.0
Loss on ignition wt% $\geq$	6.0	6.0

2.3.1.2 Influences of Coal Rank and Combustion Conditions on Fly Ash Properties

This section documents complications with fly ash classification that are largely ignored in existing practice. Subbituminous coal contains inorganic material, primarily Ca but to some extent Na and K, that forms sulfates during both fuel ashing and fuel combustion in power stations. The term *fuel ash* indicates the ash formed from a fuel sample following laboratory procedures, that is, during the determination of ash and ash composition from a fuel sample. The term *fly ash* refers to material collected near the end of a practical combustion device after the fuel burns. However, during fuel ashing the amount of sulfation generally significantly exceeds that which occurs during practical combustion.

Some terminology useful in discussing this concept is adopted in this document. The point of this discussion is that fuel ash does not faithfully represent fly ash in some ways important to fly ash classification for purposes of use in concrete.

Figure 2-3 illustrates results from 79 sample analyses focusing on SO_3 mass fractions. Fuel and fly ash samples come from the same coals in all cases, with sufficient replication to generate 95% confidence intervals for means of each data set. The data

illustrate at least two important points. First, SO_3 forms typically 20% of the total fuel ash for all subbituminous coals (first five fuels in the graph) and some lignites. Second, these SO_3 contents greatly overestimate the SO_3 contents of fly ash generated from the same fuels during entrained-flow combustion, with the fuel ash SO_3 values exceeding the fly ash results typically by a factor of 4 to 5. Both the amount of sulfur in the fly ash and the difference in the fuel ash and fly ash sulfur contents is much lower for bituminous and other high-rank fuels.

The potentially misleading SO_3 contents in fuel ash may lead to misclassification of significant amounts of fly ash for low-rank fuels. Figure 2-4 summarizes statistical data on more than 7,000 coal ash samples plotted as a function of rank. Data are presented on both an as-analyzed basis and an SO_3-free basis. The figure indicates the cumulative fraction of fuel ash samples within each rank with sums of SiO_2, Al_2O_3, and Fe_2O_3 below the value indicated on the abscissa. The limits for Class C and Class F classifications appear in the figure at 50% and 70%, respectively. Based on fuel ash analyses, about 50% of all lignites and 68% of subbituminous coals form fly ash that meets the Class C standard. However, the data in   Figure 2-3 suggest that such fuel ash analyses, while convenient, overestimate the actual amount of SO_3 in fly ashes formed from these fuels by factors ranging from 2 to 8 and typically by factors of 4 to 5. Fly ash data for the thousands of fuel samples used to generate this graph are not available. However, SO_3 issue concentration does change drastically from fuel ash to fly ash. If there were no sulfur in the fly ash, the figure indicates that the fractions of fuel that meet the Class C standard increase from 50% to about 78% for lignites and from 68% to about 80% for subbituminous coals. If the SO_3 in fly ash approximates that in the fuel ash

reduced by the 75% to 80% that the data in   Figure 2-3 suggest is typical, the percentages of fuel that meet the Class C standard increase from 50% to about 73% for lignites and from 68% to about 78% for subbituminous coals. Figure 2-4 also indicates that SO_3 forms a small fraction of high-rank fuel ashes and fuel ash provides reasonably accurate estimations of fly ash.
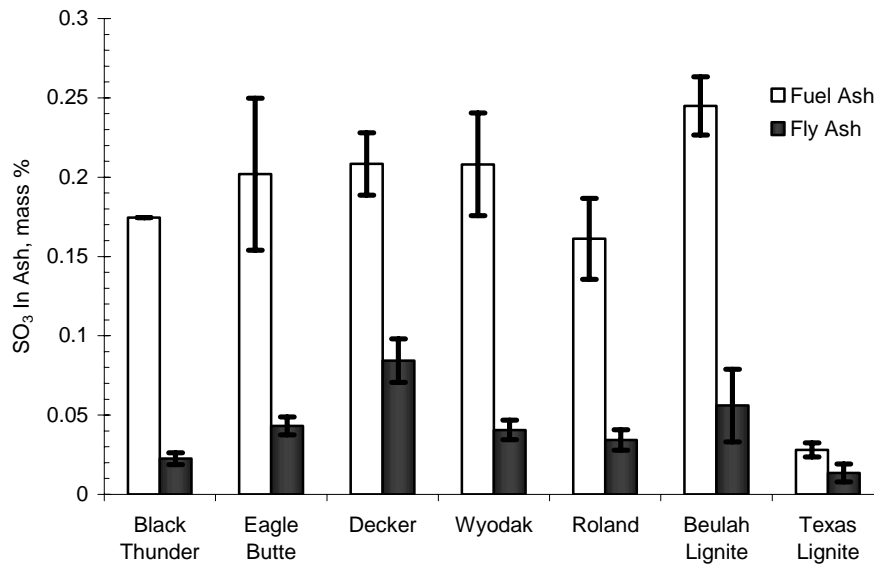
Figure 2-3 Comparison of SO₃ in fuel ash (ash analyzed from fuel sample) compared to that in fly ash samples of the same subbituminous coals (first five) and lignite.

The conclusion from the data analysis is that fly ash classification based on fuel ash is subject to significant error when applied to low-rank (subbituminous) coals and lignites. The amount of sulfur in fuel ash depends on both the fuel and on specific analytical procedures, with the data shown in Figure 2-4 being typical. Some relatively common ash characterization techniques, specifically ashing low- and high-rank fuels at the same time in the same furnace, lead to higher SO_3 contents still. There are few laboratory techniques that lead to SO_3 values lower than illustrated here.

22
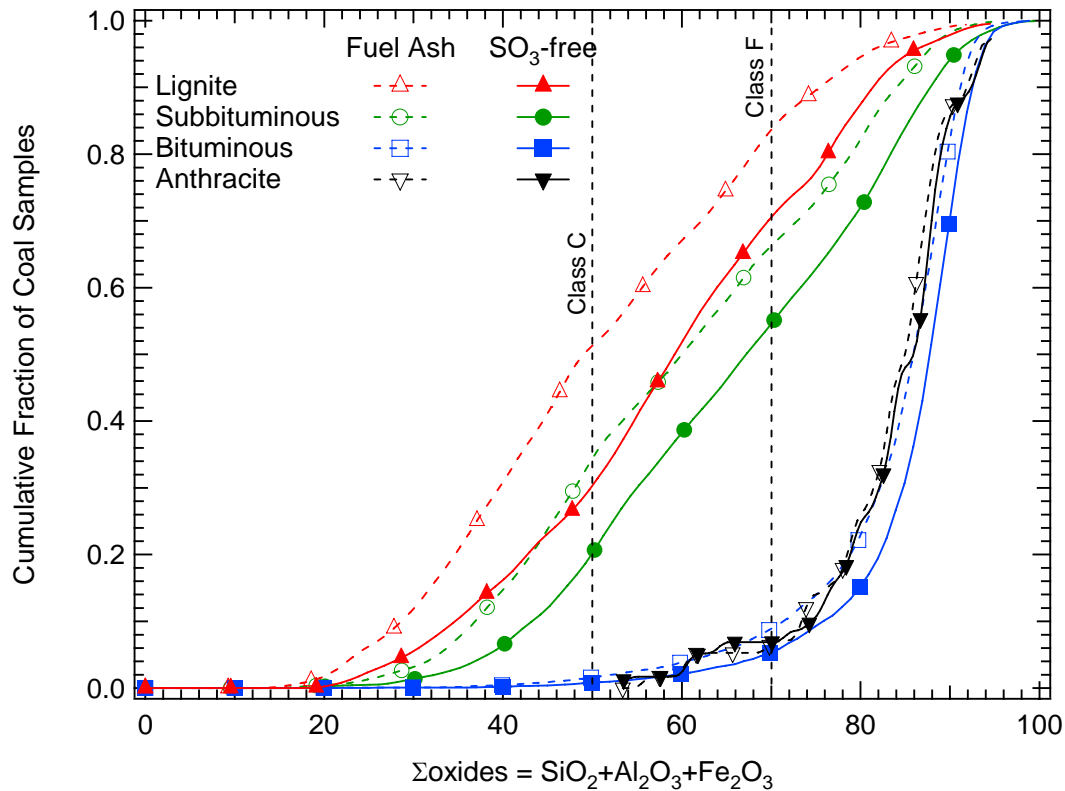
Figure 2-4 Cumulative fraction of fuel ash samples with sums of SiO_2, Al_2O_3 and Fe_2O_3 below the value indicated on the abscissa plotted as a function of coal rank and on as-analyzed and SO_3-free bases.

Fly ash classification should therefore not rely unduly on fuel ash data, especially if the fly ash falls close to the threshold for a given fuel. The morphology and composition of coal fly ash depend mainly on coal rank and burning temperature of coal (Smoot 1993).

2.3.1.3 Physical Properties of Coal Fly Ash

Most coal fly ash particles are either spherical or cenospherical; their diameters can range from submicron to 100 μm, though the great majority of the mass is generally less than 10 μm. Furthermore, their inner structure (after treatment by hydrofluoric acid) sometimes reveals a crystalline form, showing the particles' heterogeneity (Diamond 1986). The particles also include agglomerates that can be separated by sieving with

organic solvent or water. In addition, the surfaces of fly ash particles appear to be smooth when examined with an SEM.

2.3.1.4 Chemical Properties of Coal Fly Ash

Fly ash bulk composition can be determined by either Inductively Coupled Plasma (ICP), Atomic Adsorption/Emission (AA/AE) or X-Ray Florescence (XRF) spectroscopy (ASTM-D3628 2000). Many elements exist in fly ash particles and these traditionally are expressed on a mass basis as the equivalent oxides, such as SiO_2, Al_2O_3, CaO, Fe_2O_3, MgO, sulfate, Na_2O, K_2O and unburned carbon. ASTM requires that Class C bulk sum of $[SiO_2+Al_2O_3+Fe_2O_3]$ be larger than 50% and Class F greater than 70%. In addition, Class C and wood fly ash may contain higher amount of free lime than Class F.

Fly ash contains both amorphous glass and crystalline phases. Over 50% of coal fly ash is amorphous glass and the rest is crystalline, such as quartz (SiO_2), mullite ($3Al_2O_3 \cdot 2SiO_2$), magnetite (Fe_3O_4), and hematite (Fe_2O_3). Quantitative crystal analysis can be accomplished with Quantitative X-Ray Diffraction (QXRD) and infrared spectroscopy, and the amorphous glass content can be determined by deducting the weight of crystal from QXRD and loss on ignition (LOI) (Eberendu and Daugherty 1984; Helmuth 1987; Roode, Douglas et al. 1987; Pietersen 1993; Arjunan, M.R.Silsbee et al. 1997).

2.3.2 Properties of Biomass Fly Ash

2.3.2.1 Physical Properties

Wood fly ash differs in composition and particle size from those of coal-derived fly ash. When burned in dedicated biomass facilities, wood also experiences different combustion conditions (temperature, stoichiometry and combustor dimension etc.)

compared to coal particles. When sampled from such facilities, wood fly ash particles commonly exhibit irregular shapes, higher surface areas and larger average particle sizes compared to coal fly ash particles . Wood cofired with coal in a large-scale coal boiler produces fly ash with fewer physical differences from coal, but the chemical differences remain.

2.3.2.2 Chemical Properties

Direct collisions between particles in entrained-flow combustors are rare. Therefore, biomass-coal co-fired fly ash particles approximate a mixture of individual biomass fly ash particles and coal fly ash particles. However, some interactions between particles occur, mainly in the gas-phase. For example, biomass commonly has low sulfur, but high alkali and alkaline earth content relative to most coals. Aluminum is a plant toxin and generally occurs in biomass only as adventitious material like dust or dirt. Coal also generally includes more aluminum, iron, and titanium compared to biomass. Both contain high silica contents. Cofiring biomass and coal commonly sulfates the alkali and alkaline earth materials in biomass fly ash to a greater extent than what generally occurs in a dedicated biomass combustor.

Alkali-silicates form from potassium and silica during biomass combustion but generally do not occur in the original fuel. Therefore, pozzolanic activity in biomass fly ash should primarily involve silica and alkali-silicates but not aluminosilicates. Little iron or titanium exists in biomass fuels.

Herbaceous biomass commonly contains significant amounts of chlorine, over 2% of total fuel dry mass in some extreme but not rare cases. The amount of chorine and potassium varies widely with harvest time of year, method of harvesting, local soil and

climate conditions, and age of the plant. Generally, rapidly growing material in dry climates contains more chlorine (and potassium and nitrogen) than mature material in wet conditions harvested late in the growth cycle.

Woody biomass contains significant calcium and to the extent it is collected from biologically active regions of the plant, also contains high potassium and possibly chlorine. Sawdust and other materials deriving from heartwood have little ash, commonly less than 0.5%, whereas straws and other herbaceous materials contain as much as 15 % and occasionally over 20 % ash, excluding extraneous material such as soil.

Many fly ashes from biomass would qualify as Class C fly ash if they originated from coal. Combustion processes tend to concentrate alkali (mainly potassium) and chlorine in fly ash in dedicated biomass combustion facilities. However, cofiring biomass with coal leads to sulfation of available alkali (which includes nearly all alkali in clean biomass fuels), yielding fly ash with substantial depletion of chlorine and enrichment of sulfur relative to the biomass fuel composition. The reaction of mainly coal-derived sulfur with biomass-derived alkali to form alkali sulfates with accompanying depletion of chlorine represents one of the primary distinguishing characteristics of cofired fly ash compared to mixtures of fly ash from two separately fired fuels.

As a class, biomass fuels exhibit more variation in both the composition and amount of inorganic material than is typical of coal. Furthermore, this variation depends on weather and season biomass grows and is harvested, even when one restricts attention to a single type of biomass from the same location. These issues make quality control for biomass fly ash more problematic than for coal.

2.3.3 Pozzolanic Reactivity and Mechanism of Fly Ash

2.3.3.1 Pozzolanic Reactivity

Amorphous glass in fly ash reacts chemically more readily than crystalline materials. As related to pozzolanic reactivity, unburned carbon and crystals are chemically inert. The glass components can be divided into 1) network formers, 2) network modifiers, and 3) intermediates (Zachariasen 1932). Network formers are characterized by four oxygen atoms (coordination number of 4) in the form of a tetrahedron with the bond energies higher than 335 KJ/mol, all of which form an approximate three-dimensional tetrahedral network. Si and P atoms are the usual network formers. Network modifiers have bond energies less than 210 kJ/mol, with a coordination number of 6 to 8. Network modifiers include atoms as Na, K, and Ca, which depolymerize the sequence of polyhedral formers, and thus increase the activity of the glass phase. Intermediates include elements with bond energies between 210-335 kJ/mol, which typically include Mg and Al (Din 1979; Pietersen 1993; Shi 1993). Wood and Class C fly ash contain more Na, K, and Ca than Class F fly ash; therefore, if the glassy ratio of wood and Class C fly ash also has more network modifiers (Ca, Na and K) than Class F, they might be more chemically active than Class F in pozzolanic reaction.

2.3.3.2 Chemical Mechanisms

A descriptive model of high-lime fly ash hydration appears in Figure 2-5 (Grutzeck, Roy et al. 1981). Fly ash reacts little, even after three days. A glass sphere begins to react and forms an interfacial zone between the particle and surrounding solutions. Glass also dissolves and C-S-H forms in the interfacial zone slowly. As more and more C-S-H fills in the tiny voids of the interfacial zone, the concentration gradient,

and therefore the driving force of the reaction, decreases. Thus, in the short term, the rate of pozzolanic reaction increases with increased surface area of CH-fly ash paste; but in the long term, the reactivity may depend most on chemical and mineralogical properties of the fly ash involved (Hewlett 1998).

2.3.3.3 Stoichiometry of Pozzolanic Reaction Products

Silica glass has the structure of one central silicon atom surrounded by four oxygen atoms in a three-dimensional formation. When in water, the unsaturated bonded oxygen atoms take up H_2O molecules to form OH^- anions, which will eventually pull the neighboring silicon atoms away from the bulk silica glass to form $H_3SiO_4^-$. If Ca^{2+} cations are available, calcium silicate hydrates are formed (Helmuth 1987). However, not only silicates but also alumina in fly ash are reactive - alumina will react with CH to form aluminates in the absence of sulfate and ettringite in the presence of sulfate (A decomposes into $Al(OH)_4^-$ early in the process) (Helmuth 1987; Shi 1993). However, alumina is very rare in both coal and biomass – essentially all aluminum in most fuels appears in the forms of aluminosilicates or clays. The only common exception is alumina from waste paper in some biomass fuels. Equations (2-6) through (2-9) summarize the pozzolanic reactions that occur**:**

$$xCH \; + \; yS \; + \; zH \rightarrow C_x S_y H_x + z \qquad (2\text{-}6)$$

$$AS_2 \; + \; 3CH \; + \; zH \rightarrow CSH_{z\text{-}5} \; + \; C_2 ASH_8 \qquad (2\text{-}7)$$

$$Al(OH)^{4-} \; + \; CH \rightarrow C_4 AH_{13}, \; C_3 AH_6, \; etc \qquad (2\text{-}8)$$

$$Al(OH)^{4-} + 3CH + 3C \rightarrow C_3A \cdot 3C \cdot 32H \; (ettringite) \qquad (2\text{-}9)$$
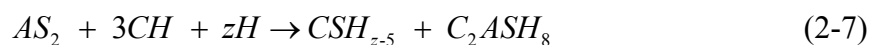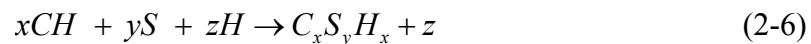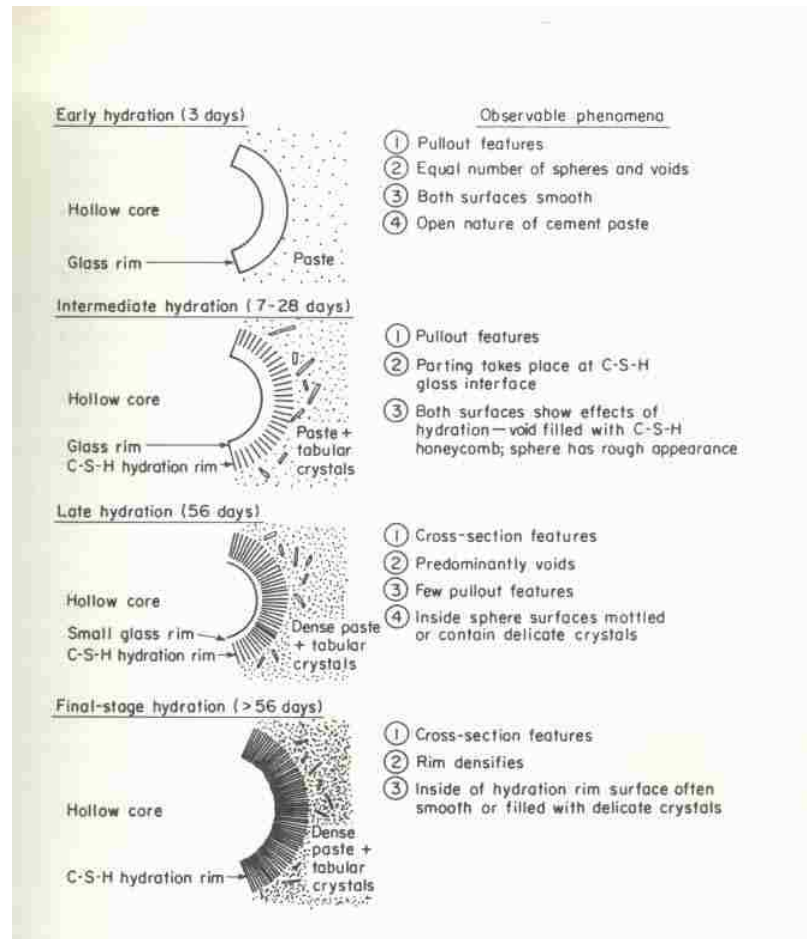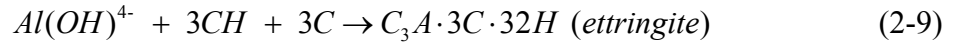
Figure 2-5 A model of high lime fly ash hydration ((Grutzeck, Roy et al. 1981)

Hydration of lime-fly ash paste generates compounds similar to those of cement hydration. The Ca to Si ratio ranges from 0.75 to 1.75 and depends on curing conditions, fly ash used, and even analytical procedures involved (Hewlett 1998). Several assumptions have been made to calculate the theoretical stoichiometric (mass) ratio of CH/fly ash. Helmuth uses the following approach(Helmuth 1987): 1) all the reactive SiO_2

in fly ash converts into Ca-Si-gel, where the Ca/Si molar ratio is unity; 2) all the reactive alumina in fly ash converts into gehlenite, which has a Ca/(Si+Al) mol ratio of unity; 3) the available additional lime produces AFm or AFt phases; and 4) fly ash has 50% reactive SiO_2, 30% reactive alumina and 20% other components (negligible of CaO content). The calculated mass ratio was 0.83 g CH/g fly ash. Researchers have pointed out the above four assumptions could be in significant error, however the assumptions are still used for the calculation of CH to fly ash mass ratio (Biernacki and Richardson 2002). The samples with 20% CH and 80% natural pozzolan (mass) have the maximum strength up to 6 months (Shi 1993).

2.3.3.4 Quantitative Kinetics of Pozzolanic Reaction

2.3.3.4.1 Quantitative Determination of CH

QXRD underestimates the CH amount by ignoring the imperfect crystalline and amorphous CH (Currell, Midgley et al. 1985; Taylor 1997). Organic liquid dissolution followed by titration overestimates the CH content because the dissolution may dissolve significant amounts of other components in the paste (Midgley 1979). Thermo Gravimetric Analysis (TGA) avoids many inaccuracies and represents a good method to analyze the CH content in cement paste (Marsh and Day 1985).

Further investigations of TGA data in the range of 300-600 ºC indicate that the weight loss includes both CH dissociation and residual water dehydration from calcium silica or calcium aluminates gels. The former accounts for the major part of the weight loss and typically forms a relatively sharp peak on a derivative curve while the latter occurs through the entire range with a very flat slope. The area under the relatively sharp

peak of weight derivative more accurately indicates CH weight than do tangent-midpoint methods (Chatterjee and Lahiri 1964; Taylor and Turner 1987).

2.3.3.4.2 Quantitative Kinetics of Pozzolanic Reaction

Pozzolanic reaction rates may be activated mechanically (fine grinding), thermally, or chemically (Shi 1993; Shi and Day 1995; Shi 1998). Pozzolanic reactions involve hydroxide and proceed most rapidly at a high pH values (>13.2) (Fraay and Bijin 1989). Some researchers assume rates of pozzolanic reactions depend on pH value, with an approximate reaction order of 0.3 (Pietersen 1993).

In dilute alkali solutions (pH~13-14), first-order dissolution with respect to the concentrations of main elements (Si, Fe, Al) from fly ash in aqueous solution was assumed by some investigators. Literature values for activation energies indicate very low values, Ea~6.5-9.2 kJ/mol. When compared to the bond energies of glassy materials (in the range of 210 kJ/mol or above), this ash dissolution could possibly be a transport-controlled diffusion process (Pietersen 1993; Biernacki, Williams et al. 2001).

Avrami (Avrami 1939) derived a nucleation-controlled rate expression with the rate given in Equation (2-10) resulting in the modified Avarami Equation (2-11):

$$-\ln\left(1-\alpha\right)^{1/3} = k_N t \qquad (2\text{-}10)$$

$$-\ln\left(1-\alpha\right)^{1/n} = k_N t \qquad (2\text{-}11)$$

where α is the extent of reaction, k_N is the reaction rate constant, and n is an unknown reaction exponent and t is time.

Similarly, a diffusion mechanism works in CH-fly ash paste. The experimental data of two low-lime UK coal fly ashes best fit the parabolic kinetics expression shown in Equation (2-12) compared to the expression that is first order with respect to CH in Equation (2-13) (Ball and Carroll 1999), where α is the reaction extent of CH, k is the reaction constant and t is the reaction time.

$$\alpha^2 = kt \qquad (2\text{-}12)$$

$$-\ln(1-\alpha) = kt \qquad (2\text{-}13)$$

The modified-Avarami Equation (2-11) is in some ways a general expression. If $n = 3$, it converts into Equation (2-10) while if $n = 1$, it converts into Equation (2-13), the first order kinetics expression.

Biernacki assumed first-order kinetics both respective to CH and to Class F fly ash in paste (water/(fly ash + CH) = 0.8) in much excess water as in Equation (2-14). Weight ratios of CH/fly ash varied from 1/7 to 3/1 and the temperature from 25 to 60 ˚C. An experimental amount of CH consumed per gram of fly ash at a certain mixing ratio, ε, was determined. Finally, by substitution of Equation (2-15) and integrating Equation (2-14), a modified first-order kinetics expression with respect to CH is obtained as given in Equation (2-16). The data agreed with the modified first-order kinetics in Equation (2-13) very well and partially fit the modified Avrami mechanisms of Equation (2-11) with $n = 2$. Furthermore, the E_a/R ratio between 4400 and 8400 (equivalent to activation energies

of 36 to 70 kJ/mol), as compared to the bond energy of glass (in the range of 210 kJ/mol or above), implies transport controlled reaction rates and a diffusion mechanism.

$$\frac{d\alpha_{CH}}{dt} = k(1 - \alpha_{CH})(1 - \alpha_{ash}) \tag{2-14}$$

$$\alpha_{ash} = \alpha_{CH} \frac{f_{CH}}{f_{Ash}} \frac{1}{\varepsilon} \tag{2-15}$$

$$\frac{1}{a-1} \ln \frac{1 - \alpha_{CH}}{1 - a\alpha_{CH}} = kt \tag{2-16}$$

where α_{CH} is the reaction extent of CH, α_{Ash} is the reaction extent of ash, t is reaction time, f_{CH} is the weight fraction of CH, ε is how many grams of calcium hydroxide one gram of ash can combine, f_{Ash} is the weight fraction of ash, and a is the proportionality constant of $f_{CH}/f_{Ash}/\varepsilon$.

Even the pozzolanic reaction between lime and sugarcane straw ash shows a kinetic-diffusive mechanism in the first several minutes through electrical conductivity testing (Villar-Cocina, Valencia-Morales et al. 2002).

Therefore, the pozzolanic reaction, both in the condition of dilute aqueous solution and paste with much excess water (water/(fly ash + CH) =0.8), exhibits significant transport control and a diffusion mechanism.

2.4 Alkali Silica Reaction

2.4.1 History

Alkali silica reactions (ASR) are the reactions between the reactive aggregates and alkali released by cement hydration (or from other sources, such as mineral admixtures). These reactions, which occur with time constants of decades, cause concrete to expand and can lead to cracks and failure, causing concrete structural failure. ASR is occasionally called "concrete cancer." A typical example of concrete failure by ASR expansion is shown in Figure 2-6 (Vanderstraeten 1987).
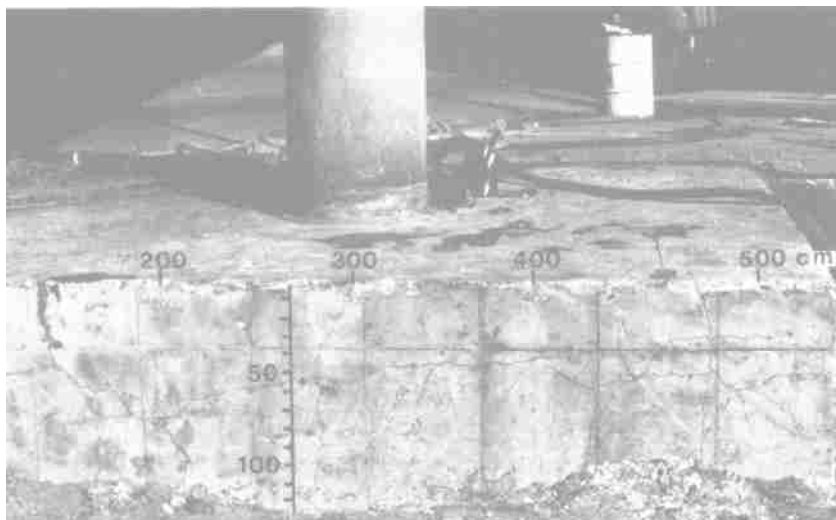
Figure 2-6 Concrete cracks caused by ASR expansion ((Vanderstraeten 1987)

Alkali silica reactions were first identified in 1940 by Stanton. Despite following standard construction procedures for a coastal road linking Monterey Bay and Los Angeles, the road experienced severe damage. The investigation (Stanton 1940) concluded that the expansion of concrete induced by an alkali silica reaction led to crack

formation and failures. A new test procedure to identify the potential for such reactions in concrete was devised.

2.4.2 Chemistry

Three components are required for ASRs to proceed: alkali, reactive silica/aggregate, and water. Alkali released from cement is calculated as Na_2O equivalent, as indicated by Equation (2-17):

$$Na_2O \text{ Equivalent } (\%) = Na_2O (\%) + 0.658 \, K_2O (\%) \tag{2-17}$$

Silica is one of the most abundant minerals on earth. It has a tetrahedron framework with a silicon atom in the center, and four oxygen atoms on the corners. Silica can be crystalline, thus being mostly chemically inert. However, amorphous silica lacks crystalline structure and has more surface area and unsaturated (reactive) bonds, which, in the presence of alkali and water, react to form alkali silica gels. The gels cause volume expansion in concrete and the mechanisms are very complicated. The reactivity of silica-rich rocks has been widely studied and includes insights about expansion (Dolar-Mantuani 1983; Alasali, Malholtra et al. 1991; Shayan 1992). There is, however, no uniform agreement about the chemical compositions of alkali-silica gels and how much expansion the gels induce. Alkali-Si gels have a wide range of stoichiometric ratios, similar to those of Ca-Si gels, although the latter do not cause expansion. Alkali-Si gels are usually mixed with Ca-Si gels. The ASR reaction appears in simplified form in Equation (2-18):

35

$$MOH \; + \; SiO_2 \rightarrow M \text{-} Si \; gel \qquad\qquad (2\text{-}18)$$

where M stands for either Na or K.

Although some alkali silica products with fixed stoichiometry have been obtained under experimental control, most of them do not have a definite composition (Wieker, Hubert et al. 1996). Reportedly, the ASRs (involving NaOH and micro silica) have a similar mechanism as that of pozzolanic reactions (CH and micro silica), except that the latter is faster than the former (Kendrick, J.R et al. 1998).

Many theories for ASR exist, among which Glasser and Diamond have postulated the two most popular ones. In Glasser's theory, silica's unsaturated bonds are attacked by OH^- or M^+ (Na^+/K^+) on the surface and silica is dissolved, which is assumed to be the controlling step of ASR (Glasser and Kataota 1981; Swamy 1992). It is found that the expansion lags far behind the chemical reaction, which acts as the basis of his two-step theory (Diamond, R.S. et al. 1981):

1) chemical formation of ASR gels

2) subsequent mechanical effects (expansive pressure) in presence of abundant moisture

Furthermore, some salts such as NaCl, $NaNO_3$, $NaNO_2$, and Na_3PO_4 can also generate ASR expansion in concrete, although the specific mechanisms are still undetermined (Chatterji, N.Thaulow et al. 1987).

2.4.3 Morphology of ASR Products

ASR products can be identified within or near ASR cracks in concrete (Davies and Oberholster 1988; Shayan and Quick 1989). SEM assisted with EDX (Energy Dispersive X-ray Analysis) has been used to identify ASR gels as amorphous, semi-

organized, and crystalline products. The crystalline products contain lamellar, acicular (fiber/filament) and rosette-like crystals, among which the rosette-like is most commonly detected (Regourd and Hornain 1986; Larive and Louarn 1992; Reis, Silva et al. 1996). Figure 2-7 a), c) and e) show the mophology of ASR gels, and Figure 2-7 b), d) and f) show the approximate chemical composition of the ASR gels by EDX, respectively. ASR gels detected have significant amounts of Na and / or K compared to Ca.

Sometimes ASR powders form on concrete specimens and can be sampled with a knife for further study. Immersion of the powders in distilled water indicates that Na-rose-shaped crystals lose most Na_2O in 84 hours, implying that Na-rose-shaped crystals are chemically unstable. By contrast, K-rose-shaped crystals are stable. Thus K-based alkali silica gels are more common than Na ones in concrete (Davies and Oberholster 1988). XRD analysis of ASR products detects multiple peaks and no conclusions have been made to match the different peaks with their respective chemical compositions (Regourd and Hornain 1986; Davies and Oberholster 1988; Reis, Silva et al. 1996).
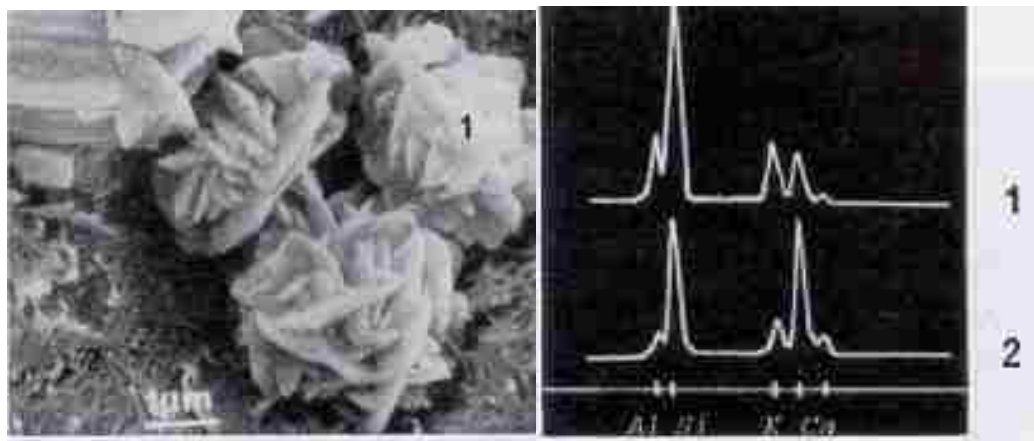
a) rosette like   b) rosette like EDX
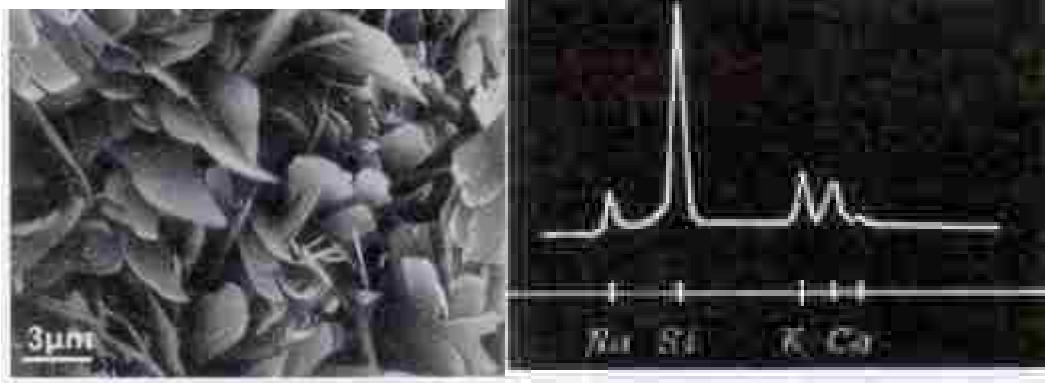
c) lamellar   d) lamellar EDX
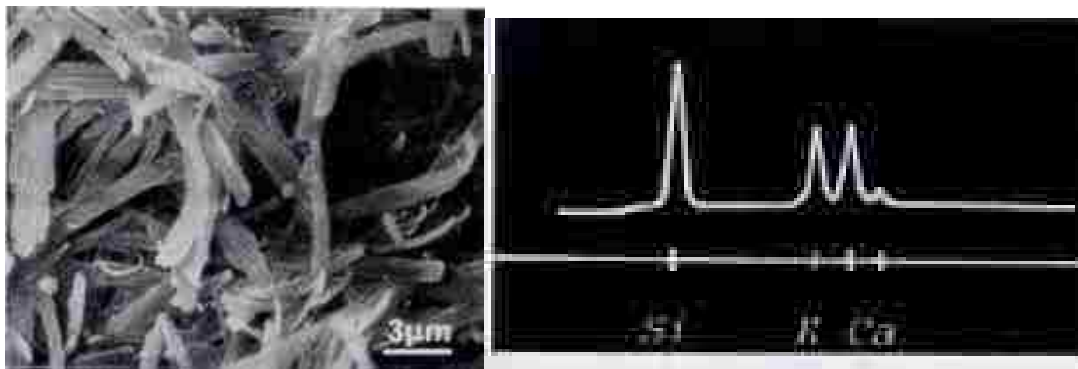
e) acicular   f) acicular EDX

Figure 2-7 Microscopic aspects of ASR gels (Regourd and Hornain 1986)

2.4.4 ASTM Tests of Reactivity of Aggregate and ASR Expansion

2.4.4.1 Reactivity of Aggregates

Reactivity of aggregates can be detected with a chemical method, ASTM C 289, or an accelerated mortar bar method described in ASTM C 1260. In ASTM C 289, 25 g of graded aggregate soaks in 1N NaOH at 80 ˚C for 24 hours, to determine the amount of dissolved silica. The standard determines the reactivity of aggregates from the amount of silica dissolved: the amount dissolved is proportional to the reactivity. Classifications

from ASTM C289 include "innocuous" and "potentially deleterious" with respect to the amount of dissolved silica. This classification overestimates the potential ASR reaction due to the severe testing procedures, which include high temperature, high alkali concentrations and finely crushed aggregates. Each of these three parameters greatly increases the dissolved silica amount and thus the reactivity of aggregates, which could result in real-world innocuous aggregates being misclassified as potentially deleterious.

ASTM C 1260 calls for graded aggregates, water, and cement to be mixed, cast into bars, and cured in a fog room for 24 hours, after which the length is recorded (at high precision). The specimens are then immersed in 1N NaOH at 80 ˚C for 14 days. The length difference of the specimens between 1 day and 14 days indicates the expansion percentage of the specimens: less than 0.1% innocuous; 0.1-0.2%, potentially deleterious; more than 0.2%, deleterious.

2.4.4.2 Cement-Aggregate Combination

ASTM C 227 specifies how the expansion of cement-aggregate combinations is to be determined (ASTM-C227 1997). Finely graded aggregates are mixed with high alkali cement (equivalent $Na_2O > 0.6\%$) to make test bars (2.5 cm X 2.5 cm X 25 cm). The bars reside in ASTM-specified containers at 38 ºC. The containers have water underneath the samples, wet wicks between samples, and wet cloth on the walls to maximize the moisture content during curing, but the samples never touch liquid water directly. Expansion is measured with a length comparator with precision of 0.0001 inch at 1, 2, 3, 4, 6, 9, and 12 months. Deleterious mixtures exhibit expansion of 0.05% at 3 months or 0.1% at 6 months according to the standard ASTM C 33.

ASTM C 441 describes the effectiveness of using ground blast-furnace slag to prevent ASR expansion (ASTM-C441 1997). The procedures follow ASTM C 227 except that 50% volume of high alkali cement (equivalent Na_2O 0.95-1.05) is replaced by slag, and graded Pyrex glass (Corning 7740) serves as the reactive aggregate. The expansion percentage is calculated by comparing results of samples to those of a control mix.

2.4.4.3 Combination of Aggregates, Cement Alkali and Curing Temperature

ASR reactivity changes from aggregate to aggregate, decreasing in the order of opal, obsidian, cristobalite, tridymite, chalcedony, cherts, cryptocrystalline volcanic rocks (andesites and rhyolites), and strained or metamorphic quartz (Metha and Monteiro 1993). Furthermore, for the same aggregate, reactivity increases with increasing surface area.

Alkali content affects the ASR reactivity as well. Higher cement alkali concentration leads to higher ASR activity, thus higher expansion. Sometimes during an experiment, adding extra NaOH or KOH leads to a higher expansion, which reduces compressive strength (Fournier, A.Bilodeau et al. 1996; Qian and Guo 1996). Alkali content must remain below 3.5 kg/m^3 of concrete to minimize compressive strength loss (Qian and Guo 1996).

High temperature results in large expansion at early curing stages but little expansion at late curing stage. Of the four factors, aggregate type, surface area, alkali concentration and curing temperature, none is dominant (Alasali, Malholtra et al. 1991).

2.4.5 Fly Ash in ASR

2.4.5.1 Performance

Pozzolanic materials, such as fly ash, slag, and silica fumes, are effective in reducing ASR expansion in concrete. Fly ash is reported to be more effective than slag (Berube and Dunchesne 1992; Blackwell, Thomas et al. 1992; Thomas and Blackwell 1996). A higher replacement ratio of fly ash leads to lower expansion, even totally eliminating the expansion (Ukita, Shigematsu et al. 1989). High-calcium fly ash might have a pessimum effect, in which at low fly ash replacement levels, the expansion, meets or exceeds that with no fly ash, but at higher replacement levels the expansion decreases. The threshold fly ash fraction above which expansion decreases is specific to the fly ash. Occasionally, fly ash may have several pessimum replacement ratios (Farbiarz, Carrasquillo et al. 1986).

The combined performances of fly ash replacement ratio, aggregates, cement, and curing temperature form a complex set of conditions influencing ASR. The combination of highly reactive aggregate and high-alkali cement generally needs a high fly ash replacement ratio to reduce ASR expansion (Shayan 1992). Also, for that situation, several fly ashes are less effective in reducing ASR expansion at 40 ºC than they are at 23 ºC, probably due to the much faster ASR reaction rate at 40 ºC (Shayan, Diggins et al. 1996).

2.4.5.2 Evaluation and Explanation

Some researchers postulate that ASR expansion reduction by fly ash works in three ways (Durand 1991; Berube and Dunchesne 1992; Thomas and Blackwell 1996): 1) dilution effect: partial substitution of cement with fly ash decreases the alkali

41

concentration in concrete; 2) permeability: the inclusion of fly ash decreases the pore size in concrete and increases the tortuosity of pores, thus reducing permeability and retarding ions transfer of concrete; and 3) chemical adsorption of alkali metals, such as Na^+ and K^+.

Pore solution chemistry reveals important ASR information. High-pressure extraction followed by ICP/AA or other chemical analysis illustrates the chemistry of concrete's pore solutions (Hewlett 1998). Some researchers provide detailed descriptions of high-pressure molds to extract aqueous pore solutions from cured concrete. However, the main disadvantages of the high-pressure extraction are: 1) only 10% of large pore solutions can be obtained; 2) the pressure is not evenly distributed through the sample; therefore, the pore solution extruded from concrete with high pressure may not be representative of the bulk pore solution in the real concrete samples.

Even after the alkali content of cement and fly ash is normalized by adding NaOH or KOH, fly ash is still effective in depressing ASR expansion; hence, fly ash contributes more than a simple diluting agent (J.Duchesne and Berube 1992). Available alkali in fly ash is calculated using the method described in ASTM C 311 (ASTM-C311 1990). Fly ash is mixed with calcium hydroxide, and the mixture is stored at 38 ºC for 28 days. Then the equivalent Na_2O is determined. The method, however, underestimates the available alkali in fly ash because fly ash releases more alkali when the mixture of cement (with known alkali content) and fly ash has been cured for 28 days and fly ash releases more alkali if the mixture of fly ash and calcium hydroxide is tested at a longer period than 28 days, such as one year (Barlow and Jackson 1988; Lee 1989).

The hypothesis that fly ash addition decreases permeability, thus retarding ion transfer and depressing ASR expansion, is still unproven. Some researchers agree

(Durand 1991) while others believe that the reduced permeability is either caused by chemical adsorption (Qian, Guo et al. 1994) or that it does not necessarily lead to retarding of ion transfer within concrete (Berube and Dunchesne 1991; Berube and Dunchesne 1992).

Fly ash addition generally diminishes available alkali content, thus depressing ASR expansion. Some researchers suggest an alkali limit, beyond which no ASR takes place; however, others argue that such a limit varies according to the reactivity of the aggregates (J.Duchesne and Berube 1992; Thomas and Blackwell 1996). Moreover, if the buffering effect of fly ash cannot reduce the alkali content below the limits at which certain reactive aggregates undergo significant ASR, fly ash, in this situation, is ineffective in depressing ASR expansion (Thomas and Blackwell 1996). Alkali concentration appears to peak within one or two weeks after concrete mixing, probably because of the high rate of cement hydration. It may decrease during the next 6 months, probably because of the increases in ASR reaction rate, thus leading to significant consumption of alkali ions (Durand, Berard et al. 1990). The pore solution's pH value is around 13-14, with sodium and potassium ions around 500 mM, calcium ions about 1 mM, and silicon less than 0.05 mM (Struble and Diamond 1989). At a high pH value, the sum of $[Na^+]$ and $[K^+]$ approximates $[OH^-]$ because other species are unimportant compared to alkali ions (Duchesne and Berube 1992). To extract the pore solutions, pressures as high as 300-500 MPa must be exerted (Barneyback and Diamond 1981; Durand, Berard et al. 1990). High water /binder ratio (~0.7) may be needed to guarantee enough pore solution for analysis (Durand, Berard et al. 1990). Ion concentrations determined by ICP/AA require relatively small samples.

43

2.5 Summary

The two critical issues of concrete are strength and durability. Pozzolanic reaction with fly ash contributes mainly to the strength buildup; freezing and thawing, rapid chloride permeability and mitigation of ASR expansion are mainly durability issues. Therefore, these topics in concrete will be the primary investigations of this project.

The literature review covers three main areas:

1) background and traditional tests: cement history, hydration chemistry, concrete mix design and tests;

2) pozzolanic reaction issues: microscopic study, mechanisms and quantitative kinetics of pozzolanic reaction as well as the characterization of fly ash; and

3) ASR issues: alkali silica reaction, the ASR expansion, fly ash's role in mitigating ASR expansion and the chemical mechanisms illustrated by pore solution squeezed by high pressure extrusion.

This investigation analyzes performance differences of coal and coal-biomass fly ash with respect to traditional properties (strength and durability tests), pozzolanic reaction and alkali silica reaction. Quantitative kinetic rates of pozzolanic reactions for six types of coal and biomass fly ash in mortar are also presented.

3. Objectives of Proposed Research

3.1 Objectives:

The objectives of this project are:

(1) To determine how fly ash addition impacts concrete strength and durability with an emphasis on biomass-coal cofired fly ash

(2) To study the rates and mechanisms of pozzolanic fly ash reactions sufficiently to produce quantitative kinetic models, and

(3) To study the influences and mechanisms of fly ash in mitigating ASR expansion

3.2 Proposed Approach

3.2.1 Investigate Fly Ash Concrete Strength and Durability

This activity will determine the strength and durability of concrete samples prepared with pure cement, cement with 25% replacement by each of Class C and Class F coal fly ash, and cement with 25% replacement by each type of coal fly ash cofired with both herbaceous and woody biomass. ASTM procedures describe the detailed measurements, which are discussed later.

3.2.2 Microscopic Study of Cementitious & Pozzolanic Reaction Products

This activity examines the pozzolanic and cementitious products microscopically: SEM and ESEM for morphology, EDX, ESEM, and EMPA for chemical analysis. The above information supports detailed investigation of products from cementitious and pozzolanic reaction.

3.2.3 Quantitative Pozzolanic Reaction Rates and Strength Buildup

This activity quantifies pozzolanic reaction rates in terms of chemical kinetics. TGA analyses will quantify calcium hydroxide concentration. Variations in calcium hydroxide concentration with initial fly ash concentration, temperature, time, and fly ash type provide quantitative global kinetic parameters for these reactions.

3.2.4 Investigation of ASR Expansion and Pore Solution Analysis

This activity determines the impact of fly ash on alkali silica reactions. ASTM C 227 and C 441 describe the test procedures, including molding bars from high-alkali cement, reactive aggregate and fly ash, and recording the swelling as a change in length. Six fly ash samples, including three biomass fly ashes, form the cementitious portion of test materials in various concentrations to conduct these tests. Changes in length are monitored from 1 day to 12 months or until a trend is clear. High-pressure (650 MPa) extraction of interstitial water and pore water for samples cured up to six months provide further quantitative concentration of alkali metals and other ions in the pore solution.

ASTM standard (ASTM-C618 1999) only allows qualified coal fly ash in concrete; therefore, the project will provide data for the performances of biomass fly ash in concrete. This investigation provides a comprehensive database of biomass (and coal) fly ash impacts on concrete, including standardized tests, qualitative microscopic

observations, quantitative kinetics of pozzolanic reactions, and quantitative study of mitigation of ASR expansion of biomass/coal fly ash, that should support a re-examination of the current ASTM standards for fly ash utilization in concrete.

4. Methods, Materials and Experimental Design

The work reported has three main categories: 1) fly ash concrete strength, durability and microscopy; 2) quantitative pozzolanic reaction rates and strength build up; and 3) mitigation of ASR expansion and the related pore solution chemistry. A summary of tests appears in Table 4-1.

4.1 Properties of Fresh and Hardened Concrete and Microscopy

4.1.1 Materials

The materials used in this investigation include cement, eight types of fly ashes, water, fine aggregate and coarse aggregate. The fine and coarse aggregate originate from Geneva Rock in Provo, Utah. The coarse aggregate was sieved according to ASTM C-33 99a, with a weight percentage of 45% (1/2 to 1 inch), 45% (3/8 to 1/2 inch), 9.5% (No.4 to 3/8 inch) and 0.5% (No.8 to No.4). The Portland cement I&II used in this investigation conforms to ASTM C-150. Fly ash types include 1) two coal fly ashes, one each of Class C and Class F; 2) two herbaceous biomass-coal cofiring fly ashes (derived from switchgrass combustion), SW1 and SW2; 3) wood fly ash from pure wood combustion and 4) two blended fly ashes, wood fly ash blended with Class C and with Class F coal fly ash.

Table 4-1 List of primary tests, objectives and methods/instrumental analysis

Investigations		Tests	Samples	Procedures /Instrumental Analysis
Fly ash concrete strength, durability and microscopy	fresh	air content	Fresh concrete	ASTM C 231
		slump		ASTM C 143
		setting time		ASTM C403
	strength	compression strength (1day -1 year)	(10 cm diameter X 20 cm height)cylinder	ASTM C 192
		flexure strength (56 day)	(15 cm X 15 cm X 50 cm) beam	ASTM C 78
	durability	freezing and thawing (up to 300 cycles of freeze and thaw)	(4.5 cm X 4.5 cm X 37.5 cm) beam	ASTM C 666
		rapid chloride permeability	(5 cm diameter X 10 cm height) cylinder	ASTM C 1202
	microscopy	morphology	small concrete pieces/ fly ash particles	SEM
		chemical analysis	polished thin sections (2.4 cm X 4.6 cm X 30 μm)	Micro probe (EMPA) and ESEM
			concrete slabs polished with 0.5 μm alumina particles	
Quantitative kinetics and strength build up (mortar of fly ash and CH, no cement)		kinetics (1 month – 1year)	powder of 5 cm cube	TGA/modelling
		compressive strength (1 month -1 year)	5 cm cube	ASTM C 109
Mitigation of ASR expansion and pore solution analysis (fly ash/cement with different ratios)		Mitigation of ASR expansion (length, 1 day – 1 year)	2.5 cm X 2.5 cm X 25 cm bar	ASTM C 490
		Alkali metals (Na^+, K^+) (1 month to 6 month)	pore solution squeezed from high pressure extrusion	Atomic absorption

Where possible, fly ash from cofired fuels was used. However, the low ash content of wood coupled with its relatively low cofiring percentage results in coal-wood fly ash streams that contain too little wood-derived material for a reasonable test. Therefore, investigations include two blended fly ashes, Wood C and Wood F, which include mixtures of pure wood fly ash with pure Class C or Class F fly ash rather than fly ash from cofiring wood and coal. The potential differences between cofired vs. blended fly ash appear in the literature review of this document and are considered to be of minor importance in this investigation.

More detailed characteristics of the fly ashes and cement appear in Table 4-2 through Table 4-4. SEM images of each fly ash sample appear in Figure 4-2. The wood fly ash agglomerates severely; therefore, it was sieved with a #10 sieve prior to use to guarantee better mixing Wood fly ash particles exhibit more irregular shapes compared to the other ash samples, most of which exhibit approximately spherical shapes. Particle size distributions of 5 fly ashes determined by a particle size laser analyzer (Coulter LS 100) appear in Figure 4-1. Class C, Class F, SW1, SW2 fly ashes have similar particle size distributions, with most of particles diameter ranging from 3 -35 μm and the most prevalent size occurring from 10-15 μm. Wood fly ash particles are much larger than the other fly ashes.

Table 4-2 Specific gravity of raw materials

Material	Specific gravity
Portland cement 1& 2	3.15
Fly ash	2.40
Fine aggregate (FA)	2.55
Coarse aggregate (CA)	2.54

Table 4-3 Specification of fly ash and cement

Type	Specification	Commercial Supplier	Average Diameter (μm)
Class C	Neat coal fly ash	Alabama Power Plant	22.0
Class F	Neat coal fly ash	Georgia Power Co.	19.0
Wood	Neat wood fly ash	Woodland Biomass Power Ltd	65.0
SW1	Co-fired with 20% switch grass and 80% Galatia coal	Southern Research Institute	13.0
SW2	Co-fired with 10% switch grass and 90% Galatia coal	Southern Research Institute	15.0
Wood C	20% Wood fly ash mixed with 80% Class C fly ash	mixed as part of this investigation	-------
Wood F	20% Wood fly ash mixed with 80% Class F fly ash	mixed as part of this investigation	--------
Portland cement I&II	-----------------	Holcim company	50.0
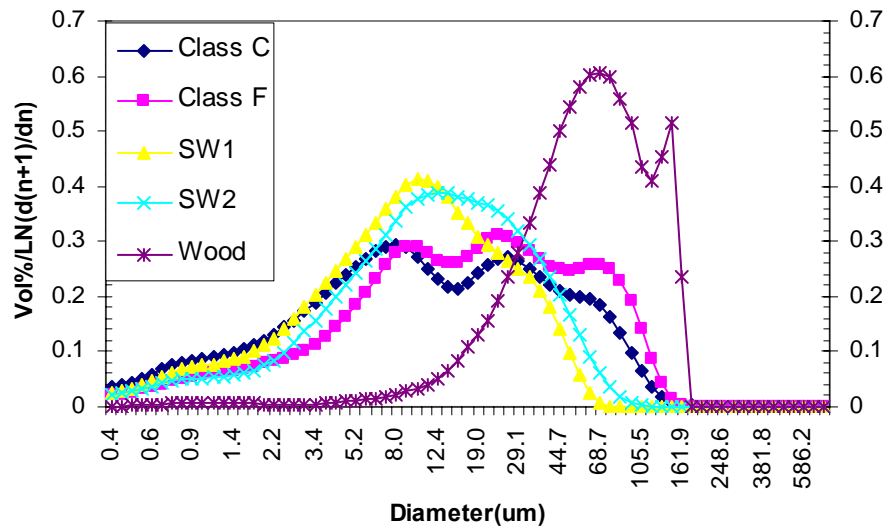
Figure 4-1 Particle size distributions of fly ashes (average of eight measurements)

52

Table 4-4 Elemental analysis and LOI of fly ash and cement

(w%)	Class C	Class F	SW1	SW2	Wood	Cement
TOTAL	100.66	99.05	100.63	99.6	99.82	99.5
SiO_2	37.26	54.91	52.16	53.02	48.94	21.5
Al_2O_3	19.62	27.79	23.55	25.78	12.47	4.2
Fe_2O_3	6.07	7.54	7.57	7.95	5.45	2.7
CaO	24.18	1.11	2.37	1.88	13.55	64.3
MgO	5.37	0.84	1.31	0.91	3.16	2.2
Na_2O	1.5	0.19	0.7	0.26	1.68	0.51
K_2O	0.43	2.4	4.01	2.14	3.37	
Cr_2O_3	0.01	0.02	0.02	0.02	0.03	0
TiO_2	1.52	1.63	1.45	1.65	0.78	0
MnO	0.01	0.02	0.04	0.02	0.12	0
P_2O_5	1.2	0.28	1.04	1.1	0.95	0
SrO	0.3	0.1	0.13	0.2	0.06	0
BaO	0.66	0.12	0.18	0.38	0.07	0
SO_3	1.83	0.38	2.25	1.23	1.3	2.6
LOI	0.7	1.72	3.85	3.06	7.89	1.3
Insoluble Residue	0	0	0	0	0	0.19

4.1.2 Experimental Design and Procedures

4.1.2.1 Concrete Mix Design and Calculation

Each fly ash combination requires a different design mix to produce a concrete sample within ASTM and experimental design parameters. The following aspects of mix design were constant for all mixes: (a) coarse aggregate weight/cubic yard (725.7 kg or 1598.4 lbs); (b) water to total cementitious material (cement plus fly ash) mass ratio (0.5); (c) percent of cement displaced by fly ash (25 % mass); (d) air entrainment (4-6% according to ASTM C 231-97); and slump (3-5 inches according to ASTM C 143/C 143M-98). The fine aggregate mass and air-entraining agent concentration represent the

principle means by which slump and other properties of the mixes were maintained constant.

a-Cement   b-Class C

c-Class F   d-SW1

e-SW2   f-Wood
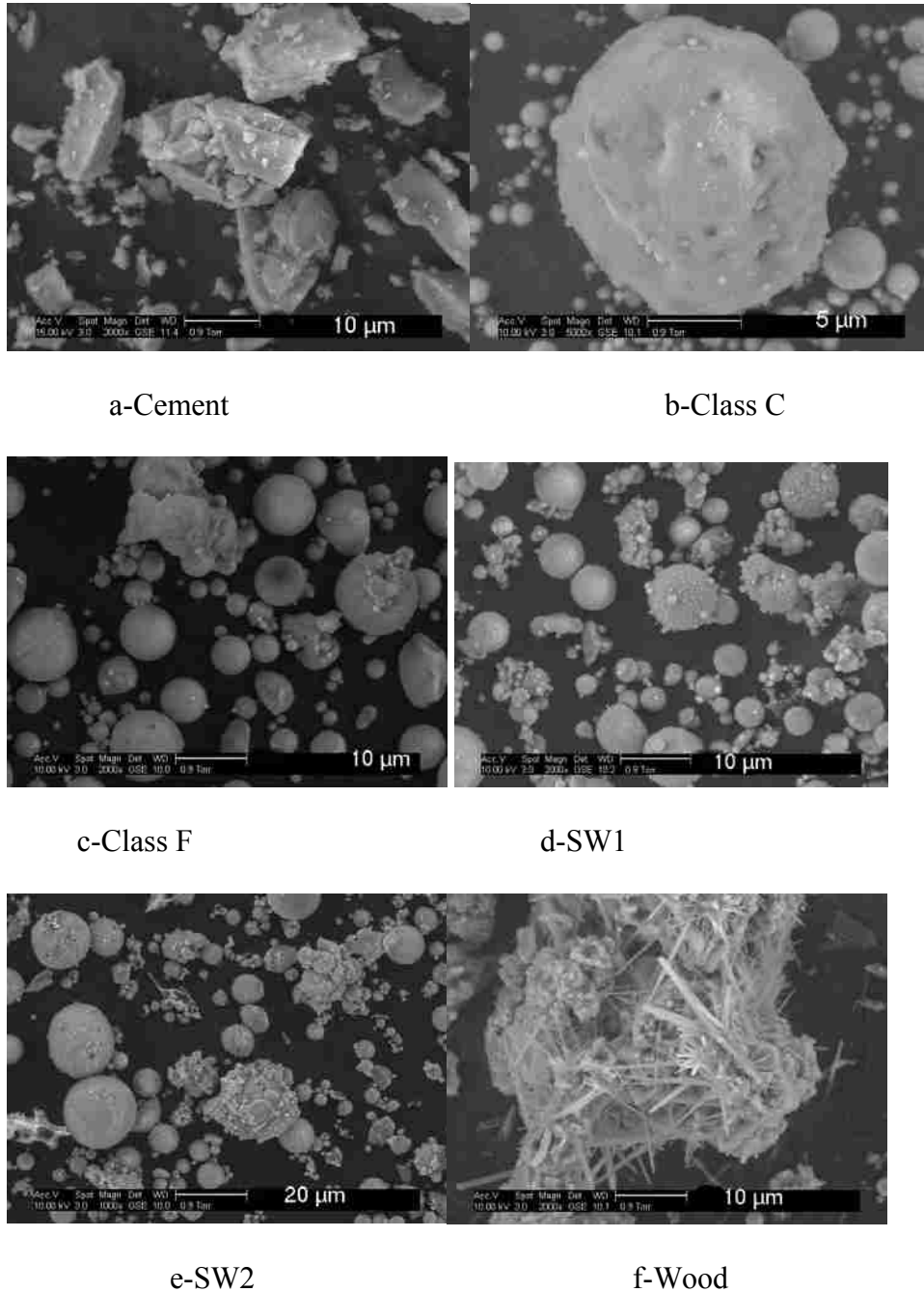
Figure 4-2 Scanning electron micrographs (SEMs) of cement and fly ash

The mixing procedure follows ASTM 192/C192 M-98. Cement and fly ash are first mixed by hand and then in the mixer. The Class F, Wood, and Wood C, Wood F fly ash do not mix readily with the other materials and require substantial effort to form a homogeneous sample. Batch sizes for casting bulk samples were nominally 4 cubic feet.

4.1.2.2 Slump and Air Content Tests

Slump is measured according to ASTM C 143. A standard cone sits on a smooth plate. About one-third of the cone is filled with fresh concrete followed by rodding (25 times) from the periphery to the center of the cone. This process was repeated twice until the cone was filled with concrete. Immediate removal of the cone causes the fresh concrete to slump and the cone height to change. The change in cone height represents the measured slump. All concrete samples have similar slump (3-5 inches), which was maintained by varying mix design parameters.

Air entrainment of the fresh concrete was measured by the pressure method described in ASTM C 231. In the procedure, fresh concrete fills one third of the tank of an air meter, followed by rodding (25 times) from the periphery to the center. This process is repeated twice until the tank is filled with fresh concrete. The tank is sealed and a pump increases the tank pressure to the full scale of the pressure meter (since the meter only shows a relative reading, no absolute pressure is indicated here). The volumetric change before and after the pressure indicates air content by assuming only air is compressed in the concrete mixture.

4.1.2.3 Setting Time Test

An additional one cubic foot mix was prepared according to the same mix design as the larger four cubic foot mix to provide the setting time sample. The procedures

follow ASTM C 403/C 403 M-99. The coarse aggregate passes through a #4 sieve and into a six-inch diameter cylinder twelve inches high. A penetrometer (device that measures force exerted on a surface by a needle) tests three separate batches of each mix as a function of time, indicating the penetration resistance as a function of time. Regression of the resulting rigidity vs. time data provides the setting time curves for each sample. The initial setting time is the elapsed time for the fresh concrete to reach a 500 psi penetration pressure and the final setting time is the time to reach a 4000 psi penetration pressure. Such thresholds are established by experience rather than scientific calculation.

4.1.2.4 Cylinder Compression Test

For each mix, three 4 inch (diameter) x 8 inch (height) cylindrical specimens were removed from curing conditions (humidity and temperature controlled, observing ASTM C 192/ 192 M-98) and tested on days 1, 3, 7, 28, 56, 91, and 365 from the time of mixing. The procedures follow ASTM C 39/ C 39M-99. Each sample was sulfur capped on each end according to ASTM C 617-98 before tested on the Baldwin Universal Testing Machine. A photograph of the test apparatus appears in Figure 4-3.

4.1.2.5 Beam Flexural Strength Test

For each mix, three 6 inch x 6 inch x 20 inch beams were removed from curing conditions and tested on the fifty-sixth day from the time of mixing. The test apparatus is illustrated in Figure 4-4. The specimen is supported by a steel rod on one end and a steel ball on the other. The specimen is adjusted so that the two steel balls of the compression head lay on its two positions at one third length. The specimens were tested using a

Baldwin Universal Testing Machine in accordance with ASTM C78 – 94 and the means were obtained from the average of the three specimens.

Figure 4-3 Cylindrical compression strength
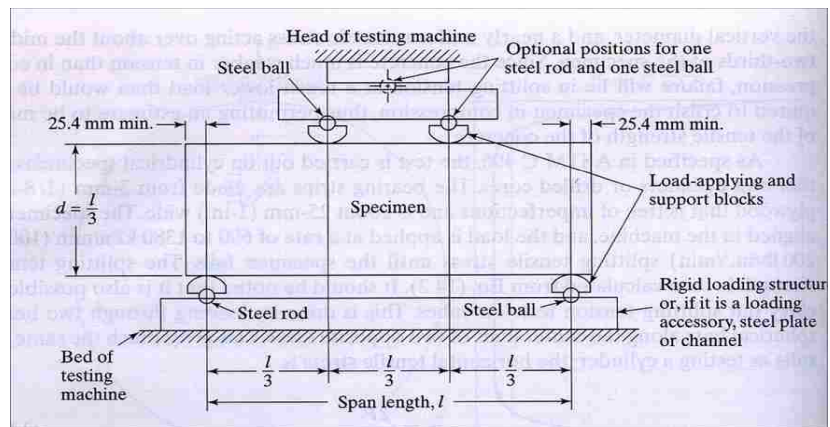
Figure 4-4 Flexure strength test by three point method

4.1.2.6 Freezing and Thawing

ASTM C666 describes the freezing and thawing procedures to test concrete specimens. Specimens cured for a certain time period are submerged in icy water in a freeze-thaw chamber. The temperature automatically varies from 0 to 40 ˚F within 2-5 hours for each cycle. The sample weight is measured from 0 to 300 cycles.

Three prisms (3-inch X 3-inch X 15-inch) prepared from each of the concrete mixes provide the primary test specimens. Each specimen, after demolding, was cured in a fog room for 28 days, then in air for the next 26 days, and finally back in a fog room for 2 days according to ASTM C 192C. Freezing and thawing experiments performed according to ASTM C666 Procedure A for up to 300 cycles generated the data for comparison. Weight loss percentage, instead of durability factor, is reported in this project, because the frequency measurement encounters some problems, which can not generate the necessary data for durability factor calculation. The air contents in the concrete mixes are controlled within 4-6% with air-entraining agent, which is supposed to be durable with respective to freezing and thawing tests (Woods 1968).

4.1.2.7 Rapid Chloride Permeability

ASTM C 1202 describes the rapid chloride permeability test. One sliced concrete sample is soaked first with water and then sealed into the instrument with one side contacting the solution of 3.0% NaCl and the other side with 0.3N NaOH. A 60V potential is applied across the sample and the temperature is maintained between 68 and 77 ˚F. After 6 hours, the total charge/current that passes through the sample is obtained by integrating the measured current as a function of time.

On the 55th day of curing in a fog room, two 2-inch thick specimens were prepared from a 4- inch (diameter) x 8-inch (height) cylinder for each mix. Each specimen was cut from the middle section of the cylinder using a water-cooled diamond saw. A belt sander removed the rugged edges and notches to produce a flat surface on both sides of the specimen. The specimens were tested according to ASTM C 1202-91 and the values are averaged.

4.1.2.8 Chemical and SEM Analysis

Image analysis of specimens obtained from fragments of concrete samples used primarily for compressive strength analyses provide the sample suite for this investigation. Images primarily from unpolished surfaces of these fragments allow evidence of crystallization and other chemical reactions. SEM-based images come from either a Philips XL30 ESEM FEG or a JEOL JSM840a, both of which are located in the BYU Microscopy Lab. ESEM samples are polished by 0.5 μm alumina polishing component. EPMA samples (24 x 46 mm polished thin section with epoxy impregnation) prepared by Wagner Petrographic Company in Provo, UT are analyzed on a Cameca SX50 EMPA in the geology department at BYU.

4.2 Quantitative Kinetics of Pozzolanic Reaction and Strength Build-up

4.2.1 Materials

This investigation uses Portland cement I & II, six fly ashes, calcium hydroxide, industrial silica sand and distilled water. The Portland cement is the same as the one used previously. Industrial silica sand passed through No. 30 and is from Granusil Mineral Fillers with 90.5% SiO_2, which has a durable performance based on its past history. The six fly ashes include Classes C and F, wood from pure wood combustion, 10P (10%

switchgrass cofired with 90% Powder River Basin Coal), 20P (20% switchgrass cofired with 80% Powder River Basin Coal) and SAW (20% sawdust cofired with 80% Powder River Basin Coal). The elemental analysis of fly ashes by X-Ray Florescence (XRF) appears in Table 4-5.

A laser particle size laser (Coulter LS 100) determined particle size distributions, which appear in Figure 4-5. Most wood fly ash particles fall in the range of 15-150 μm; while the remaining fly ashes have quite similar particle sizes ranging from 1-50 μm.

Table 4-5 Elemental analysis of fly ash

(w%)	Class C	Class F	SAW	10P	20P	Wood
TOTAL	100.66	99.05	102.25	101.51	102.02	99.82
SiO_2	37.26	54.91	35.23	36.22	38.27	48.94
Al_2O_3	19.62	27.79	20.87	20.88	21.1	12.47
Fe_2O_3	6.07	7.54	6.22	6.2	6.33	5.45
CaO	24.18	1.11	21.86	20.78	18.28	13.55
MgO	5.37	0.84	5.12	5.06	4.65	3.16
Na_2O	1.5	0.19	1.72	1.61	1.39	1.68
K_2O	0.43	2.4	1.89	2.01	2.49	3.37
Cr_2O_3	0.01	0.02	0.01	0.01	0.01	0.03
TiO_2	1.52	1.63	1.42	1.36	1.4	0.78
MnO	0.01	0.02	0.07	0.06	0.06	0.12
P_2O_5	1.2	0.28	1.73	1.73	1.75	0.95
SrO	0.3	0.1	0.33	0.32	0.3	0.06
BaO	0.66	0.12	0.62	0.59	0.54	0.07
SO_3	1.83	0.38	3.87	3.35	3.64	1.3
LOI	0.7	1.72	1.29	1.33	1.81	7.89
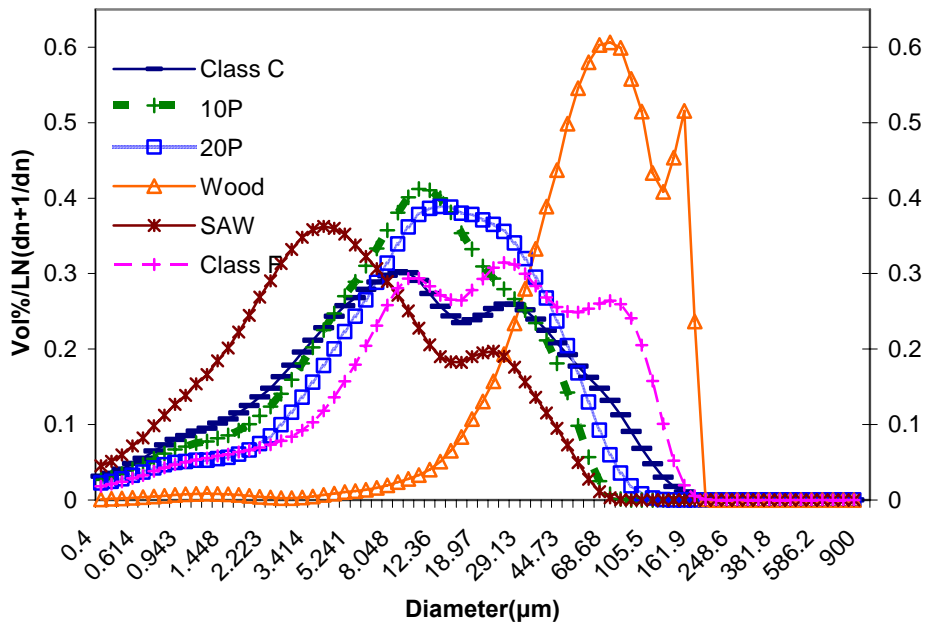
Figure 4-5 Fly ash particle size distribution (average of six measurements)

4.2.2 Experimental Design and Procedures

The experimental design involving six fly ashes, three mass ratios of fly ash to CH, three temperatures and six testing dates ranging up to one year requires 730 5-cm mortar cubes. The mortar had mass ratios of (fly ash + CH) to sand to distilled water of 1:2:0.5 except that a ratio of 1:2:0.65 was required to obtain the proper workability with pure wood fly ash mixtures. Fly ash to CH ratios of 80:20, 70:30 and 60:40 provide a range of mass loadings. The mortars filled 5-cm cubic molds, were de-molded after 24 hours and cured at three temperatures, 23 ºC, 43 ºC and 63 ºC. The samples were vacuum sealed to protect them from atmospheric CO_2 attack. The compression strength of the cubes and the reaction extent of CH were tested at 28, 56, 91, 182, 273 and 364 days after molding. Duplicate samples helped provide statistical information. Following the same

61

matrix design except the fly ash/CH ratio, the cement mortar cubes were molded and tested as a control.

4.2.3 Sample Preparation and Curing

Fly ash and CH were homogeneously mixed by hand. Modifications to ASTM C 109 provided improved mixing as follows. Approximately 1/3 of the sand was poured into the mixing bowl, followed by distilled water from a graded cylinder. The mixture of fly ash and CH was added and mixed for one minute at low speed, followed by 1.5 minutes at medium-speed. During the mixing, the bowl was covered with a polymer sheet to prevent water evaporation.

The molds were oiled with a thin film of lubricant to guarantee easy sample removal. Molding procedures followed ASTM C 109. The samples in molds were cured in a fog room (23 ºC) for 24 hours. Aluminum foil placed lightly over the samples prevented dripping water from affecting the samples while still allowing free moisture exchange.

All samples, except those from Class F, were demolded after 24-hours of fog room curing. The Class F samples from all three ratios of fly ash to CH were too soft to be demolded after 24 hours - they were cured in the fog room for two weeks so that they were hard enough to be safely demolded. TGA analysis illustrates that slow strength development is consistent with low CH reaction extent at the temperatures of fog room.

The samples cured for up to 12 months in temperature-regulated ovens in CO_2-evacuated, moisture-saturated, sealed, 473 ml (one pint)-Mason jars, as illustrated in Figure 4-6. A 0.6 cm thick piece of PVC ring at the bottom of the Mason jar prevented the samples from contacting 0.6 cm high distilled water in the bottom of the jar (to

maintain moisture saturation). Two cubes were stacked on top of the ring in each jar with a piece of wax paper between them to prevent them from reacting with or sticking to each other. Nitrogen purged the jar for 1 minute after which the jar was sealed with a hand vacuum pump (approx. 0.5 atm). In this manner the cubes cured in a CO_2-free environment with saturated moisture but not directly touching water. Cubes cured at each of three temperatures (23, 43 and 63 ºC) and for each of six dates (28, 56, 91, 182, 273 and 364 days) prior to strength and reaction extent testing. The strength and reaction extent at time 0 are each zero.

4.2.4 Cube Compression Tests

Compression tests followed ASTM C 109 procedures using an Instron compression-testing machine. The maximum load (one kip- one thousand pounds) was automatically computer recorded as a function of time and later converted into pressure with the surface area of the sample.

Figure 4-6 Vacuum and moisture curing of 2 in cube samples

4.2.5 TGA

After compression tests, the sample core was removed with a hammer and pulverized. Powder samples not able to be tested immediately were stored in a plastic vial at -20 ℃ in a freezer to minimize reaction during the storage.

The TGA tests were conducted from 25 to 700 °C at 25 °C/min in an inert N_2 flow environment. The main derivative peak in the temperature range of 300 to 600 °C associated with CH decomposition was integrated by the Pyrex software to obtain the CH amount. Since at the initial testing weight, moisture content changed from sample to sample, the mass ratio of CH to the ignited (700 ℃) sample mass instead of CH to initial sample mass was applied in the analysis. To determine the initial CH content, the fresh mortar (right after mixing) was tested by TGA. Although such a simple improvement, it was procedurally consistent with the other TGA measurements and proved much better than calculating the CH content from the mixing ratio by directly assuming 100% purity of CH product.

4.3 Mitigation of ASR Expansion and Pore Solution Analysis

4.3.1 Materials

High-alkali cement, opal, six fly ashes (Class C, Class F, Wood, 10P, 20P and SAW) and high purity silica sand are the raw materials used in the experiment. The six fly ashes are the same as the ones used in the quantitative kinetics of pozzolanic reaction.

Opal from Virgin Valley, Nevada substituted for the Corning Glass required by ASTM C 441 for economic, availability, and technical reasons. This opal, ground to pass No. 50 mesh (0.3 mm) and retained on No. 100 standard sieve (0.15mm), replaces the same size of high-purity quartz sand with a mass ratio of 5% based on the pessimum

effect recorded in the literature and experimentally verified in this project (Mcconnell, Mielenz et al. 1947; Barneyback 1983; Struble 1987).

The high purity silica sand was 99.9% quartz and the sum of equivalent alkali was less than 0.05%, which guarantees no significant extra leaching alkali to the system. The high purity quartz also acts as ASR expansion control based on its excellent performance of minimal ASR activity and expansion. The cement with high alkali content is from the eastern states and contains 1.15% alkali, which is much higher than the ASTM limit (< 0.6%). In practice, ASR expansion can require 10-30 years to detect. Use of high-alkali cement provides a means of accelerating the reaction and expansion and acts as a control sample.

The fly ash's equivalent alkali as determined by the procedures in ASTM C33 and the alkali of cement appears in Table 4-6. The size and mass percentages of opal and sand (in terms of total mass of sand plus opal) appear in Table 4-7. To minimize the source and amount of alkali metals, except those from fly ash and cement, distilled water was used in this investigation.

Table 4-6 Available alkali content of fly ash and equivalent alkali of cement

Item	Cement	Class C	Class F	Wood	10P	20P	SAW
$Na_2O\%_{avail/\,equiv)}$	1.15	1.03	0.73	1.78	2.71	2.46	2.88

Note: by ASTM C 33

Table 4-7 Size distribution of sand and opal

Sand mass%					Opal mass%
No.4-8	No.8-16	No.16-30	No.30-50	No.50-100	No.50-100
10	25	25	25	10	5

4.3.2 Design and Manufacture of High-Pressure Mold

Pore solution exists in concrete macro and meso pores, whose chemistry provides concentrations of alkali metals (Na^+ and K^+) and other ions, and thus insight into mechanisms of alkali silica reactions. Analyzing the alkali concentrations of pore solution can directly study the effect of fly ash's role rather than computation of alkali concentration by the available alkali from ASTM C 33, since only partially available alkali leaches out and contributes to alkali silica reactions (ASTM-C311 1990).

The pore solution was successfully derived from high-pressure extrusion (Longuet, Burglen et al. 1973). There are several modified versions of the high pressure mold (Barneyback and Diamond 1981; Durand, Berard et al. 1990).

The high-pressure mold manufactured for this project followed the ideas from Barneyback and Diamond (Barneyback and Diamond 1981). The mold has a pre stressed double layer cylinder that can withstand the high extrusion pressure (as high as 650 MPa). The pre-stressed design reduced by over 75% the amount of material required for the pressure cell compared to a single wall design and more even distributed the stresses, making the design much safer. For a single wall design, the estimated weight of the mold including the other parts (piston, base, and possibly supporter) is about 200 to 300 lbs; while in the present design, the mold weighs about 50 lbs.

The crucial design of the high-pressure mold is the pre stressed cylinders. The outer diameter of the inner cylinder is 3.6352 in, while the inner diameter of the outer cylinder is 3.6280 in, which provides a 0.0072 in difference. The outer cylinder was heated to 500 °C and the inner cylinder was cooled to -20°C so that the thermal expansion and shrinkage from the outer and inner cylinders exceeded the initial diameter difference

at ambient temperature. The inner cylinder was inserted into the outer cylinder immediately and the two cylinders locked tightly as their temperatures returned to ambient. The heating temperature of the outer cylinder was carefully chosen so that enough clearance was produced for the successfully inserting the inner cylinder into the outer cylinder (high temperature produce high clearance) and heating temperature was as low as possible to reduce negative impact on the mechanical properties of the materials.

The bottom platen has a circle groove on the top surface and four small channels connect to the groove for pore solution collection. Six long bolts fix the top plate, the cylinder mold, and the bottom platen. After the sample (2 in diameter X 4 in height concrete cylinder) is placed in the mold, a Teflon disk (0.2 in thick X 2.10 in diameter) is inserted between the concrete specimen and piston to seal the chamber and prevent pore solution loss. A photograph of the mold and a sketch appear in Figure 4-7 and Figure 4-8 , respectively.

Figure 4-7 High pressure mold
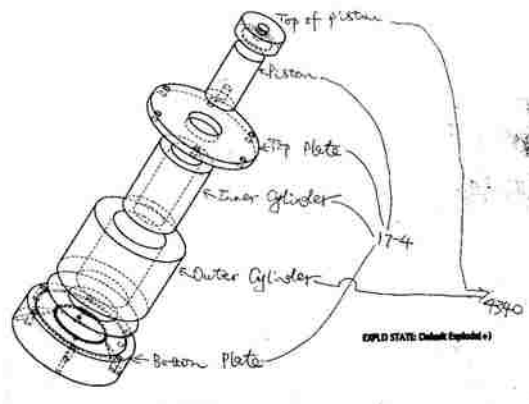
Figure 4-8 Mold sketch

There are several improvements from previous designs, illustrated in Figure 4-7 and Figure 4-8. Stainless steel P 17-4 forms the inner cylinder wall instead of 4340 carbon steel, rendering the mold more durable against high-alkaline pore solution attack (AK-Steel-Corporation-Website 2000). Six bolts secure the cylinder to the base, improving safety and stability. Four holes rather than two are drilled in the base, with two for nitrogen purging and the other two for pore solution collection. Threaded brass fittings connect the base to Teflon hoses to prevent leaks and guarantee easy assembly.

All parts except the outer cylinder were fabricated of stainless steel P 17-4 to improve corrosion resistance to high-alkaline pore solutions. The outer layer of the cylinder was made of 4340 carbon steel for cost reduction. The heat-treated parts from 4340 carbon steel have a yield strength of 90 metric tons and the parts with stainless steel P 17-4 have a yield strength of 81 metric tons. The pressure safety factor in the design is 2.9, somewhat lower than the standard 3.5 most commonly used (see Appendix D for more details).

4.3.3 Experimental Design and Procedures

4.3.3.1 Available Alkali of Fly Ash

Not all the alkali in the fly ash from the bulk chemical analysis is available in the fly ash cement hydration system, since some alkali is bonded tightly in the crystalline phases of fly ash, which cannot leach out during hydration. Knowing the amount of available alkali from the fly ash and sand is crucial for this investigation. However, the total alkali of the high purity sand is less than 0.01%, rendering the available alkali from sand can be confidently ignored.

The fly ash available alkali was tested according to ASTM C 311. Five grams of fly ash and two grams of CH was transferred into a 25 ml plastic vial; ten ml deionized water was added, stirred, and the vial was capped and sealed by tape. The capped and tape sealed plastic vial was also stored under vacuum in a 1 pint mason jar to further prevent the disturbance of atmospheric CO_2 and moisture loss.

The sample was stored at 38±2 ℃ for 28 days and then it was ground with necessary water addition. The homogeneous slurry was then diluted into 200 ml and filtered. The filtrate was neutralized with 1:3 HCl (by weight) and then the total amount of Na and K were analyzed by AA and reported as equivalent percentages of sodium oxide (Na_2O).

4.3.3.2 Mixing, Sample Making and Curing

An experimental design of 20 mixes, which include the cement with opal, cement without opal, and 15%, 25% and 35% (mass) cement replaced by the six fly ash samples, provides the basic approach. A ratio of water to sum of cement plus fly ash was fixed at 0.6 for all mixes except for three wood mixes with a ratio of 0.65. This ratio provides

enough pore solution for analysis up to tests at 6 months after samples curing (Barneyback and Diamond 1981).

The mixing procedures follow ASTM C 109 with a mechanically driven mixer. To improve mixing, three extra procedures were taken in addition to the ones in ASTM C 109: 1) fly ash and cement were premixed by hand in a bucket; 2) opal was mixed with quartz sand by hand in advance; and 3) a 1/3 sand and opal mixture was placed into the mixing bowl before the cementitious materials (cement + fly ash) so that the cement would not stick to the mixer's inner wall.

Photographs of steel molds 1 in x 1 in x 10 in (ASTM C 490) for ASR bar samples appear in Figure 4-9. Before the mortar was poured, a piece of foil lined each old and a thin film of viscous gear oil spread over the foil, which prevented the bars from breaking during demolding due to strong adhesion to the mold walls. Also, such procedures protected the molds from erosion. Two machined studs were cast into each end of the bars. For pore solution extrusion, six 2 in (diameter) x 4 in (length) cylinders were prepared simultaneously with the bars from each fly ash mixture at each ratio.

Figure 4-9 Steel molds and end studs for ASR bars

Bars rested for approximately 24 hours prior to demolding. A digital length comparator determined their length before curing in 100% moisture in standardized containers (ASTM C 227). The ends of the two machined studs served as the length measurement points as illustrated in Figure 4-10.

The bar samples were cured in containers manufactured as part of this project to meet ASTM standards, as shown in Figure 4-11 and Figure 4-12.

The bottom of the container contains water and the bar samples stay on a plate about five cm above the water. Cotton strings (water wicks) run between the samples, connecting the plate supporting the samples separated by the grids.

Figure 4-10 ASR bar length measurement (precision $\pm 10^{-4}$ in)

The strings are tied on the girds on one end. The other end was weighted with a fishing weight suspended in the water to keep them straight but water-soaked during

71

curing. To further ensure relatively homogeneous curing conditions, the positions of the samples are exchanged from the center to the edge after each length measurement.

The cylinders were cured in 473 ml (1 pint) Mason Jars under vacuum and in a CO_2-free, water saturated environment, as illustrated in Figure 4-13. The samples sat above, but did not touch distilled water in the bottom of the jar. The walls of the mason jars were covered with tightly stretched wet cotton cloth extending into the water to wick moisture up the side of the container. Such a treatment simulates the curing conditions of the bars in the ASTM containers so that the pore solution extruded from the cylinders would closely resemble that from the bar samples.

Figure 4-11 ASR bars cured in ASTM containers
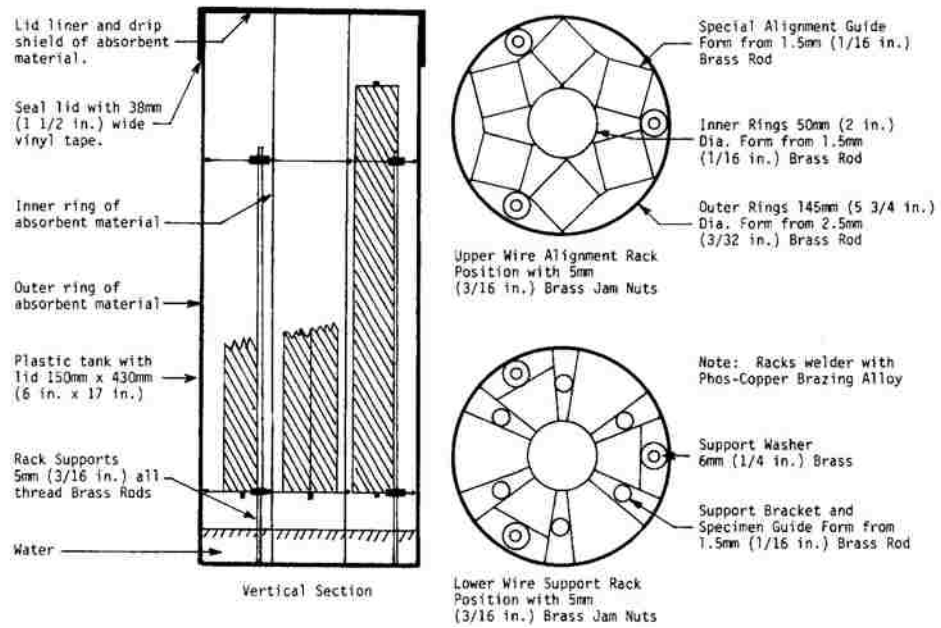
Figure 4-12 Illustration of ASR container from ASTM C 227

Figure 4-13 Vacuum Sealing of ASR cylinders for pore solution extrusion

5. Results and Discussions

5.1 Properties of Fresh and Hardened Concrete and Microstructure

5.1.1 Concrete Mixing and Parameters

Table 5-1Mix designs, slumps, air content and air surfactant

	Slump	Water	Cement	Fly Ash	Fine Aggregate	Coarse Aggregate	Surfactant	Air
	in	lbs/yd^3					oz/100lbs cementitious	%
Cement-1*	5.0	300	600	0	1041	1776	0.42	5.0
Cement-2	3.4	298	596	0	1228	1598	0.45	4.5
Class C-1	5.3	288	432	144	1233	1598	0.79	4.3
Class C-2	3.2	287	431	144	1238	1598	0.79	4.0
Class F-1	3.0	270	405	135	1312	1598	1.17	3.2
Class F-2	4.0	295	443	148	1203	1598	1.76	5.5
SW1-1	4.0	303	455	152	1169	1598	2.36	4.0
SW1-2	5.0	303	455	152	1171	1598	2.50	5.5
SW2-1	3.8	295	443	148	1205	1598	1.80	6.1
SW 2-2	3.4	297	445	148	1197	1598	1.67	5.3
Wood-1	4.3	318	477	159	1106	1598	0.79	4.3
Wood-2	3.8	318	477	159	1106	1598	0.81	5.4
Wood- 3	3.0	318	477	159	1106	1598	0.81	5.0
Wood C-1	3.5	290	435	145	1225	1598	0.90	4.5
Wood C-2	3.9	293	440	147	1212	1598	0.92	4.6
Wood F-1	3.0	295	443	147	1203	1598	1.52	3.7
Wood F-2	5.0	298	447	149	1186	1598	1.56	6.0
Wood F-3	3.8	298	447	149	1186	1598	1.56	4.5

* Each mix was repeated 2 or 3 times; for example, Cement-1 is the first mix of cement.

The mix design and performance parameters appear in Table 5-1. The data include results from two or three mixes of each material and typically three samples of each mix, for a total of six to nine analyses for each condition. The tests that involve

time-varying results (compression test, for example) include replicates at each time for each mix design. Replications help prevent spurious results from influencing the conclusions and provide means of determining statistical significance of the results.

In many cases, air entrainment and especially slump differed in the large batches compared to the small batches used to develop specific mix designs. Coarse aggregate segregation and washing improved the consistency of performance between small and large batches. The great majority of the mixes summarized above fall within the target range of slump and air entrainment, but four batches of the first round, Class C-1, Class F-1, SW2-1 and Wood F-1 fall slightly outside these ranges (slump 3-5 inches, air content by volume 4-6%). There proved to be no consistent or statistically significant difference in the strength or durability from these samples compared to their replicates, so data from them are included in the overall data set.

5.1.2 Water Demand

Figure 5-1 illustrates water amount with average of two samples for each design mix. All samples except wood mix have similar or lower water demand than pure cement mixes. The higher water amount of wood mix could arise from the irregular particle shape, high porosity (see Figure 5-2) and higher LOI (see Table 4-4) (Helmuth 1987; Wesche 1991; Fouad, Copham et al. 1998; Naik and R. 2003). The generally lower water amount of fly ash represents a commonly observed advantage relative to pure cement and apparently arises from the high-temperature treatment of the particles producing less porous and more spherical material (Ravina and Metha 1986; Wesche 1991). These spherical particles reduce the effective viscosity of wet concrete mixtures such that concrete flows more easily at a given moisture content or can be prepared with lower

moisture content at a given level of workability, the latter commonly leading to higher overall strength after setting.
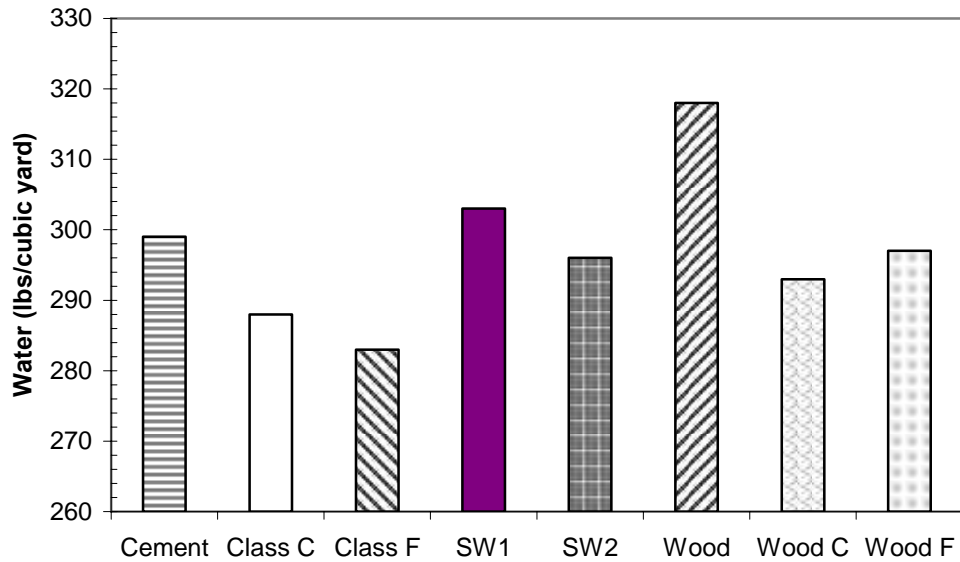
Figure 5-1 Water amount for each of the concrete mixes (average of two samples)
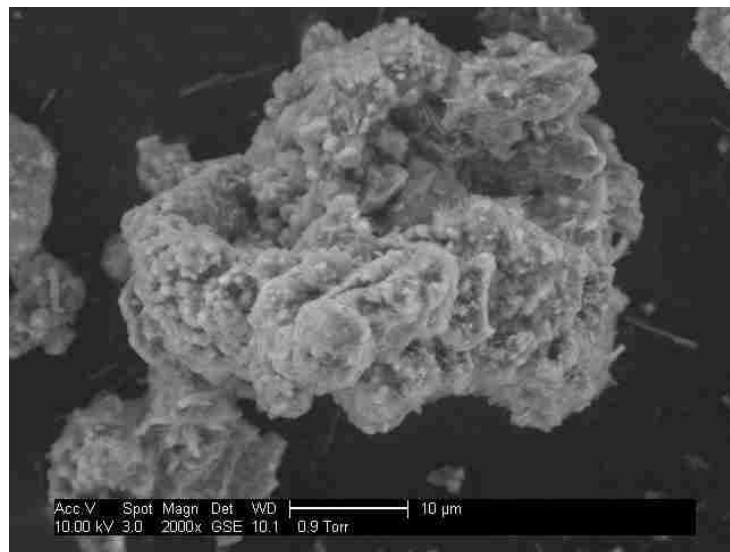
Figure 5-2 SEM picture of wood: porous and non spherical morphology

5.1.3 Air Surfactant
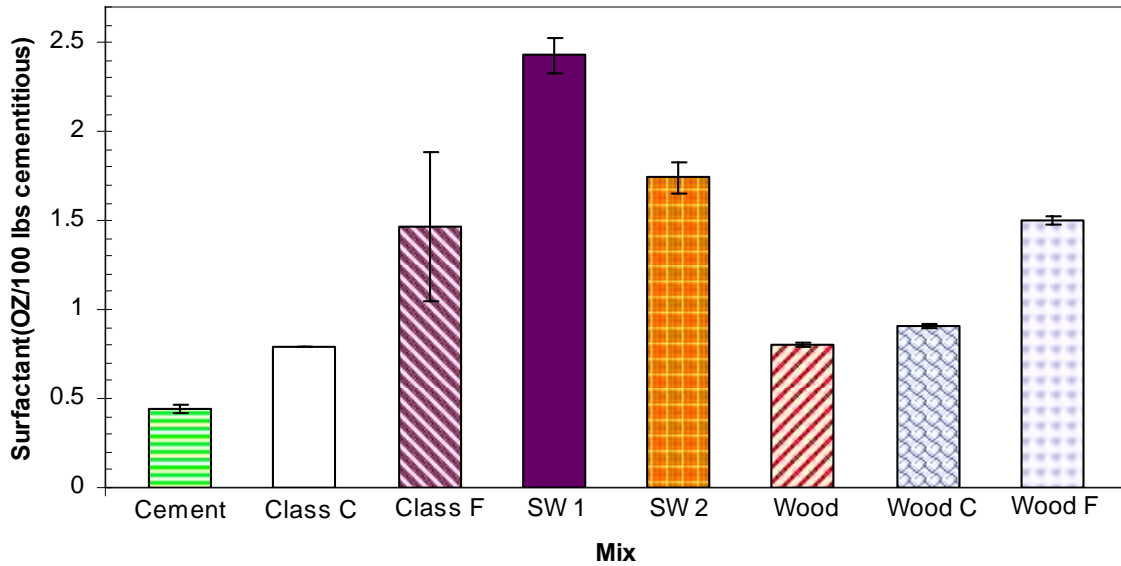
Figure 5-3 Air surfactant amount of concrete mix

Among the most practically significant results in these data, so far as day-to-day cement production is concerned, is the amount of air entraining agent to meet the target slump and entrained-air values, as illustrated in Figure 5-3. Fly ash addition in general, and biomass fly ash addition in particular, increase the amount of required entraining agent (Helmuth 1987; Wesche 1991; Mindness, Young et al. 2002). Such findings present no economical concerns, since all amounts represent a few ounces per hundred pounds of total cementitious material (cement plus fly ash). However, there is a processing concern in that commercial fly ash use, often neglects careful monitoring and control of air entrainment. Since air entrainment varies with type and amount of fly ash used, but fly ash preparation commonly proceeds on the basis of a design mix rather than

measured air entrainment, additional measures must be applied in preparing concrete with fly ash to assure proper air entraining agent amounts and consistent quality.

While fly ash addition does not appear to substantially affect the freezing and thawing behavior of concrete when a sufficient amount of air is entrained, fly ash addition strongly impacts that amount of air-entraining agent required to meet the specification (ASTM C 666). Figure 5-4 illustrates the amount of air-entraining agent for each of the concrete mixes (with 95% confidence levels). Mixes can be approximately divided into three groups: 1) SW1 fly ash requires the highest amount of air-entraining agent to meet ASTM standards; 2) SW2, Class F and Wood F have medium air-entraining agent requirement; 3) Wood, Wood C, Class C and pure cement have the lowest air-entraining agent requirement.
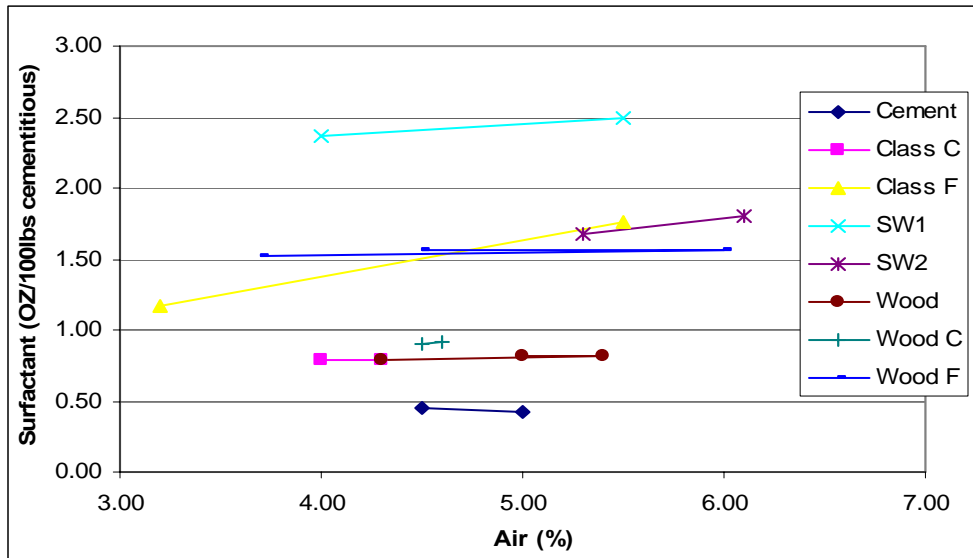
Figure 5-4 Air Entrainment amount to create air content for all concrete mixes

Further investigation of air entrainment agent related to unburned carbon appears in Figure 5-5, which can partially explain the results obtained (Helmuth 1987; Wesche 1991). The amount of air entrainment increases almost linearly with increasing LOI % in the fly ash samples of cement only, Class C, Class F, SW1 and SW2, independent of the type of the fly ash. These findings are consistent with the results and expectations from other researchers (Helmuth 1987; Wesche 1991) since LOI or carbon in fly ash commonly absorbs and removes air entraining agents from the mixture by their relative larger surface areas. The reasons that wood fly ash appears largely uncorrelated with this trend may arise from the larger average particle size and hence lower surface area to volume ratio of wood compared to the other fly ash (Figure 4-1) or possible differences in carbon forms (Hill 1997). Therefore, not only the total carbon or LOI content, but also the surface areas and the forms of carbon of the fly ash influence the amount of surfactant to achieve the sufficient amounts of entrained air.
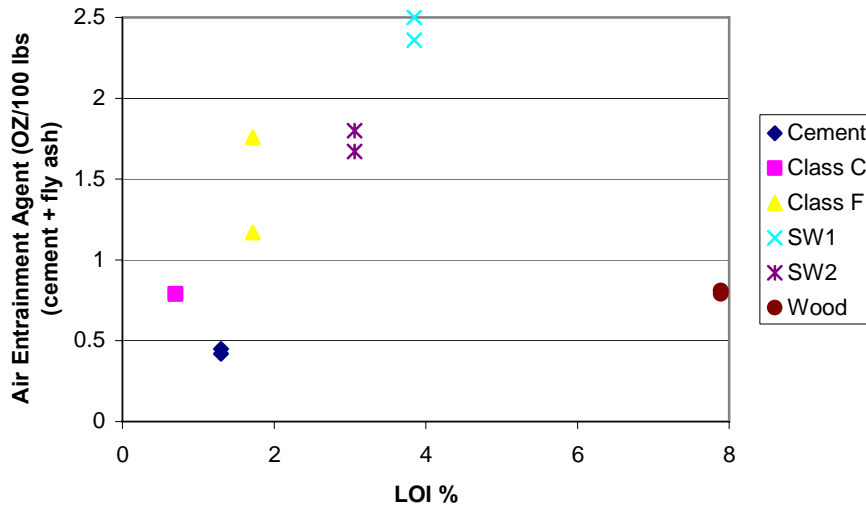
Figure 5-5 Relationship between air entrainment requirements and LOI %

80

5.1.4 Setting Time

Transient strength development of each concrete mix appears as a function of time in Figure 5-6. None of the samples develops significant strength within 300 minutes. Fly ash addition of any type delays strength build up, as is evident in the data and well documented in the literature with respect to coal fly ash (Ravina and Metha 1986; Wesche 1991; Hewlett 1998; Brooks 2002). Results for the various biomass fly ashes lie within or near the range of results from coal fly ashes, indicating the biomass fly ash does not disproportionately impact concrete strength development rate (setting time).
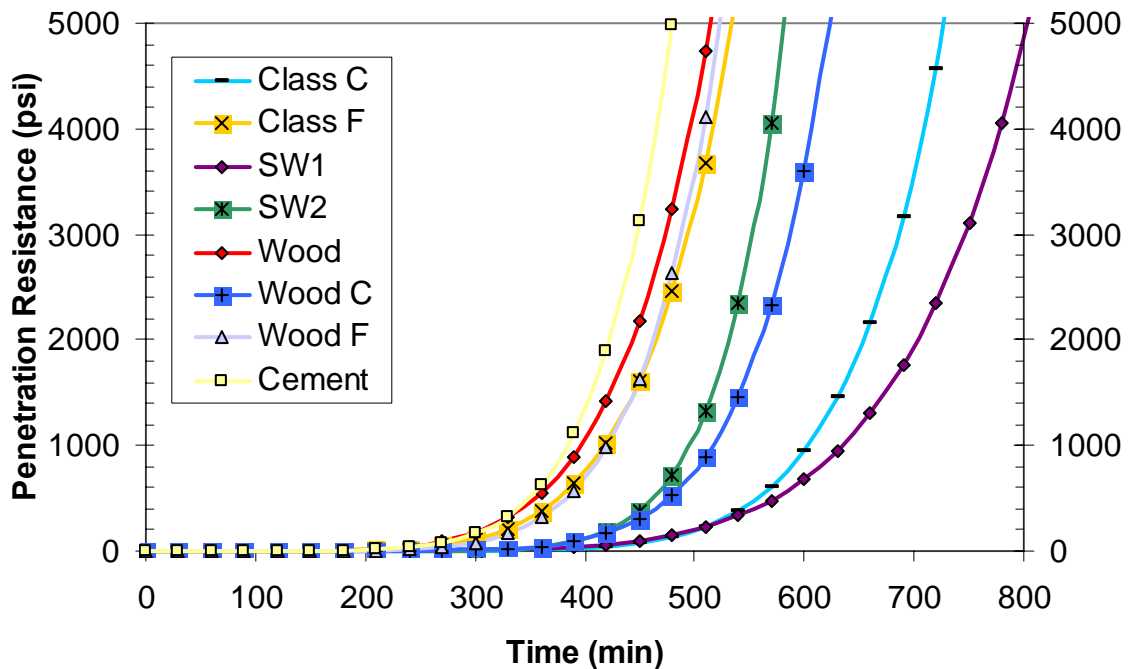
Figure 5-6   Setting time for each concrete mix

5.1.5 Cylindrical Compression

Figure 5-7 illustrates compression strength as a function of time (note the non-linear time scale) with 95% confidence intervals calculated from the pooled standard

deviations and the replicates of each mix at a fixed date. The cement mix exhibits the highest strength up to 7 days; from 28 days to one year, the compressive strength of all fly ash samples except wood become comparable to that of pure cement. Similar results have been obtained by other researchers for coal fly ash (Ukita, Shigemastu et al. 1989; Hewlett 1998; Mindness, Young et al. 2002; Sengul, Tasdemir et al. 2005). Wood C, Wood F, SW1 and SW2 mixes generally lie within the range of pure coal fly ash results, indicating that neither wood- nor herbaceous-derived biomasses disproportionately affect strength development. The wood results provide useful comparison data. Its lower strength results from larger particle size (Erdogdu and Turker 1998) and possibly other unclear reasons due to limited and contradictory information (Fouad, Copham et al. 1998; Naik, Kraus et al. 2003; Naik and R. 2003). These data support the mechanistic view of fly ash influence on concrete. That is, fly ash reacts slowly (hence the early low strength) but effectively with calcium hydroxide through pozzolanic reactions. Since the fly-ash-containing samples here displace cement with fly ash, the long-term data indicate that the pozzolanic reactions, associated only with calcium hydroxide and fly ash, ultimately develop as much strength as the cementitious reactions common to traditional concrete. That is, 75% cement and 25% fly ash ultimately develops as much strength as 100% cement.

5.1.6 Beam Flexure

Figure 5-8 illustrates flexure strength results at 56 days, again with 95% confidence intervals based on pooled standard deviations and replicates for each mix. The 56 days flexure strengths of all fly ash mixes except pure wood lie within the 95% confidence interval of values for pure cement. More significantly for the subject of this

investigation, the values from the biomass containing fly ash, either cofired or blended, do not differ significantly or systematically from those for pure coal fly ash. The wood behavior is consistent with its low compressive strength, with similar underlying reasons: larger particle size and potentially other properties compromising its flexure strength (Fouad, Copham et al. 1998; Naik, Kraus et al. 2003; Naik and R. 2003).
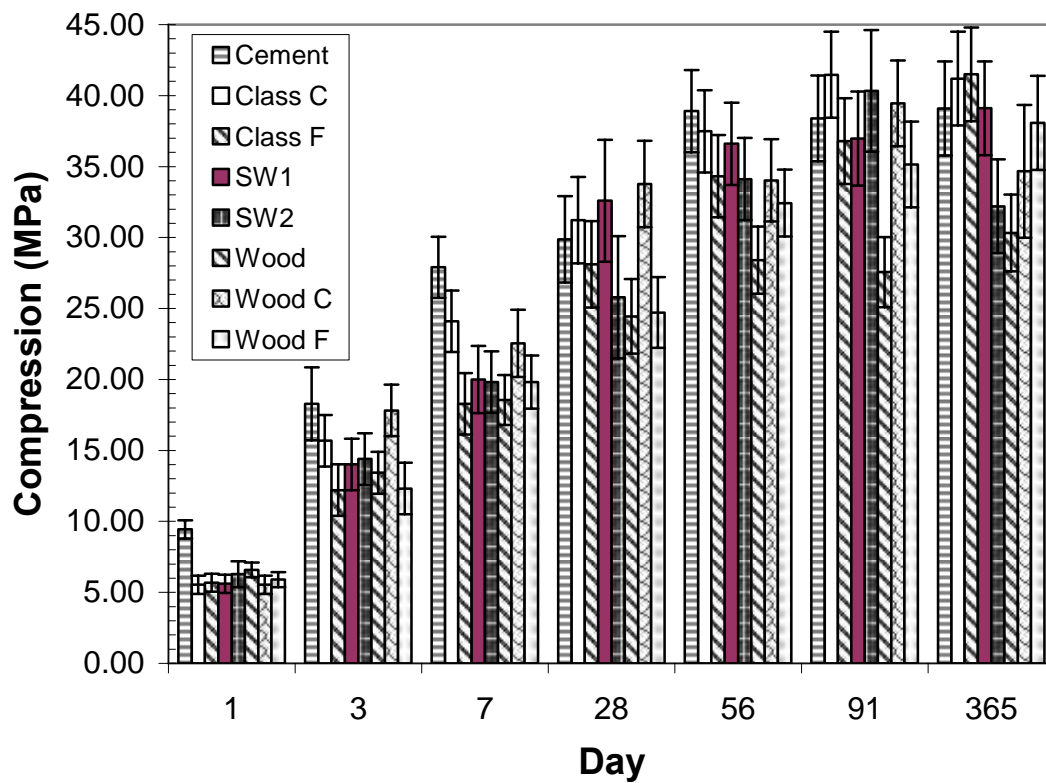
Figure 5-7 Compressive strength for each sample material

5.1.7 Freeze-Thaw Behavior

Figure 5-9 illustrates that the weight loss of all fly ash concrete mixes except Class C (coal) fly ash is less than or equal to the control cement mix, within the statistical uncertainty of the measurements (95% confidence interval).

Such results are consistent with previously reported results from coal fly ash alone and suggests that fly ash, either Class C, Class F or wood, has little impact on freezing and thawing behavior (Woods 1968; Helmuth 1987; Wesche 1991; Fouad, Copham et al. 1998).
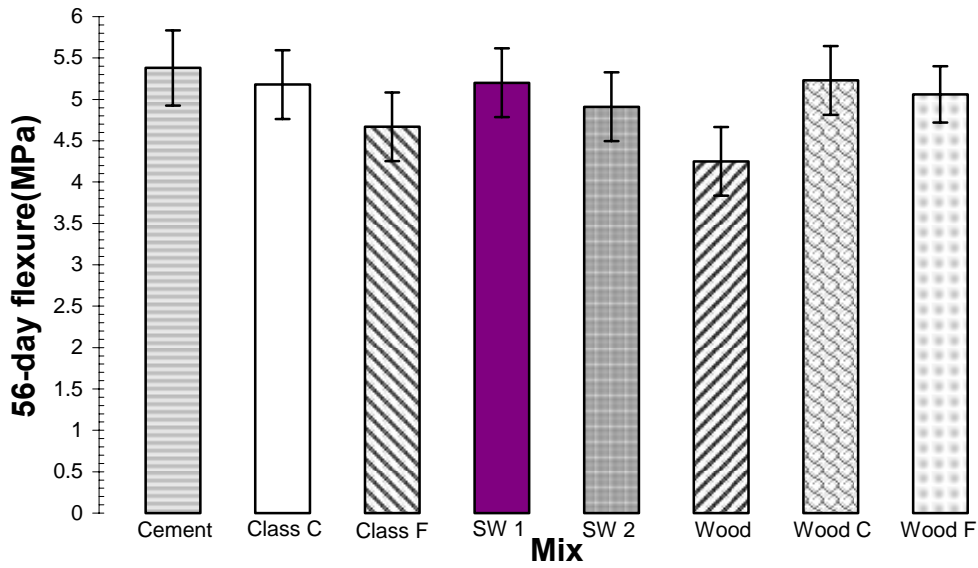
Figure 5-8 Flexure strength 56 days after casting for each sample material

Figure 5-9 Freezing and thawing behavior of fly ash concrete samples

The weight gain phenomena might be attributed to water gain of samples in the freezing and thawing machine, which lost too much moisture during the 26-day exposure to air to be compensated by the ASTM standard of 2 days in fog room prior to testing.

Figure 5-10 shows durability factors of Class F and wood mix, which correlated roughly with the weight loss percentages shown in Figure 5-9.
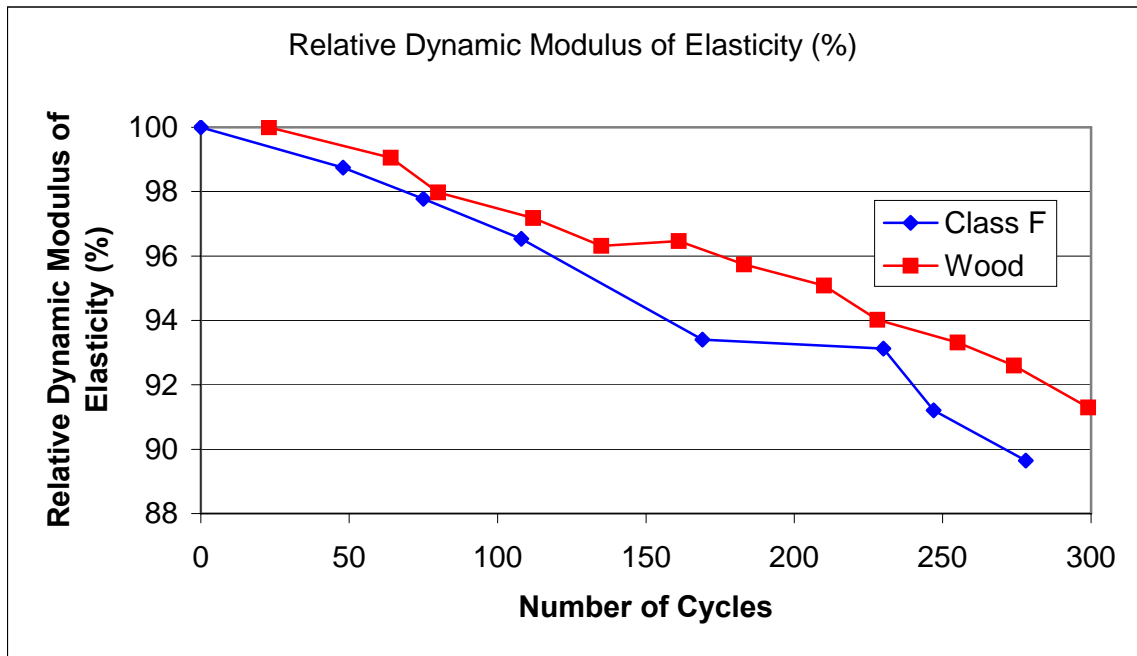
Figure 5-10 Durability Factors of class F and wood mix (note: all other mixes are not included here due to the improper performance of test machine)

5.1.8 Rapid Chloride Permeability

Rapid chloride permeability depends strongly on the water to cementitious material ratio, curing conditions and curing days (Alhozaimy, Soroushian et al. 1996; Scanlon and Sherman 1996; Zhang, Bilodeau et al. 1999).
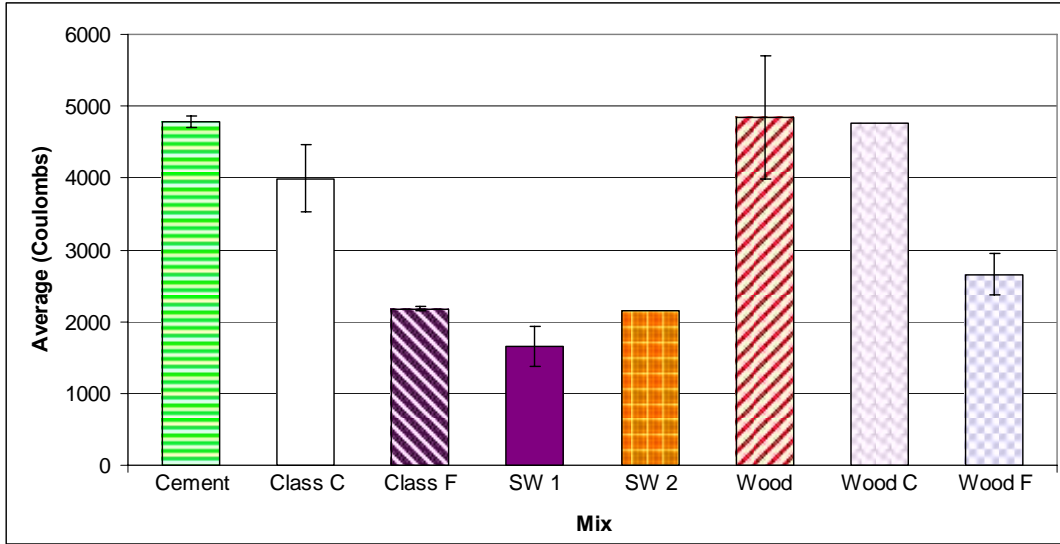
Figure 5-11 Rapid chloride permeability (56th day, average of two samples)

Since the ratio of water to sum of cement plus fly ash is fixed at 0.5, curing conditions are the same by ASTM C192 and testing time is fixed at the 56th day after mixing, these data show how fly ash will affect RCPT.

Figure 5-11 summarizes the results of RCPT. Wood mixes have similar ions passed as pure cement mix; Class C has lower permeability than Wood mixes; Class F, SW1 and SW2 mixes have the lowest permeability; and the blended Wood C and Wood F samples exhibit permeability intermediate between those of the mix components.

Permeability differences relate to fly ash particle size, modification of pore size distribution due to pozzolanic reaction, and changes of pore solution chemistry. The following factors are taken into consideration for the evaluation of permeability. First, wood fly ash has a much coarser particle size than Class C, Class F, SW1 and SW2. Second, Class C, Class F and wood fly ash have quite similar pozzolanic reactivity indicated by the hydrated lime consumption at two months (Wang, Dalton et al. 2007).

Finally, equivalent alkali percentage by ASTM C 33 vary accordingly - wood fly ash 1.78, Class C 1.03 and Class F 0.53 (Wang, Dalton et al. 2007).

If similar pozzolanic reactivity infers similar pore size modification, then Class C, Class F and wood fly ash should be similar. Since pore solution mainly contains OH^-, Na^+ and K^+, equivalent alkali from fly ash will play the main role of pore solution modification. Because wood fly ash has a larger particle size and high equivalent alkali compared to other samples, wood mixes should and do exhibit the highest permeability among fly ash concrete mixes. Class C has higher equivalent alkali percentage than Class F fly ash, and this may be reason that it has higher permeability. The coal results are also consistent with many other researchers (Alhozaimy, Soroushian et al. 1996; Shi 2004).

5.1.9 Microscopy

Many features of fly ash reactions in concrete exhibit morphological behaviors observed from SEM images. The data, even when accompanied by composition analysis, can at most be semi-quantitative since they represent isolated instances and the quantitative data are subject to errors associated with surface roughness and matrix effects. Nevertheless, images often provide substantial, if qualitative, information about mechanisms and phenomena. The quantitative extent of fly ash reaction appears in subsequent sections of this discussion while this section focuses on qualitative and semi-quantitative results.

5.1.9.1 Reactive Fly Ash Particles by SEM and EDX Analysis

Figure 5-12 shows a CH crystal, the products of cement hydration, and the reactants of the pozzolanic reaction. The fly ash particles in the concrete react slowly with CH to form a C-S-H gel, and the reaction may go on for years. Figure 5-13 shows

barely reacted Class F fly ash particles in a 56-day-old concrete sample. The smooth particle surfaces indicate minimal reaction.

Figure 5-14a shows a broken cenosphere of SW1 fly ash in a concrete mix after 573-days of curing. The morphology suggests the shell and the inner components come from different sources and the EDX spectrum in Figure 5-14 b and c confirms that they have different chemical compositions.

Particle cross sections provide detailed information on the conversion rate. The remainder of this discussion uses such samples to illustrate qualitatively, with semi-quantitative composition profiles, the pozzolanic reactions that form the center of this discussion.
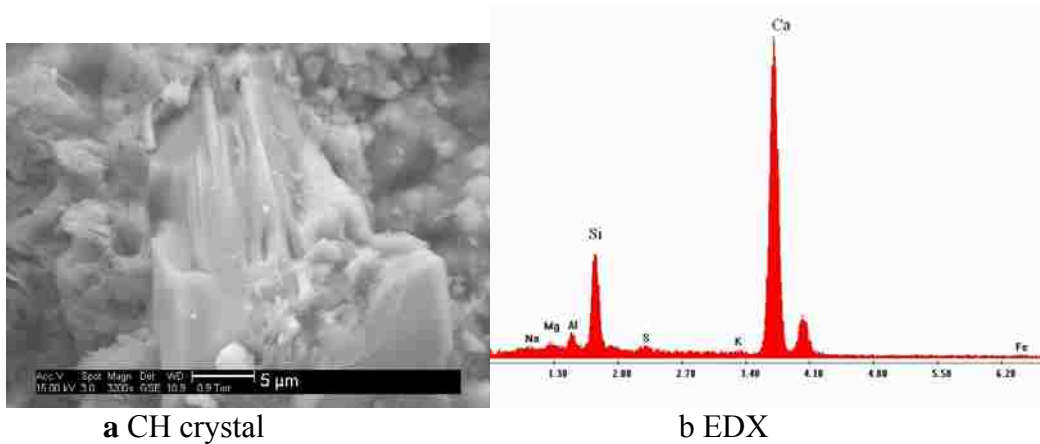
a CH crystal   b EDX

Figure 5-12 Laminated CH crystal in Wood mix (658-day)
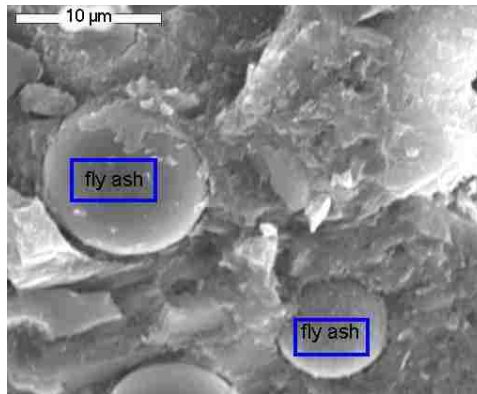
Figure 5-13 Barely reactive fly ash particle in Class F mix (56-day)
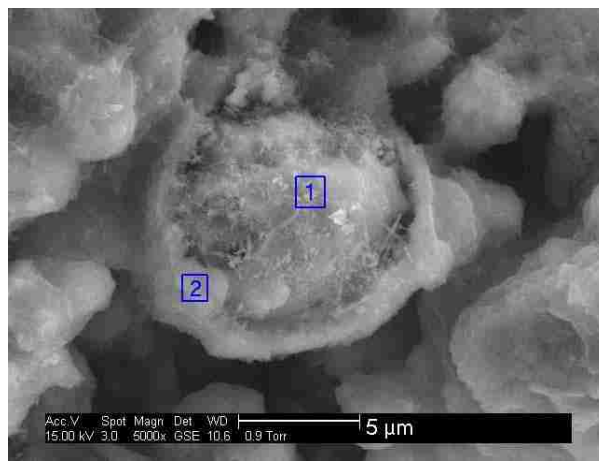
a SW1 fly ash particle
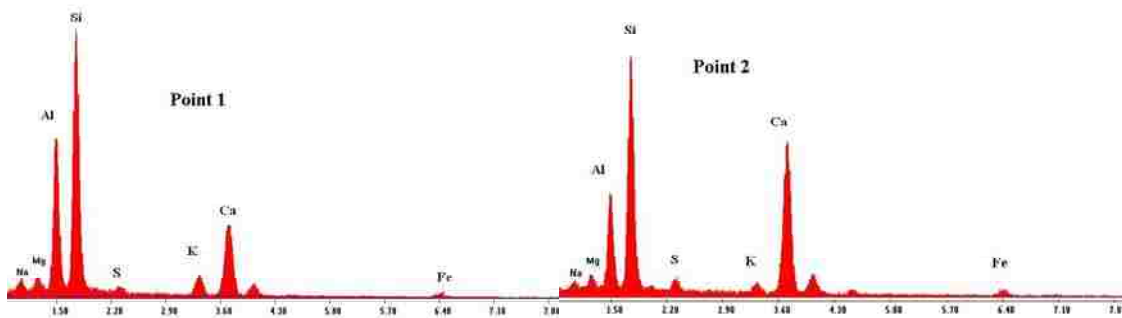
b EDX point 1   c EDX point 2

Figure 5-14 The spectrum of reactive fly ash particle in SW1 mix (573-day)

Many of the particles analyzed are relatively large, providing optimal illustration of gradients, etc., but perhaps underestimating of the conversion rate of the samples.

5.1.9.2 Chemical Analysis by ESEM

All the reactive fly ash particles samples are polished thin sections except that the raw SW1 and SAW fly ash particles in Figure 5-19 and Figure 5-25 are polished concrete slabs. Figure 5-15 illustrates a reactive fly ash particle after one year in concrete. The outer parts are in several broken layers, which are most probably caused by pozzolanic reaction. The inner part is still in a solid state and seems to stay inert.

The scanning voltage was first set at 8 kV, and several reasons for such setting are listed below. Major elements in fly ash concrete, such as Al, Si, Ca and Fe, have the absorption edge voltage as 1.560, 1.840, 4.037 and 7.110 kV, respectively. The above four elements can be only detected with acceleration voltage higher than their absorption edge voltage. Furthermore, for a good quantitative analysis of one element, the acceleration voltage should be at least 2-3 times of the element's absorption edge voltage. For example, to get a good quantitative analysis, the acceleration voltage of Ca should be at least 8.074 (4.037 X 2) kV and that of iron 14.220 (7.011 X 2) KV. However, higher excitation voltage leads to higher excitation volumes for the same density of materials. Assuming the densities of C-S-H gel and typical fly ash particles are 2.0 g/cm^3 and 2.5g/cm^3, respectively, the diameter of the excitation volume becomes approximately 1.2 µm at 8 kV and 2-2.5 µm at 15 kV). Therefore, accurate and spatially resolved chemical analysis of the thin reaction ring of fly ash is difficult, since many rings are about 1 µm thick, possibly less. A dilemma arises between accurately quantifying the chemical composition of the small spot and the total elements interested. Quantitative chemical

analyses used 8 kV accelerating voltage in the absence of Fe, with spatial separation of at least 1 μm, thus avoiding interference from neighboring points.

A reactive Class C fly ash particle image is illustrated in Figure 5-15. The quantitative chemical analysis of three individual points, A, B and C, on the reaction ring of the particle, measured at 8 kV and 15 kV, appear in Figure 5-16. This analysis indicates relatively little compositional difference among the three points and between the two acceleration voltages, 8kV and 15kV. Such findings support the previous guideline that 2-3 times the absorption edge voltage suffices for an acceleration voltage for quantitative chemical analysis.

Figure 5-15 Reactive class C fly ash particle at one year of curing

Results from SW1 fly ash particle line scans, where pozzolanic reactions are clearly evident, appear in Figure 5-17. Line A extends 10.71 μm and required 5 seconds dwelling time on each of the equally spaced points. Line B 2.23 μm follows with the

91

same procedures. Line A was on the main body of SW1 fly ash particle and was inert while Line B was on the reaction ring of ash particle.

Chemical analysis results from this exercise appear in Figure 5-18 and confirm those points. Line A exhibits an almost constant Ca to Si mol ratio about 0.02 (essentially no CH reaction and little included Ca) whereas Line B exhibits a much higher ratio of Ca to Si (mol) in the range of 0.5-1.7, a typical range of C-S-H gel.

a)   b)

c)
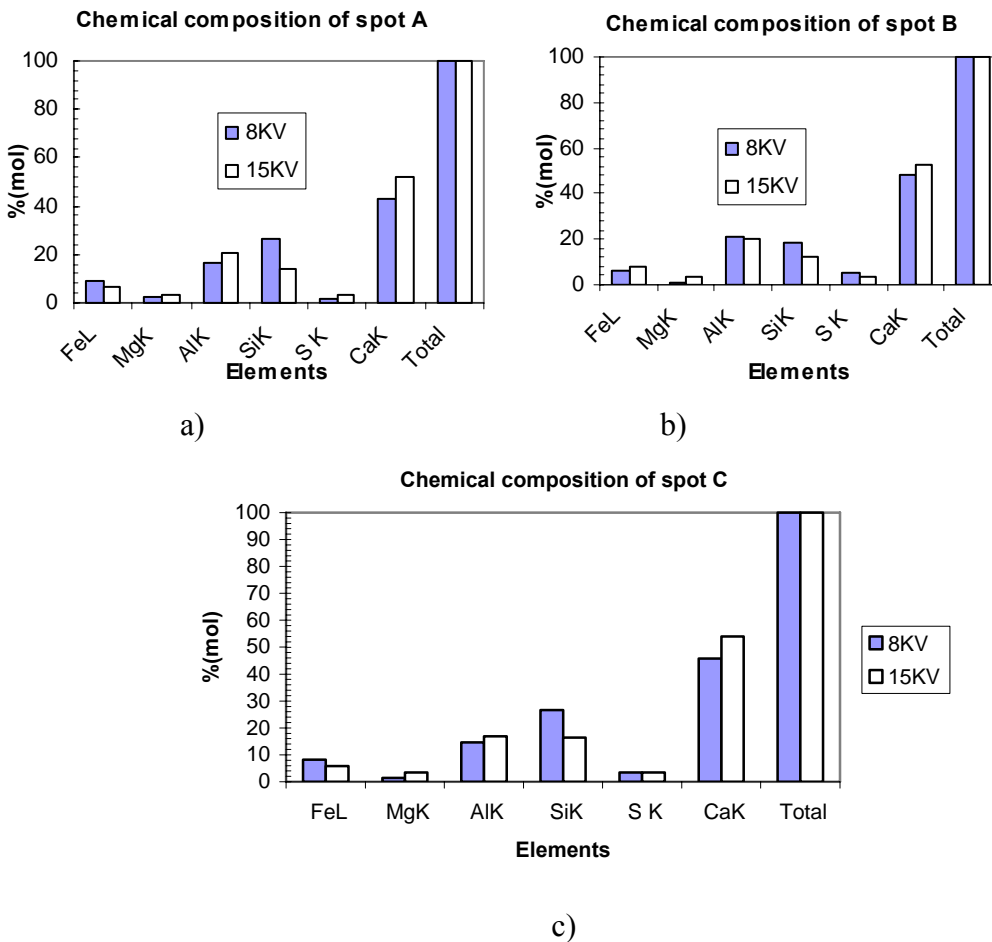
Figure 5-16 Spot chemical analysis of Class C fly ash particle

Figure 5-19 illustrates a raw SW1 fly ash particle and the chemical analysis results. Results shown in Figure 5-17 through Figure 5-19 are very consistent - the raw SW1 fly ash particles have the Ca to Si mol ratio about 0.02.

A similar analysis of a SW2 fly ash particle with an approximate diameter of 11 μm appears in Figure 5-20 and Figure 5-21. Points 2 through 9 are on the main inert body of the particle confirmed by the chemical analysis (Ca: Si mol ratio of 0.05). Point 1 and 10 are in the reaction ring of the particle supported by the chemical analysis (Ca:Si mol ratio of 1.6).
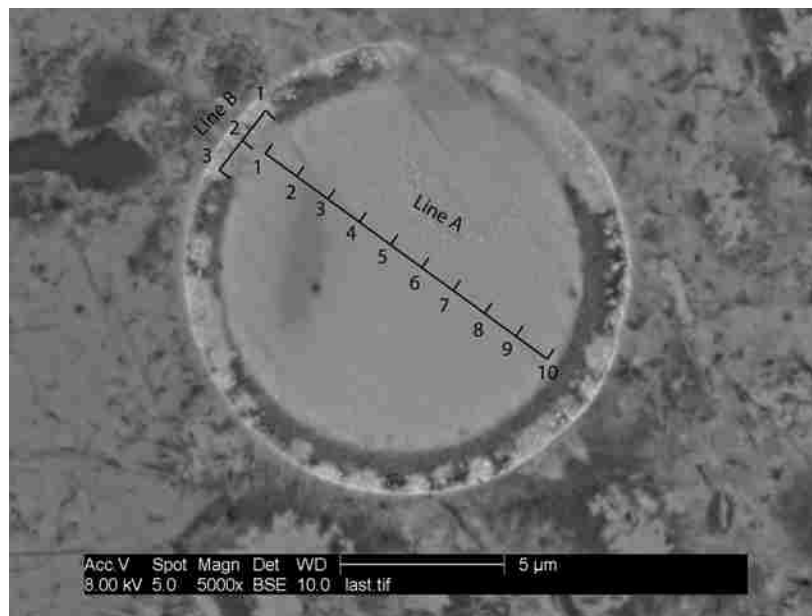
Figure 5-17 Reactive SW1 fly ash particle one year

Two smaller reactive SW2 fly ash particles (diameters approximately 5 μm) and corresponding chemical analyses appear in Figure 5-22 through Figure 5-24, Points 1, 2, 3 and 8, 9, 10 of particle 1 lie on the reaction ring while points 4, 5, 6, and 7 lie on the solid (unreacted), inner body of the particle.
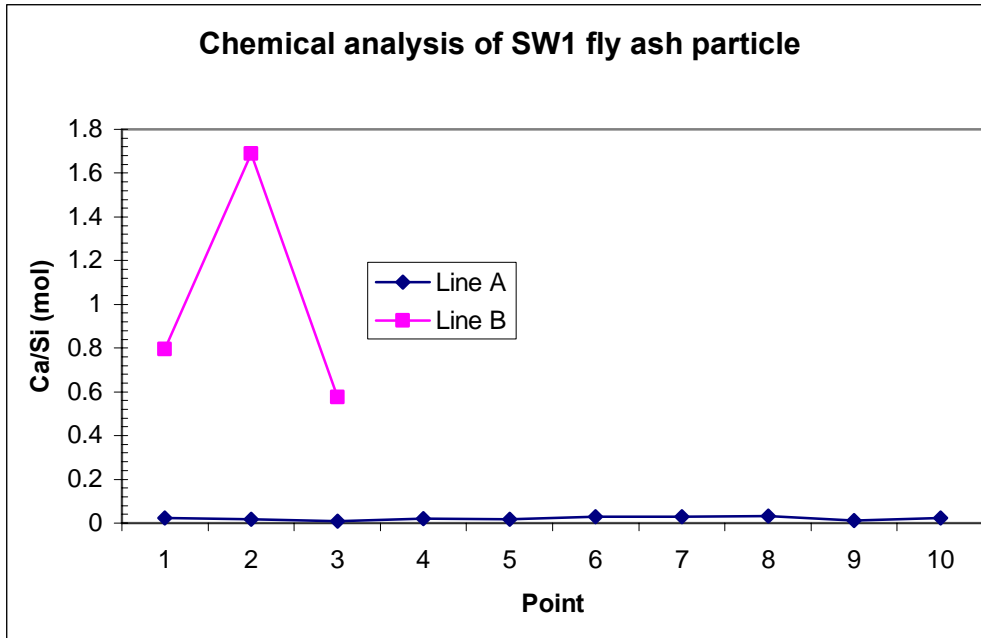
Figure 5-18 Line A and B scanning of SW1 fly ash particle (one year)

a Raw SW1 fly ash   b ESEM chemical analysis
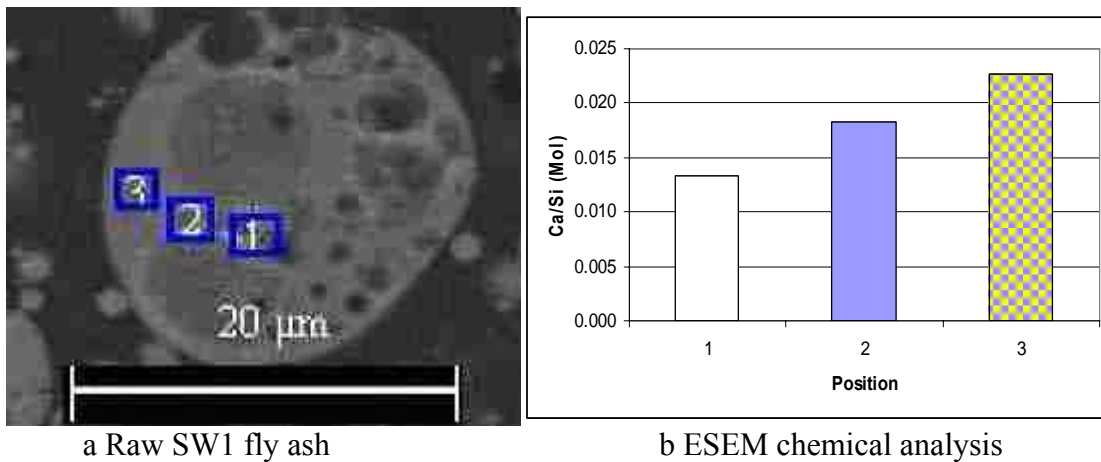
Figure 5-19 Chemical analysis of raw SW1 fly ash particle

Accounting for the excitation volume, points 2 and 9 reasonably represent the chemical composition of the ring. Figure 5-23 shows that points 2 and 9 have the Ca/Si mol ratio of about 0.7, a strong evidence of pozzolanic reaction. By comparison, points 5

and 6 represent the unreacted portion of the particle and exhibit a Ca:Si mol ratio about

0.05.
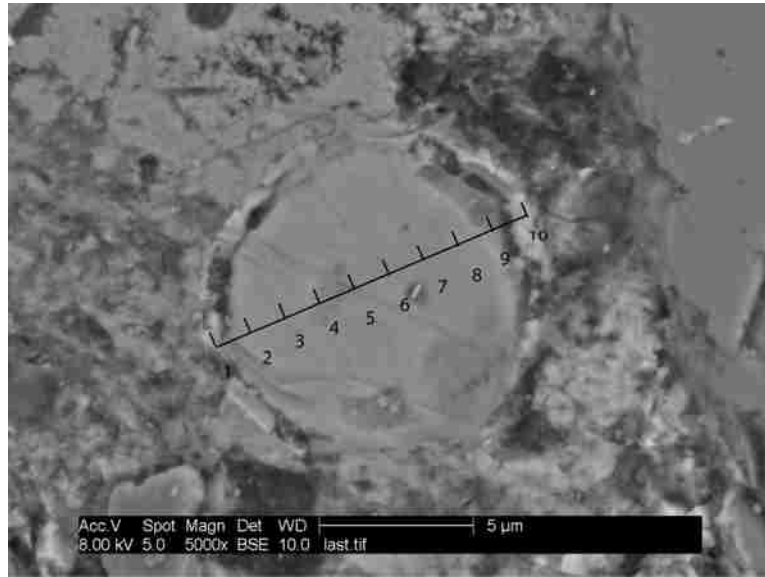
Figure 5-20 Reactive SW2 fly ash particle one year
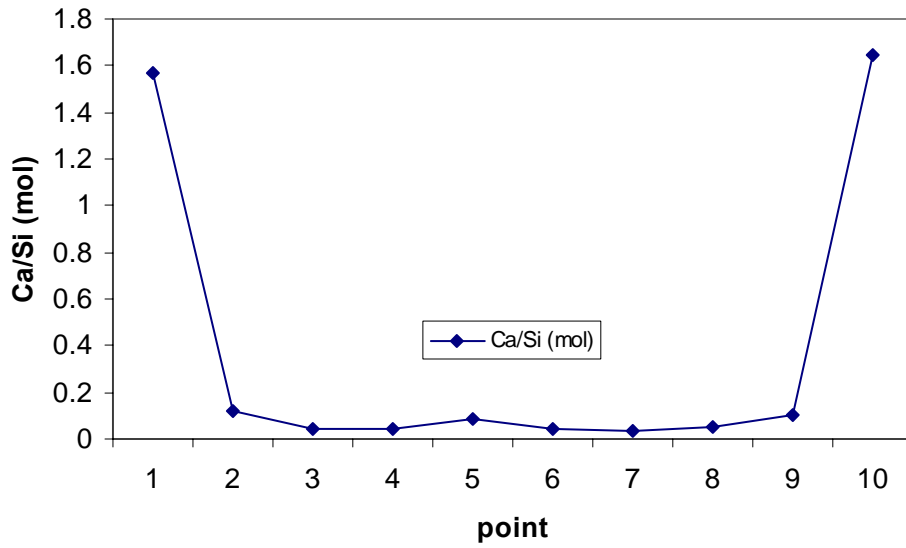
Figure 5-21 Chemical composition of reactive SW2 fly ash particle

Analysis of particle 2 largely agrees with those from Particle 1. Points 2 and 8 show the chemical composition of the ring with a Ca:Si ratio of 0.4-0.9 - evidence of pozzolanic reaction. Point 5 shows the chemical composition of the unreacted particle with a Ca:Si (mol) ratio as 0.01, indicating little or no reaction.

A comparison of SW2 fly ash particles shown in Figure 5-20 and Figure 5-22 indicates that smaller fly ash particles have higher reaction extent than larger ones, consistent with mass transfer effects and surface-area-to-volume ratios. However, the Ca to Si mol ratio near the centers of the smaller and larger particles approaches zero, indicating mass transfer might be the main factor influencing pozzolanic reactivity.
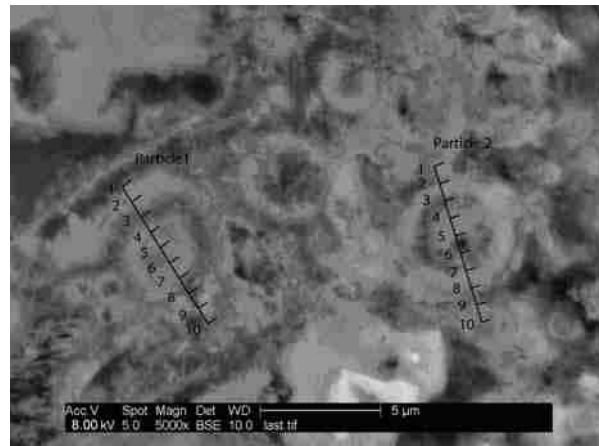
Figure 5-22 Two reactive SW2 fly ash particles with smaller size

A raw SW2 fly ash particle image and its chemical analysis appear in Figure 5-25. Comparison of the raw and reactive SW2 fly ash particles from Figure 5-20 through Figure 5-24 indicates that the results are consistent: raw SW2 fly ash particles have very low Ca:Si mol ratios, in all cases well less than 0.1.
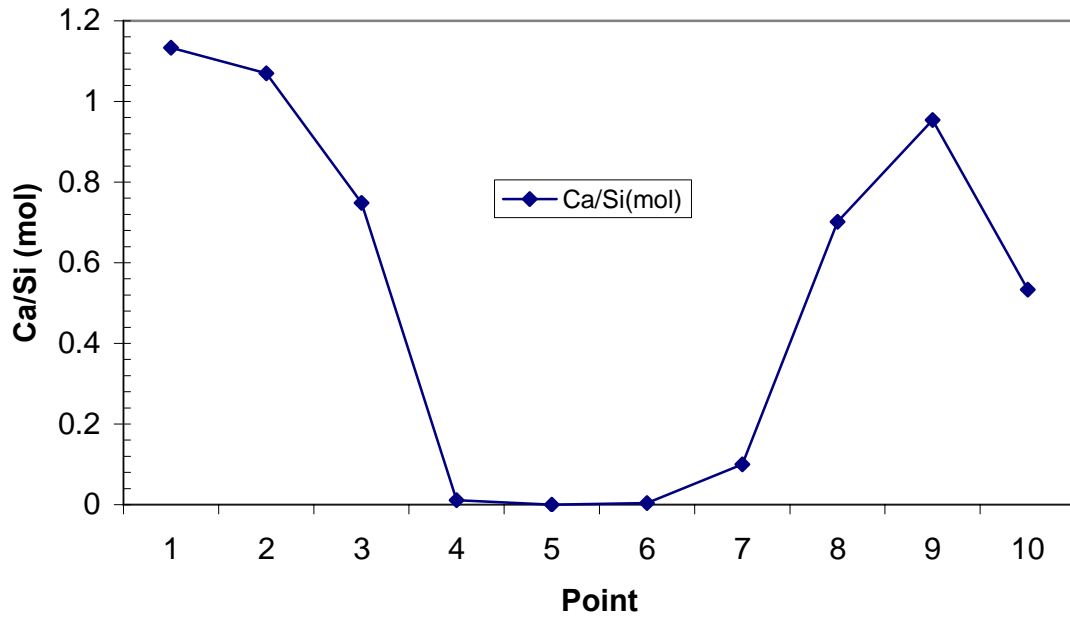
Figure 5-23 Chemical analysis of SW2 fly ash with smaller particle size (particle 1)
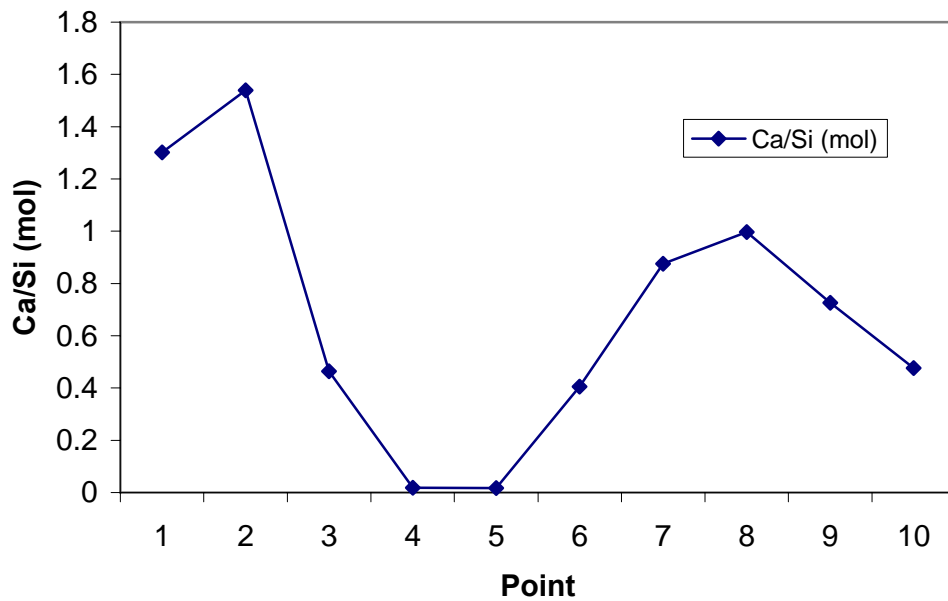
Figure 5-24 Chemical analysis of SW2 fly ash with smaller particle size (particle 2)

a Raw SW2 fly ash   b ESEM chemical analysis
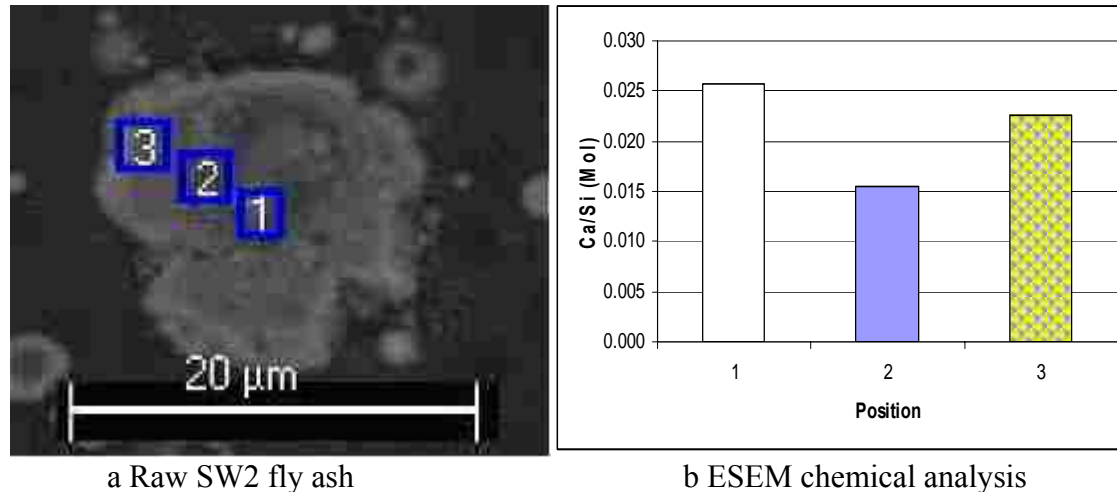
Figure 5-25 Chemical analysis of raw SW2 fly ash particle

A reactive iron rich particle image appears in Figure 5-26. The indicated iron mole fraction was about 5% at 8 kV and 55% at 15 kV for Line A. Therefore, the line scan was conducted at 15 kV for more precise analysis of iron (consistent with the much higher iron edge voltage). Composition data from Line A (Figure 5-27) provide additional evidence of pozzolanic reactions: points 2-9 have the Ca/Si mol ratio about 0.05, no evidence of pozzolanic reaction; points 1 and 10 have the Ca/Si mol ratio about 0.3, strong evidence of pozzolanic reaction. Chemical analysis of Line B (Figure 5-27) on the ring has the Ca to Si mol ratio in the range of 1.8 to 2.6, which is strong evidence of pozzolanic reaction, is consistent with analysis of Line A.

5.2 Quantitative Kinetics of Pozzolanic Reaction and Strength Build-up

The following discussion highlights results from mixtures of calcium hydroxide (CH) with each fly ash samples. Cement was also used to provide comparative data. The purpose of these experiments is to provide quantitative data on pozzolanic reaction rates in the absence of traditional cementitious reactions (except for the cement sample).

98
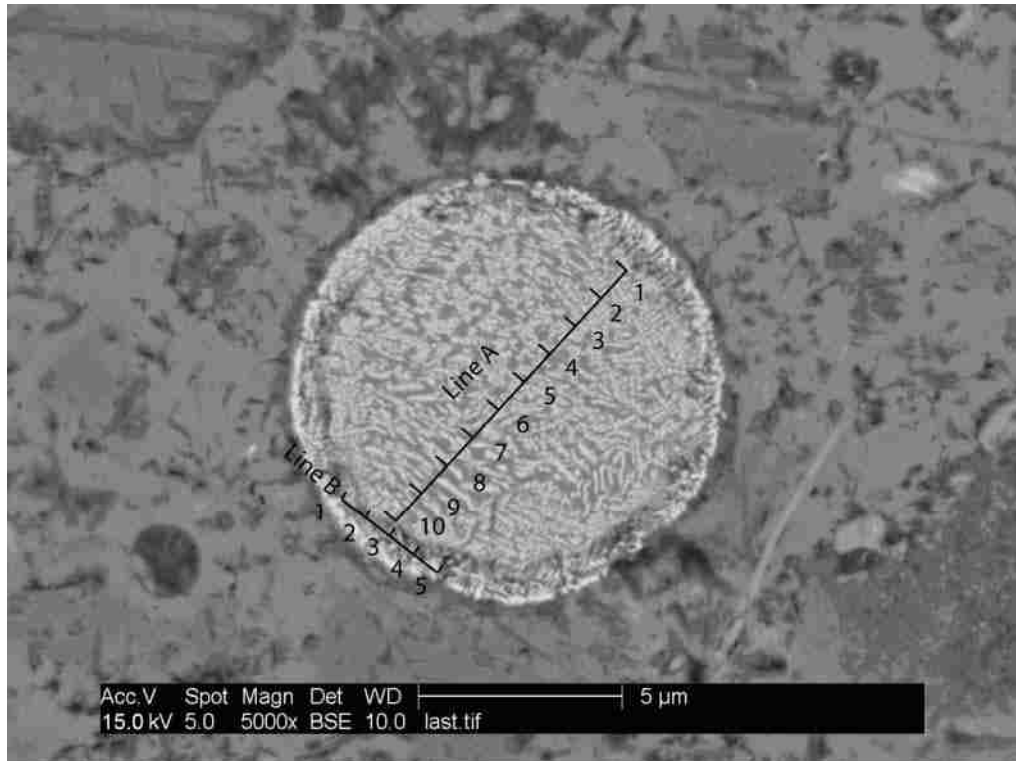
Figure 5-26 Reactive iron ash particle one year
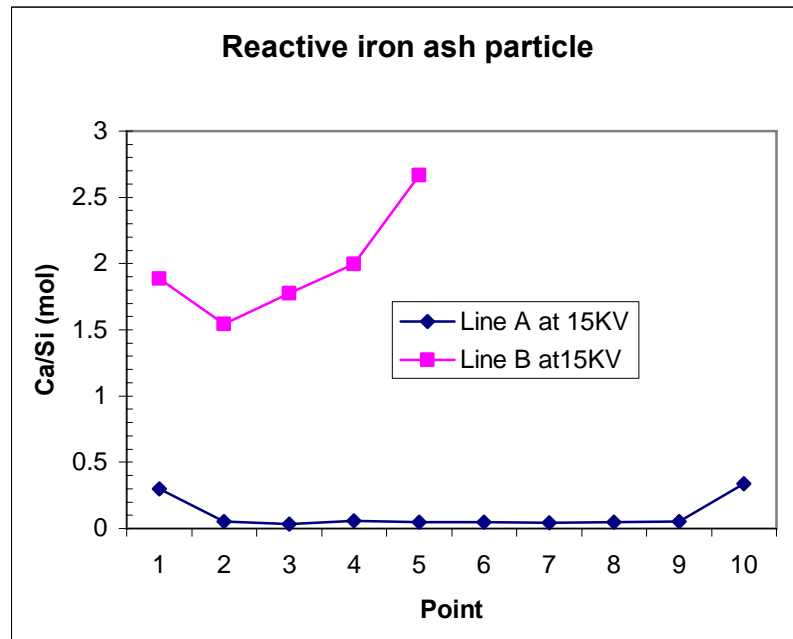
Figure 5-27 Chemical analysis of reactive iron fly ash particle one year

Data for traditional concrete formulations (including cement and possibly also fly ash) was presented earlier, but it is difficult to separate the effects of cementitious reactions from pozzolanic reactions in the previously presented data since the pozzolanic reactions are much slower than cementitious reactions and make a minor (but significant) contribution to the total strength. In addition, the large variation of compounds found in traditional concrete makes quantitative analysis of the CH reaction extent difficult. Therefore, the following discussion with respect to fly ash and calcium hydroxide provides much less complex and more focused results from pozzolanic reactions.

5.2.1 Strength Development

Sample strength development in the fly ash/calcium hydroxide cubes depends on the water/cementitious ratio (here cementitious refers to sum of fly ash and calcium hydroxide), the sample size and dimension, the fly ash composition, the ratio of fly ash to calcium hydroxide, the curing temperature and time, and possibly other factors. Since the first two factors do not vary among all samples, the strength analysis here focuses on the remaining factors.

Results from a designed experiment and a systematic one way ANOVA (Analysis of Variables) on the full set of cube strength data (at 95% confident interval) appear in Figure 5-28 through Figure 5-31. The general conclusions are: 1) biomass fly ash 10P, 20P and SAW samples develop about 3 times the strength of Class C and F ones, and about 6 times strength of Wood ones; 2) compressive strength increases with increase in initial fly ash concentration - the strength increases from fly ash to CH (weight) ratio 60/40, 70/30 to 80/20 consistently, but not at a statistically significant level (95% confidence level); 3) strength increases with decreasing curing temperature – samples

cured at 23 ˚C obtained the maximum strength, samples cured at 43 ˚C intermediate strength, and ones at 63 ˚C minimum strength, but the differences are not significant at a 95% confidence level; and 4) at one-month curing time, samples have developed most (typically 80-90%) of their one-year strength. The detailed discussions of these four main factors and their interactions follow.

5.2.1.1 Fly Ash Type

Compression strengths of 10P, 20P and SAW samples generally increase consistently with curing time up to one year, with the majority of the strength developing in the first month. The coal-biomass fly ash ultimate strength development compares to that of other samples as follows: 1) two- to three-times higher than that of (coal-derived) Class C or Class F fly ash; 2) six times than that of neat wood fly ash; and 3) approximately 50 to 80% of that of pure cement samples. Figure 5-32 through Figure 5-34 summarize these findings for three different ratios and three temperatures, and are typical of all mixing ratios and temperatures. Complete data sets appear in the Appendix C.

The amount of combined calcium hydroxide is a helpful tool for explaining the hardening mechanisms, but it does not necessarily correlate well with the strength build-up of the fly ash-CH systems. Furthermore, some high-lime fly ash (typically Class C and many biomass fly ashes) might contain inherent C_2S and develop compressive strength with calcium hydroxide as high as 30-40 MPa at a curing time of 3 to 4 months, which comes from the combined effects of pozzolanic and cementitious reaction of the C_2S. Such could be the case for 10P, 20P and SAW samples. Wood fly ash has larger particles than the other fly ash and wood ash mortar mixes have a higher water ratio (0.65 vs. 0.5,

101

water/(fly ash + calcium hydroxide) by weight), which accounts for lower strength of wood ash samples.
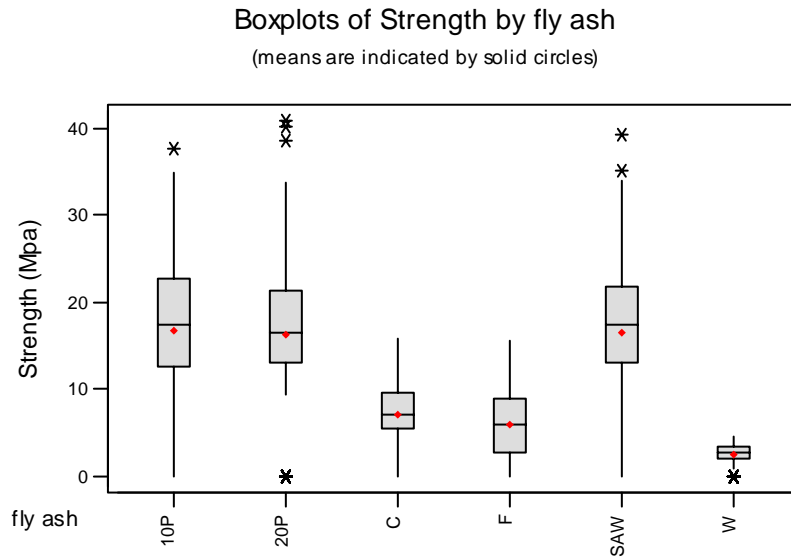
Figure 5-28 One way ANOVA of cube compressive strength by fly ash type
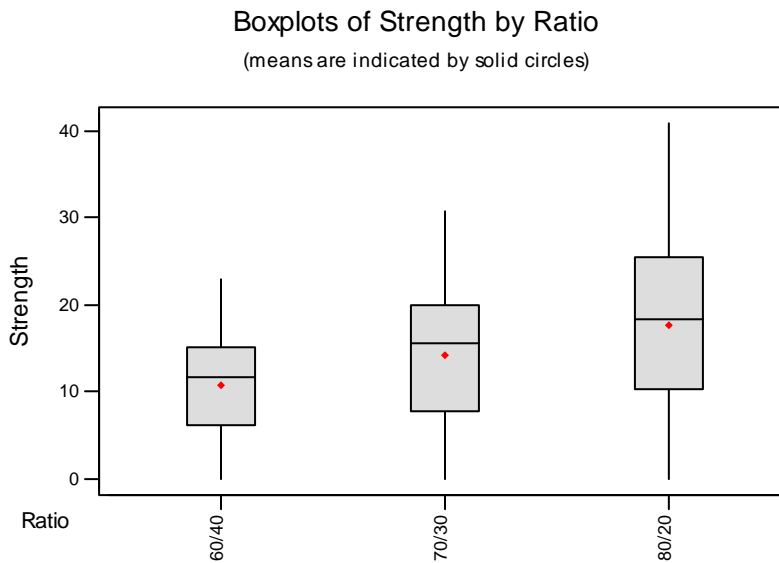
Figure 5-29 One way ANOVA of cube compressive strength by mixing ratio
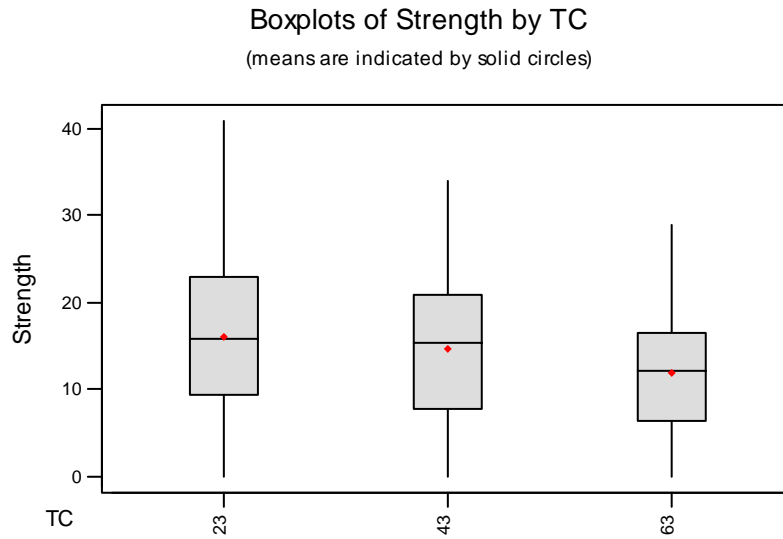
Figure 5-30 One way ANOVA of compressive strength by curing temperature (ºC)
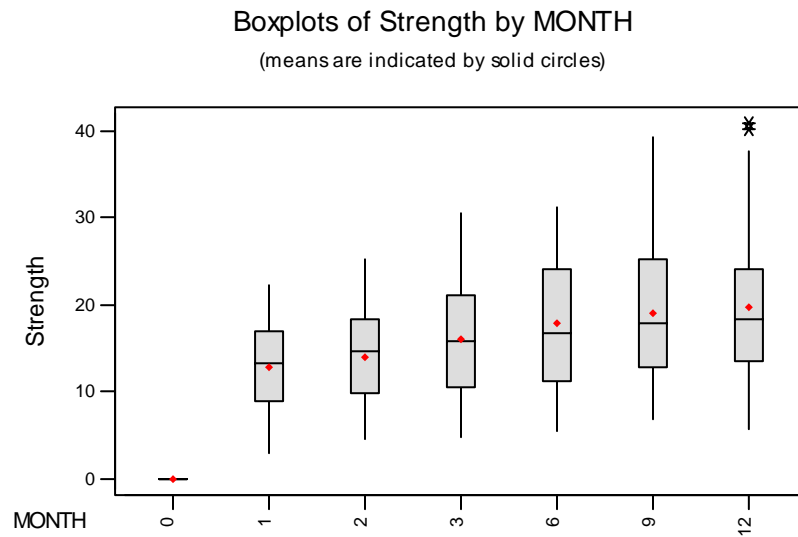
Figure 5-31 One way ANOVA of compressive strength by curing month
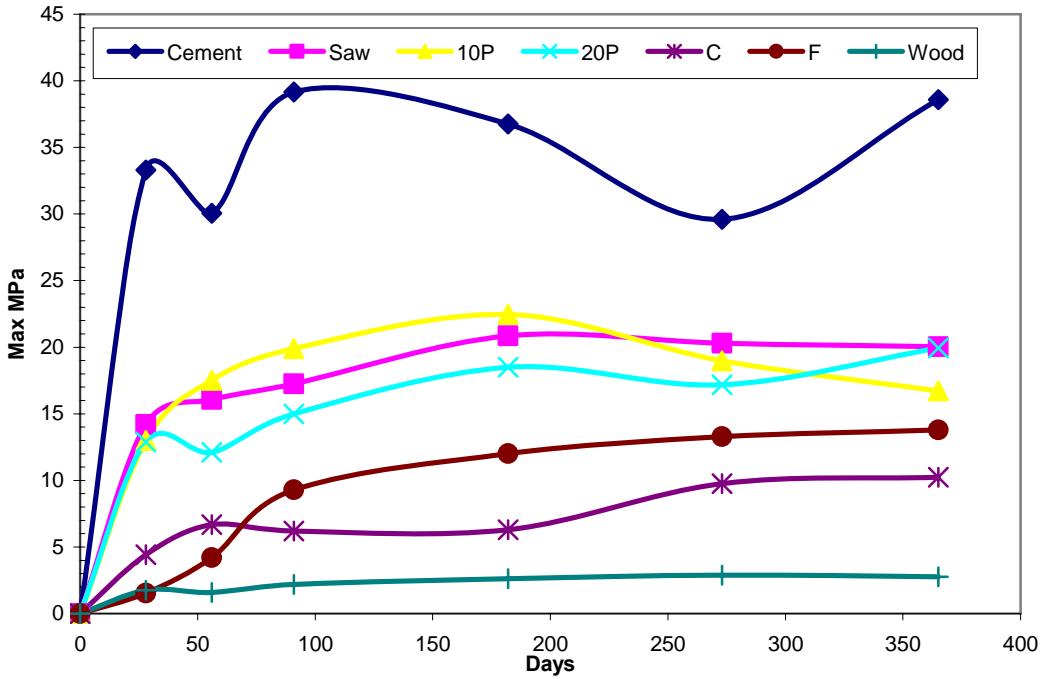
Figure 5-32 Compressive strength for 60/40 mixture ratio, 23ºC up to one year
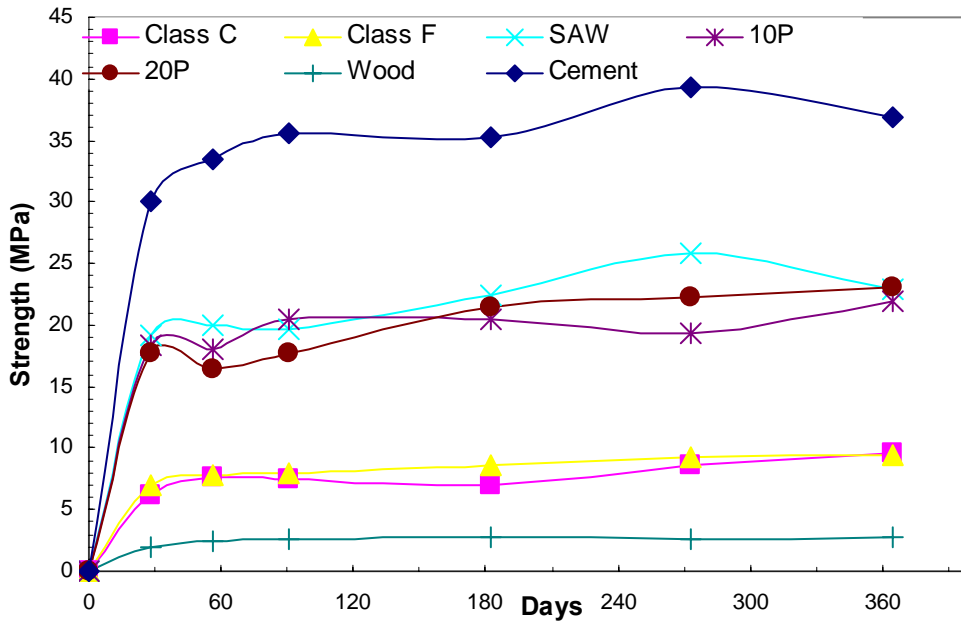
Figure 5-33 Compressive strength for 70/30 mixing ratio, 43ºC up to one year
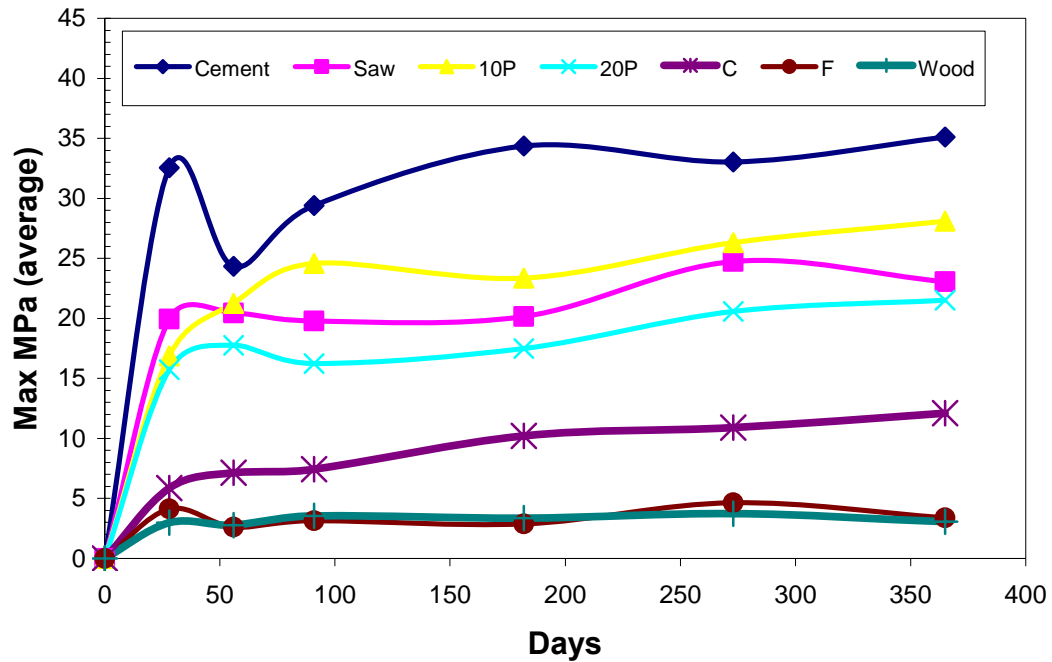
Figure 5-34 Compressive strength for 80/20 mixing ratio, 63ºC up to one year

5.2.1.2 Mixing Ratios

Strength dependence on mix ratios of fly ash with CH follows consistent and clear trends. For all fly ashes except Class F, compressive strength increases with increasing fly ash content as shown in Figure 5-35 and Figure 5-36. Strength decreases by 20 to 40% with each 10% decrease in fly ash mass fraction (weight ratio of fly ash / calcium hydroxide = 80/20, 70/30 and 60/40), but such a change is not statistically significant at a 95% confidence level. The pure cement samples have similar compressive strengths at all temperatures and mixing ratios and have higher strengths than all fly ash samples, though only marginally higher than the 80:20 biomass fly ash samples.
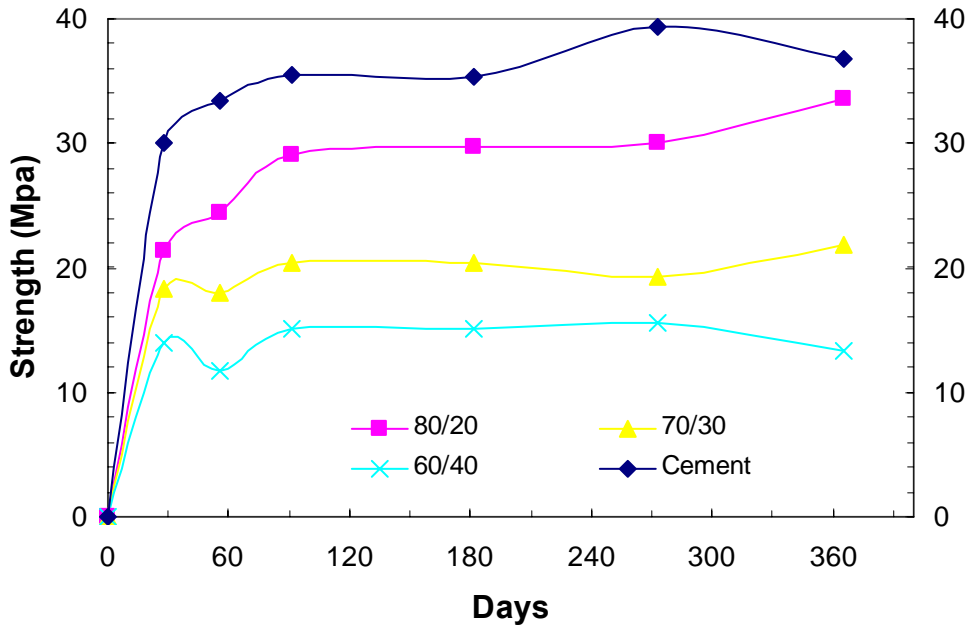
Figure 5-35 Dependence of compressive strength on mixture ratios (10 P 43ºC)
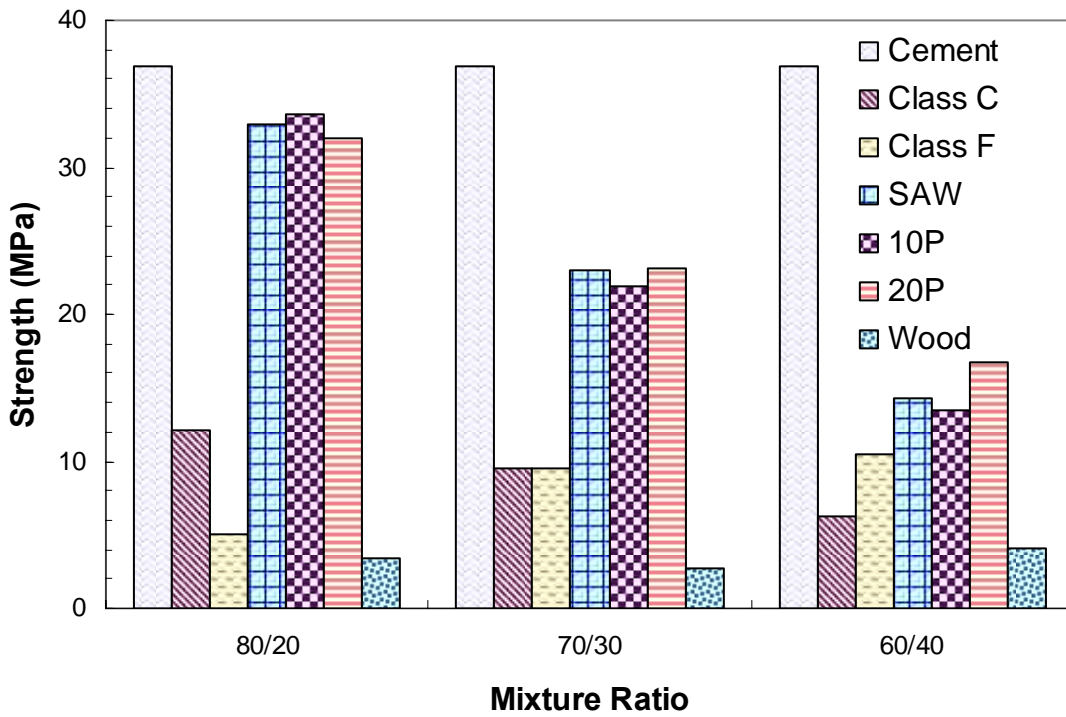
Figure 5-36 One year compressive strength at 43 ºC with different mixture ratios

106

The mixture ratio of pozzolan and calcium hydroxide has an important influence on the sample's strength. The strength increases with the ratio of calcium hydroxide and pozzolan to some extent and decreases after that limiting ratio; after which, the strength does not change with mixture ratio, no matter what it is. That limiting ratio changes from fly ash to fly ash, but most possibly lies within the range of 20 to 33%. It is postulated that calcium hydroxide does not contribute to the strength build up in the pure cement concrete, nor does it in the fly ash-calcium hydroxide system. The results confirm such assumptions.

5.2.1.3 Temperature

Excluding wood fly ash, all fly ash strengths change consistently with respect to temperature (Figure 5-38 through Figure 5-40). Samples cured at 63 ºC consistently exhibit the lowest strengths, while samples cured at 43 ºC exhibit greater strength for the first three months, after which the samples cured at 23 ºC show the greatest strength. For Class F fly ash, the samples cured at 23 ºC are the weakest of all temperatures for the first three months; after which Class F mixtures behave similar to the other fly ash mixtures - at 23 ºC the strongest; at 43 ºC the medium strength; and at 63 ºC the weakest.

Cement samples exhibit similar trends to most fly ash samples, and exhibit similar strength development dependence on temperature. Such trend is consistent with literature observations for cement (Mindness, Young et al. 2002).

The general trend of decreasing strength with increasing curing temperature may appear inconsistent with the trend of increasing extent of reaction with increasing curing temperature (latter tend discussed later). There are several potential explanations. One explanation is that concrete strength formation proceeds similarly to polymer formation,

except with long silicate strands as opposed to polymers. During many polymer (and possibly pozzolanic) reactions, chain terminating (or radical producing) reactions are more temperature sensitive than chain forming reactions, leading to higher extents of reactions but shorter chains and hence less strength and higher curing temperature. Specifically, high curing temperature introduces more radicals for polymerization, which increases termination rates. An additional or alternative explanation is that temperatures greater than 40 ˚C produces thermal cracks and uneven hydration shells of fly ash, thus much larger pores/more fracturing and lower strength.
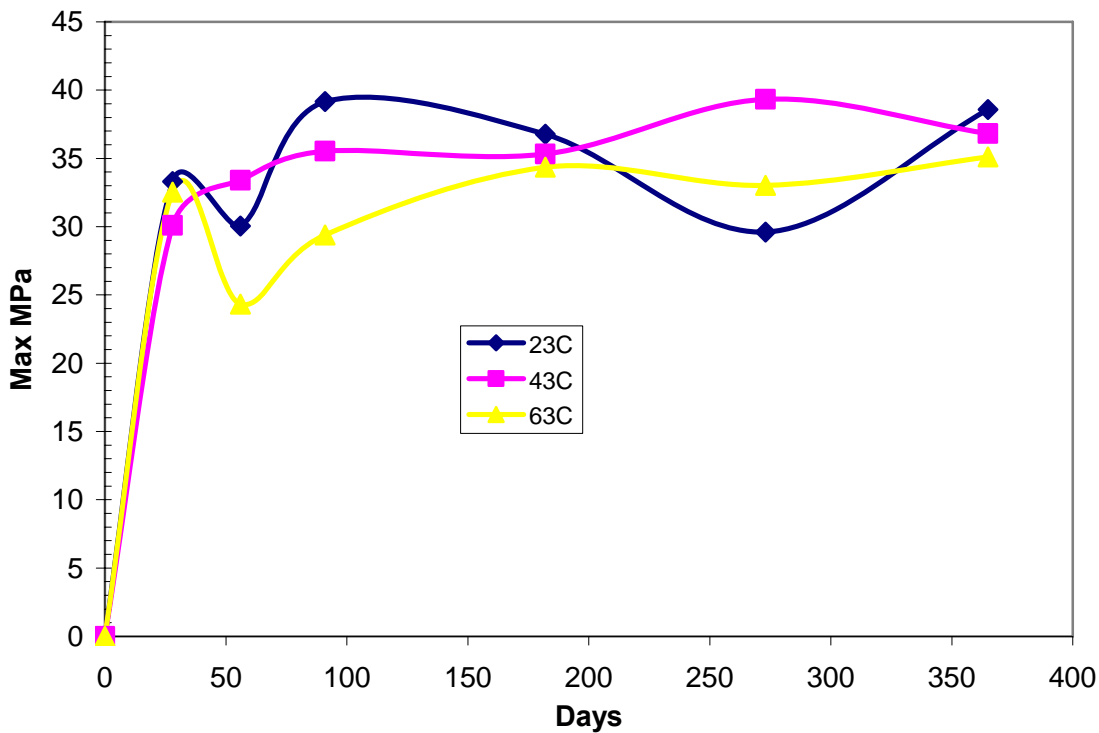
Figure 5-37 Dependence of compression strength on temperature for cement
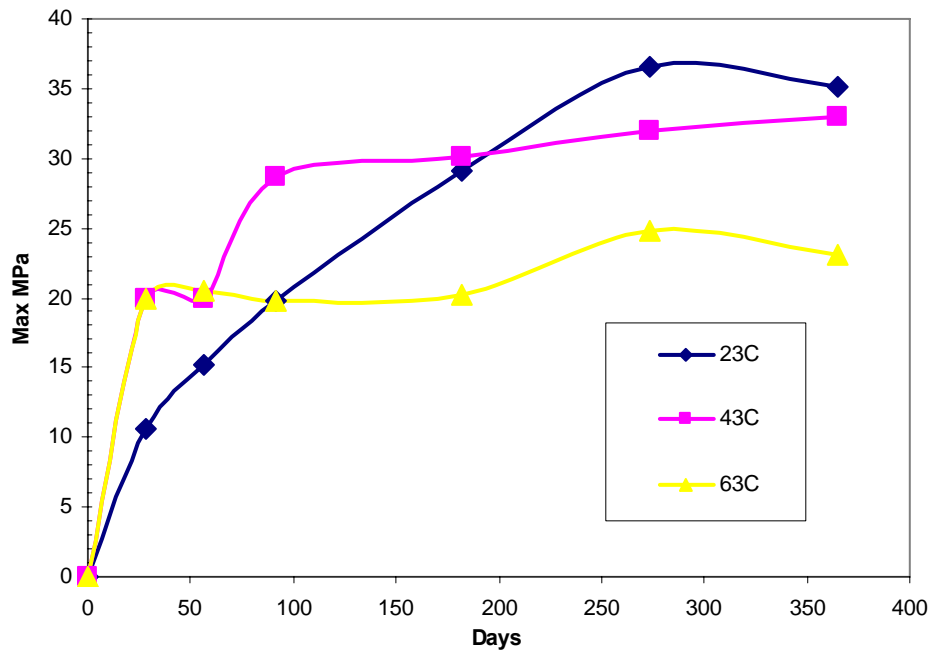
Figure 5-38 Dependence of compression strength on temperature for SAW 80/20
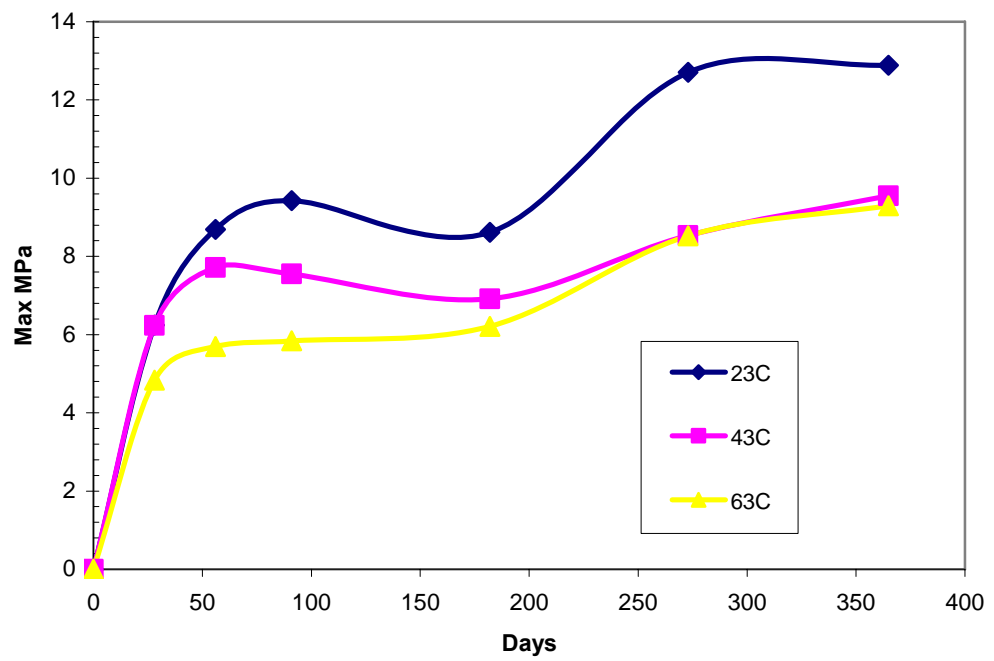
Figure 5-39 Dependence of compression strength on temperature for C70/30
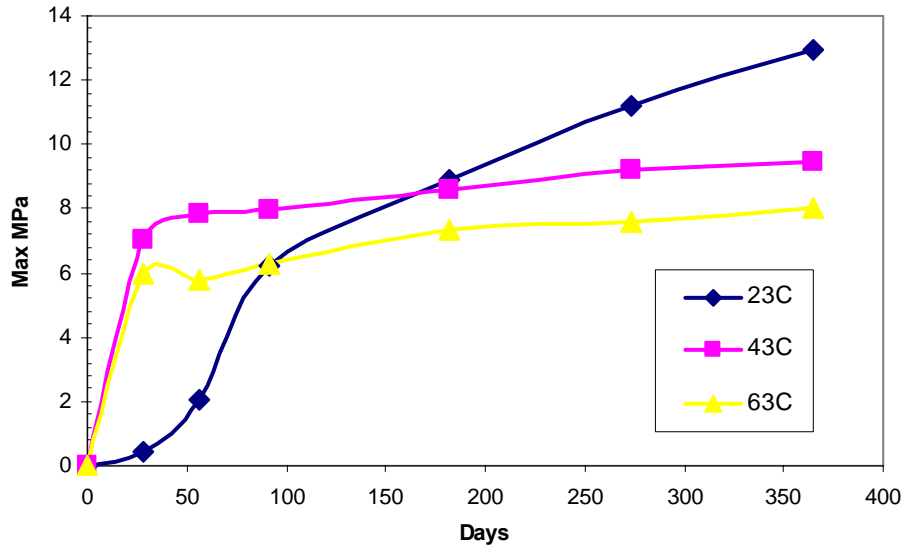
Figure 5-40 Dependence of compression strength on temperature for Class F 70/30

5.2.1.4 Curing Time

Figure 5-41 illustrates the strength development among different fly ash samples normalized by the strength at one year. The data shown represent behaviors of all samples, with the full set data is attached in Appendix C. After one month, all three biomass-coal and Class F fly ash samples have developed about 60% of their ultimate strength. However, Class C, wood fly ash, and pure cement samples all reach approximately 70 to 80 % of their one-year strength by one month. At two months, the wood and cement mixtures increase strength slowly and monotonically from 90 to 100% up to one year; the other five mixtures increase their strength in similar patterns from 60 to 85% at two months of exposure to 100% at one year, although different mixture ratios develop strength at different rates.
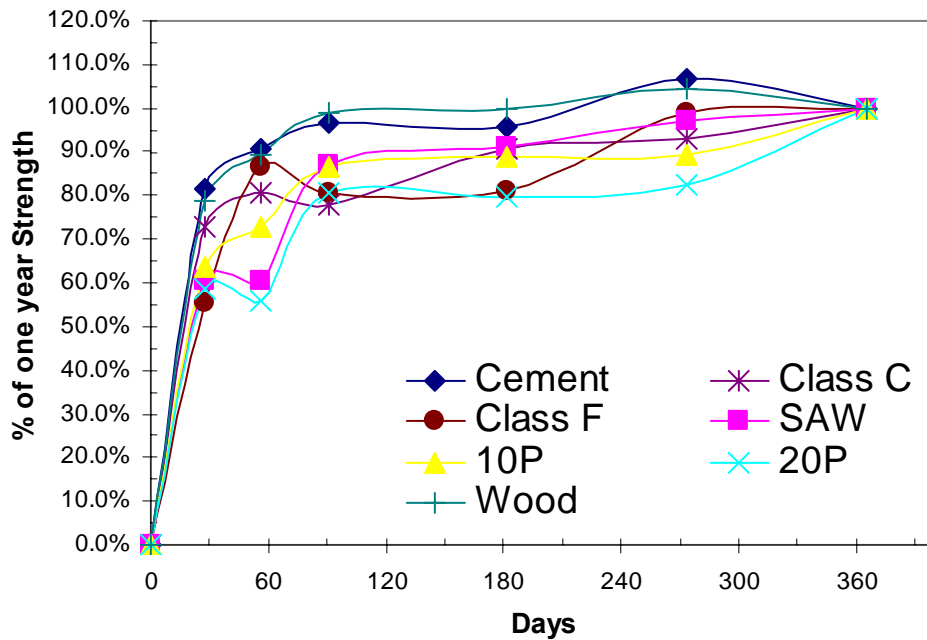
Figure 5-41 Percent of one year strength for each fly ash with at 80/20 and 43ºC

5.2.2 Reaction Extent

The results of reaction extent trends follows the same pattern as strength build up discussed above; trends are discussed as a function of 1) fly ash type, 2) mixing ratio, 3) curing temperatures and 4) curing time.

5.2.2.1 Fly Ash Type

Figure 5-42 illustrates the extent of reaction as calculated by measuring the amount of CH in the sample at the testing date compared to the initial amount in the fresh mix (mixtures with fly ash: CH = 70:30 at 43 ºC as examples). All fly ash mixes exhibit similar reaction extents, from 46 to 76%, at one month of exposure time, with reaction extent increasing with exposure time up to twelve months. At 12-month exposure time, reaction extents range from 82 to 93%.
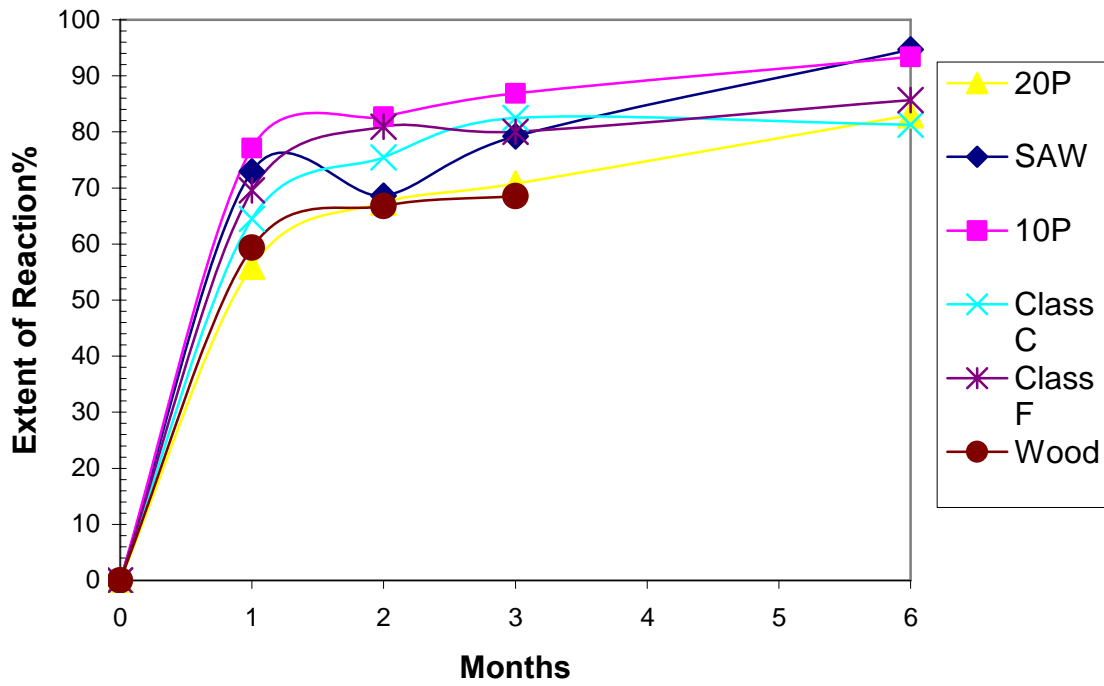
Figure 5-42 Reaction extent of different fly ash at mixing ratio of 70/30 at 43 ºC
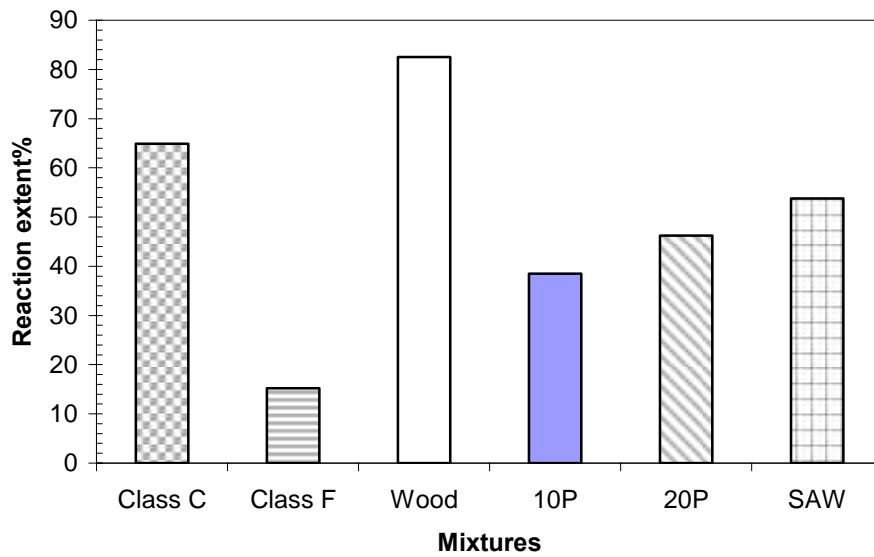
Figure 5-43 Reaction extents of different mixtures at 80/20 and 23 ºC at one month

112
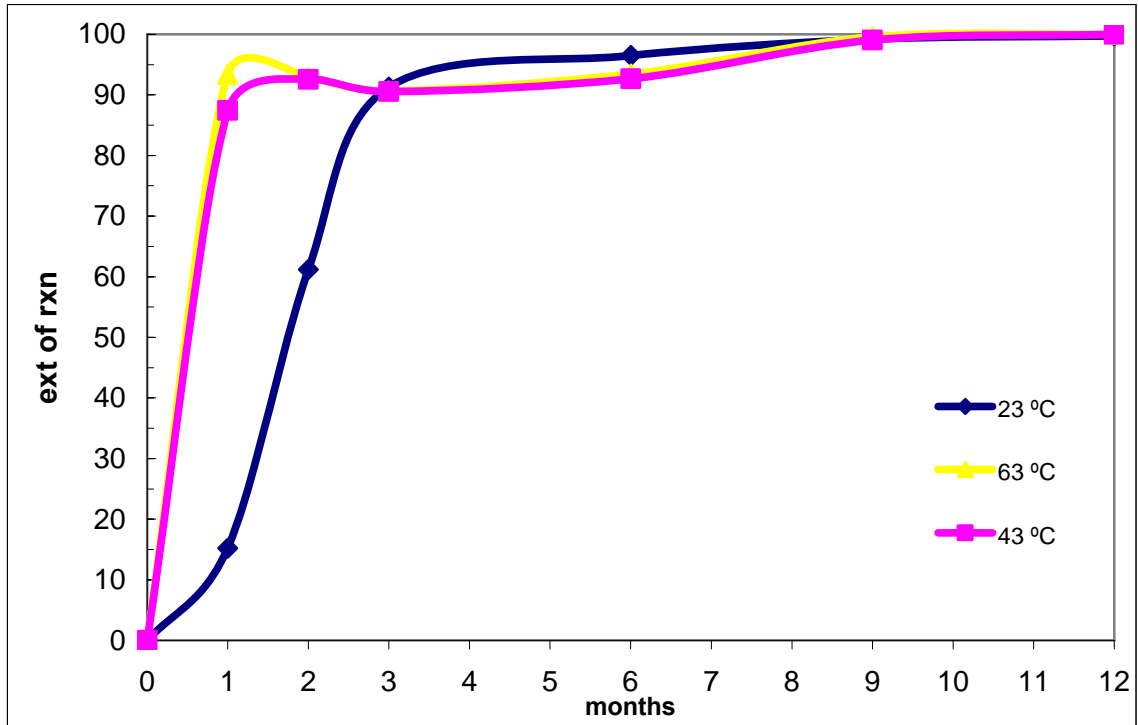
Figure 5-44 Reaction extent of Class F at 80/20 mixing ratio up to one year

Figure 5-43 shows the relatively low reaction extent of Class F in mixture ratios of 80/20 (with similar results at 70/30 and 60/40) cured at 23 ºC at one month, which is a probable reason that Class F mixtures were too soft to be demolded (see section 4.2.3 Sample Preparation and Curing). However, as the temperature increases to 43 ˚C or 63 ˚C, the reaction extent of CH greatly increases from 15% to 87% or 93%, which indicates that Class F sample reactivity is highly temperature sensitive, as shown in Figure 5-44.

5.2.2.2 Mixture Proportions

Calcium hydroxide reaction extent generally increases with increasing fly ash content for all temperatures and for all samples, with typical data shown in Figure 5-45 and Figure 5-46. All samples show similar qualitative behavior but differ in minor details not listed here.
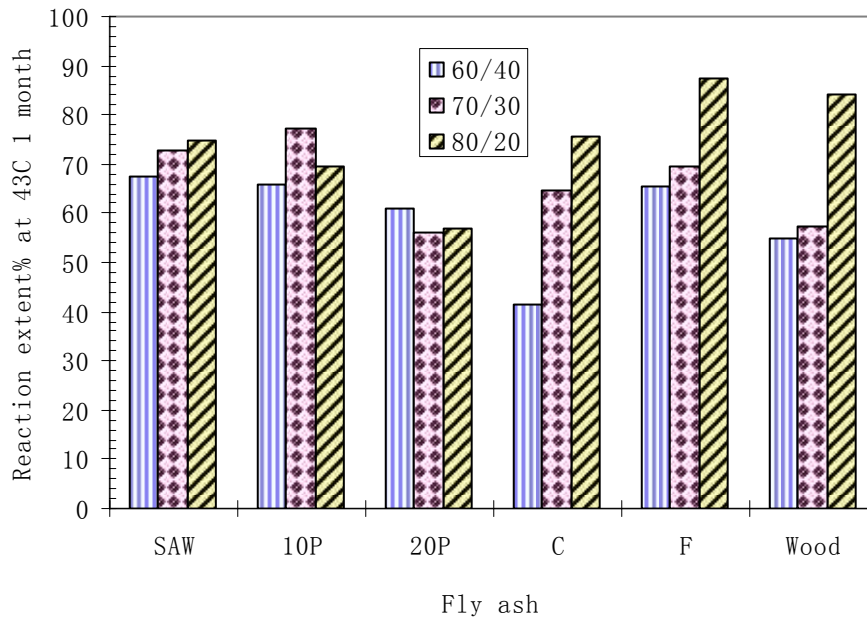
Figure 5-45 Reaction extent of fly ash at 43˚C one month for all three mixing ratios
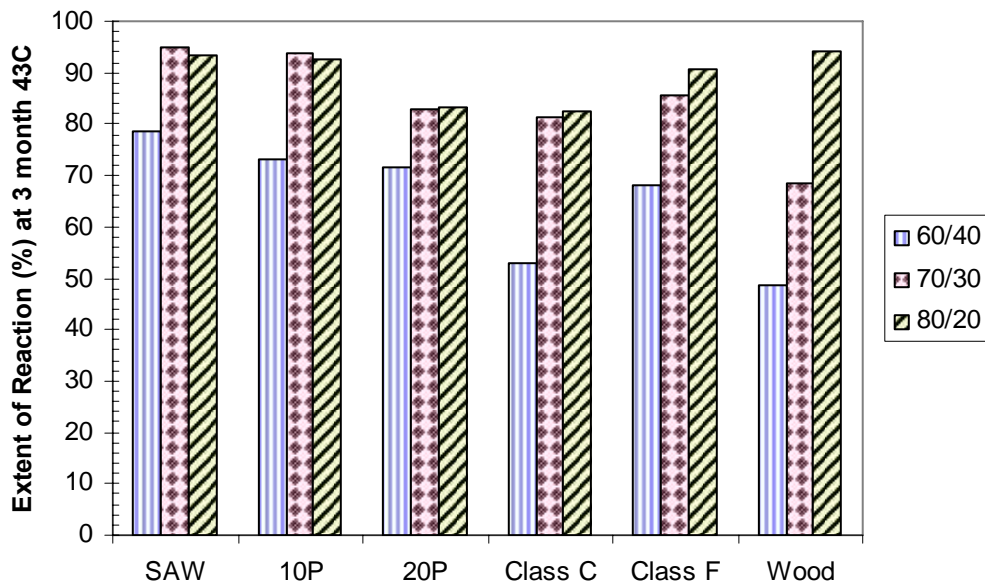
Figure 5-46 Extent of reaction for different fly ash at 43ºC at 3 months

114
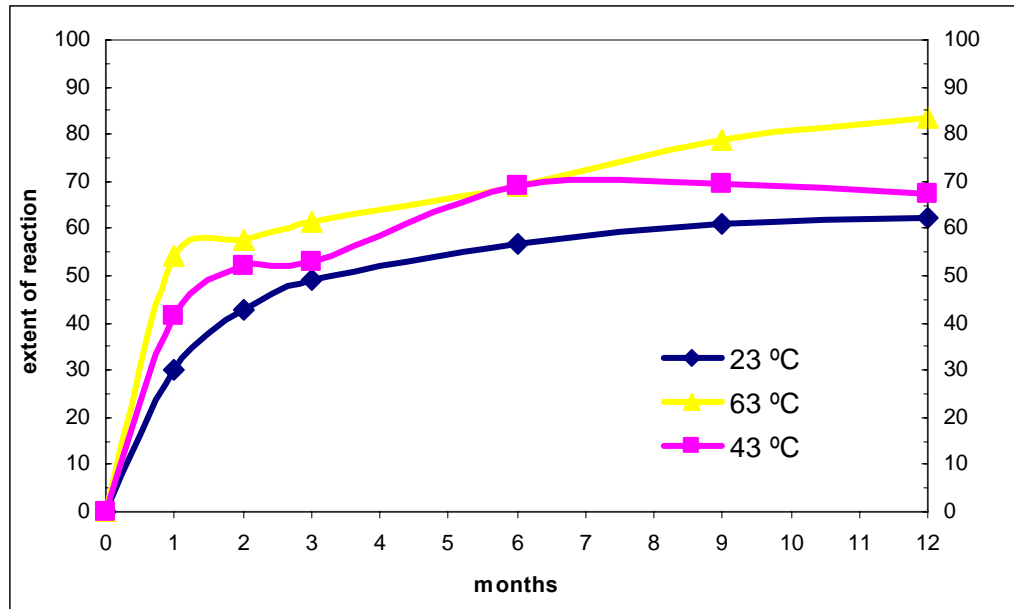
Figure 5-47 Dependence of reaction extent on temperature (Class C 60/40)

5.2.2.3 Temperature

Reaction extent increases with increasing temperature, especially at the higher CH ratio (60/40), as indicated in Figure 5-47. As mentioned previously, samples of high-temperature data have the lowest strengths but, as seen here, have the highest extents of reaction. The data indicate that, while pozzolanic reactions develop strength, there are factors other than the extent of reaction that impact long-term strength and that appear to be adversely impacted by temperature, such as the shorter chain and larger pores (as discussed earlier).

5.2.3 Quantitative Kinetics of Pozzolanic Reaction

5.2.3.1 Global Kinetics

The kinetics data in Appendix D provide systematic and quantitative results from which pozzolanic reaction kinetics (reaction extent of CH) can be developed. The

following analysis indicates that a model that is first order in both calcium hydroxide and
fly ash content and that contains no mass transfer limitations adequately fits all of the
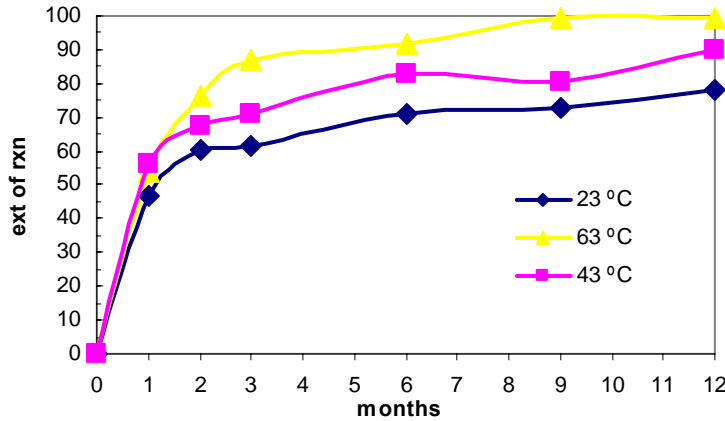
Figure 5-48 Dependence of reaction extent on temperature (20P 70/30)
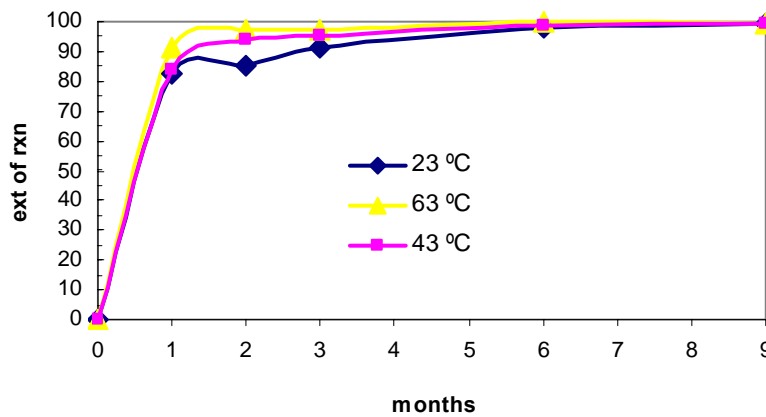
Figure 5-49 Dependence of reaction extent on temperature (Wood 80/20)

data of any given sample. However, the actual kinetics surely involves much more
complex reaction networks and pronounced transport effects. These data, while quite
comprehensive, do not provide the fidelity required to resolve all of these complexities.

116

In addition to this model, this discussion analyzes other models discussed in the literature and reviewed in Chapter 2 and their adequacy (or lack thereof) in fitting these data. The discussions include: (1) first-order kinetics with respect to calcium hydroxide in Equation (2-13); (2) a parabolic diffusion expression for mass transfer in Equation (2-12) (Ball and Carroll 1999); and (3) a modified second-order expression proposed by Biernacki Equation (2-16)(Biernacki, Williams et al. 2001).

Before comparing those models, a statistical analysis of reaction extent respective to fly ash, curing time, mixture ratio (fly ash /calcium hydroxide) and curing temperature is illustrated in Figure 5-50. All those factors have significant influences on reaction extent of calcium hydroxide and the effect of mixture ratio cannot be ignored; therefore, the diffusion-controlled parabolic mechanisms in Equation (2-12) and first-order kinetics with respective to calcium hydroxide in Equation (2-13) represent poor models of these data because their equations do not include the factor of mixture ratio of fly ash and calcium hydroxide. For the same reason, the modified Avrami mechanism in Equation (2-11) does not adequately represent these data.

Three new pozzolanic reaction models were derived as part of this work, with the detailed derivations appearing in Appendix F. The only one of these that bears any similarity to literature derivations is the first, which assumes first-order dependence on calcium hydroxide and fly ash mass fractions and ignores transport and particulate effects. This derivations assumes that a stoichiometric ratio exists between fly ash and calcium hydroxide as in Equation (5-1),
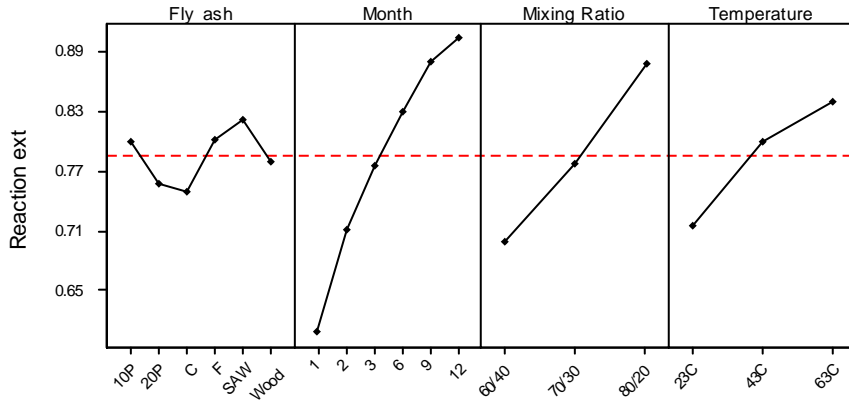
Figure 5-50 Statistical main effects of four factors on reaction extent of Ca(OH)$_2$

$$\alpha_{FA} = a + b\alpha_{Ca(OH)_2} \tag{5-1}$$

where, *a* is an excess parameter of fly ash; positive *a* indicates excess fly ash and negative *a* indicates fly ash is deficient. *b* is the stoichiometric parameter; one gram of fly ash combines with *b* grams of Ca(OH)$_2$.

Given equation (5-1) and the other assumptions of the, the following equation describes the time dependence of overall calcium hydroxide conversion as a function of the experimental variables used here (temperature, time, initial concentrations):

$$\alpha = 1 - \frac{\alpha_{Ca(OH)_2,0}(1+b)-1}{b\alpha_{Ca(OH)_2,0} + \left(\alpha_{Ca(OH)_2,0}-1\right)\exp\left[-\left(\alpha_{Ca(OH)_2,0}(1+b)-1\right)k^0\exp\left(-E_A/RT\right)t\right]} \tag{5-2}$$

where k^0 is the reaction rate pre-exponential factor, $Ca(OH)_{2,0}$ is the starting mass ratio of $Ca(OH)_2$, t is the time in month, E_A is the activation energy, T is the temperature; R is the Gas law constant.

The modified second-order (first order with respect to fly ash and first order to calcium hydroxide) mechanism in Equation (2-16) accounts for the effect of mixing ratio. The data provide the following parameter estimates for each type of fly ash through non-linear, least-squares regression: 1) b, the mass stoichiometric coefficient of calcium hydroxide to fly ash; 2) the pre-exponential reaction rate constants, k_0; and 3) the activation energy (E_A/R). The resulting parameters appear in summary form in Table 5-2. This could lead to the false impression that the reaction potentially vary by many orders of magnitude. However, the predicted reaction rate over the temperature range measured (23-63 °C in this investigation) vary by far less, as indicated in Figure 5-52. In the mid-temperature range, the ratio of the highest to lowest predicted reaction rate coefficient is about 2.5.

This misleading impression given by examining the parameters arises from the highly coorelated nature of the parameters in the Arrhenius function, as inherent property of this function that leads to the result that a wide tange of valuses for one parameter reasonably fits data set if other parameter is adjusted to optimize the fit. More details of the parameter uncertainty will be discussed shortly.

The approximate correlation coefficients (variation described by model divided by total data variation based on a linear analysis) exceed 90% for all cases, indicating most of the total variation is captured by this model. The reaction extent data of all six fly

ash samples appear in the Appendix D. Figure 5-51 illustrates typical data and model predictions for the reaction extents (in this case, 3 Class F data sets and model results).

Reaction rates and kinetic parameters for different fly ash types should vary. This analysis produces a range of pre-exponential and normalized activation energy values approaching five orders of magnitude and exceeding one order of magnitude, respectively.

Table 5-2 Modeling parameters for the modified second order equation

	k^0	E_A/R	b	R^2
	month^{-1}	K	-	-
Class F	199453	3639	1.875	0.95
Class C	38.71	986.2	2.28	0.94
Wood	5.05	191.1	2.99	0.93
10P	2408	2316	1.74	0.94
20P	2535	2391	1.86	0.93
Sawdust	245700	3688	1.71	0.96

The mass stoichiometric ratios (mass of fly ash that reacts with a unit mass of calcium hydroxide) vary by a factor of 1.74. Again, there is no reason to expect mass stoichiometric ratios to be consistent for different fly ashes. However, they uniformly exceed unity and this relatively modest variation is consistent with the physical interpretation of this parameter.

The nominal pozzolanic reaction between unreacted silica (SiO_2) and calcium hydroxide is expressed in Equation (1-2), which indicates a mass ratio of fly ash (SiO_2) to calcium hydroxide of $(2 \times 60.08)/(3 \times 74.09) = 0.27$, where 2 and 3 are the stoichiometric molar ratio of SiO_2 and $Ca(OH)_2$ in Equation (1-2), and 60.08 and 74.09 are their molecular weight, respectively.
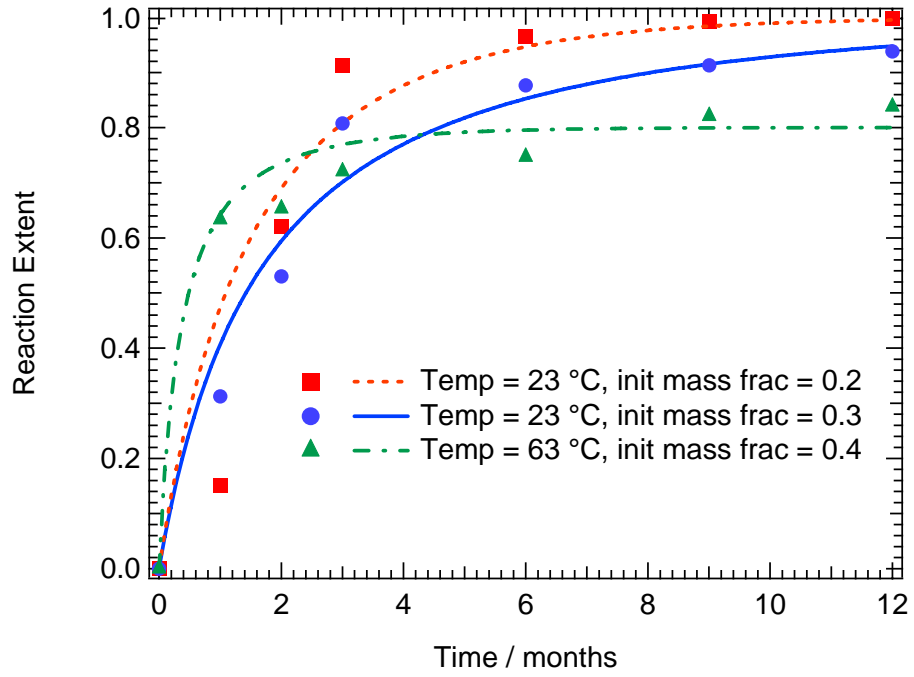
Figure 5-51 Predicted and measured extents of reaction of Class F (examples).
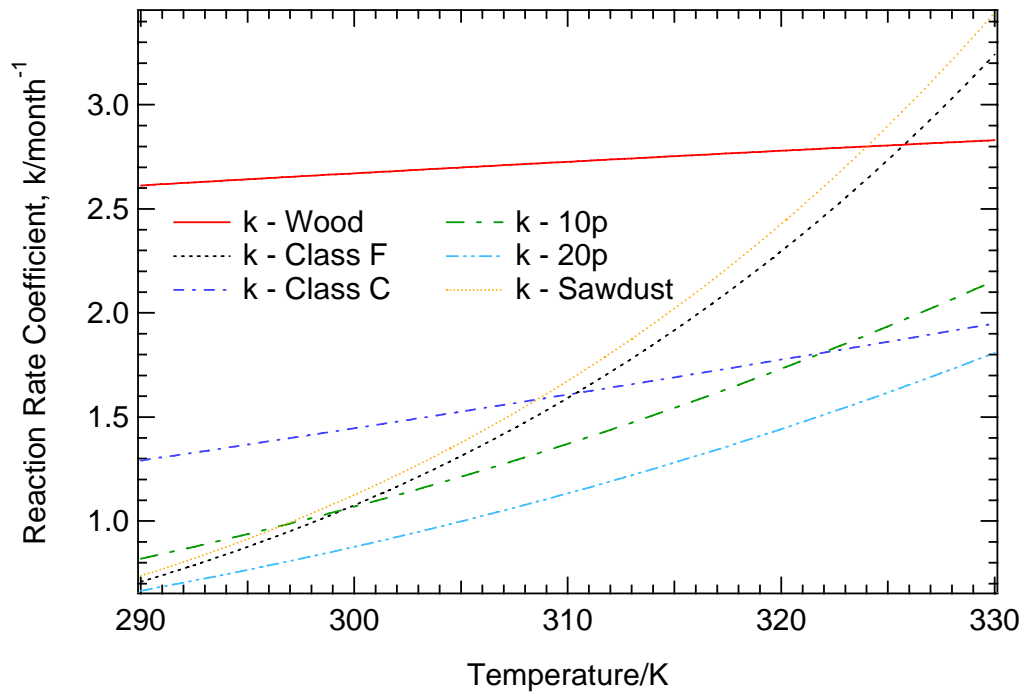
Figure 5-52 Predicted reaction rate coefficients over 23-63ºC

The parameter *b* represents the ratio between each fly ash and calcium hydroxide, which averages about 2.1 and exceeds the ratio in the nominal pozzolanic reaction by about a factor of 8. This indicates that the fly ash behaves as if about 13 %, of it were reactive and the remainder is inert. While it is difficult to know exactly what fraction of the fly ash reacts, this estimate of 13 % seems reasonable since fly ash contains many compounds that do not react with calcium hydroxide. The variation of this parameter with fly ash type is also reasonable, as shown in Table 5-2.

The excess parameter (*a*) depends on the mass stoichiometric ratio (*b*) and the initial calcium hydroxide mass fraction (see Eq. 5-1), which varies from 0.2 to 0.4 (Table 5-3). It is not independently fit to the data. A positive value of this parameter (*a*) indicates an excess of fly ash while a negative value indicates excess calcium hydroxide. The data follow the expected trend, that calcium hydroxide excess increases with increasing initial calcium hydroxide content. The computed values also bracket the stoichiometrically balanced ratio.

The parameter confidence intervals can be computed several ways. The technique used in traditional linear and non-linear regression produces large approximate error bars for the Arrhenius parameters, reflecting the highly correlated nature of the parameters of an Arrhenius expression. In addition to being large, the interval includes negative values for the pre-exponential factor – a result that is difficult to rationalize conceptually. The confidence interval for the stoichiometric coefficient (which is essentially independent of the Arrhenius parameters) spans a relatively small and in all cases reasonable range. Confidence intervals based on non-linear but local analyses of the parameters appear in Table 4-5.

Table 5-3 Values of excess parameter, a, as a function of initial Ca(OH)$_2$ % (mass).

	$x_{Ca(OH)2,0}$		
	0.2	0.3	0.4
Class F	0.425	0.1375	-0.15
Class C	0.344	0.016	-0.312
Wood	0.202	-0.197	-0.596
10P	0.452	0.178	-0.096
20P	0.428	0.142	-0.144
Sawdust	0.458	0.187	-0.084

A better, indeed exact, method for computing such confidence intervals can be derived based on nonlinear-least squares, maximum likelihood, sampling theory, Bayesian, and other techniques. In the case that the errors in the data are additive and normally distributed about the model mean with the same variance for each error (all common, reasonable but not necessarily trivial assumptions), several of these theories collapse to the same expression (all of the ones listed if the Bayesian approach assumes no prior knowledge of the parameters). This expression accurately (exactly under these assumptions) predicts the confidence region, but the level of confidence represented by the region is approximate. The confidence regions arise from a parameter set that satisfies the following equation

$$\frac{S(\Theta) - S(\hat{\Theta})}{S(\hat{\Theta})} \leq \frac{p}{n-p} F_{p,n-p}^{\alpha} \qquad (5\text{-}3)$$

where the set of parameters is represented by the vector Θ and the caret modifier indicates the optimum values, $S(\Theta)$ represents the sum of squares of the differences between the model predictions and the data for the given values of Θ (see below), p represents the number of parameters (3 in this case) and n the number of data points (typically 126 in this case), and $F_{p,n-p}^{\alpha}$ represents the upper- α quantile of the Fischer-F-distribution with p and $n\text{-}p$ degrees of freedom. Everything in this function except $S(\Theta)$ is a constant for a given data set and model. The function $S(\Theta)$ is formally defined as

$$S(\Theta) \equiv \sum_{i=1}^{n} \left[y_i - f(x_i;\Theta) \right]^2 \qquad (5\text{-}4)$$

where the function f is the model, the measured data are y_i, and the values of the independent variables at which the measurements are taken are x_i. The values of the independent variables are also assumed to be know exactly (another very common, possibly reasonable, but non-trivial assumption). These equations describe a p-dimensional region of parameter space within which the best estimate of the p parameters should lie (exactly within these assumptions) with approximately $1\text{-}\alpha$ % confidence. One property of such regions for Arrhenius models is that the activation energy and pre-exponential factor portions of this region are highly correlated and curved, improving the approximations for these intervals discussed earlier, as illustrated in Figure 5-53.

124

This curvature and the relatively narrow band of reasonable values of confidence intervals is an inherent property of Arrhenius-type equations and convey substantially different information than traditional ranges.

Table 5-4 Best estimates of the kinetic parameters

	k^0	95% CI$_{k0}$	E_A/R	95% CI$_{EA}$	b	95% CI$_b$
	month^{-1}	month^{-1}	K	K	-	-
Class F	199453	-430000-848000	3639	2676-4602	1.875	1.73-2.02
Class C	38.71	-66.4-144	986.2	139-1833	2.28	2.12-2.44
Wood	5.05	-20.2-30.3	191.1	-1381-1763	2.99	2.78-3.20
10P	2408	-4107-8925	2316	1481-3152	1.74	1.57-1.91
20P	2535	-3863-8933	2391	1610-3172	1.86	1.68-2.04
Sawdust	245700	-412000-903600	3688	2872-4504	1.71	1.59-1.83

Note : based on approximately 128 measured data points at 65 conditions for each type of fly ash.

For example, the confidence intervals based on an advanced non-linear analysis – considerably more sophisticated than the more common linearized analysis – appear in Table 5-4 and differ significantly from the more accurate analysis that appears in Figure 5-53.

The unreacted fly ash comprises Region *I*, the particle film or shell comprises Region *II*, and the surrounding matrix comprises Region *III*. The dashed line is the initial particle diameter. As the particle reacts, it forms an inner and an outer interface, each represented by a solid line.
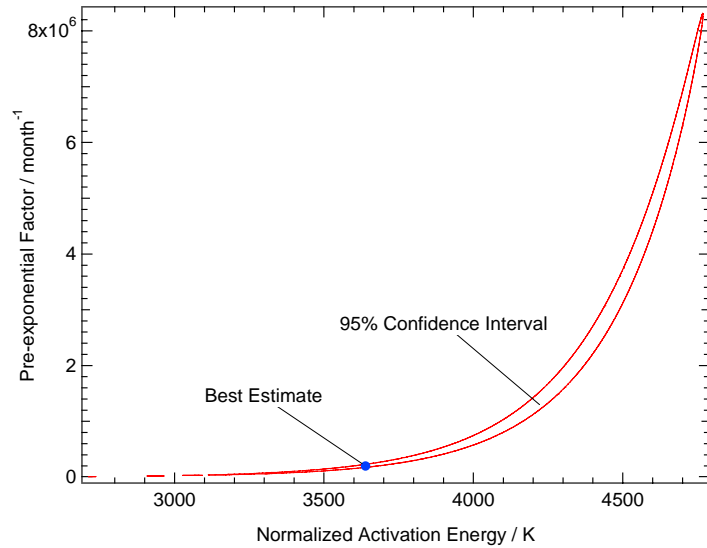
Figure 5-53 Best estimate and its 95% confidence interval for Class F ash kinetic parameters (based on best estimate of the parameter *b*)

Table 5-5 Comparisons of quantitative kinetics of Pozzolanic reactions

	(Biernacki, Williams et al. 2001)	(Pietersen 1993)	Wang & Baxter
Eact (kJ/mol)	30.7-69.8	6.5-9.2	12.0-30.6
Kinetic expressions	First order, modified second order and Avarami	First order	Modified second order
Curve fitting reactants	CH by TGA	Fly Ash elements leach out (Si, Al and K)	CH by TGA
Samples	Paste [H₂O/(CH + fly ash)] = 0.8	Aqueous solution	Mortar [H₂O/(fly ash + CH) /sand = 0.5 :1 :2]
T (˚C)	25-60	20-40	23-63
Testing (days)	16	17	365
Fly ash types	1	5	6

The outer interface marks the reaction front between the matrix and the reaction products. The inner one marks a similar front between the fly ash and reaction products.

Both fronts move with time in the directions indicated by the small, dashed arrows. The region between these interfaces consists of reaction products mixed with presumably small amounts of reactants. The original particle diameter is R, the fly-ash-reaction-product interface is r_i, and the calcium-hydroxide-reaction-product interface is r_p. These lower-case radii with lower-case subscripts should not be confused with the volumetric mass reaction rate r_A.

The discussion describing this model appears below in the order of (a) the chemical reaction term, (b) the shell, (c) the particle interface, and (d) the gradient in the surrounding matrix. The equations developed in each area combine to form a single expression involving only the surrounding matrix. This is combined with expressions for the reaction rate, and solutions to this model are applied to the current data. A schematic representation of a particle-based analysis appears in Figure 5-54.

A volumetric reaction rate expression for the reaction on the surface and in the interior of the fly ash particles follows from the following assumptions: (a) the reaction is first-order in calcium hydroxide mass fraction and zero order in fly ash except when all the fly ash is consumed, in which case the reaction stops; (b) a Thiele modulus adequately describes the effect of calcium hydroxide diffusion into the particle; and (c) (c) the particle interface, and (d) the gradient in the surrounding matrix. The equations developed in each area combine to form a single expression involving only the surrounding matrix. This is combined with expressions for the reaction rate, and solutions to this model are applied to the current data.

Figure 5-54 Schematic diagram of reacting ash particle in concrete/Ca(OH)$_2$ matrix.

$$-r_A \equiv -\frac{d\left(\overline{\rho}\,\overline{x}_A\right)}{dt} = -\overline{\rho}\frac{d\,\overline{x}_A}{dt} = A_{ex}kE(Th)\rho''_{A,i}$$

$$= A_{ex}\rho''_i kE(Th)x''_{A,i} = 4\pi r_i^2 \frac{n_p}{V}\rho''_i kE(Th)x''_{A,i} \qquad (5\text{-}5)$$

$$-r_A \equiv -\frac{d\left(\overline{\rho}\,\overline{x}_A\right)}{dt} = 4\pi r_i^2 \frac{n_p}{V}\rho''_i kE(Th)x''_{A,i}$$

where n_p represents the number of particles per unit volume, $\overline{\rho}$ is the overall density, ρ'' is the density of Region *II*, and overall mass conservation indicates $\overline{\rho}V$ is a constant (hence moving out of the derivative), $\overline{x}_A$ is the overall average mass fraction of component *A* (calcium hydroxide), A_{ex} is the volumetric surface area of the particles (m^2 surface area/m^3 of concrete = $4\pi r_i^2 \frac{n_p}{V}$), $x''_{A,i}$ (with no overbar) represents the mass

128

fraction of A at the *i* interface, that is, the mass fraction at the surface of the reacting fly ash particle, $E(Th)$ is the effectiveness factor that depends on the Thiele modulus, *Th*, and r_A and k have dimensions of mass of calcium hydroxide/(volume time) and length/time, respectively.

Combining this kinetic expression with transport expressions and eliminating intermediate values (details in the Appendix) yields

$$
-r_A = \frac{\dfrac{n_p}{V} x_{A,b}^{III}}{f(r_i, r_p)}
$$

$$
f(r_i, r_p) = \underbrace{\frac{1}{4\pi k E(Th)\rho'' c_\gamma \left(1 - x_{\Sigma,b}''\right) r_i^2}}_{\text{reaction front / kinetics}} + \underbrace{\frac{r_p - r_i}{4\pi \rho'' D_{e,A}'' r_i r_p}}_{\text{shell}} + \underbrace{\frac{\left(r_p - r_i\right)\left(1 - c_\gamma \left(1 - x_{\Sigma,b}''\right)\right)}{4\pi \rho'' D_{e,A}'' c_\gamma \left(1 - x_{\Sigma,b}''\right) r_i r_p}}_{\text{p-interface}} +
$$

$$
\underbrace{\frac{1}{2\pi Sh_A \rho''' D_{e,A}''' r_p}}_{\text{matrix}}
\tag{5-6}
$$

where D_e represents and effective diffusivity of calcium hydroxide, $x_{\Sigma,b}''$ represents the sum of all mass fractions other than calcium hydroxide, *Sh* represents the Sherwood number, and c_γ is a thermodynamic activity correction factor that should be approximately unity.

This expression includes several time-dependent terms, most notably both radii. Since there is essentially no volume change on reaction, these terms can be related through a volume balance (details in the Appendix). This yields a differential equation for r_p only, namely

$$\frac{d\,r_p}{dt} = \frac{c_\gamma \left(1 - x_{\Sigma,b}^{II}\right)}{Y}$$

Where

$$Y = \frac{\rho^{III} r_p^2}{kE(Th)\rho^{II}\left[(1+b)R^3 - br_p^3\right]^{2/3}} + \frac{\rho^{III}}{\rho^{II} D_{e,A}^{II}}\left\{\frac{r_p^2}{\left[(1+b)R^3 - br_p^3\right]^{1/3}} - r_p\right\} \qquad (5\text{-}7)$$

$$+ \frac{2c_\gamma\left(1 - x_{\Sigma,b}^{II}\right)r_p}{Sh_A D_{e,A}^{III}}$$

$$\frac{d\,r_p^3}{dt} = \frac{3c_\gamma\left(1 - x_{\Sigma,b}^{II}\right)}{Y}$$

Where

$$Y = \frac{\rho^{III}}{kE(Th)\rho^{II}\left[(1+b)R^3 - br_p^3\right]^{2/3}} + \frac{\rho^{III}}{\rho^{II} D_{e,A}^{II}}\left\{\frac{1}{\left[(1+b)R^3 - br_p^3\right]^{1/3}} - \frac{1}{r_p}\right\} \qquad (5\text{-}8)$$

$$+ \frac{2c_\gamma\left(1 - x_{\Sigma,b}^{II}\right)}{Sh_A D_{e,A}^{III} r_p}$$

The reaction rate relates to the time-dependent diameter change as follows (again, see the appendix for the details)

$$-r_A = 4\pi \frac{n_p}{V} \rho^{III} x_{A,b}^{III} r_p^2 \frac{d\,r_p}{dt}$$

$$= \frac{4\pi \frac{n_p}{V} x_{A,b}^{III} c_\gamma \left(1 - x_{\Sigma,b}^{II}\right)}{Y}$$

$$\qquad (5\text{-}9)$$

$$Y = \frac{1}{kE(Th)\rho^{II}\left[(1+b)R^3 - br_p^3\right]^{2/3}} + \frac{1}{\rho^{II} D_{e,A}^{II}}\left\{\frac{1}{\left[(1+b)R^3 - br_p^3\right]^{1/3}} - \frac{1}{r_p}\right\}$$

$$+ \frac{2c_\gamma\left(1 - x_{\Sigma,b}^{II}\right)}{Sh_A D_{e,A}^{III} \rho^{III} r_p}$$

An analytical, explicit solution to the diameter equation would allow the reaction rate equation to be written in terms of time only. However, both equations are difficult to solve analytically. They could be solved numerically with appropriate estimates of their parameters.

In principal, the dataset generated in this project could be used to determine the unknown parameters, either by numerically solving the equation and using the solution to fit the data (the statistically preferred method), or by differentiating the data and fitting the results to the differential equation (more convenient, but statistically problematic). The primary unknown parameters include two solid-solid diffusion coefficients and a kinetic rate constant. Secondary unknown parameters – those for which reasonable estimates could be made from sources other than the data – include the activity parameter (about 1), two densities (about 2500 kg/m^3), and the mass fraction of non-hydroxide in the shell (SEM images could provide an estimate, which is typically about 0.8). There are over 150 data points for each type of fly ash, more than enough to determine the primary and even secondary unknown parameters from a degree-of-freedom standpoint. In practice, these parameters are too closely related to make meaningful estimates. For example, the temperature dependence of the solid-solid diffusion coefficients generally has an Arrhenius-type dependence identical in form and similar in effective activation energy to that of the kinetic constant. Finally, although this work generated a large dataset, determining values for these closely related parameters with acceptable statistical precision will require large data sets and higher precision.

Despite the difficulties in determining precise parameters, some indication of the equation behavior can be developed. Since the kinetic resistance approaches infinity as the reaction approaches completion, these equations result in a reaction rate prediction that asymptotically approaches zero. This is a consequence of the first-order kinetic assumption. The shell resistance also approaches infinity if there is an excess of calcium hydroxide, since the particle inner diameter approaches zero and the shell eventually becomes infinitely thick relative to this diameter. If there is excess fly ash, the shell resistance increases to a finite value with increasing extent of reaction. The external matrix diffusion resistance increases with increasing extent of reaction but remains finite in Figure 5-55.

The differential expression for the rate of calcium hydroxide mass fraction change includes external transport, internal transport, and kinetic resistances. However, the kinetic and internal transport resistances occur in the same form in the equation. Furthermore, diffusion coefficients for such systems are very difficult to determine but indicate a temperature dependence identical to that of kinetics (exponentially dependent on inverse temperature). This makes the kinetic and particle film resistances essentially impossible to distinguish from experimental data such as ours. One way to distinguish them is to vary particle size, as that impacts internal film resistance but not kinetics. However, simply separating fly ash by size will not provide a reliable result since fly ash composition varies significantly with size. The scope of this work falls short of a more detailed investigation of the kinetics of this reaction, but these equations represent a starting point for such an analysis.
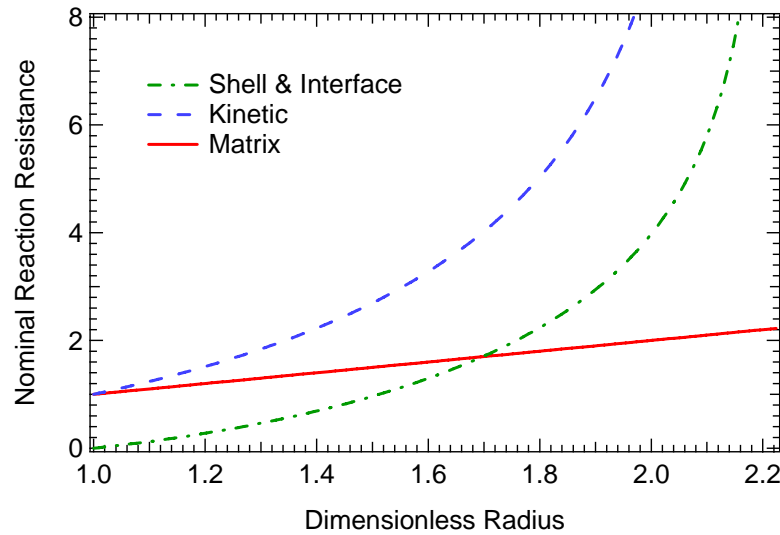
Figure 5-55 Changes in resistances with the matrix, shell, and kinetics during reaction
    [These normalized data assume b = 0.1. The progression is from an unreacted
    (abcissa=1) to a fully reacted particle. Both the kinetic and the shell/interface
    resistances approach infinity as the reaction extent approaches unity.]

A final analysis promises to be the most insightful. The previous model assumes, among other things, that the material does not swell or shrink and therefore conserves both mass and volume locally. All mass transfer occurs through diffusion in the previous model. However, it is possible to drive mass fluxes without diffusion by inducing pressure gradients. This model assumes that the matrix does not swell but that the pressure induced by the growing shell of products forces reactants through the pores in the shell and that transport is dominated by this pressure-induced convection. In this model, the concentration of calcium hydroxide in the unreacted matrix, x_A^{III}, does not change with time. This material convects without reaction to the surface of the particle, where it reacts to form silicate products that expand the shell. However, the overall concentration of calcium hydroxide, $\overline{x}_A$, changes because the amount of unreacted

133

matrix decreases with increasing time as increasingly larger fractions of it react with the fly ash particle surface to form silicate products.

A conceptual diagram appears below and is similar in many ways to that of the last model except that the silicate products appear as spokes of a wheel, in a manner in which they sometimes appear in SEM images and commonly appear in the literature. Also, there is a ring of material formed at the location r_p. The motivation for this model is this observation that the shell commonly takes on a spoke-and-ring structure. The spokes could result from the convective flow; a diffusion-based process such as the previous model describes would tend to destroy rather than create such a structure. The outer ring of concentrated material could result from the pressure-driven expansion of the particle. Again, the diffusion-based model of the previous section predicts an opposite trend – calcium hydroxide concentration decreasing near the outer ring of the shell. The pressure relates directly to the reaction rate, and the spoke-and-ring structure would be expected to dissipate after reaction completes, again consistent with SEM observations (fully reacted particles commonly have neither the ring nor the spoke structure). Finally, our data indicate that while the extent of reaction increases with increasing temperature, the ultimate strength decreases with increasing temperature. One (of several) explanations for this behavior is that higher temperatures lead to more rapid reaction and hence greater pressures. Large pressures lead to matrix microfractures, which would compromise strength. This model quantifies most of these phenomena and evaluates this conceptual model compared to the data.

This model asserts that the flow through the porous layer obeys Darcy's law, as is common for flows in porous media, that is

$$Q_A = -\frac{\kappa A_x \Delta p}{\mu L} \tag{5-10}$$

where Q_a represents the volumetric flow [vol/time], κ is the permeability [length^2], A_x is the cross-sectional area perpendicular to the flow, Δp is the pressure difference [force/area] across the distance L, and μ is the fluid viscosity [force*time/area]. In terms of volumetric fluxes and gradients, this can be generalized as

$$\vec{q}_A = -\frac{\kappa}{\mu}\vec{\nabla}p \tag{5-11}$$

where q is the volumetric flow per unit cross-sectional area (volumetric flux) and $\vec{\nabla}$ is the gradient operator. The remainder of this model is one-dimensional and the vector notation is no longer maintained.

If all materials are incompressible, this model leads to the non-intuitive result that neither the matrix nor the shell resistances affect the reaction rate, since the expansion of the shell layer quantitatively forces the reactants to the reaction front, r_i. It also suggest that the macromolecular reaction products in the shell will orient themselves along the flow paths to minimize flow resistance and that the matrix near the outer edge of the shell is compressed and therefore may be more highly concentrated in all materials, including calcium, than the bulk of the matrix due to the force of the expanding particle. The effects of viscosity and permeability influence the pressure gradient, but if all materials are incompressible, they do not influence the flow at a given reaction rate. As with the previous model, this model neglects the mass of calcium hydroxide in the shell.
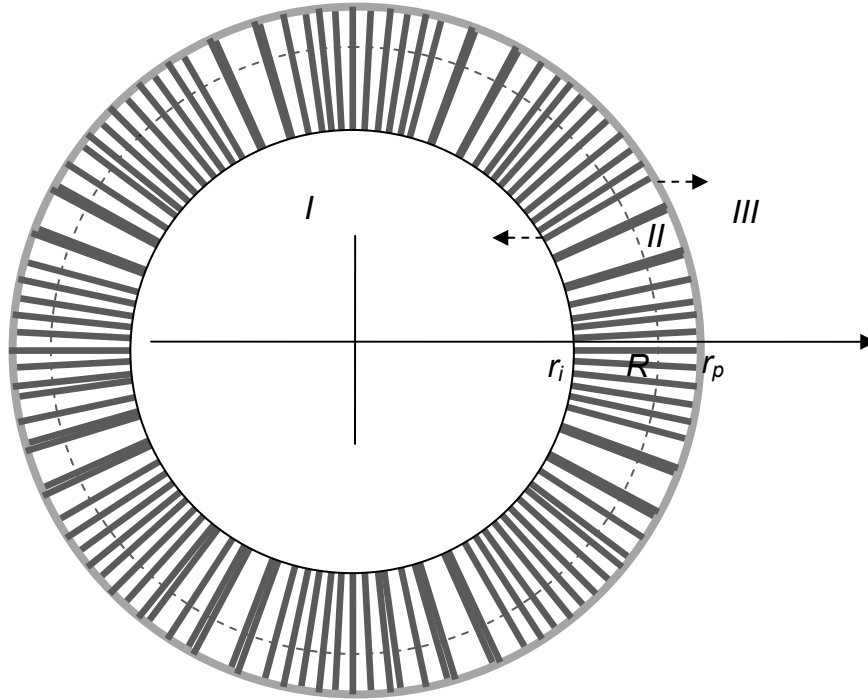
Figure 5-56 Schematic diagram of reacting fly ash particle in concrete/Ca(OH)₂ matrix (pozzolanic reaction) for the convective model indicating nomenclature and highlights the ring and spoke structures often seen in such particles.

Returning to the volume balance of the previous model, an expression for the pressure gradient as a function of *r* in the shell is

$$-\left(1+b\right)\frac{d\left(\rho^{III}V_A x_A^{III}\right)}{x_A^{III}\rho^{III}dt}=\frac{d\left(\rho^{II}V_{Si8}x_{Si8}^{II}\right)}{x_{Si8}^{II}\rho^{II}dt}$$

$$-\left(1+b\right)\frac{\dfrac{V}{n_p}r_A}{x_A^{III}\rho^{III}}=-q_A 4\pi r^2=-\frac{\kappa}{\mu}\nabla p 4\pi r^2=\frac{d\left[\dfrac{4}{3}\pi\left(r_p^3-r_i^3\right)\right]}{dt} \qquad (5\text{-}12)$$

$$\nabla p = -(1+b)\frac{\mu\dfrac{V}{n_p}r_A}{4\pi\kappa x_A^{III}\rho^{III}r^2} \tag{5-13}$$

This model ultimately results in a much simpler expression for the reaction rate than the previous model. The derivation follows that of the previous model precisely except (a) there are no mass transfer resistances in the shell or bulk layer, and (b) the activity parameter is assumed unity since there is no phase change at the outer shell surface, just flow of material and two non-chemically-interacting phases. The details appear in the appendix.

$$\overline{x}_A(\tau) = \begin{cases} \overline{x}_A^0 - \dfrac{n_p}{V}\dfrac{4\pi R^3 \rho^{III}}{b\overline{\rho}}x_{A,b}^{III}\tau\left(1-\tau+\dfrac{1}{3}\tau^2\right) & 0 \le \tau \le 1 \\[2em] \overline{x}_A^0 - \dfrac{n_p}{V}\dfrac{4\pi R^3 \rho^{III} x_{A,b}^{III}}{3b\overline{\rho}} & \tau > 1 \end{cases} \tag{5-14}$$

In terms of the dimensional variable the first and second equations become

$$\overline{x}_A(t) = \overline{x}_A^0 - \frac{n_p}{V}\frac{4\pi R^2 kE(Th)\left(1-x_{\Sigma,b}^{II}\right)\rho^{II}x_{A,b}^{III}t}{\overline{\rho}}\times$$

$$\left\{1 - \frac{bkE(Th)\left(1-x_{\Sigma,b}^{II}\right)\rho^{II}t}{\rho^{III}R} + \frac{1}{3}\left[\frac{bkE(Th)\left(1-x_{\Sigma,b}^{II}\right)\rho^{II}t}{\rho^{III}R}\right]^2\right\}$$

$$\tag{5-15}$$

for $0 \le t \le \dfrac{\rho^{III}R}{bkE(Th)\left(1-x_{\Sigma,b}^{II}\right)\rho^{II}}$, and

$$\overline{x}_A(t) = \overline{x}_A^0 - \frac{n_p}{V}\frac{4\pi R^3 \rho^{III} x_{A,b}^{III}}{3b\overline{\rho}} \tag{5-16}$$

for $t > \dfrac{\rho''' R}{bkE(Th)\left(1 - x_{\Sigma,b}''\right)\rho''}$

$\qquad\qquad\qquad\qquad\qquad\qquad\qquad\qquad\qquad\qquad\qquad$ (5-17)

and where the dimensionless time is given by

$$\tau \equiv \dfrac{bkE(Th)\left(1 - x_{\Sigma,b}''\right)\rho'' t}{R\rho'''}$$

$\qquad\qquad\qquad\qquad\qquad\qquad\qquad\qquad\qquad\qquad\qquad$ (5-18)

This derivation prevents fly ash concentration from becoming negative by setting zero as a lower bound on r_i. However, the derivation has not yet specifically enforced overall mass conservation for calcium hydroxide, that is, has not explicitly required that calcium hydroxide mass fraction be a non-negative number. The equations above predict eventual negative concentrations if fly ash is in stoichiometric excess. Stoichiometric excess fly ash in this model results from having more potential to react calcium hydroxide than the amount of calcium hydroxide in the mixture, which occurs whenever the following inequality is met,

$$\overline{x}_A^0 \overline{\rho} < \dfrac{n_p}{V} \dfrac{4}{3b} \pi R^3 \rho''' x_{A,b}'''$$

$\qquad\qquad\qquad\qquad\qquad\qquad\qquad\qquad\qquad\qquad\qquad$ (5-19)

where the left side represents the overall concentration of calcium hydroxide present in the mixture and the right side represents the calcium hydroxide concentration that could potentially react with the fly ash.

In terms of the extent of reaction, the time-dependent portion of the composition equations becomes Equation (5-20). Figure 5-57 illustrates the time-dependent portion of the normalized reaction extent, $\dfrac{V}{n_p}\dfrac{3\overline{x}_A^0 b\overline{\rho}}{4\pi R^3 \rho^{III} x_{A,b}^{III}}\alpha$.

Formal expressions for the times at which the calcium hydroxide concentration reaches zero when it is limiting are

$$\tau_{max,CaOH\ limiting} = 1 - \frac{\left[\left(\dfrac{n_p}{V}R^3\rho^{III}x_A^{III}\right)^2\left(4\dfrac{n_p}{V}\pi R^3 \rho^{III} x_A^{III} - 3b\overline{\rho}\overline{x}_A^0\right)\right]^{1/3}}{2^{2/3}\dfrac{n_p}{V}\pi^{1/3}R^3\rho^{III}x_A^{III}}$$

(5-20)

and

$$t_{max,CaOH\ limiting} =$$

$$\frac{R\rho^{III}}{bkE(Th)\left(1 - x_{\Sigma,b}^{II}\right)\rho^{II}} - \frac{\left[\left(\dfrac{n_p}{V}R^3\rho^{III}x_A^{III}\right)^2\left(4\dfrac{n_p}{V}\pi R^3 \rho^{III} x_A^{III} - 3b\overline{\rho}\overline{x}_A^0\right)\right]^{1/3}}{2^{2/3}\dfrac{n_p}{V}\pi^{1/3}R^2 x_A^{III}bkE(Th)\left(1 - x_{\Sigma,b}^{II}\right)\rho^{II}}$$

(5-21)

This indicates that the reaction extent reaches (non-asymptotically) an ultimate value at a dimensionless time of 1. Depending on the relative amounts of fly ash and calcium hydroxide, the ultimate conversion may be as high as unity. It plateaus either at unity if fly ash is in stoichiometric excess or at some value less than unity if calcium hydroxide is in stoichiometric excess.

$$\alpha \equiv 1 - \frac{\overline{x}_A}{\overline{x}_A^0} = \frac{\overline{x}_A^0 - \overline{x}_A}{\overline{x}_A^0} = \frac{n_p}{V} \frac{4\pi R^3 \rho^{III} x_{A,b}^{III}}{\overline{\rho} \overline{x}_A^0 b} \tau \left(1 - \tau + \frac{1}{3}\tau^2\right)$$

$$= \frac{n_p}{V} \frac{4\pi R^2 kE(Th)\left(1 - x_{\Sigma,b}^{II}\right)\rho^{II} x_{A,b}^{III} t}{\overline{\rho} \overline{x}_A^0} \times$$

$$\left\{1 - \frac{bkE(Th)\left(1 - x_{\Sigma,b}^{II}\right)\rho^{II} t}{\rho^{III} R} + \frac{1}{3}\left[\frac{bkE(Th)\left(1 - x_{\Sigma,b}^{II}\right)\rho^{II} t}{\rho^{III} R}\right]^2\right\}$$

$$\tag{5-23}$$

$$\nabla p = \frac{-(1+b)\mu \dfrac{V}{n_p} r_A}{4\pi\kappa x_A^{III} \rho^{III} r_p^2} = \frac{-(1+b)\mu kE(Th)\left(1 - x_{\Sigma,b}^{II}\right)\rho^{II} (\tau - 1)^2}{\kappa\rho^{III}\left\{1 + \dfrac{1}{b}\left[3\tau - \tau^2(3 - \tau)\right]\right\}^{2/3}} \tag{5-24}$$

$$\frac{\kappa\rho^{III}\nabla p}{-(1+b)\mu kE(Th)\left(1 - x_{\Sigma,b}^{II}\right)\rho^{II}} = \frac{(\tau - 1)^2}{\left\{1 + \dfrac{1}{b}\left[3\tau - \tau^2(3 - \tau)\right]\right\}^{2/3}} \tag{5-25}$$

An expression for the pressure gradient at the matrix-shell interface (at r_p) as a function of time results from substituting the time-dependent expressions for the radius and the reaction rate into the previously derived expression for pressure gradient based on Darcy's law, as shown below. The expressions include a dimensioned and a dimensionless expression for pressure gradient. The latter also appears in Figure 5-57, which illustrates a high initial gradient followed by a more measured approach to the ultimate value of zero as the reaction rate approaches zero. Although the initial dimensionless pressure gradient may appear to approach infinity, it is identically unity on this normalized plot. The pressure gradient is even higher (though the pressure is lower)

at the fly-ash-shell interface (r_i), approaching infinity as the particle size approaches zero. The primary interest in the pressure gradient is its potential for forming microfractures in the matrix, which will be proportional to the pressure gradient at r_p.

Kinetic expressions for polydisperse particles in fly ash mixtures appear in Appendix F.
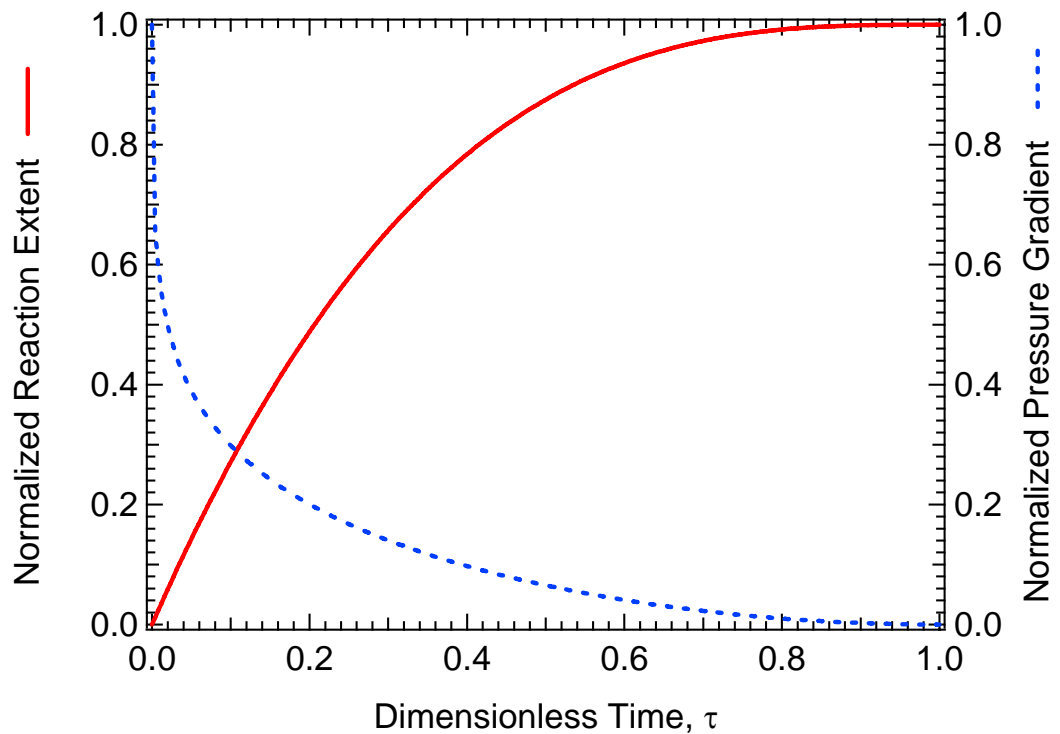
**Figure 5-57 Change in normalized reaction extent and pressure gradient
(at the shell outer radius (r_p) with dimensionless time predicted by the convective model)**

5.3 ASR Expansion and Pore Solution Analysis

The final analysis of fly ash in concrete involves ASR expansion. Expansion results drawn from the coal, biomass, and cofired samples in this sample provide a

systematic method of comparing the effectiveness of biomass fly relative to coal fly ash and no fly ash in preventing this deleterious reaction.

The ASR expansion results appear in Figure 5-58 through Figure 5-60. High-purity silica sand and pure cement mixes with and without opal logically and experimentally represent upper and lower limits, respectively, limits of ASR expansion. Experimentally, the former mix has the highest expansion in all the data from 14 days to 6 months; while the latter mix has the lowest expansion.

Large variations in ASR expansion mitigation exist among the samples. Trends appear both as a function of the amount and the type of fly ash. All samples produce qualitatively similar trends in ASR expansion with time. The following sections address each of these issues separately.

5.3.1 ASR Expansion

The conceptual model that provides a foundation for the experimental design of ASR expansion analysis is as follows: reactive (leachable) alkali reacts with crystalline silica to form alkali silicates that occupy greater volume than the volume of the reactants whereas amorphous silica reacts more readily with similar reactive alkali with little or no net expansion. Calcium does not generate much expansion upon reacting with crystalline silica but does react with both amorphous and crystalline silica, with the amorphous reactions again being more rapid. The calcium reactions with amorphous silica decrease the reaction rates of amorphous silica with alkali; Therefore, ASR reactions and the related expansion tend to increase with increasing calcium content. Fly ash contains more amorphous silica than most aggregates owing in part to the silicate-forming and silica-melting reactions during combustion. Some fly ash, notably fly ash from biomass and

some low-rank coals, also includes significant quantities of leachable alkali and calcium. Cement contains varying amounts of leachable alkali. Therefore, the combinations of cement, aggregate, and fly ash potentially can produce a complex pattern of ASR results.

The reactions with crystalline silica are slow, which is the reason that ASR issues commonly require 20 or more years to become evident. Such slow reactions are inconvenient for laboratory analysis. Higher concentrations of alkali and aggregate materials with highly amorphous or, alternatively, crystalline contents accelerate these reactions so they produce results measurable within constraints of laboratory procedures. The following section outline results from an experimental design formulated with this background.

5.3.1.1 Fly Ash Type

The data clearly indicated that high fly ash loading generally provides the best mitigation of ASR expansion. The most important chemical elements leading to ASR expansion are probably calcium and leachable sodium and potassium. The leachable alkalis presumably combine with aggregate crystalline silica to cause ASR expansion. Calcium most probably combines with amorphous silica in the fly ash, reducing the reaction rate with alkali in the pore solution and thus increasing the reaction with crystalline silica and expansion. That is, the effectiveness of fly ash addition in mitigating ASR expansion appears inversely correlated with the amounts of leachable alkali and the ratio of CaO to SiO_2, as well as the absolute amount of CaO and SiO_2 in the sample.

With respect to the available alkali content in Table 4-6, the six fly ashes fall roughly into two groups: 1) Class C and Class F; and 2) Wood, 10P, 20P and SAW. Based on the alkali contribution to ASR expansion, the fly ash samples should have

143

similar expansion performance within each of these two groups. The expansion curves in Figure 5-58 through Figure 5-60 show that 10P, 20P and SAW have similar mitigation of ASR expansion.

As for the ratio of CaO to SiO_2 as well as the absolute amount of those two components (see Table 4-5), the six fly ashes fall into three groups: 1) Class F with a ratio almost zero and the least amount of lime; 2) 10P, 20P, SAW and Class C with a ratio narrowly ranging from 0.48 to 0.65 and lime content in the narrow range of 18 to 24 %; and 3) Wood with the ratio and absolute percentage of lime between those two groups. Thus, Class F is the most efficient in depressing ASR expansion, Wood the second and 10P, 20P SAW and Class C the least.

The expansion curves shown in Figure 5-58 through Figure 5-60 support these two conclusions.   There are, however, additional influences not considered or systematically varied in these data. Wood has more leachable alkali and silica than Class C, and wood have high expansion at 15% ratio but lower expansion at 25 and 35% ratio compared to Class C, which implies that the two factors, leachable alkali and silica, compete with each other: alkali was compromised by silica at higher replacement ratio of 25-35% for wood mixes, in which situation some alkali is absorbed into the silica and less expansion is produced. However, 10P, 20P and SAW have much higher leachable alkali and almost the same amount of silica as Class C, but they have an equal and even better performance in mitigating ASR expansion, implying that some factors other than the two listed above, play important roles in this situation. The most plausible explanation is that there is a premium stoichiometric ratio between the silica and alkali content in the ASR system, at which the maximum expansion is generated, higher and

144

lower ratios will cause lower expansion than that at the premium ratio. The ratio of class C is closer to the premium ratio than 10P, 20P and SAW.

5.3.1.2 Replacement Ratio

In essentially all cases, ASR expansion decreases with increasing fly ash content. Except Class F fly ash with lower available alkali content than cement, all other fly ashes contain similar or much higher leachable alkali (by ASTM C 33) than cement.
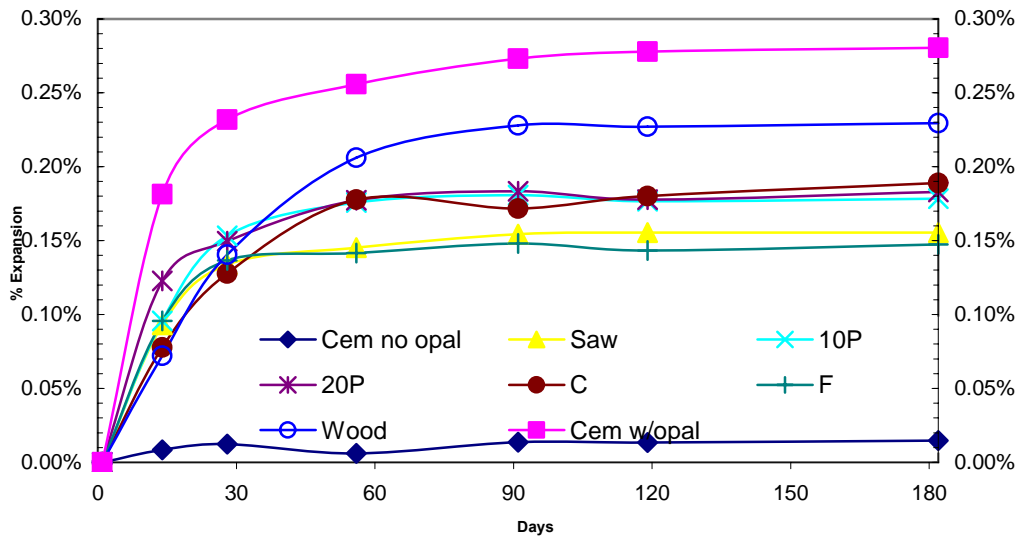
Figure 5-58 ASR expansion with 15% fly ash replacement (mass)

Therefore, the decrease in expansion with high alkali fly ash addition must primarily arise from the fly-ash-associated compounds that preemptively react with alkali without expansion (amorphous silica) and not by dilution of the available alkali in the cement. With respect to replacement ratios, different fly ashes perform differently. Class F and wood fly ashes mitigate ASR expansion with increasing weight ratio, as has been noted by other researchers. With respect to high-calcium fly ash, 10P, 20P and SAW samples are even more efficient than Class C for expansion reduction when increasing

145

replacement ratio, even though the biomass-derived fly ashes having much higher alkali and the similar silica contents with Class C.
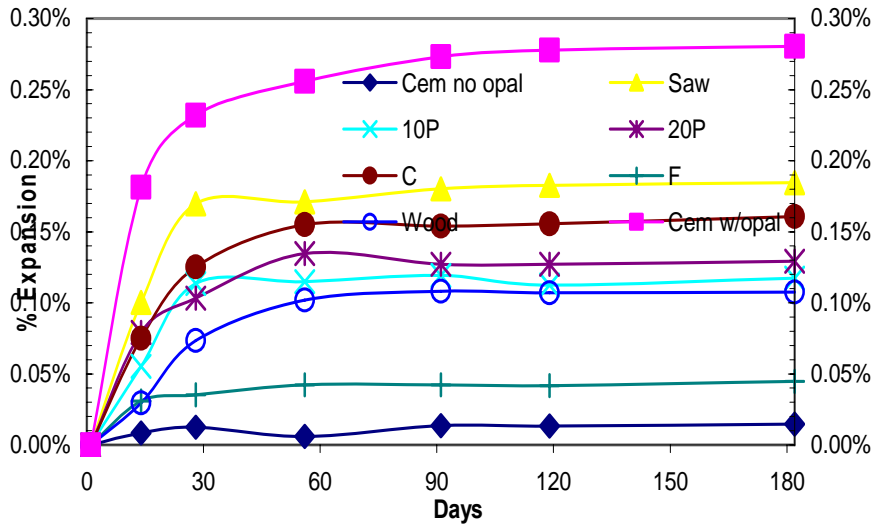
Figure 5-59 ASR expansion with 25% fly ash replacement (mass)
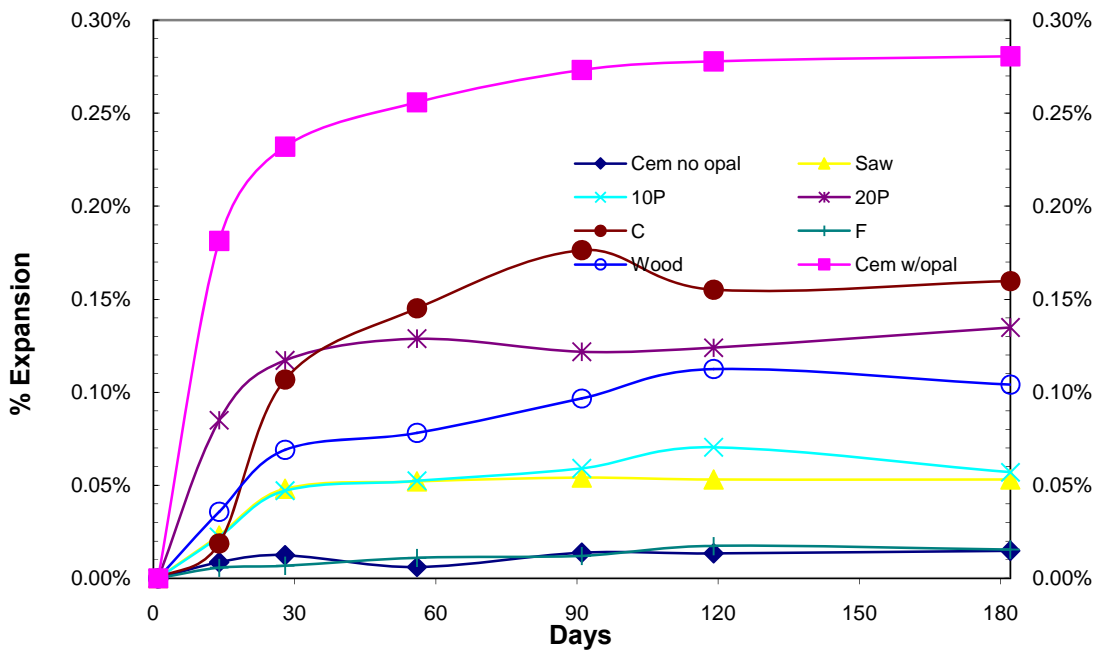
Figure 5-60 ASR expansion with 35% fly ash replacement (mass)

This implies that the alkali in 10P, 20P and SAW must form non expansive products in the system, thus reducing the ASR expansion despite higher leachable alkali.

5.3.1.3 Curing Time

All mixes develop 70 to 90% of their ultimate (12 month) expansion within one month, indicating that opal is a highly reactive aggregate and the opal-derived ASR expansion takes place rapidly. Since some of the samples contain fly ash that competes with opal for alkali reactions, these fly ash reactions must be faster still.

5.3.2 Pore Solution

The sum of $[Na^+]$ and $[K^+]$ reasonably represent the pore solution chemistry since the two cations dominate the overall cation concentrations. The results of pore solution analyses appear in Figure 5-61 and Figure 5-63. These results are again discussed as functions of fly ash type, fly ash amount, curing temperature, and curing time.
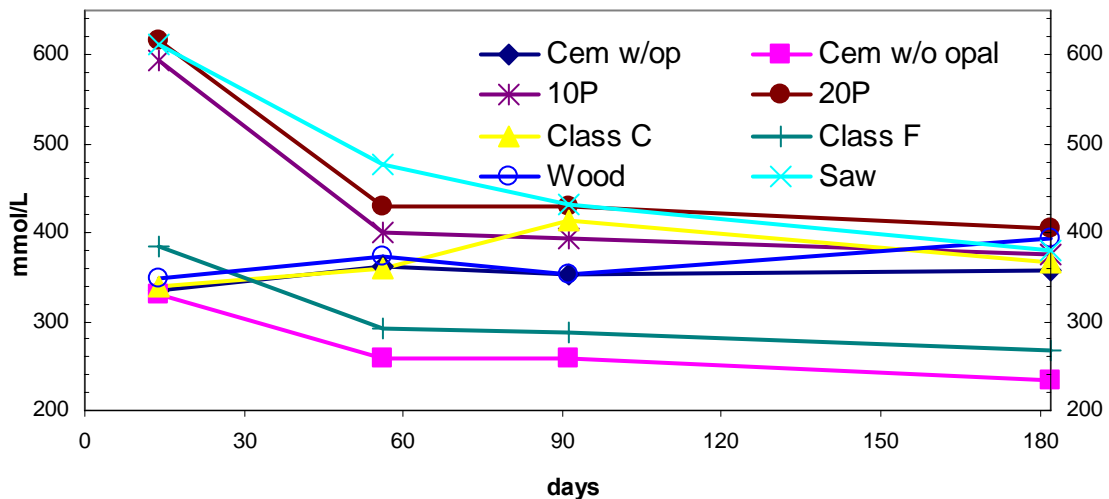
Figure 5-61 $[Na^+ + K^+]$ with 15% fly ash replacement (mass)
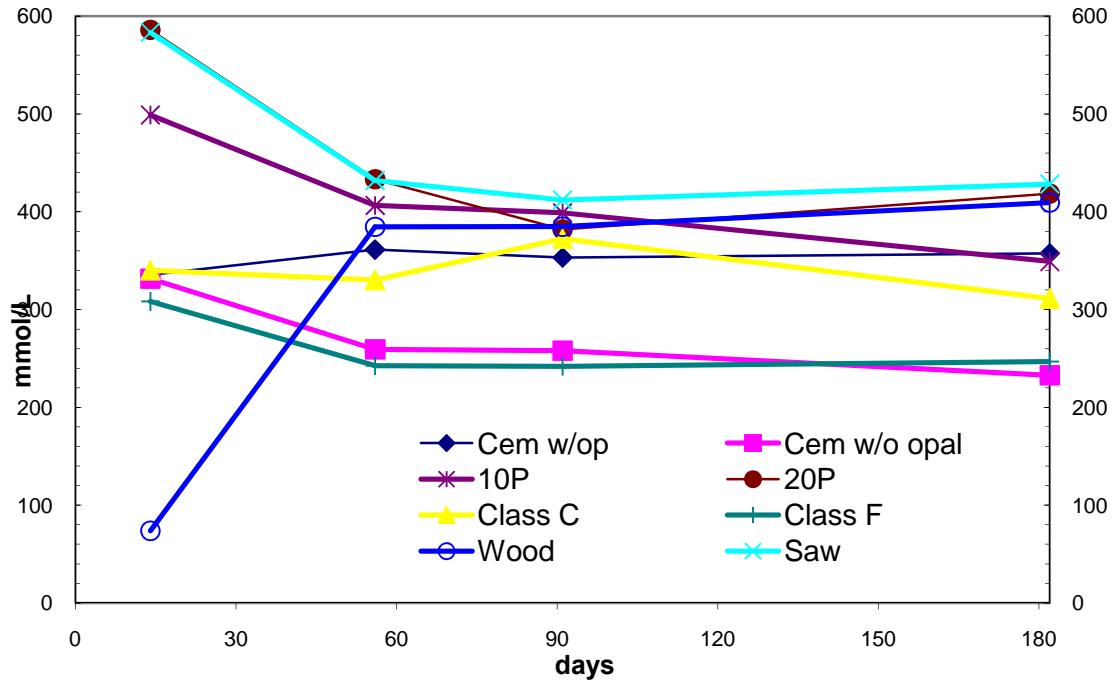
Figure 5-62 [Na$^+$+ K$^+$] with 25% fly ash replacement (mass)
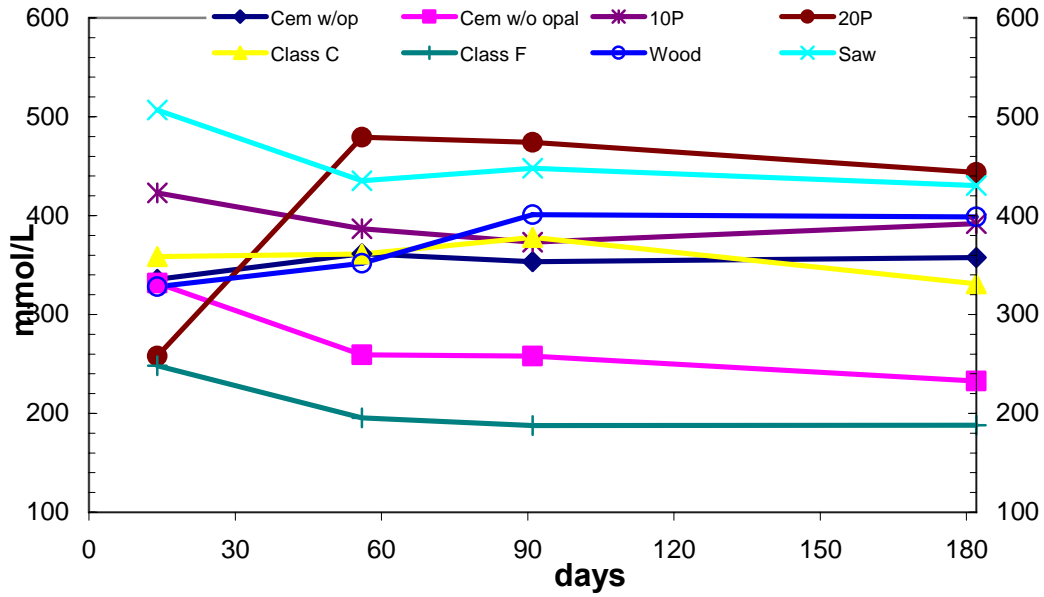
Figure 5-63 [Na$^+$+ K$^+$] with 35% fly ash replacement (mass)

5.3.2.1 Fly Ash Type Dependence

The samples fit into three classes based on ion concentration of pore solution and are quite consistent with their equivalent alkali content (see Table 4-6): 1) high ion concentration material (SAW, 10P and 20P); 2) intermediate ion concentration material (cement with opal, Class C and Wood); and 3) low ion concentration material (cement without opal and Class F). The major trends in the data are discussed in these three categories, although there is some overlap between categories.

The combination of the expansion data and the pore solution ion concentration data provides important information regarding the ASR-associated expansion mechanism. ASR expansion requires at least two elements: alkali and silica. The highest expansion occurs with opal and cement. However, these pore solution alkali ion concentrations are average and nearly equivalent to all except two samples - Class F and cement without opal. The remaining samples have essentially the same pore solution alkali concentration and the same opal content but at different rates and to different extents. One extreme example is the 35% SAW sample, which has a consistently high alkali ion concentrations and relatively low expansion implying that mechanisms in addition to the combination of soluble alkali with silica influence expansion. The ion concentration data indicate that with fixed amount of opal, the alkali ion concentration (and most possibly the total amount of alkali in pore solution) is only significant up to a threshold, above which more alkali does not necessarily lead to higher ASR expansion. This implies that the amount of opal can be the limiting reactant. Further comparison of high ion concentration material (SAW, 10P and 20P) and intermediate ion concentration material (Class C and Wood)

indicates that they have different forms of silica that absorb leach out alkali in the pore solution and form non expansive products with different efficiency .

5.3.2.2 Mix Ratio

Perhaps surprisingly, the mix ratio only appears to impact ion concentrations for Class F fly ash in any systematic way. Such observation, however, is consistent with the previous discussion in that Class F appears to contribute the lowest alkali to the solution while being the most effective at absorbing it. The remaining mixes contribute comparable or more alkali to the solution than is contained in the cement with opal samples and so do not appreciably impact the measured ion concentration. Nevertheless, they do reduce ASR expansion, presumably by decreasing the yield of expansive alkali silica gels.

5.3.2.3 Curing Time

Alkali concentration decreases in the first few weeks of curing and then stabilizes for all samples. The decrease corresponds closely in time to the expansion, indicating that they are causally related.

5.3.2.4 Alkali Leaching Percentage

The ASR bars in the moisture curing environment have leached alkali into the water below them, presumably by continual dripping of condensate on the bars and return of the solution to the bottom of the container. The alkali leaching percentage for the three containers is 8.6, 7.6 and 9.5% separately, with an average of 8.6%. The leaching percentage is not significant compared to the alkali in the bars but is quite significant compared to the amount extruded in the pore solution, say at six month: the alkali

leachout at one year will be about 10 times of that in the 6 month pore solution. The curing method leaches out too much alkali and is under strong criticism (Hooton 1986).

Distilled in the curing containers begins with a PH of 7. At one year curing period, the solution in the three curing containers of the ASR bars was titrated by 1 N HCl with phenolphthalein as indicator. The initial weight of the ASR 2 in (D) X 4 in (H) cylinder was recorded before putting them into the curing Mason Jars that simulate the curing conditions of the water tanks with wicks running between the ASR bars. The cement and fly ash amount was calculated based on the mixing ratio. The leachable alkali of each bar was calculated as the sum of the equivalent alkali of cement and the available alkali of fly ash.

From the plots in Figure 5-61 to Figure 5-63, the $[Na^+ + K^+]$ of pore solution is can be estimated to be approximately 0.3 mol/L; the three cycles of high pressure extrusion only produced about 8 ml of pore solution. Assuming that 1) the pore solution at six month is approximately equal to that at one year (the alkali concentrations are very flat even at 1 month curing); 2) 10 ml of pore solution is available for each 2 in (D) X 4 in (D) cylinder (actually only about 5-7 ml of pore solution was obtained during the three cycle of pore solution and less than 1 ml can be available with one more extrusion); 3) the average alkali concentration of pore solution is 0.3N; and 4) the curing conditions of bars simulates that of the water tank containers (Figure 4-11) and thus the pore solution of the cylinders is the same as that of the bars. Using the volume of the bars (1 in X 1 in X 10 in) and the cylinders (2 in diameter and 4 in height), it can be estimated that the total alkali content in the pore solution can be estimated to be approximately 0.06 mol. However, the total alkali leached in the three water tank containers is 0.462 (0.15 + 0.18

+ 0.132) mol and 9.5 times the alkali amount in the pore solution, which indicates that the alkali leaching rate is large compared to that in the pore solution, which indicates this curing condition might cause affection to the ASR bars expansion and thus "inappropriate" for the ASR bars curing. Hooton (Hooton 1987) compared the containers with and without wick and concluded that the samples with wick had much lower ASR expansion than those without wick, and thus the containers with wick will have severe alkali leaching.

5.3.3 Effect of ASR Expansion, Fly Ash and Replacement Ratio on Strength

The compressive strength of one year ASR cylinders appears in Figure 5-64. All other fly ash mixes exhibit similar strength except wood mixes, which have much higher water/ (cement + fly ash) ratios and much larger fly ash particle sizes; except wood and saw mixes, all other fly ash mixes indicate increasing strength with increasing replacement ratio. Cement without opal has higher strength than cement with opal, but the difference is not statistically different at 95% confident interval. Further investigation of ASR expansion and compressive strength appears in Figure 5-65. There is no correlation between expansion and compressive strength at one year; however, the total strength in these samples comes from the combination of pozzolanic and cementitious reactions, with the pozzolanic reaction generally contributing only 25% of the strength.

Investigations by other researchers have similar results in related to ASR expansion. Opal and fused silica as reactive aggregate in 1986 and 1987 (1986; Swamy and Asali 1988) have shown that ASR expansion affects more compressive strength than flexure strength.

152

Boxplots of Strength by Mix

(means are indicated by solid circles)
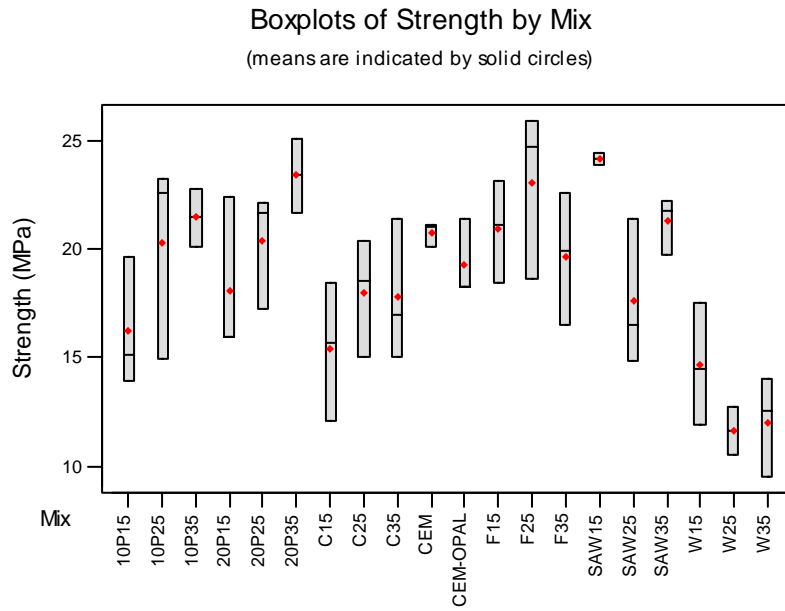
Figure 5-64 One way ANOVA of one year compressive strength
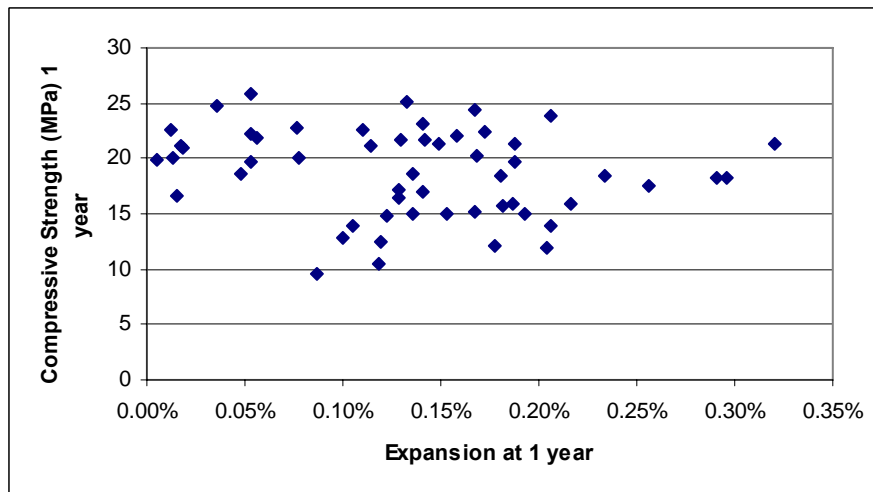
Figure 5-65 ASR expansion and compressive strength at 1 year

At 0.05% and 0.1% ASR expansion, the compressive strength was reduced only by 11%,

which is similar to the result obtained here for cement with and without opal.

153

6. Conclusions

This investigation compares biomass fly ash cofired with coal at levels of 10 or 20% switchgrass (herbaceous) and sawdust (woody) material with traditional coal Class C and Class F fly ash and with cement in terms of suitability for use in concrete. High-rank Galatia coal produces Class F fly ash if burned by itself; SW1 or SW2 include 10 or 20% switchgrass replacement of Galatia coal, with final fly ash composition that still qualifies as Class F. Powder River Basin coal produces Class C fly ash; 10 or 20% replacement by switchgrass or sawdust, 10P, 20P and SAW still qualify the fly ash as Class C.

Five years investigation of biomass fly ash on the properties of concrete indicates that biomass fly ash performs comparable to, or better than, coal fly ash in terms of concrete workability, strength, durability, pozzolanic reaction, ASR mitigation, and other concrete properties. The overall conclusion is that ASTM C 618 should be revised to allow biomass fly ash in concrete.

The specific conclusions include aspects of concrete mix design, strength, durability and quantitative kinetics of pozzolanic reaction and ASR mitigation, as discussed separately below:

6.1 Fresh Concrete Properties, Strength, Durability and Microscopy

1. Coal fly ash addition reduces water demand in concrete. Biomass-coal cofired and blended fly ashes exhibit slightly greater water demand than traditional Class C and Class F fly ash, but the difference is marginally significant.

2. Pure wood fly ash mix has consistently 6% higher water demand than pure cement mix.

3. All fly ash mixes, including coal, blended biomass and coal, biomass-coal cofired, and wood fly ash, increase air-entraining agent demand. Biomass-containing fly ash results fall within the range of observed pure-coal fly ash results.

4. All fly ash mixes, including coal, blended biomass and coal, biomass-coal cofired, and wood fly ash, increase setting time. Biomass-containing fly ash results fall within the range of observed pure-coal fly ash results.

5. Biomass-coal blended and biomass-coal cofired fly ash exhibit similar performance to coal fly ash with respect to impacts on concrete compressive strength in that they lower the compression strength during the first few weeks, but develop similar strength from 1 month to 1 year, relative to pure cement. The biomass-fly-ash-containing samples produce results similar to those of coal fly ash samples in this regard.

6. Pure wood fly ash exhibits similar compression strength to that of other fly ash mixes from 1 to 7 days; but from 1 month to 1 year, it develops statistically less strength than pure cement and other fly ash mixes.

7. All fly ash except pure wood fly ash mixes generally do not impact 56 day flexure strength relative to pure cement.

8. Pure wood fly ash samples compromise 56-day flexure strength relative to pure cement and all other fly ash samples.

9. Special attention is required to entrain appropriate air content in coal and biomass fly ash concrete mixes. The air-entraining agent required to meet ASTM specifications varies considerably and complexly among the samples. Variations for biomass-containing samples are no more extreme or complex than that for coal fly ash.

10. With a similar amount of air content, the freezing and thawing tests show that all fly ashes mixes, including coal fly ash and all kinds of biomass fly ash, perform similar to that of the pure cement mix.

11. Biomass fly ash SW1 and SW2 have similar performance of coal fly ash in reducing permeability of concrete.

12. Wood and blended wood fly ash samples produce higher chlorine permeability than other samples. The higher permeability of wood and blended wood fly ash relates to the much coarser particle size of wood fly ash.

13. Coal fly ash particles undergo pozzolanic reaction at two months and have significant pozzolanic reaction after one year in concrete;

14. Biomass-coal cofired fly ash particles in concrete have undergone significant pozzolanic reaction at 1 year and have comparable reaction performance with coal fly ash particles.

6.2 Quantitative Reaction Rate of Pozzolanic Reaction and Strength Build up

1. Three biomass fly ash samples, 10P, 20P and SAW, consistently have 2-3 times the strength of coal and wood fly ash samples and comparable strength to that of pure cement samples.

2. An increase in temperature increases early strength (up to three months), but decreases long-term strength (from three months to one year) development from pozzolanic reactions.

3. Increasing fly ash ratio from 60/40, 70/30 to 80/20 (fly ash/CH) increases strength of all samples except Class F (coal) and Wood samples.

4. During the first month, all samples, including six fly ash samples and cement, develop more than 60% of their ultimate (one-year) strength.

5. Calcium hydroxide reaction extent depends on fly ash type in complex ways.

6. Calcium hydroxide reaction extent increases with increasing temperature decreasing initial calcium-hydroxide -to-fly-ash ratio.

7. Cofired biomass fly ashes investigated in this project have similar calcium hydroxide reaction extent as indicated by TGA and uniformly perform as well or much better than pure coal and wood fly ash with respect to strength build up by pozzolanic reaction.

6.3 Mitigation of Alkali Silica Reaction and Pore Solution Analysis

1. Opal-derived alkali-silica reactions (ASR) cause early expansion and significant even in the first four weeks of curing.

2. ASR expansion mitigation depends strongly on fly ash type: Class F being the most effective and Class C being the least effective. Biomass fly ash and wood fly ash generally lie between these two extremes.

3. All six fly ashes in this investigation, irrespective of their equivalent alkali content, depress ASR with increasing replacement ratio.

4. ASR expansion scales inversely with pore solution ion concentration when such ion concentrations are relatively low, possibly within a certain range. Ion concentrations are a limiting reactant in expansion-inducing chemical processes when their concentration is low.

5. Biomass fly ash more effectively mitigates ASR expansion in the presence of high alkali ion concentrations than cement or coal fly ash, probably because biomass fly ash contains more amorphous (non-expanding) silica.

6. Biomass-containing fly ashes are at least as effective as Class C fly ash in mitigating ASR expansion, and are less effective than Class F fly ash. In some specific cases, they are much better than Class C, although they have much higher equivalent alkali. Given the acceptance of Class C fly ash in concrete, there appears to be little justification in excluding biomass-coal cofired fly ash from similar use, based on ASR expansion issues.

7. References

(1986). <u>Alkalies in Concrete ASTM STP 930</u>. Influence of alkali-silica reaction on the engineering properties of concrete. Philadelphia, PA, American Society for Testing and Materials.

AK-Steel-Corporation-Website (2000). Product Data Bulletin :17-4 PH Stainless Steel, AK Steel Corporation.

Alasali, M. M., V. M. Malhotra, et al. (1991). "Performance of Various Test Method For Assessing The Potential Alkali Reactivity Of Some Canadian Aggregates." <u>ACI Materials Journal</u>: 613-619.

Aldridge, L. P. (1982). "Accuracy and Precision on X-Ray Diffraction Method For Analyzing Portland Cement." <u>Cement and Concrete Research</u> **12**: 437-446.

Alhozaimy, A., P. Soroushian, et al. (1996). "Effects of Curing Conditions and Age on Chloride Permeability of Fly Ash Mortar." <u>ACI Materials Journal</u> **93**(1): 87-95.

Arjunan, P., M.R.Silsbee, et al. (1997). <u>Quantitative Determination of the Crystalline and Amorphous Phases in Low Calcium Fly Ashes</u>. Proceedings of 10th Intl. on the Chemistry of Cement.

ASTM-C143/C143M-98 (1998). Standard Test Method for Slump of Hydraulic-Cement Concrete.

ASTM-C192/192M-98 (1998). "Standard Practice for Making and Curing Concrete Tests Specimens in the Laboratory."

ASTM-C227 (1997). Standard Test Method for Potential Alkali Reactivity of Cement-Aggregate Combinations (Mortar-Bar Method), ASTM.

ASTM-C293 (1994). "Standard Test Method for Flexural Strength of Concrete (Using Simple Beam with Center-Point Loading)."

ASTM-C311 (1990). Standard Test Methods for Sampling and Testing Fly Ash or Natural Pozzolans for Use as a Mineral Admixture in Portland-Cement Concrete, ASTM.

ASTM-C441 (1997). Standard Test Method for Effectiveness of Mineral Admixtures of Ground Blast-Furnace Slag in Preventing Excessive Expansion Due to the Alkali-Silica Reaction, ASTM.

ASTM-C617 (1998). "Standard Practice for Capping Cylindrical Concrete Specimens."

ASTM-C618 (1999). Standard Specification for Coal Ash and Raw Calcined Natural Pozzolan for Use as a Mineral Admixture in Concrete. ASTM annual book. **4.02**.

ASTM-C666 (1997). Standard Test Method for Resistance of Concrete to Rapid Freezing and Thawing.

ASTM-C1202 (1997). Standard Test Method for Electrical Indication of Concrete's Ability to Resist Chloride Ion Penetration.

ASTM-D3628 (2000). Standard Test Method for Major and Minor Elements in Combustion Residues from Coal Utilization Processes.

Avrami, M. (1939). "Kinetics of Phase Change-I." Journal of Chemical Physics **7**: 1103-1112.

Ball, M. C. and R. A. Carroll (1999). "Studies of Hydrothermal Reactions of UK Pulverized Fuel Ashes. Part I: Reactions Between Pulverized Fuel Ash and Calcium Hydroxide." Advances in Cement Research **11**(2): 53-61.

Barlow, D. F. and P. J. Jackson (1988). "The Release of Alkalis from Pulverized-Fuel Ashes and Ground Granulated Blast Furnace Slags in the Presence of Portland Cements." Cement and Concrete Research **18**: 235-248.

Barneyback, R. S. and S. Diamond (1981). "Expression and Analysis of Pore Fluids from Hardened Cement Pastes and Mortars." Cement and Concrete Research **11**: 279-285.

Berube, M. A. and J. Dunchesne (1991). The Effectiveness of Silica Fume in Suppressing Expansion Due to Alkali-Aggregate Reaction. Canmet/ACI International Workshop on Use of Silica Fume in Concrete, Ottawa, Canada.

Berube, M.-A. and J. Dunchesne (1992). Does Silica Fume Merely Postpone Expansion Due to Alkali-Aggregate Reactivity. 9th International Conference on Alkali-Aggregate Reaction in Concrete, London, UK.

Biernacki, J. J. and J. M. Richardson (2002). "Kinetics of Slag Hydration in the Presence of Calcium Hydroxide." Journal of American Ceramic Society **85**(9): 2261-2267.

Biernacki, J. J., P. J. Williams, et al. (2001). "Kinetics of Reaction of Calcium Hydroxide and Fly Ash." ACI Materials Journal: 340-349.

Blackwell, B. Q., M. D. A. Thomas, et al. (1992). The Use of Fly Ash to Suppress Deleterious Expansion Due to AAR in Concrete Containing Greywacke Aggregate. 9th International Conference on Alkali-Aggregate Reaction in Concrete, London, UK.

Brooks, J. J. (2002). "Prediction of Setting Times of Fly Ash Concrete." ACI Materials Journal **99**(6): 591-597.

Brown, P. W., J. Pommersheim, et al. (1985). "A Kinetic Model for the Hydration of Tricalcium Silicate." Cement and Concrete Research **15**: 35-41.

Chatterjee, M. K. and D. Lahiri (1964). "Estimation of Free Calcium Hydroxide Present in Hydrated Cements by Differential Thermogravimetric Analysis." Transactions of the Indian Ceramic Society **23**(4): 198-202.

Chatterji, S., N.Thaulow, et al. (1987). "Studies of Alkali Reaction. Part 4. Effect of Different Alkali Salt Solutions on Expansions." Cement and Concrete Research **17**: 777-783.

Currell, B. R., H. G. Midgley, et al. (1985). "A Study of Portland Cement Hydration by Trimethylsilylation Techniques." Cement and Concrete Research **15**: 889-900.

Davies, G. and R. E. Oberholster (1988). "Alkali-Silica Reaction Products and Their Development." Cement and Concrete Research **18**: 621-635.

Diamond, S. (1976). In Hydraulic Cement Pastes: Their Structure and Properties, Tapton Hall, University of Sheffield, American Concrete Association, Slough.

Diamond, S. (1986). "Particle Morphologies in Fly Ash." Cement and Concrete Research **16**: 569-579.

Diamond, S., B. R.S., et al. (1981). On the Physics and Chemistry of Alkali-Silica Reaction. 5th International Conference of Alkali Aggregate Reaction in Concrete, Cape, Town, South Africa.

Din, Z. (1979). The Physical Chemistry of Silicates (in Chinese), Chinese Construction Industry Press.

Dolar-Mantuani, L., Ed. (1983). Handbook of Concrete Aggregates: A Petrographic and Technological Evaluation. Park Ridge, New Jersey, USA, Noyes Publications.

Durand, B. (1991). Preventive Measures Against Alkali-Aggregate Reactions. In: Petrography and Alkali-Aggregate Reactivity-Course Manual. Ottawa, Canada, Canmet/EMR**:** 399.

Durand, B., J. Berard, et al. (1990). "Alkali-silica reaction: the relation between pore solution characteristics and expansion tests results." Cement and Concrete Research **20**: 419-428.

Durand, B., J. Berard, et al. (1990). "Alkali-Silica Reactions: The Relation between Pore Solution Characteristics and Expansion Test Results." Cement and Concrete Research **20**: 419-428.

Eberendu, A. R. N. and K. E. Daugherty (1984). "The Quantitative Determination of Glass in Slag by Infrared Spectroscopy." Cement and Concrete Research **14**: 873-883.

Erdogdu, K. and P. Turker (1998). "Effects of Fly Ash Particle Size on Strength of Portland Cement Fly Ash Mortars." Cement and Concrete Research **28**(9): 1217-1222.

Farbiarz, J., R. Carrasquillo, et al. (1986). Alkali-Aggregate Reaction in Concrete Containing Fly Ash. 7th International Symposium of Alkali Aggregate Reaction in Concrete, Ottawa, Canada.

Fouad, F. H., C. A. Copham, et al. (1998). Evaluation of concrete containing fly ash with high carbon content and / or small amounts of wood, Department of civil engineering The University of Alabama at Birmingham.

Fournier, B., A.Bilodeau, et al. (1996). Canmet/Industry Research Consortium on Alkali-Silica Reactivity (ASR). 10th International Symposium of Alkali Aggregate Reaction in Concrete, Melbourne, Australia.

Fraay, A. L. A. and J. M. Bijin (1989). "The Reaction of Fly Ash in Concrete: A Critical Examination." Cement and Concrete Research **19**: 235-246.

Glasser, D. and N. Kataota (1981). "The Chemistry of Alkali-Aggregate Reaction." Cement and Concrete Research **11**: 1-9.

Grutzeck, M. W., D. M. Roy, et al. (1981). Hydration Mechanisms of High-Lime Fly ash in Portland-Cement Composites. Effects of Fly Ash Incorporation in Cement and Concrete Symposium N Materials Research Society Annual Meeting, Materials Research Society, Boston.

Helmuth, R. (1987). "Fly Ash in Cement and Concrete."

Hewlett, P. C. (1998). Lea's Chemistry of Cement and Concrete (4th edition), Reed Educational and Professional Publishing, Ltd.

Hill, R. (1997). "An Examination of Fly Ash Carbon and Its Interaction with Air Entraining Agent." Cement and Concrete Research **27**(2): 193-204.

Hooton, D. (1987). Effect of Storage Containers on Expansion of Mortar Bars Made With Spratt Aggregate (siliceous Stone). Minutes of Meeting of CSA Subcommittee A5, Cement Aggregate Reactivity. Quebec City, Laval University.

http://www.usbr.gov/dataweb/dams/mt00565.htm.

J.Duchesne and M.-A. Berube (1992). <u>An Autoclave Mortar Bar Test for Assessing the Effectiveness of Mineral Admixtures in Suppressing Expansion Due to AAR</u>. 9th International Conference on Alkali-Aggregate Reaction in Concrete, London, UK.

J.Duchesne and M.-A. Berube (1992). <u>Relationships between Portlandite Depletion, Available Alkalis and Expansion of Concrete Made with Mineral Admixtures</u>. 9th International Symposium of Alkali Aggregate Reaction in Concrete, London, UK.

Kendrick, D. A., J.R>parsonage, et al. (1998). "Interaction of Alkali and Alkali Earth Metal Hydroxides with Microsilica." <u>Cement and Concrete Research</u>: 1537-1544.

Larive, C. and N. Louarn (1992). <u>Diagnosis of Alkali-Aggregate Reaction and Sulphate Reaction in French Structures</u>. 9th International Conference on Alkali-Aggregate Reaction in Concrete, London, UK.

Lee, C. (1989). <u>Active Alkalis in Cement-Fly Ash Paste</u>. 8th International Symposium of Alkali Aggregate Reaction in Concrete, Kyoto, Japan.

Longuet, A., L. Burglen, et al. (1973). "The liquid phase of hydrated cement (in french)." <u>Review material construction</u>(676): 35-41.

Marsh, B. K. and R. L. Day (1985). "Pozzolanic and Cementitious Reactions of Fly Ash in Blended Cement." <u>Cement and Concrete Research</u> **18**: 301-310.

Mcconnell, D., R. C. Mielenz, et al. (1947). "Cement-Aggregate Reaction in Concrete." <u>Journal of American Concrete Institute</u> **19**(2): 93-128.

Metha, P. K. and P. J. M. Monteiro (1993). <u>Concrete: Structure, Properties, and Materials</u>. Englewood Cliffs, New Jersey, Prentice Hall.

Midgley, H. G. (1979). "Determination of Calcium Hydroxide in Set Portland Cement." <u>Cement and Concrete Research</u> **9**: 77-82.

Mindness, S., J. F. Young, et al. (2002). <u>Concrete</u>, Pearson Education, Inc.

Naik, T., R. Kraus, et al. (2003). "Controlled low-strength materials containing mixtures of coal ash and new pozzolanic material." <u>ACI Materials Journal</u> **100**(3): 208-215.

Naik, T. and K. R. (2003). "A new source of pozzolanic material." <u>Concrete International</u> **25**(12): 55-62.

Pietersen, H. S. (1993). Reactivity of Fly Ash and Slag in Cement. <u>Geochemistry</u>. Delft, Delft University of Technology.

Qian, C. and H. Guo (1996). <u>Influence of Alkali Content on the Properties of Concrete Containing Beijing Aggregate</u>. 10th International Symposium of Alkali Aggregate Reaction in Concrete, Melbourne, Australia.

Qian, C., H. Guo, et al. (1994). "Mechanism of Mineral Admixture Suppressing Alkali-Silica Reaction: Part II. Retardation of the Transport of Na, K and OH Ions in Pore Strusture Caused by Acidic Action of Mineral Admixture Particles in Matrix." Cement and Concrete Research **24**(7): 1327-1334.

Ravina, D. and P. K. Metha (1986). "Properties of Fresh Concrete Containing Large Amounts of Fly Ash." Cement and Concrete Research **16**(2): 227-238.

Regourd, M. and H. Hornain (1986). Microstructure of Reaction Products. 7th International Symposium of Alkali Aggregate Reaction in Concrete, Ottawa, Canada.

Reis, M. O. B., H. S. Silva, et al. (1996). AAR in Portuguese Structures. Some Case Histories. 10th International Symposium of Alkali Aggregate Reaction in Concrete, Melbourne, Australia.

Robert S. Barneyback, J. (1983). Alkali-Silica Reactions in Portland Cement Concrete. Civil Engineering. West Lafayette, IN, Purdue University.

Roode, M. V., E. Douglas, et al. (1987). "X-Ray Diffraction Measurement of Glass Content in Fly Ashes and Slags." Cement and Concrete Research **17**: 183-197.

Scanlon, J. M. and M. R. Sherman (1996). "Fly Ash Concrete: An Evaluation of Chloride Penetration Testing Methods." Concrete International(7): 57-62.

Sengul, O., C. Tasdemir, et al. (2005). "Mechanical Properties and Rapid Chloride Permeability of Concrete with Ground Fly Ash." ACI Materials Journal **102**(6): 414-421.

Shayan, A. (1992). "Prediction of Alkali Reactivity Potential of Some Australian Aggregates and Correlation with Service Performance." ACI Materials Journal: 13-23.

Shayan, A., R. Diggins, et al. (1996). Long-Term Effectiveness of Fly Ash in Preventing Deleterious Expansion Due to Alkali-Aggregate Reaction in Concrete. 10th International Symposium of Alkali Aggregate Reaction in Concrete, Melbourne, Australia.

Shayan, A. and G. Quick (1989). Microstructure and Composition of AAR Products in Conventional Standard and New Acclerated Testing. 8th International Symposium of Alkali Aggregate Reaction in Concrete, Hyoto, Japan.

Shebl, F. A. and F. M. Helmy (1985). "A New Approach on the Hydration Mechanism of Tricalcium Silicate." Cement and Concrete Research **15**: 747-757.

Shi, C. (1993). Activation of Natural Pozzolans, Fly Ashes and Blast Furnace Slags. Civil Engineering. Calgary, University of Calgary.

Shi, C. (1998). "Pozzolanic Reaction and Microstructure of Chemical Activated Lime-Fly Ash Pastes." ACI Materials Journal **95**(5): 537-545.

Shi, C. (2004). "Effect of Mixing Proportions of Concrete on Its Electrical Conductivity and the Rapid Chloride Permeability Test (ASTM C1202 or ASSHTO T277) Results." Cement and Concrete Research **34**: 537-545.

Shi, C. and R. L. Day (1995). Chemical Activation of Lime-Slag Blends. 5th International Conference of Fly Ash, Slag, Silica Fume and Natural Pozzolans, Milwaukee, Wisconsin, ACI.

Smoot, L. D. (1993). Fundamentals of Coal Combustion: for Clean and Efficient Use.

Stanton, T. E. (1940). "Expansion of Concrete through Reaction between Cement and Aggregate." Proceedings of American Society of Civil Engineers **66**: 1781-1811.

Struble, L. (1987). The influence of Pore Solution on Alkali-Silica Reaction. Civil Engineering. West Lafayette, IN, Purdue University.

Struble, L. and S. Diamond (1989). Influence of Cement Pore Solution on Expansion. 8th International Conference on Alkali-Aggregate Reaction in Concrete, Kyoto, Japan.

Swamy, R. N., Ed. (1992). The Alkali-Silica Reaction in Concrete. East Kilbride, Scotland, Thomson Litho Limited.

Swamy, R. N. and M. M. Asali (1988). "Engineering properties of concrete affected by alkali silica reaction." ACI materials journal **85**(5): 367-3333374.

Taylor, H. F. W. (1997). Cement Chemistry, Thomas Telford Services Ltd.

Taylor, H. F. W. and A. B. Turner (1987). "Reactions of Tricalcium Silicate Paste with Organic Liquids." Cement and Concrete Research **17**: 613-623.

Thomas, M. D. A. and B. Q. Blackwell (1996). Summary of Bre Research on the Effect of Fly Ash on Alkali-Silica Reaction in Concrete. 10th International Symposium of Alkali Aggregate Reaction in Concrete, Melbourne, Australia.

Ukita, K., S. Shigemastu, et al. (1989). Improvements in the Properties of Concrete Utilizing 'Classified Fly Ash'. in Fly Ash, Silica Fume, Slag, and Natural Pozzolans in Concrete. Proceedings of Third CANMET/ACI International Conference SP -114, Norway.

Ukita, K., S.-i. Shigematsu, et al. (1989). Effect of Classified Fly Ash on Alkali Aggregate Reaction(AAR). 8th International Symposium of Alkali Aggregate Reaction in Concrete, Kyoto, Japan.

Vanderstraeten, A. T. (1987). Repair of Alkali-Aggregate Reaction Damage to the Motorway Structures of the Pell Street Interchange, Port Elizabeth, Republic of South Africa. Proceedings of 7th International Conference on Concrete Alkali-Aggregate Reaction, Ottawa, Canada, Noyes Publications.

Villar-Cocina, E., Valencia-Morales, et al. (2002). "Kinetics of the Pozzolanic Reaction between Lime and Sugar Cane Straw Ash by Electrical Conductivity Measurement: A Kinetic-Diffusive Model." Cement and Concrete Research **33**: 517-524.

Wang, S., R. Dalton, et al. (2007). Mitigation of ASR Expansion by Biomass/Coal Fly Ash. 9th Canmet/ACI International Conference on Fly Ash, Silica Fume, Slag and Natural Pozzolans, Warsaw, Poland.

Wang, S., R. Dalton, et al. (2007). Quantitative Kinetics of Pozzolanic Reaction and Strength Build-up in the Mortar of Biomass/Coal Fly Ash with Calcium Hydroxide. 9th Canmet/ACI International Conference on Fly Ash, Silica Fume, Slag and natural Pozzolans, Warsaw, Poland.

Wesche, K. (1991). Fly Ash in Concrete: Properties and Performance. New York, Chapman & Hall.

Wieker, W., C. Hubert, et al. (1996). Contribution to the Chemical Reaction Mechanism of the Alkali-Aggregate-Reaction. 10th International Symposium of Alkali Aggregate Reaction in Concrete, Melbourne, Australia.

Woods, H. (1968). Durability of Concrete Construction. Detroit, Mich, American Concrete Institution.

Zachariasen, W. H. (1932). "The Atomic Arrangement in Glass." Journal of American Chemical Society **54**: 3841-3851.

Zhang, M.-H., A. Bilodeau, et al. (1999). "Concrete Incorporating Supplementary Cementing Materials: Effect on Compressive Strength and Resistance to Chloride-Ion Penetration." ACI Materials Journal **96**(2).

Appendix A.   ASTM Standards

C 618 Standard Specification for Coal Ash and Raw Calcined Natural Pozzolan for Use as a Mineral Admixture in Concrete (2001)

C 617 -98 (2003) Standard Practice for Capping Cylindrical Concrete Specimens

C192 Standard Practice for Making and Curing Concrete Tests Specimens in the Laboratory

C143 Standard Test Method for Slump of Hydraulic-Cement Concrete

C231 Standard Test Method for Air Content of Freshly Mixed Concrete by the Pressure Method

C403 Standard Test Method for Time of Setting of Concrete Mixtures by Penetration Resistance

C39 Standard Test Method for Compressive Strength of Cylindrical Concrete Specimens

C293 Standard Test Method for Flexural Strength of Concrete (Using Simple Beam with Center-Point Loading)

C666 Standard Test Method for Resistance of Concrete to Rapid Freezing and Thawing

C1202 Standard Test Method for Electrical Indication of Concrete's Ability to Resist Chloride Ion Penetration

C289 Standard Test Method for Potential Alkali-Silica Reactivity of Aggregates (Chemical Method)

C1260 Standard Test Method for Potential Alkali Reactivity of Aggregates (Mortar-Bar Method)

C227 Standard Test Method for Potential Alkali Reactivity of Cement-Aggregate Combinations (Mortar-Bar Method)

C33 Standard Specification for Concrete Aggregate

C78 Standard Test Method for Flexural Strength of Concrete (Simple Third-Point Loading)

C441 Standard Test Method for Effectiveness of mineral Admixtures of Ground Blast-Furnace Slag in Preventing Excessive Expansion Due to the Alkali-Silica Reaction

C311 Standard Test Methods for Sampling and Testing Fly Ash or Natural Pozzolans for Use as a Mineral Admixture in Portland-Cement Concrete

Appendix B.   Acronyms

10P	cofired fly ash (10% switchgrass and 90% Powder River Basin coal)
20P	cofired fly ash (20% switchgrass and 80% Powder River Basin coal)
AA	Atomic Absorption Spectrometry
AE	Atomic Emission
ASTM	ASTM International, formerly American Society for Testing and materials
ASR	Alkali Silica Reaction
Class C	fly ash from low rank coal, typically $50\% < SiO_2 + Al_2O_3 + Fe_2O_3 < 70\%$
Class F	fly ash from high rank coal, typically $SiO_2 + Al_2O_3 + Fe_2O_3 > 70\%$
EDX	Energy Dispersive X-Ray analysis
ESEM	Environmental Scanning Electron Microscopy
EMPA	Electron Microprobe Analysis
ICP	Inductively Coupled Plasma
LOI	Loss on Ignition
QXRD	Quantitative X-Ray Diffraction
RCPT	Rapid Chloride Permeability Test
SAW	cofired fly ash (20% sawdust and 80% powder river basin coal)
SW1	cofired fly ash (20% switchgrass and 80% Galatia coal)
SW2	cofired fly ash(10% switchgrass and 90% Galatia coal)

SEM   Scanning Electron Microscopy

TGA   Thermo Gravimetric Analysis

Wood   (wood fly ash from pure wood combustion)

Wood C blended fly ash (20% Wood ash blended with 80% Class C fly ash)

Wood F blended fly ash (20% Wood ash blended with 80% Class F fly ash)

XRF   X-Ray Florescence

XRD   X-Ray Diffraction

Appendix C.   Results of Strength Buildup of 2 inch Cubes

80/20 23C
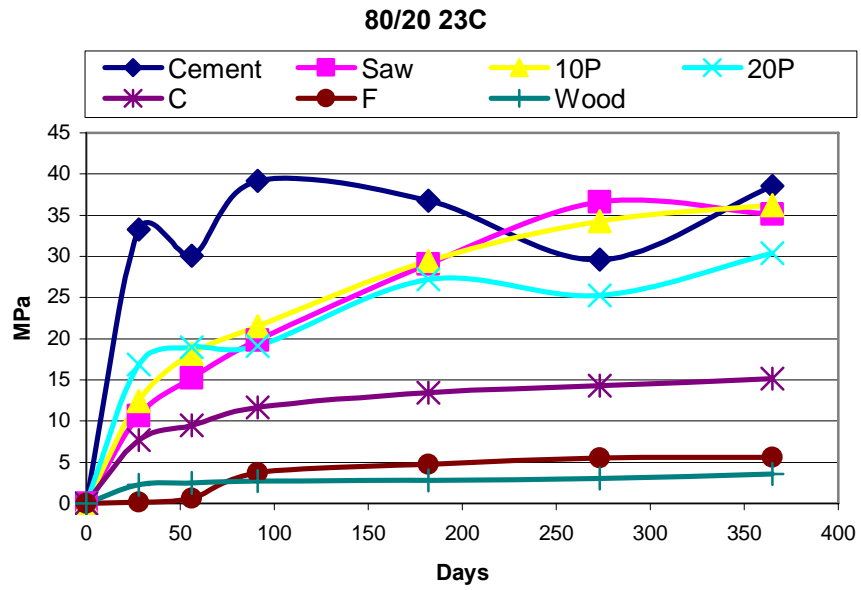
Figure C-1 Strength build up of 2 in cubes (fly ash: CH = 80/20)
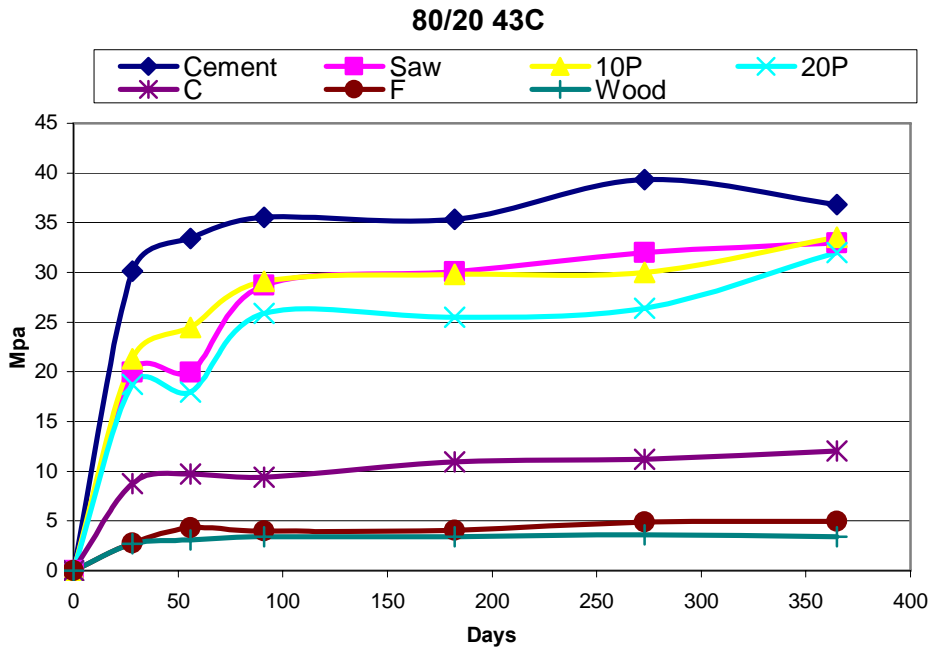
Figure C-2 Strength build up of 2 in cubes (fly ash: CH = 80/20)
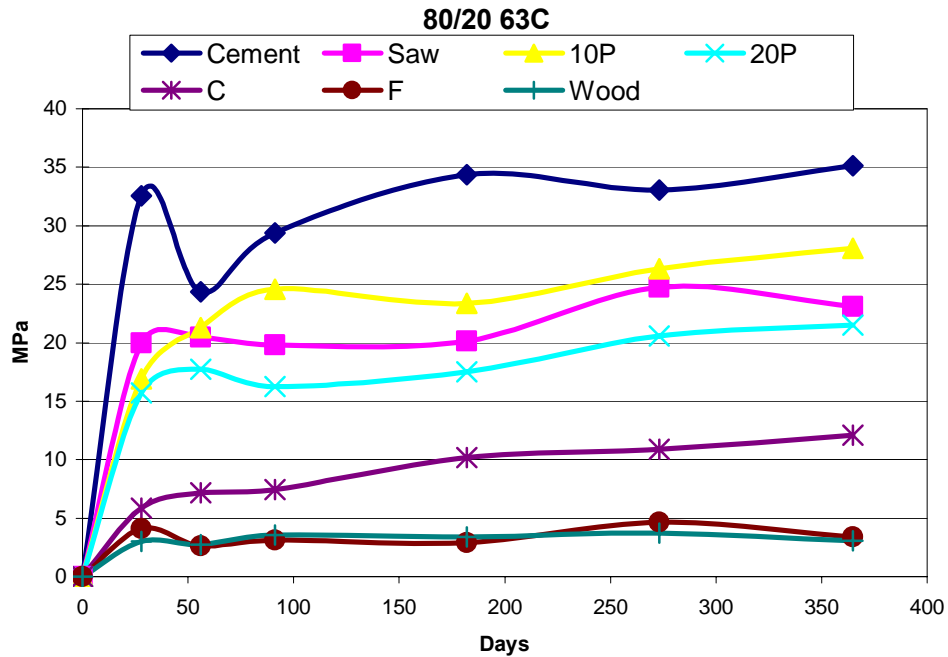
Figure C-3 Strength build up of 2 in cubes (fly ash: CH = 80/20)

70/30 23C
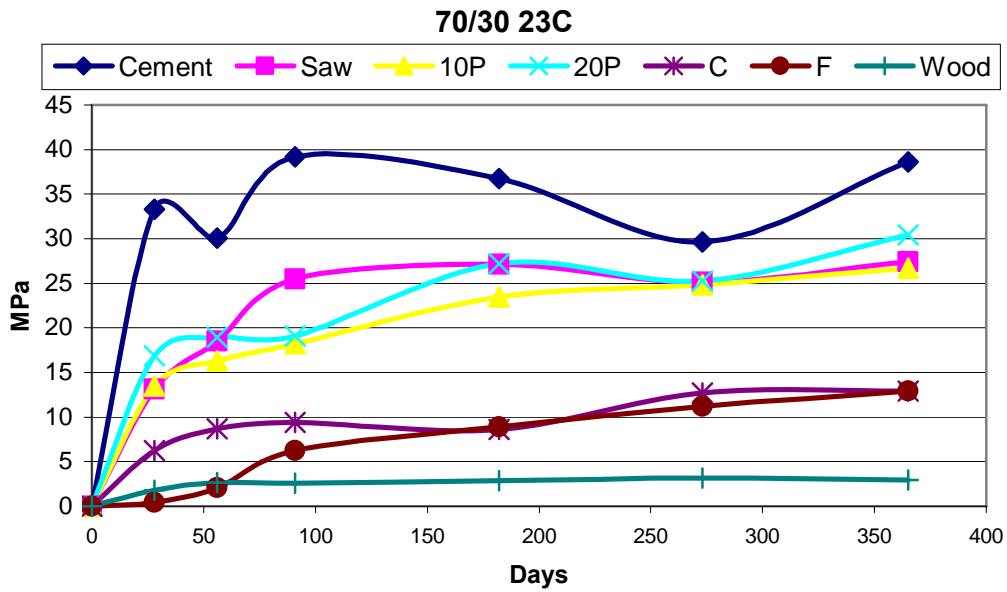
Figure C-4 Strength build up of 2 in cubes (fly ash: CH =70/30)

70/30 43C
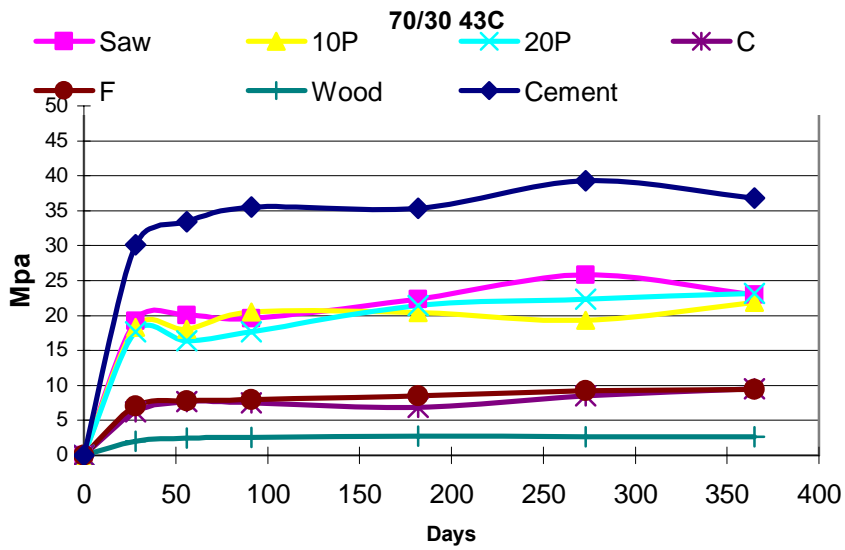
Figure C-5 Strength build up of 2 in cubes (fly ash: CH = 70/30)

70/30 63C
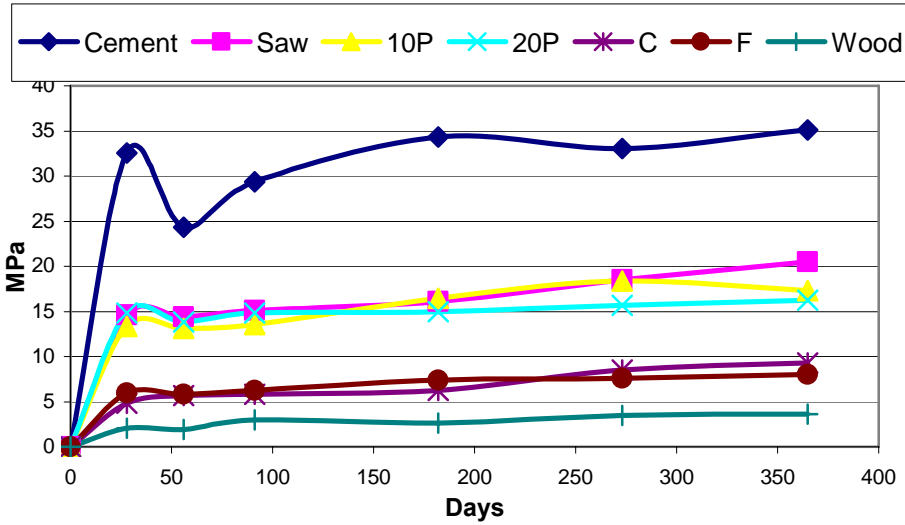
Figure C-6 Strength build up of 2 in cubes (fly ash: CH = 70/30)

60/40 23C
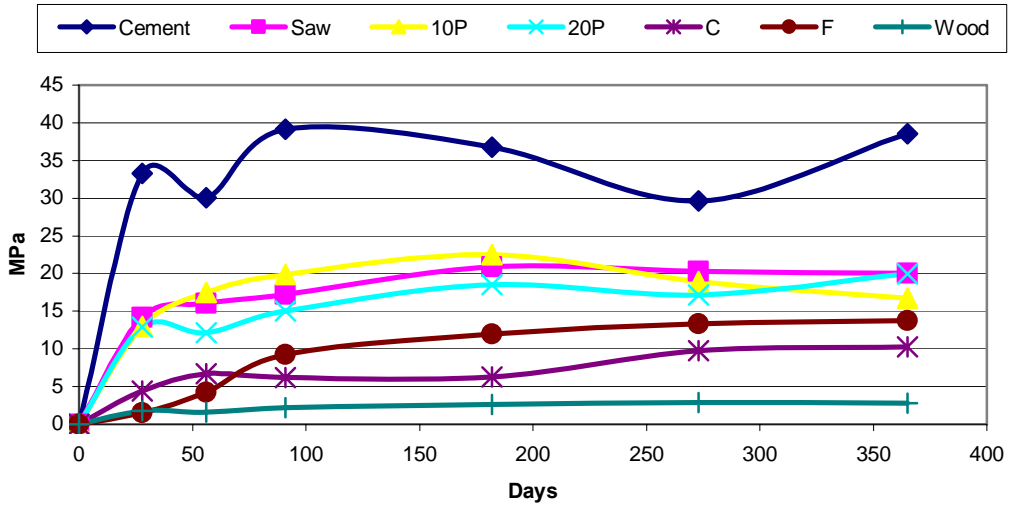
Figure C-7 Strength build up of 2 in cubes (fly ash: CH = 70/30)

176

60/40 43C
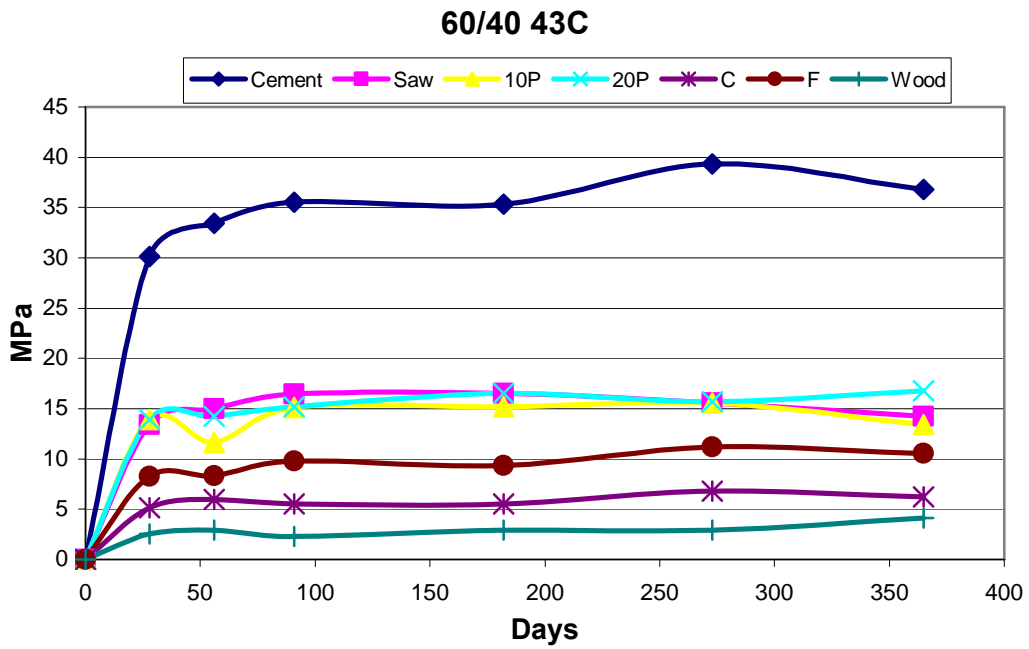
Figure C-8 Strength build up of 2 in cubes (fly ash: CH = 70/30)

60/40 63C
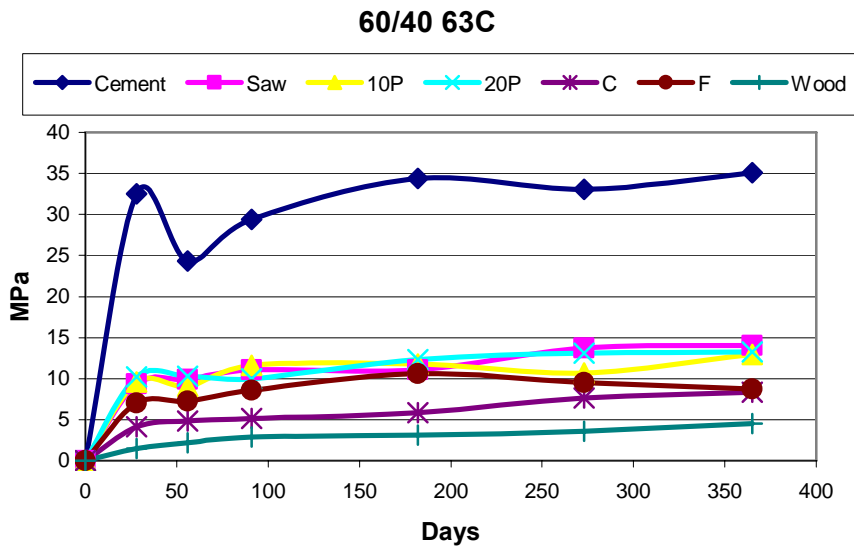
Figure C-9 Strength build up of 2 in cubes (fly ash: CH = 70/30)

177

Appendix D.   Reaction Extents of CH at 2 inch cubes
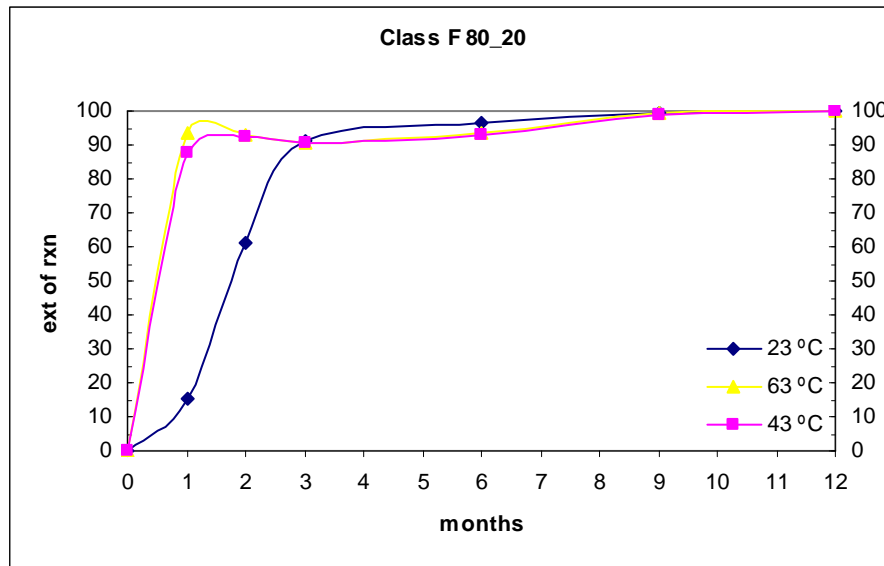
Figure D-1 Reaction extent of CH in 2 in cube (Class F: CH=80/20)
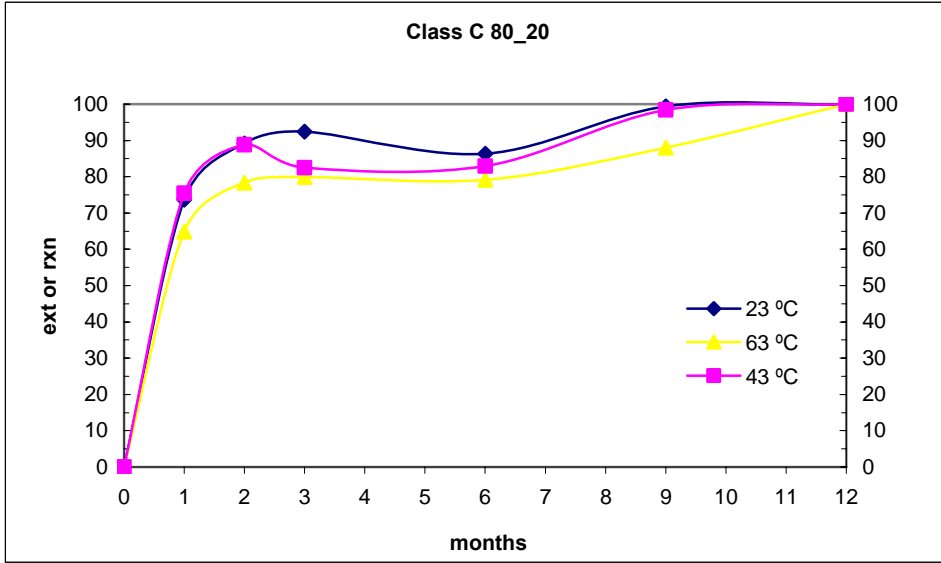
Figure D-2 Reaction extent of CH in 2 in cube (Class C: CH=80/20)
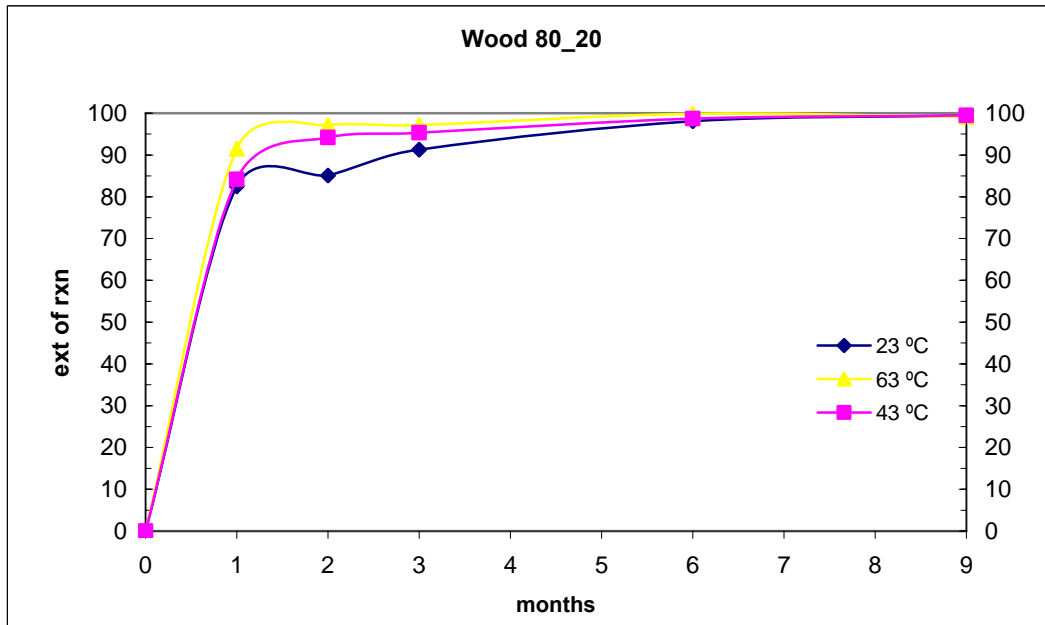
Figure D-3 Reaction extent of CH in 2 in cube (Wood: CH=80/20)
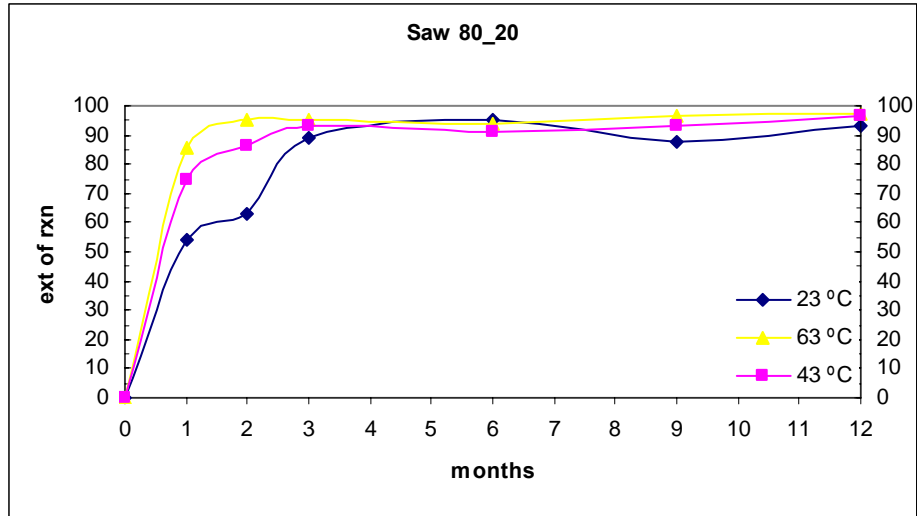
Figure D-4 Reaction extent of CH in 2 in cube (Saw: CH=80/20)
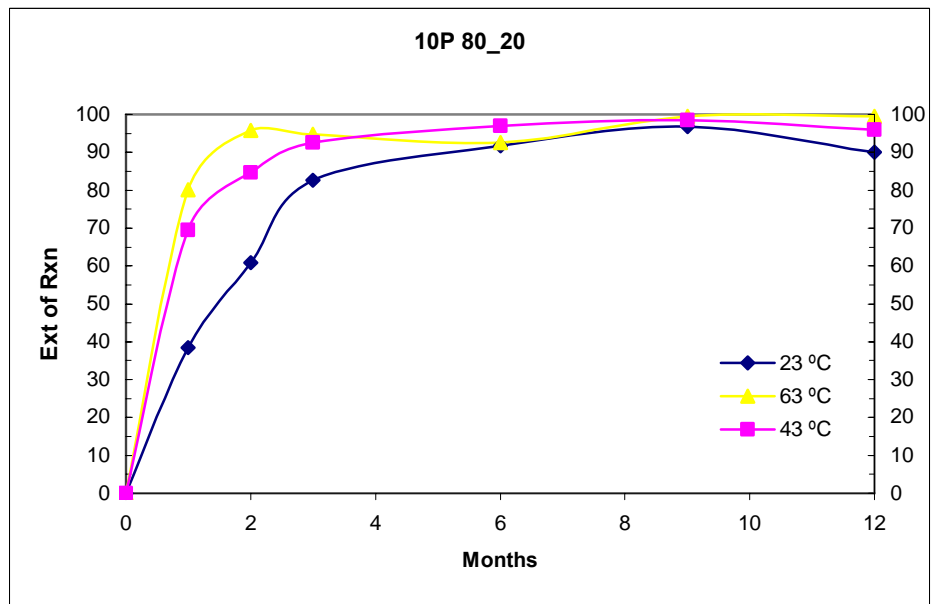
Figure D-5 Reaction extent of CH in 2 in cube (10P: CH=80/20)
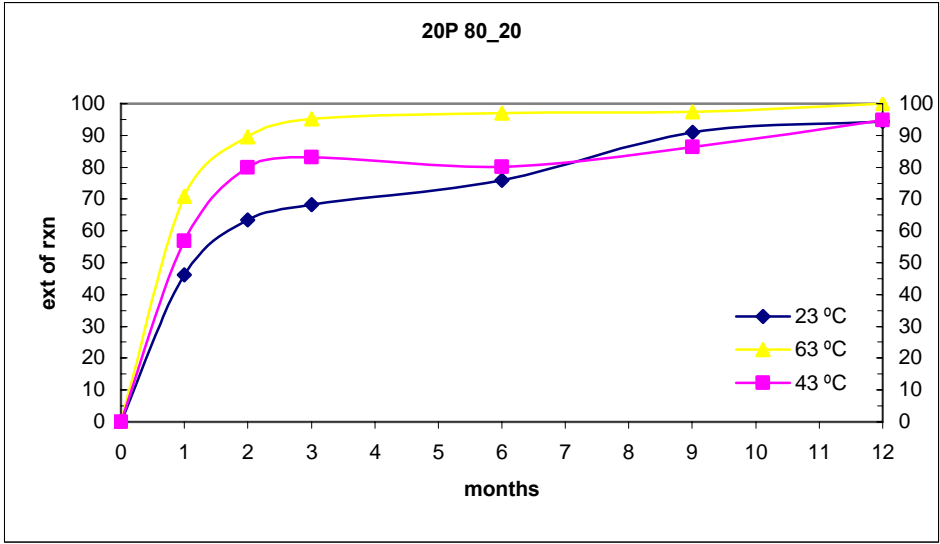
Figure D-6 Reaction extent of CH in 2 in cube (20P: CH=80/20)
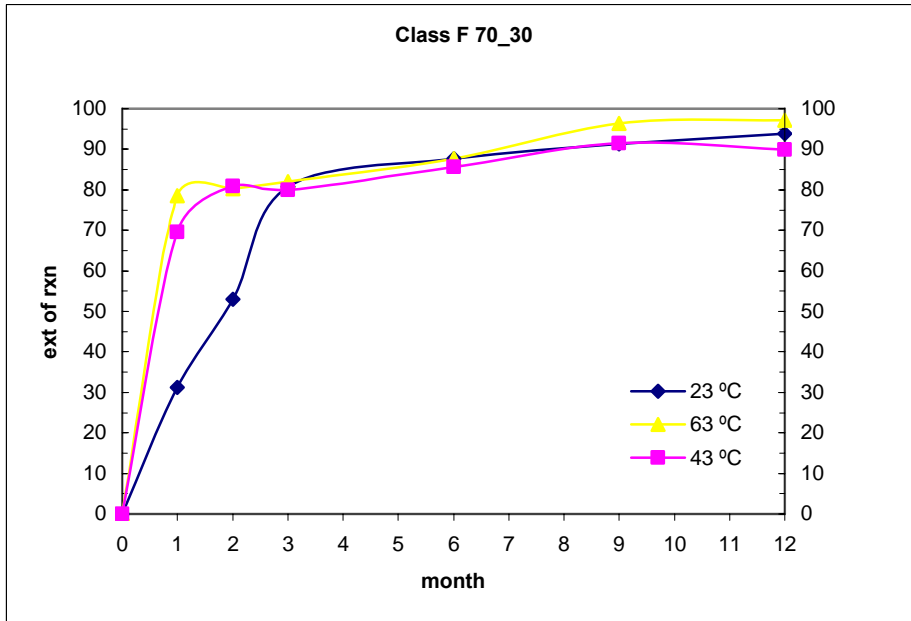
Figure D-7 Reaction extent of CH in 2 in cube (Class F: CH=70/30)
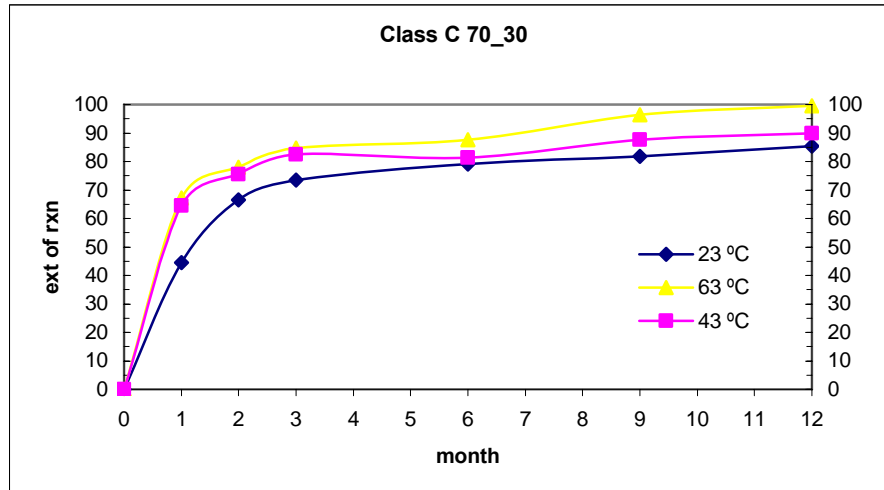
Figure D-8 Reaction extent of CH in 2 in cube (Class C: CH=70/30)
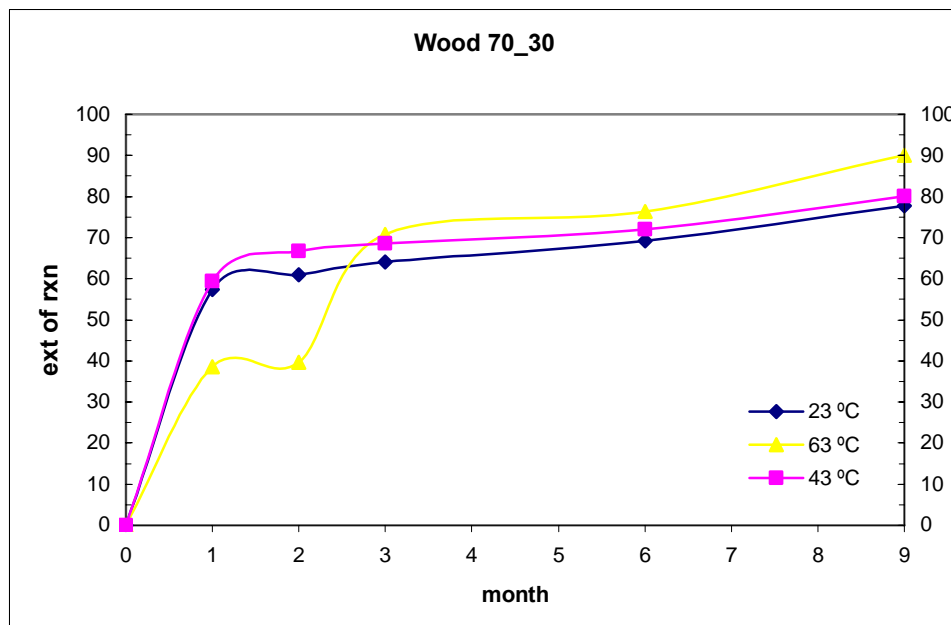
Figure D-9 Reaction extent of CH in 2 in cube (Wood: CH=70/30)
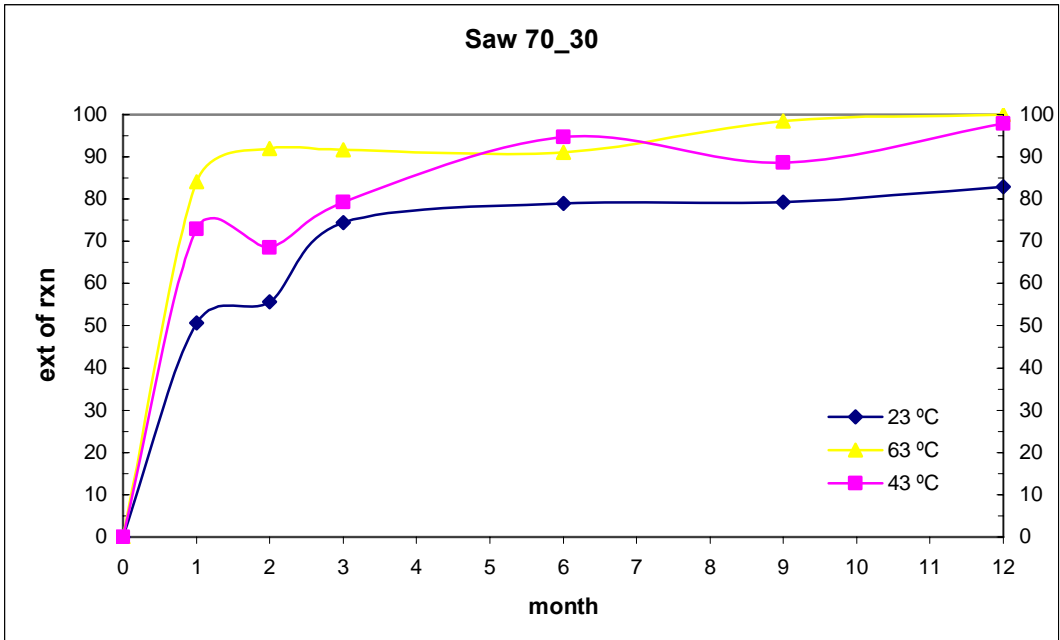
Figure D-10 Reaction extent of CH in 2 in cube (Saw: CH=70/30)
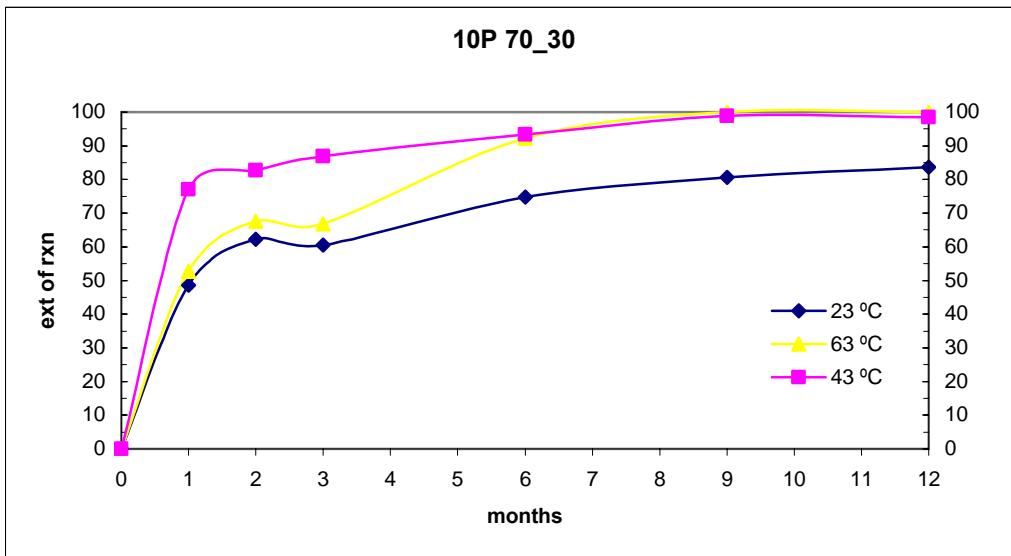
Figure D-11 Reaction extent of CH in 2 in cube (10P: CH=70/30)

184
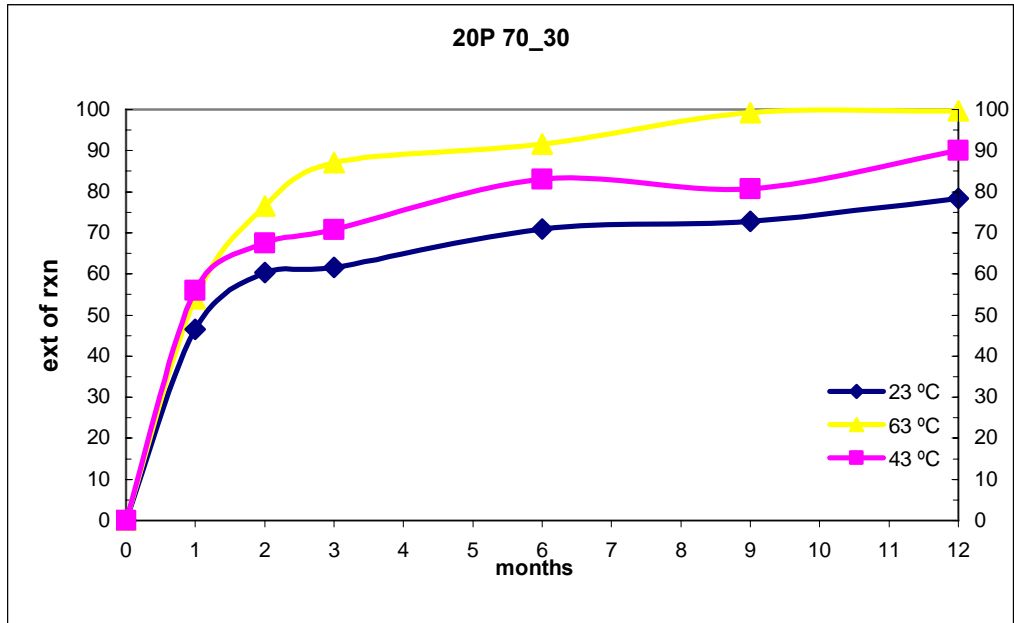
Figure D-12 Reaction extent of CH in 2 in cube (20P: CH=70/30)
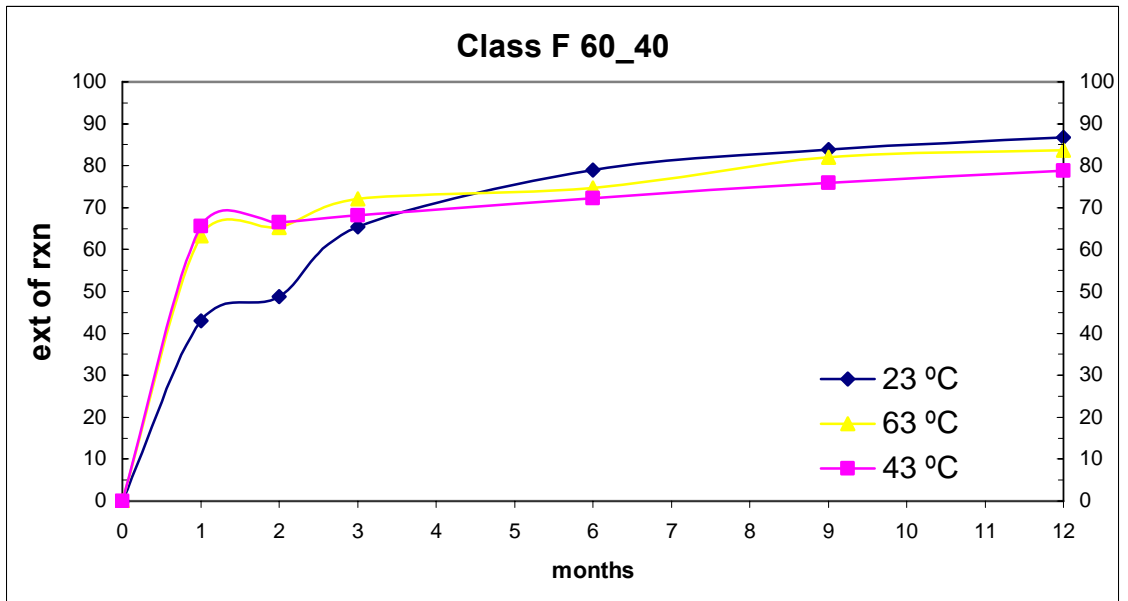
Figure D-13 Reaction extent of CH in 2 in cube (Class F: CH=60/40)

185
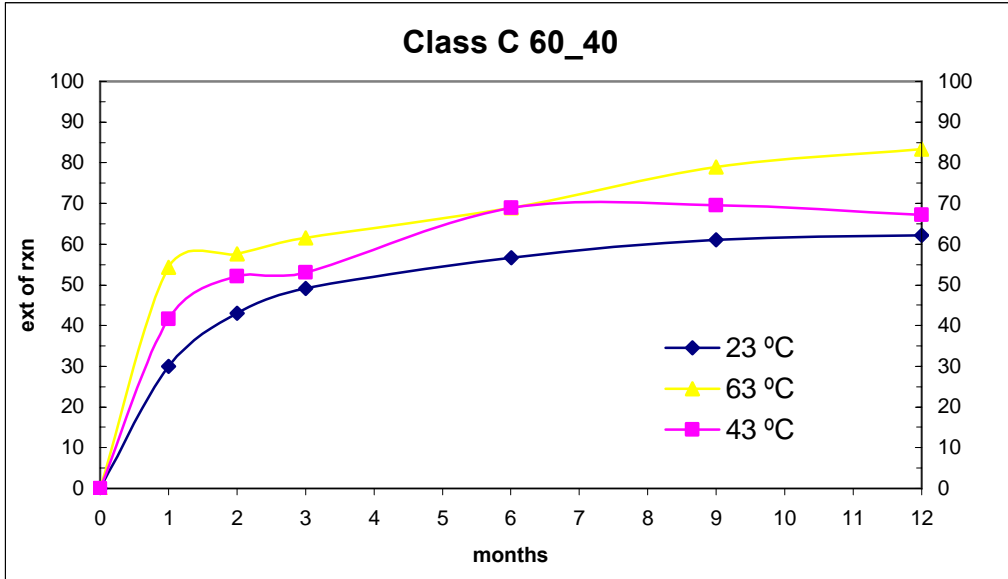
Figure D-14 Reaction extent of CH in 2 in cube (Class F: CH=60/40)
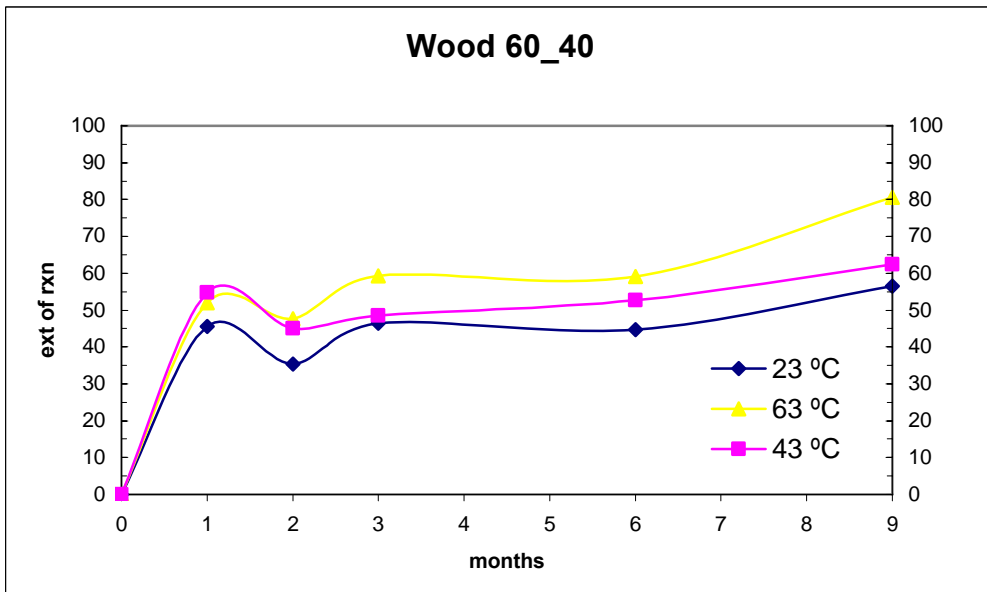
Figure D-15 Reaction extent of CH in 2 in cube (Wood: CH=60/40)
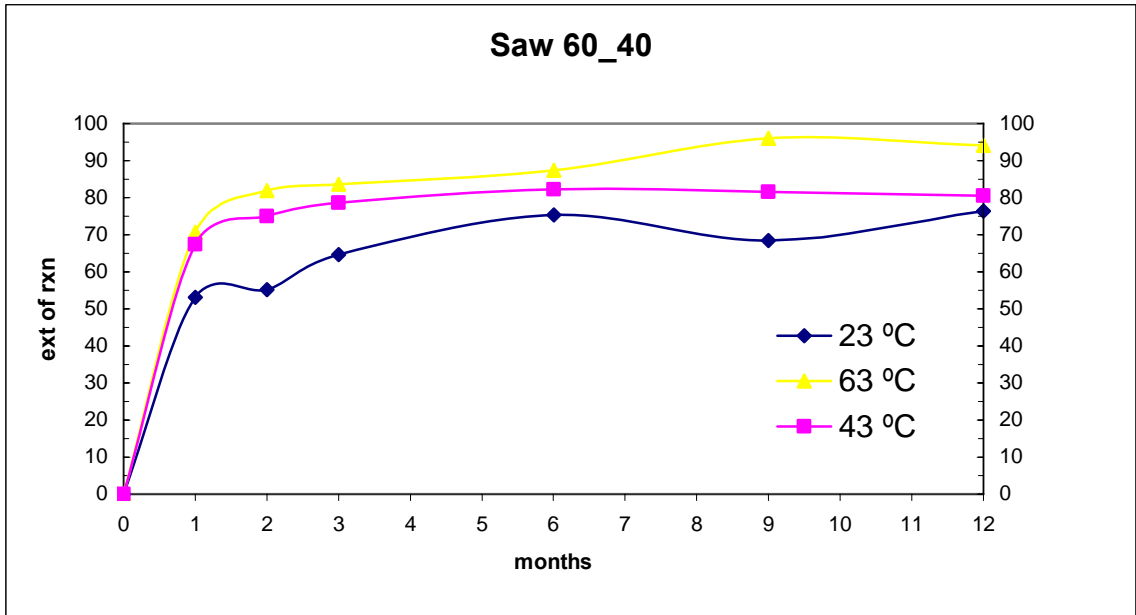
Figure D-16 Reaction extent of CH in 2 in cube (Saw: CH=60/40)
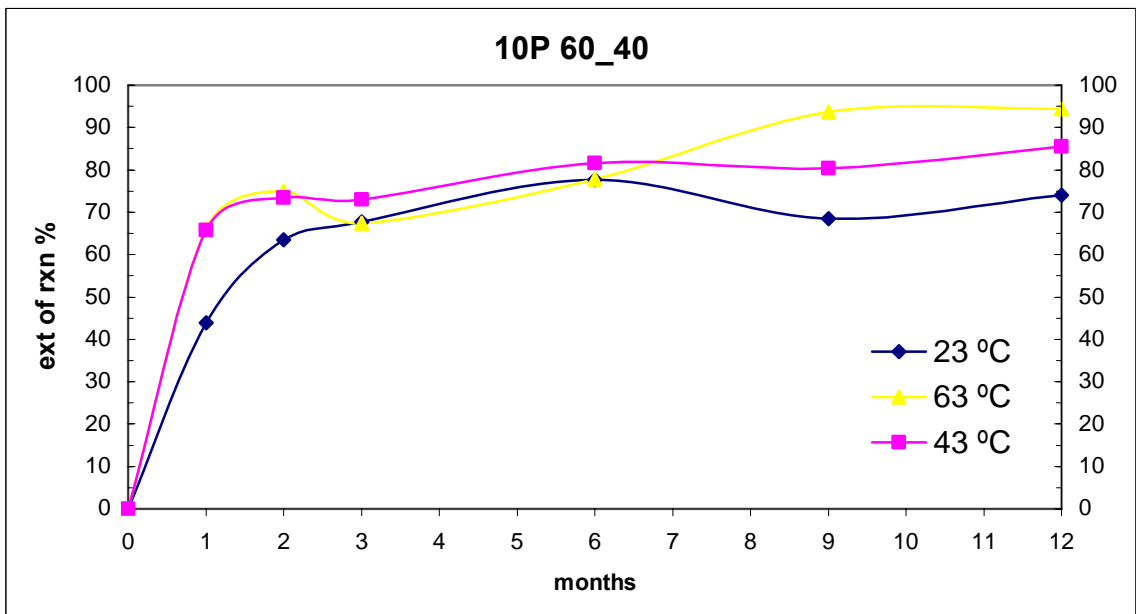
Figure D-17 Reaction extent of CH in 2 in cube (10P: CH=60/40)
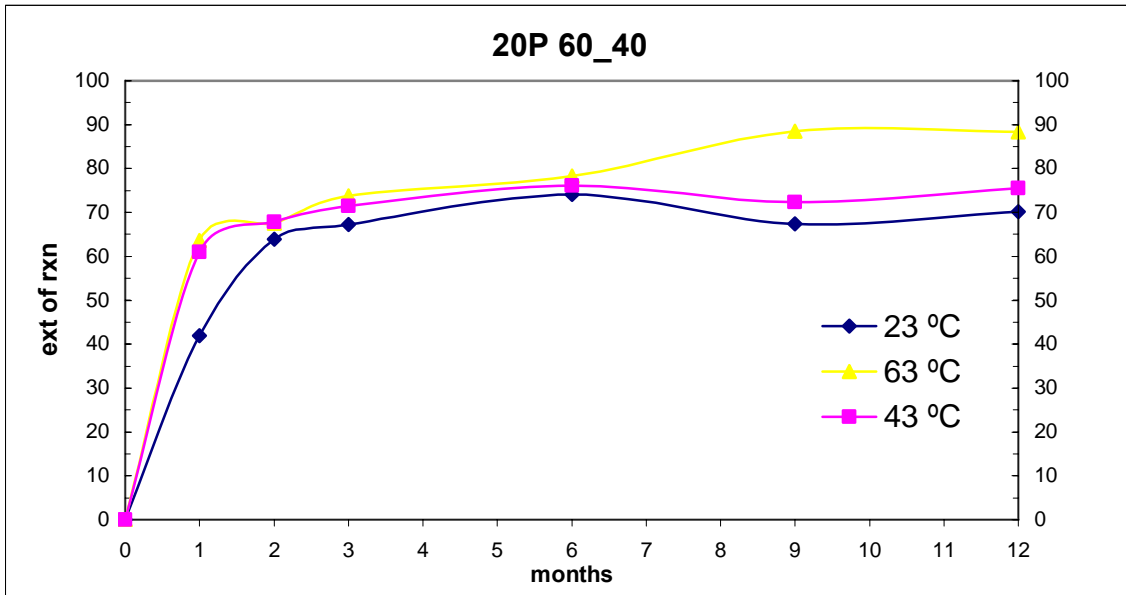
Figure D-18 Reaction extent of CH in 2 in cube (20P: CH=60/40)

Appendix E.   Drawings for the High Pressure Mold

Figure E-1 Mold Assemble
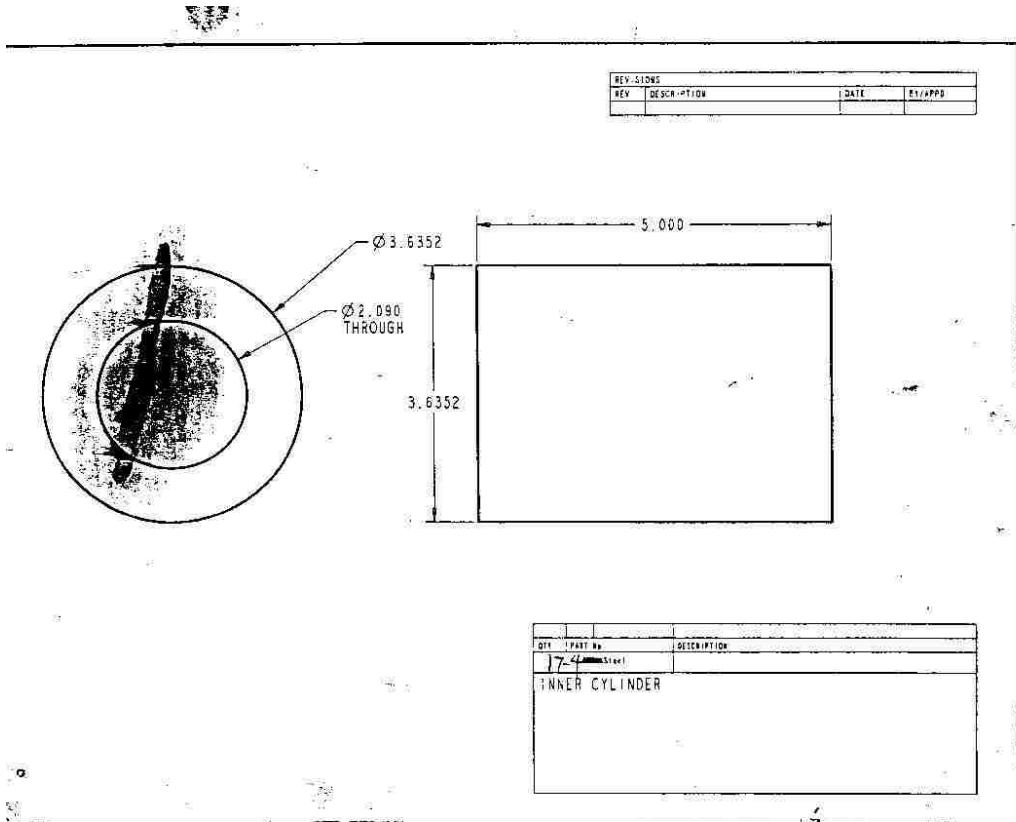
Figure E-2 Inner cylinder

Ø6.311

Ø3.6280
THROUGH

5.000

QTY | PART NO
REF | DESCRIPTION

OUTTER JACKET
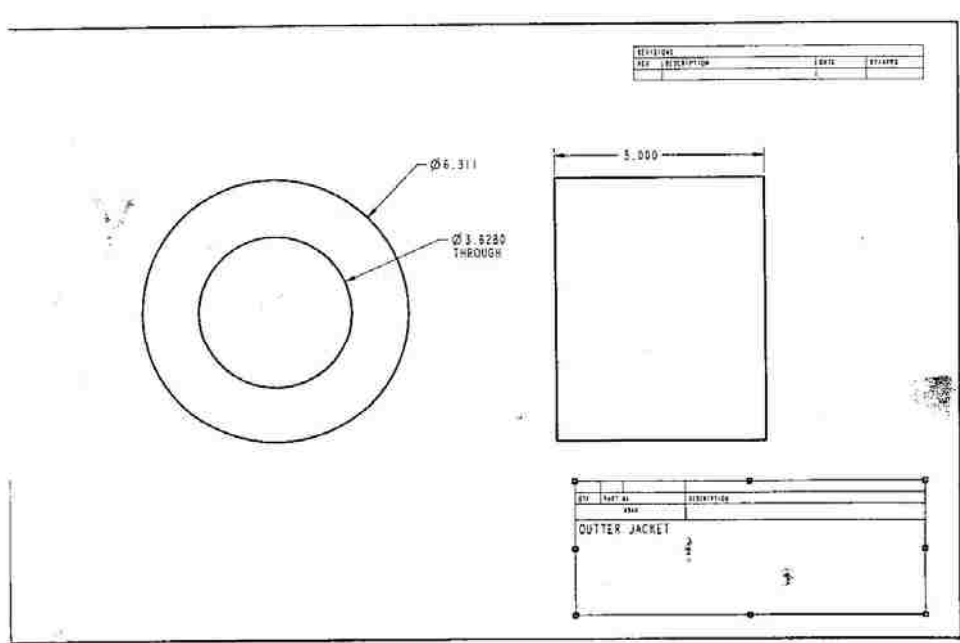
Figure E-3 Outer cylinder
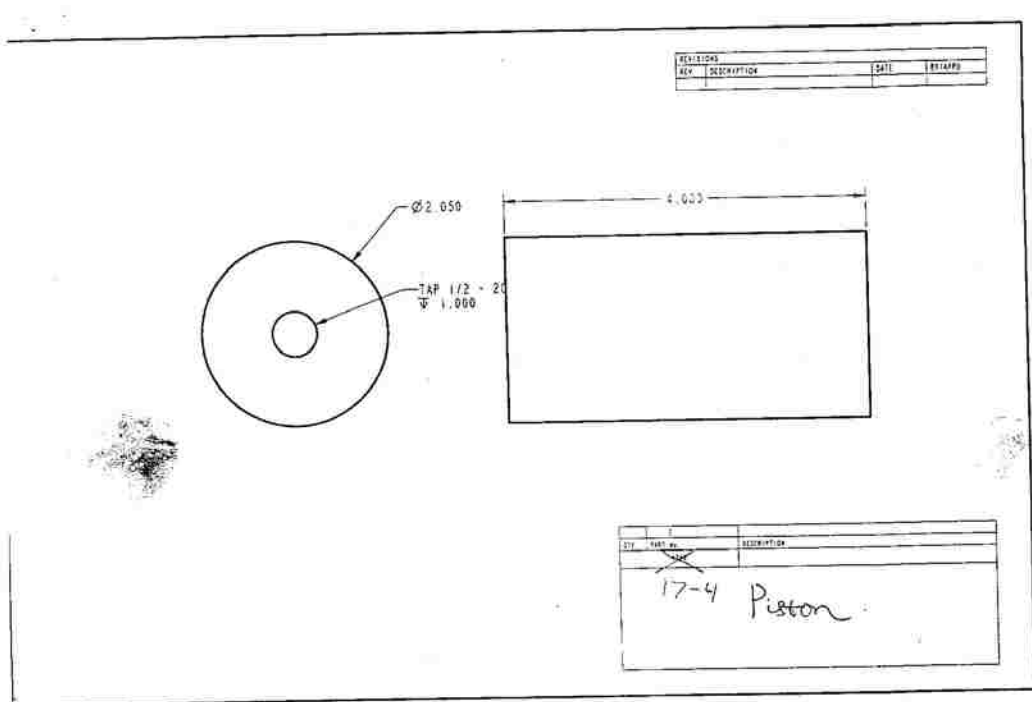
Figure E-4 Piston
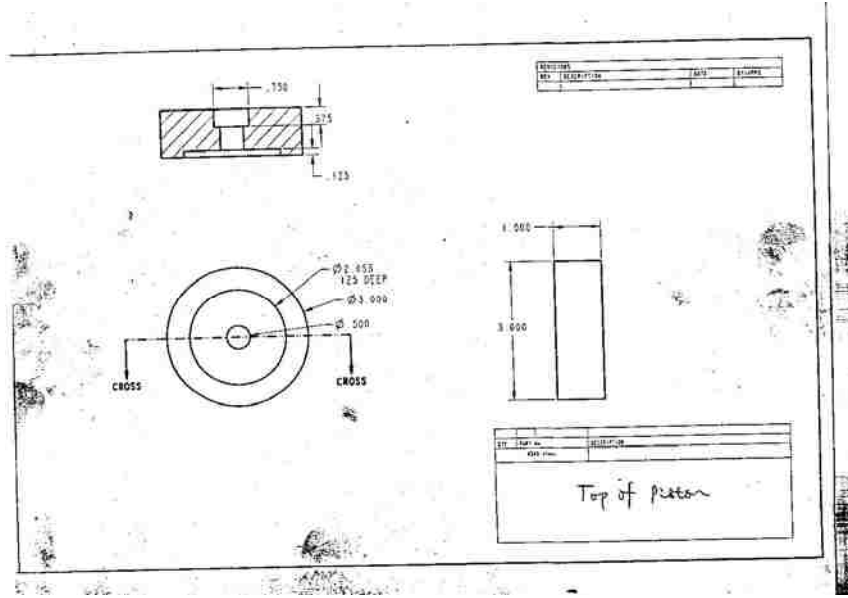
Figure E-5 Top of piston
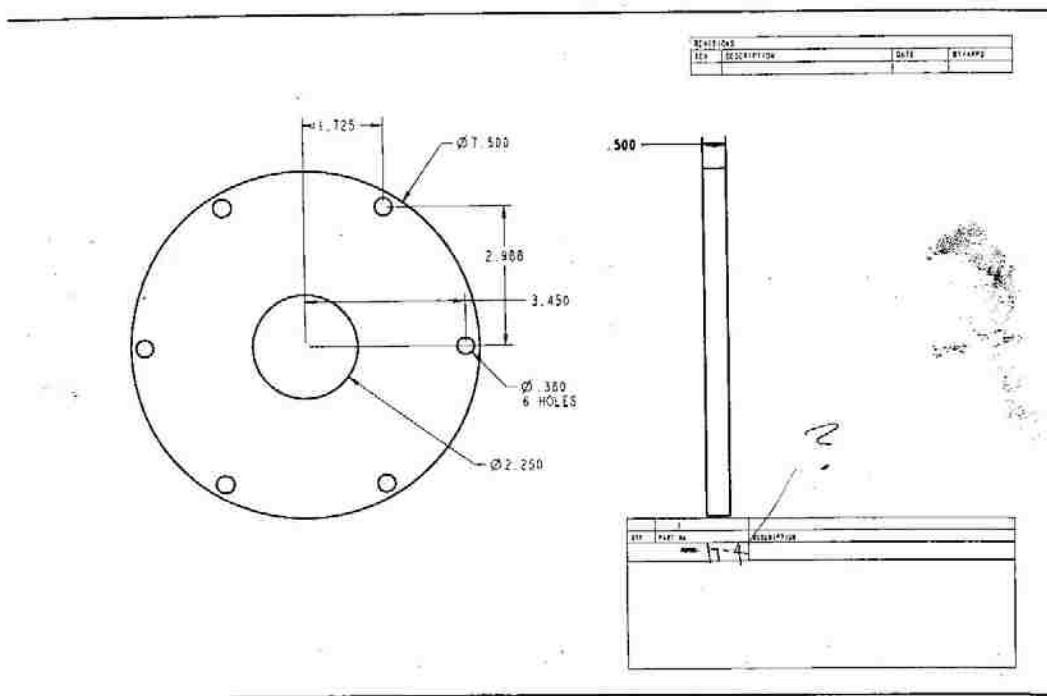
Figure E-6 Top plate
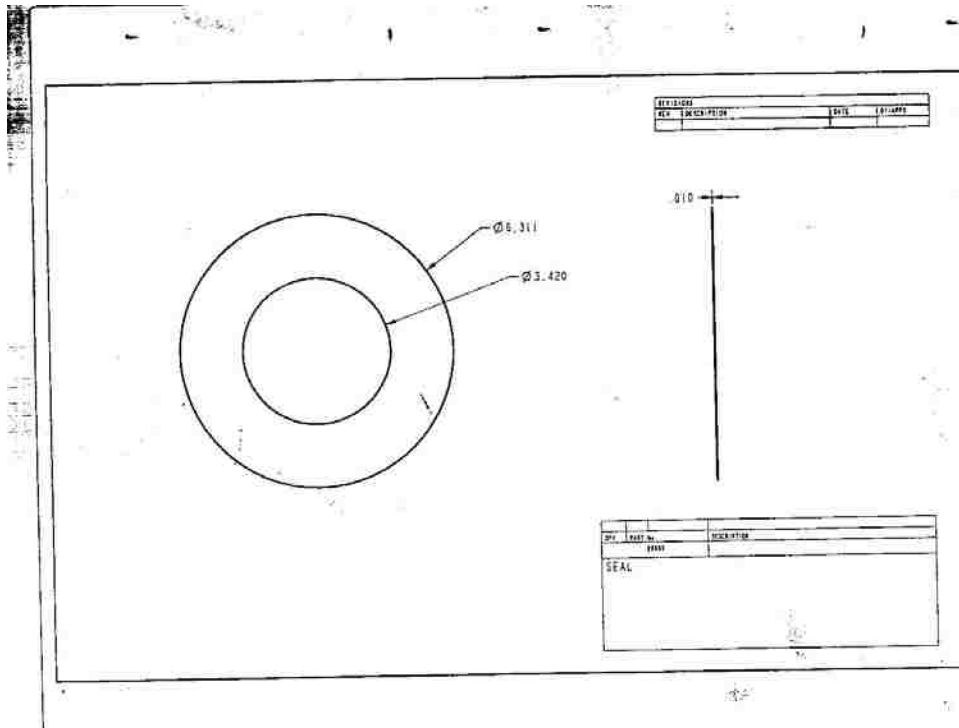
Figure E-7 Copper seal
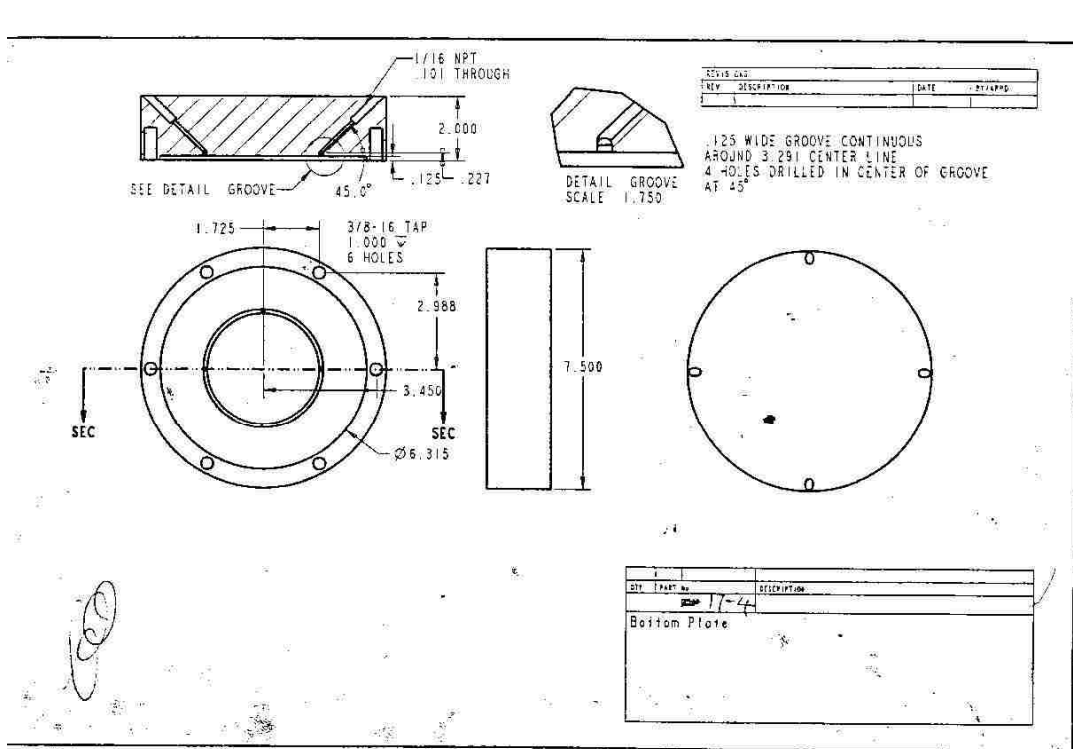
Figure E-8 Bottom plate

Appendix F.   Three Models for Pozzolanic Reactions

Pozzolanic reactions proceed through many pathways, and investigators indicate that reactions with reagent-grade silicates are not representative of reactions in practical concrete. Nevertheless, a mechanistic and quantitatively predictive or at least correlative expression for pozzolanic reactions would be useful in many respects. The nominal pozzolanic reaction is

$$3Ca(OH)_2 + 2SiO_2 + nH_2O \Rightarrow 3CaO \bullet 2SiO_2 \bullet (3+n)H_2O \qquad \text{(F-1)}$$

Silica, shown here as a reactant, represents reactive silica and silicates in fly ash and there exits many potential products, most of which form polymer-like macromolecular structures. Also, there exists a range of waters of hydration involved with silicates, with n in the above reaction typically being 0 or q, depending on the specific silicate species involved as products or reactants. However, the above expression captures the most essential aspects of the reaction. There is little fundamental theory to guide the formulation of rate expressions for this condensed-phase reaction. Three approaches are discussed here.

1 Homogeneous Kinetic Approach

A rational approach is to assume the reaction is first order with respect to each reactant.

$$-\frac{d[CaOH]}{dt} = k'[CaOH]'[FA]'[H_2O]$$

(F-2)

where $[\ ]'$ represents molar concentration and k' is a reaction rate constant with dimensions of volume^2/(time mole^2). Since fly ash (and silicate reaction product) molecular weight, and therefore concentration, does not lend itself to objective determination and, in any case, varies widely from fly ash to fly ash, and since fly ash *mass* presents no measurement or interpretation challenges, an expression involving mass proves more useful than a traditional molar concentration expression. Multiplying both sides of the above expression by the ratio of calcium hydroxide molecular weight to overall density yields

$$-\frac{dx_{CaOH}}{dt} = k'x'_{CaOH}[FA]'[H_2O]$$

(F-3)

where x'_i represents calcium hydroxide mass fraction. Similarly, factoring the ratio of overall density to fly ash and water molecular weights from the remaining concentration terms and including them in the reaction rate constant yields an expression free of molar units.

$$-\frac{dx_{CaOH}}{dt} = k''x'_{CaOH}x'_{FA}x_{H_2O}$$

$$k'' = k'\frac{\rho^2}{MW_{FA}MW_{H_2O}}$$

(F-4)

where ρ is the bulk density. Since condensed-phase density depends very slightly on temperature, the new (double primed) reaction rate constant is as accurately assumed to follow an Arrhenius expression as is the original (single-primed) version.

Using the chemical expression above as a guide, the molar rates of calcium hydroxide, fly ash (silica), and water consumption are 3:2:1, respectively. With nominal molecular weights of 74, 60, and 18, respectively, this corresponds to mass ratios of 62:33:5, respectively. The data used to determine reaction kinetics below includes initial calcium hydroxide mass fractions ranging from 0.6 to 0.8 on a dry basis. The initial moisture mass fraction is 0.5 in all cases. Assuming all of the calcium hydroxide reacts, the most moisture that would be consumed on a mass basis is 0.8 mass % CaOH (dry basis)*0.5 dry mass/total mass * (5 mass units of H_2O/62 mass units of CaOH) = 0.03. Thus, the 0.5 water mass fraction changes at most by 6 relative % (0.5 to 0.47) during the course of a reaction. The actual changes will be even less for several reasons (higher effective molecular weight of fly ash, excess calcium hydroxide, reaction product mass offsetting reactant mass loss, and incomplete reactions). This small change in water mass fraction renders its mass fraction essentially constant and the expression can be conveniently written in terms of water-free mass fractions as follows

$$-\frac{dx_{CaOH}}{dt} = kx_{CaOH}x_{FA}$$

(F-5)

Where

$$k = k''x_{H_2O}\left(1 - x_{H_2O}\right)^2 \tag{F-6}$$

and the mass fractions without primes indicate values on a water-free basis.

This reaction rate constant, in which the effect of water was removed, indicates how the effects of any inert material can be included in the rate expression, namely

$$k = k''x_{\Sigma inert}\left(1 - x_{\Sigma inert}\right)^2 \tag{F-7}$$

$$\frac{dx_{FA}}{dt} = b\frac{dx_{CaOH}}{dt}$$

$$\Rightarrow x_{FA} = a + bx_{CaOH} \tag{F-8}$$

where $\Sigma inert$ represents the sum of all non-reacting species (water, large aggregate, etc.).

Designating the stoichiometric mass ratio of fly ash to calcium hydroxide consumption as b, the following relationship between fly ash and calcium hydroxide exists at all times

The quantity a is an integration constant, the sign of which represents whether fly ash or calcium hydroxide is in excess, as discussed later. This same relationship exists at the beginning of the reaction, when the only components present (on a water-free basis) are calcium hydroxide and fly ash. This can be used to determine a in terms of b and the initial mass fractions, which in turn provides a general expression for the mass fraction of fly ash.

$$x^0_{FA} = a + bx^0_{CaOH}$$

$$\Rightarrow a = x^0_{FA} - b\,x^0_{CaOH} = \left(1 - x^0_{CaOH}\right) - bx^0_{CaOH} = 1 - x^0_{CaOH}\left(1 + b\right) \tag{F-9}$$

$$\Rightarrow x_{FA} = 1 - x^0_{CaOH}\left(1 + b\right) + bx_{CaOH}$$

This equation leads an expression for the consumption of calcium hydroxide that yields an analytical solution, as follows.

$$\Rightarrow -\frac{dx_{CaOH}}{dt} = kx_{CaOH}\left(1 - x^0_{CaOH}\left(1 + b\right) + bx_{CaOH}\right)$$

$$\frac{-dx_{CaOH}}{kx_{CaOH}\left(1 - x^0_{CaOH}\left(1 + b\right) + bx_{CaOH}\right)} = dt$$

$$t = \frac{\log\left(\dfrac{[CaOH]}{1 + bx_{CaOH} - \left(1 + b\right)x^0_{CaOH}}\right)}{\left[x^0_{CaOH}\left(1 + b\right) - 1\right]k} + A'$$

$$\Rightarrow x_{CaOH} = \frac{x^0_{CaOH}\left(1 + b\right) - 1}{b - \exp\left[-\left(x^0_{CaOH}\left(1 + b\right) - 1\right)kt\right]} + A$$

$$x_{CaOH}\left(t = 0\right) = x^0_{CaOH}$$

$$\Rightarrow A = \frac{1 - 2x^0_{CaOH}}{b - 1}$$

$$\Rightarrow x_{CaOH} = \frac{x^0_{CaOH}\left(1 + b\right) - 1}{b - \exp\left[-\left(x^0_{CaOH}\left(1 + b\right) - 1\right)kt\right]} + \frac{1 - 2x^0_{CaOH}}{b - 1} \tag{F-10}$$

The reaction extent, defined as,

$$\alpha = 1 - \frac{x_{CaOH}}{x^0_{CaOH}} \tag{F-11}$$

represents a conveniently dimensionless parameter and can be expressed as

$$\alpha = 1 - \frac{x_{CaOH}^0 (1+b) - 1}{bx_{CaOH}^0 + \left(x_{CaOH}^0 - 1\right)\exp\left[-\left(x_{CaOH}^0(1+b) - 1\right)kt\right]}$$

(F-12)

Assuming an Arrhenius form for the reaction rate constant

$$k = k^0 \exp\left(-\frac{E}{RT}\right) = k^0 \exp\left(-\frac{E'}{T}\right)$$

(F-13)

where $E' = E/R$, produces the final expression

$$\alpha = 1 - \frac{x_{CaOH}^0 (1+b) - 1}{bx_{CaOH}^0 + \left(x_{CaOH}^0 - 1\right)\exp\left[-\left(x_{CaOH}^0(1+b) - 1\right)k^0 \exp\left(-\frac{E'}{T}\right)t\right]}$$

(F-14)

The essential data collected in this investigation include areas under curves from a thermogravimetric analyzer, which are interpreted as mass of calcium hydroxide. Errors in the data enter as errors in this measurement. The initial mass of calcium hydroxide is known to high precision relative to these measurements, so the distribution of errors in the extent of reaction should be the same as the distribution of errors in calcium hydroxide measurements. The Central Limit Theorem in statistics indicates these errors are likely normally distributed whereas errors in a nonlinear transformation of this expression would not be normally distributed. Therefore, this expression forms the basis of the statistical analysis.

A non-linear, least-squares regression algorithm produces estimates of the parameters b, E', and k^0 from experimental conversion data at varying initial compositions (initial hydroxide mass fractions of 0.2, 0.3, and 0.4), curing temperatures (23 °C, 43 °C, and 63 °C), and times (0, 1, 2, 3, 6, 9, and 12 months). The three parameters should be the same over this set of variables. The parameters likely differ, however, for each type of fly ash examined (Class C, Class F, Wood, 10P, 20P, and sawdust). The resulting estimations of the three parameters for each type of fly ash are as follows. The raw data and the optimized parameters appear for each type of fly ash.

2 Particle- and Diffusion-based Model

The above analysis ignores the particulate nature of the fly ash and with it the potential transport limitations associated with calcium hydroxide diffusing to the particle surface (external film resistance) and passing through the reacted layer (particle film resistance) to react with the unreacted core (kinetic resistance). An alternative model that considers the transport effects can be based on the concepts illustrated below. The figure illustrates a single fly ash particle in a calcium-hydroxide containing matrix, The unreacted fly ash is Region *I*, the particle film or shell is Region *II*, and the surrounding matrix is Region *III*. The dashed line is the initial particle diameter. As the particle reacts, it forms an inner and an outer interface, each represented by a solid line. The outer interface marks the reaction front between the matrix and the reaction products. The inner one marks a similar front between the fly ash and reaction products. Both fronts move with time in the directions indicated by the small, dashed arrows. The region between these interfaces consists of reaction products mixed with presumably small amounts of reactants. The original particle diameter is *R*, the fly-ash-reaction-product interface is r_i,

and the calcium-hydroxide-reaction-product interface is r_p. These lower-case radii with lower-case subscripts should not be confused with the volumetric mass reaction rate r_A.

The discussion describing this model appears below in the order of (a) the chemical reaction term, (b) the shell, (c) the particle interface, and (d) the gradient in the surrounding matrix. The equations developed in each area combine to form a single expression involving only the surrounding matrix. This is combined with expressions for the reaction rate, and solutions to this model are applied to the current data.

Figure F-1 Schematic diagram of reacting ash particle in concrete/Ca(OH)$_2$ matrix.

2-1 Chemical Reaction at the Fly Ash Interface

A volumetric reaction rate expression for the reaction on the surface and in the interior of the fly ash particles follows from the following assumptions: (a) the reaction is

first-order in calcium hydroxide mass fraction and zero order in fly ash except when all the fly ash is consumed, in which case the reaction stops; (b) a Thiele modulus adequately describes the effect of calcium hydroxide diffusion into the particle; and (c)

$$-r_A \equiv -\frac{n_p}{V}\frac{d\left(\overline{\rho}V\overline{x}_A\right)}{dt} = -\overline{\rho}\frac{d\,\overline{x}_A}{dt} = A_{ex}k\rho_{A,i}^{II} = A_{ex}\rho_i^{II}kE(Th)x_{A,i}^{II}$$

$$= 4\pi r_i^2 \frac{n_p}{V}\rho_i^{II}kE(Th)x_{A,i}^{II}$$

$$-r_A \equiv -\frac{n_p}{V}\frac{d\left(\overline{\rho}V\overline{x}_A\right)}{dt} = 4\pi r_i^2 \frac{n_p}{V}\rho_i^{II}kE(Th)x_{A,i}^{II} \tag{F-15}$$

where n_p represents the number of particles per unit volume, $\overline{\rho}$ is the overall density, ρ^{II} is the density of Region II, and overall mass conservation indicates $\overline{\rho}V$ is a constant (hence moving out of the derivative), $\overline{x}_A$ is the overall average mass fraction of component A (calcium hydroxide), A_{ex} is the volumetric surface area of the particles (m^2 surface area/m^3 of concrete $= 4\pi r_i^2 \frac{n_p}{V}$), $x_{A,i}^{II}$ (with no overbar) represents the mass fraction of A at the i interface, that is, the mass fraction at the surface of the reacting fly ash particle, $E(Th)$ is the effectiveness factor that depends on the Thiele modulus, Th, and r_A and k have dimensions of mass of calcium hydroxide/(volume time) and length/time, respectively. The effectiveness factor has the functional form of

$$E(Th) = \frac{3\tanh\left(\dfrac{mr_i}{3}\right)}{mr_i} \tag{F-16}$$

where

$$mr_i = r_i \left(\frac{kA_{ex}}{D_e^l} \right)^{1/2}$$

(F-17)

An alternative and equivalent expression in terms of fluxes is

$$-r_A'' \equiv -\frac{1}{A_{ex}V} \frac{d\left(\bar{\rho} V x_A\right)}{dt} = \frac{r_A}{A_{ex}} = -\frac{\bar{\rho}}{A_{ex}} \frac{d\bar{x}_A}{dt} = kE(Th)\rho_{A,i}^{ll} = \rho_i^{ll} kE(Th) x_{A,i}^{ll}$$

(F-18)

where r_A'' has units of mass flux, that is, mass of A/(surface area * time). The ll superscript that designates a region of the system and the double prime that represents flux units should not be confused. These expressions are the mass- or density-based analogs of traditional kinetic expressions involving molar concentrations, the latter being difficult to define since the molecular weights of fly ash and the reaction product are not well defined. This discussion focuses on the volumetric expression.

In a quasi-steady-state reaction, the flux-based reaction rate, r_A'', times the local surface area should be constant, that is

$$S_A(r)r_A''(r) = S_A(r)j_A(r)$$

(F-19)

where (r) designates functional dependence on r, not multiplication, and S represents the surface area orthogonal to the flux at position r, which in spherical coordinates is $4\pi r^2$.

2-2 The Shell Layer

Differential transport equations describe the calcium hydroxide mass fraction profile in a spherically symmetric shell as

$$\rho \frac{d\, x_A''}{dt} = \frac{\rho'' D_e''}{r^2} \frac{d}{dr}\left(r^2 \frac{d\, x_A''}{dr}\right) + r_A''$$

(F-20)

where r_A'' is the reaction rate (mass/(time*volume)) of calcium hydroxide in the shell (Region II), D_e'' is the effective diffusivity of calcium hydroxide in the shell, and other variables have their normal meanings. This analysis assumes that no calcium hydroxide reactions occur in the particle shell and that transport through the product layer is at a quasi steady state (profiles instantaneously adjust to changes in bulk concentration and shell thickness). Under these assumptions, the previous equation provides the form of the concentration profile

$$x_A''(r) = \frac{\left(x_{A,p}'' - x_{A,i}''\right)\left(r_p r - r_p r_i\right)}{\left(r_p - r_i\right)r} + x_{A,i}''$$

$$\frac{d\, x_A''(r)}{dr} = \frac{\left(x_{A,p}'' - x_{A,i}''\right) r_p r_i}{\left(r_p - r_i\right)r^2}$$

$$4\pi r^2 \rho D_e \left.\frac{d\, x_A''(r)}{dr}\right|_i = 4\pi r^2 \rho D_e \left.\frac{d\, x_A''(r)}{dr}\right|_p = \frac{r_A}{\dfrac{n_p}{V}}$$

$$4\pi\rho D_e \frac{\left(x_{A,p}'' - x_{A,i}''\right) r_p r_i}{\left(r_p - r_i\right)} = \frac{V}{n_p} r_A$$

$$\Rightarrow x_{A,i}'' = x_{A,p}'' - \frac{\dfrac{V}{n_p} r_A\left(r_p - r_i\right)}{4\pi\rho D_e r_p r_i}$$

(F-21)

where $\dfrac{n_p}{V}$ is the number of particles per unit volume and (r) designates functional dependence on r, not multiplication.

2-3 The Matrix-Shell Interface

At the p interface, $x_{A,p}^{II}$ relates to $x_{A,p}^{III}$ thermodynamically. Activity coefficients defined in terms of mass fractions appear here since molecular weights, and hence mole fractions, cannot be unambiguously assigned for fly ash, calcium silicate reaction products, etc. If the transition is viewed as a physical phase transformation, that is, the CaOH dissolves into a solid solution of CaOH and calcium silicate reaction products with no chemical reaction,

$$a_{A,p}^{II} = a_{A,p}^{III}$$

$$x_{A,p}^{II} \gamma_{A,p}^{II} = x_{A,p}^{III} \gamma_{A,p}^{III}$$

$$x_{A,p}^{II} = x_{A,p}^{III} \dfrac{\gamma_{A,p}^{III}}{\gamma_{A,p}^{II}}$$

(F-22)

It is difficult to know how the activity coefficients of calcium hydroxide vary with composition or temperature. However, a reasonable upper bound is that the activity in Region II is approximately the inverse of the bulk mass fraction in Region II. Such an activity coefficient approximates the value at which two phases form. The SEM images show substantial heterogeneity, consistent with the formation of two phases, in the shell region. Applying this upper bound for activity,

$$x_{A,p}^{II} = x_{A,p}^{III} \dfrac{\gamma_{A,p}^{III}}{\gamma_{A,p}^{II}} \approx x_{A,p}^{III} \dfrac{\gamma_{A,p}^{III}}{1/x_{A,b}^{II}} = x_{A,p}^{III} \dfrac{\gamma_{A,p}^{III}}{1/\left(1-x_{\Sigma,b}^{II}\right)} = x_{A,p}^{III} \gamma_{A,p}^{III} \left(1-x_{\Sigma,b}^{II}\right)$$

(F-23)

where $x^{II}_{\Sigma,b}$ represents the sum of all non-A mass fractions. Assuming the activity coefficient of the nearly pure material at the interface to be near unity, we obtain the estimate

$$x^{II}_{A,p} \approx x^{III}_{A,p}\left(1 - x^{II}_{\Sigma,b}\right)$$

(F-24)

which is equivalent to assuming the silicate reaction product forms a non-interacting second phase in Region II, so the mass fraction of calcium hydroxide is the same as in Region III, adjusted for the presence of this second phase. More realistically, the activity coefficient of calcium hydroxide in Region III will generally be somewhat less than the inverse of its mass fraction, making the last factor in the above equation slightly too small.

In addition, the activity coefficient on the Region III side of the p interface probably differs and is likely greater than unity. Combining these unknown but potentially small affects into a single variable, c_γ leaves the final expression at the interface as

$$x^{II}_{A,p} = c_\gamma x^{III}_{A,p}\left(1 - x^{II}_{\Sigma,b}\right)$$

(F-25)

where c_γ probably slightly exceeds unity and is defined by this equation.

2-4 The Matrix

Traditional engineering mass transfer correlations relate the mass flux of calcium hydroxide to the particle surface

$$4\pi r^2 n_A' = \frac{V}{n_p} r_A = 4\pi r^2 h_{m,A} \rho^{III} \left(x_{A,p}^{III} - x_{A,b}^{III} \right)$$

$$= \pi r^2 \frac{Sh_A D_{e,A}^{III}}{r_p} \rho^{III} \left(x_{A,p}^{III} - x_{A,b}^{III} \right) = \frac{V}{n_p} r_A$$

$$\Rightarrow x_{A,p}^{III} = \frac{\frac{V}{n_p} r_A}{4\pi r_p^2 h_{m,A} \rho^{III}} + x_{A,b}^{III} = \frac{\frac{V}{n_p} r_A}{2\pi r_p Sh_A D_{e,A}^{III} \rho^{III}} + x_{A,b}^{III} \tag{F-26}$$

where n_A' is the mass flux of A, $h_{m,A}$ is the effective mass transfer coefficient, $D_{e,A}^{III}$ is the effective diffusivity of A in region III, Sh is the Sherwood number, and other terms have already been defined. The Sherwood number would be 2 in these expressions if the shell diameter, r_p, were constant.

F-2-5 Rate in Terms of Matrix Composition

These equations describing mass fractions at the fly ash interface, both sides of the shell interface, and in the external matrix can be combined into a single expression involving only the external matrix concentration. Specifically, the following equations can be combined to eliminate all terms involving mass fraction except $x_{A,b}^{III}$

$$-r_A = 4\pi r_i^2 \frac{n_p}{V} \rho_i^{II} k E(Th) x_{A,i}^{II} \tag{F-27}$$

$$x_{A,i}^{II} = x_{A,p}^{II} - \frac{\frac{V}{n_p} r_A (r_p - r_i)}{4\pi \rho^{II} D_{e,A}^{II} r_p r_i} \tag{F-28}$$

$$x^{II}_{A,p} = c_\gamma x^{III}_{A,p}\left(1 - x^{II}_{\Sigma,b}\right)$$

(F-29)

$$x^{III}_{A,p} = x^{III}_{A,b} - \frac{\dfrac{V}{n_p}r_A}{2\pi r_p Sh_A D^{III}_{e,A}\rho^{III}}$$

(F-30)

to obtain

$$-r_A = 4\pi r_i^2 \frac{n_p}{V}\rho^{II}_i kE(Th)\left[c_\gamma\left(1 - x^{II}_{\Sigma,b}\right)\left(x^{III}_{A,b} - \frac{\dfrac{V}{n_p}r_A}{2\pi r_p Sh_A D^{III}_{e,A}\rho^{III}}\right) - \frac{\dfrac{V}{n_p}r_A\left(r_p - r_i\right)}{4\pi\rho^{II}D^{II}_{e,A}r_p r_i}\right]$$

(F-31)

which is expressible explicitly in terms of r_A as

$$-r_A = \frac{4\pi\dfrac{n_p}{V}c_\gamma\left(1 - x^{II}_{\Sigma,b}\right)x^{III}_{A,b}}{\dfrac{1}{kE(Th)\rho^{II}r_i^2} + \dfrac{1}{\rho^{II}D^{II}_{e,A}}\left(\dfrac{1}{r_i} - \dfrac{1}{r_p}\right) + \dfrac{2c_\gamma\left(1 - x^{II}_{\Sigma,b}\right)}{Sh_A\rho^{III}D^{III}_{e,A}r_p}}$$

(F-32)

and more insightfully as

$$-r_A =$$

$$\frac{\dfrac{n_p}{V}x^{III}_{A,b}}{\underbrace{\dfrac{1}{4\pi kE(Th)\rho^{II}c_\gamma\left(1 - x^{II}_{\Sigma,b}\right)r_i^2}}_{reaction\ front\ /\ kinetics} + \underbrace{\dfrac{r_p - r_i}{4\pi\rho^{II}D^{II}_{e,A}r_i r_p}}_{shell} + \underbrace{\dfrac{\left(r_p - r_i\right)\left(1 - c_\gamma\left(1 - x^{II}_{\Sigma,b}\right)\right)}{4\pi\rho^{II}D^{II}_{e,A}c_\gamma\left(1 - x^{II}_{\Sigma,b}\right)r_i r_p}}_{p-interface} + \underbrace{\dfrac{1}{2\pi Sh_A\rho^{III}D^{III}_{e,A}r_p}}_{matrix}}$$

(F-33)

The terms in the denominator represent the effects that different phenomena/regions of the particle have on the overall reaction rate. Specifically, initially the shell and p-interface represent no barrier to reaction since neither exists ($r_p=r_i$). As the mass fraction of non-CaOH in the shell, $x^{II}_{\Sigma,b}$, approaches unity or the activity coefficient factor, c_γ, approaches zero, the kinetics and p-interface resistances become large and the rate approaches zero since the amount of Ca(OH)$_2$ at the p-interface side of the shell decreases. Similarly, all resistances except that in the matrix become large and the rate approaches zero as the reaction approaches completion (r_i approaches zero) because the shell becomes large compared to the particle and the fist-order kinetics approach zero in this limit. If the transport coefficient of any region is large or if the kinetic rate constant is large, the resistance of the corresponding region/rate becomes negligible. As the Sherwood number increases, the matrix resistance becomes negligible. The overall reaction rate proceeds proportional to the mass fraction of calcium hydroxide in the bulk and to the particle concentration. Dependencies on r_p are minimal because its range is small, as is discussed shortly. Each of these trends meets intuitive expectations and finds quantitative expression in this equation.

This equation is structurally similar to classical kinetic analyses but differs in some significant ways. Aside from the details of the expression, the calcium hydroxide mole fractions, radii, and reaction rate variables in this expression all change with time, although the term $x^{II}_{\Sigma,b}$ should change very slowly if at all with time. The same expression with the primary time dependencies explicitly indicated by (*t*) appears below

212

$$-r_A = \cfrac{4\pi \dfrac{n_p}{V} c_\gamma \left(1 - x_{\Sigma,b}^{II}\right) x_{A,b}^{III}(t)}{\dfrac{1}{kE(Th(t))\rho^{II} r_i^2(t)} + \dfrac{r_p(t) - r_i(t)}{\rho^{II} D_{e,A}^{II} r_i(t) r_p(t)} + \dfrac{2c_\gamma \left(1 - x_{\Sigma,b}^{II}\right)}{Sh_A \rho^{III} D_{e,A}^{III} r_p(t)}} \tag{F-34}$$

While this equation indicates the effects of the three particle regions identified in the model on the overall reaction rate, the existence of three dependent variables in one equation make it relatively useless for analysis. Relationships between the time-dependent terms must be developed to apply it.

2-6 Reduction in Dependent Variables

Since the samples minimally swell/shrink as they react, the total volume of the system must be constant. The volumetric decrease caused by calcium hydroxide and fly ash consumption must equal the increase caused silicate production,

$$-\underbrace{\frac{d\left(\rho^{III} V_A x_A^{III}\right)}{x_{A,b}^{III} \rho^{III} dt}}_{\substack{\text{volume change rate of} \\ \text{CaOH in Region III}}} - \underbrace{\frac{d\left(\rho^{I} V_{FA} x_{FA}^{I}\right)}{x_{FA}^{I} \rho^{I} dt}}_{\substack{\text{volume change rate of} \\ \text{FA in Region I}}} = \underbrace{\frac{d\left(\rho^{II} V_{Si8} x_{Si8}^{II}\right)}{x_{Si8}^{II} \rho^{II} dt}}_{\substack{\text{volume change rate of} \\ \text{silicate in Region II}}} \tag{F-35}$$

where the factors in parentheses represent total mass of the indicated reactants/products and the terms on the left are individually negative (masses/volumes are decreasing), so the left side produces a positive number, consistent with the increasing volume/mass of silicates. Substituting the reaction rate for the volumetric rate of change of calcium hydroxide, assuming the densities of each region do not change in time (mass/volume of each region changes, but densities do not), and assuming that the mass fractions of fly ash

213

in Region *I* and silicate in Region *II* are constant (the volumes and hence the masses are not constant, but the mass fractions are constant in Regions *I* and *II*, but not in *III*),

$$-\frac{\frac{V}{n_p}r_A}{x_{A,b}^{III}\rho^{III}} - \frac{d\left[\frac{4}{3}\pi r_i^3\right]}{dt} = \frac{d\left[\frac{4}{3}\pi(r_p^3 - r_i^3)\right]}{dt}$$

$$\Rightarrow -\frac{V}{n_p}r_A = \rho^{III}x_{A,b}^{III}\frac{d\left[\frac{4}{3}\pi(r_p^3 - r_i^3)\right]}{dt} + \rho^{III}x_A^{III}\frac{d\left[\frac{4}{3}\pi r_i^3\right]}{dt}$$

$$\Rightarrow -\frac{V}{n_p}r_A = 4\pi\rho^{III}x_{A,b}^{III}r_p^2\frac{dr_p}{dt}$$

(F-36)

Substituting this expression in the overall expression for reactivity reduces the total number of dependent variables from three to two.

$$-\frac{V}{n_p}r_A = 4\pi\rho^{III}x_{A,b}^{III}r_p^2\frac{dr_p}{dt} =$$

$$\frac{c_\gamma\left(1 - x_{\Sigma,b}^{II}\right)x_{A,b}^{III}}{\dfrac{1}{4kE(Th)\pi\rho^{II}r_i^2} + \dfrac{r_p - r_i}{4\pi\rho^{II}D_{e,A}^{II}r_i r_p} + \dfrac{c_\gamma\left(1 - x_{\Sigma,b}^{II}\right)}{2\pi Sh_A\rho^{III}D_{e,A}^{III}r_p}}$$

(F-37)

$$\frac{dr_p}{dt} = \frac{c_\gamma\left(1 - x_{\Sigma,b}^{II}\right)}{\dfrac{\rho^{III}r_p^2}{kE(Th)\rho^{II}r_i^2} + \dfrac{\rho^{III}r_p(r_p - r_i)}{\rho^{II}D_{e,A}^{II}r_i} + \dfrac{2c_\gamma\left(1 - x_{\Sigma,b}^{II}\right)r_p}{Sh_A D_{e,A}^{III}}}$$

(F-38)

A relationship between r_p and r_i would allow this expression to have a single dependent variable and hence potentially solvable. This relationship depends on the relative volumes of fly ash and calcium hydroxide consumed during the reaction. Similar

to the homogeneous kinetics model discussed previously, this model defines a linear relationship between the fly ash and calcium hydroxide consumption. In this model, the relationship is volumetric rather than mass-based,

$$\frac{d\left(\rho' V_{FA} x^I_{FA}\right)}{dt} = b\frac{d\left(\rho''' V_A x^{III}_A\right)}{dt}$$
$$\Rightarrow \rho' V_{FA} x^I_{FA} = a + b\rho''' V_A x^{III}_A$$

(F-39)

This allows the mass fraction of fly ash to be written in terms of the mass fraction of calcium hydroxide, though this model differs in from the previous model in that the reaction is zero order in fly ash. Therefore, this expression is useful in determining the amount of unreacted fly ash remaining, but not necessary to solve the differential equation describing calcium hydroxide concentration.

$$\rho' V^0_{FA} x^{I,0}_{FA} = a + b\rho''' V^0_A x^{III,0}_A$$
$$\Rightarrow a = \rho' V^0_{FA} x^{I,0}_{FA} - b\rho''' V^0_A x^{III,0}_A = \rho' V^0_{FA} - b\rho''' V^0_A x^{III,0}_A$$
$$\Rightarrow \rho' V_{FA} x^I_{FA} = \rho' V^0_{FA} - b\rho''' V^0_A x^{III,0}_A + b\rho''' V_A x^{III}_A = \rho' V^0_{FA} + b\rho''' V_A \left(V_A x^{III}_A - V^0_A x^{III,0}_{CaOH}\right)$$
$$\Rightarrow x^I_{FA} = \frac{\rho' V^0_{FA}}{\rho' V_{FA}} - \frac{b\rho'''}{\rho' V_{FA}}\left(V^0_A x^{III,0}_{CaOH} - V_A x^{III}_A\right)$$

(F-40)

Substituting the above equation defining b into the volumetric balance leads to an expression dependent only on calcium hydroxide and shell parameters.

$$-\frac{d\left(\rho'''V_A x_A'''\right)}{x_A'''\rho'''dt}-\frac{d\left(\rho'V_{FA}x_{FA}'\right)}{x_{FA}'\rho'dt}=\frac{d\left(\rho''V_{Si8}x_{Si8}''\right)}{x_{Si8}''\rho''dt}$$

$$-\frac{d\left(\rho'''V_A x_A'''\right)}{x_A'''\rho'''dt}-b\frac{d\left(\rho'''V_A x_A'''\right)}{x_A'''\rho'''dt}=\frac{d\left(\rho''V_{Si8}x_{Si8}''\right)}{x_{Si8}''\rho''dt}$$

(F-41)

Substituting the expression for the shell volume and completing the differentiation yields

$$-(1+b)\frac{d\left(\rho'''V_A x_A'''\right)}{x_A'''\rho'''dt}=\frac{d\left(\rho''V_{Si8}x_{Si8}''\right)}{x_{Si8}''\rho''dt}$$

$$-(1+b)\frac{\dfrac{V}{n_p}r_A}{x_A'''\rho'''}=\frac{d\left[\dfrac{4}{3}\pi\left(r_p^3-r_i^3\right)\right]}{dt}$$

$$r_i^2\frac{dr_i}{dt}=r_p^2\frac{dr_p}{dt}+(1+b)\frac{\dfrac{V}{n_p}r_A}{4\pi x_A'''\rho'''}$$

(F-42)

Replacing the time-dependent reaction term with the previously derived relationship to the changes in diameters results in a differential relationship between the two interfaces

$$r_i^2\frac{dr_i}{dt}=r_p^2\frac{dr_p}{dt}-(1+b)r_p^2\frac{dr_p}{dt}$$

$$r_i^2\frac{dr_i}{dt}=-br_p^2\frac{dr_p}{dt}$$

(F-43)

Integrating both sides and applying the condition that both interfaces equal R at time zero to evaluate the integration constant yields an algebraic expression for the fly ash interface in terms of the particle interface as follows:

216

$$r_i^3 = (1+b)R^3 - br_p^3$$

$$r_i = \left[(1+b)R^3 - br_p^3\right]^{1/3}$$

$$r_p = \left[\frac{(b+1)R^3 - r_i^3}{b}\right]^{1/3} = \left[\left(1+\frac{1}{b}\right)R^3 - \frac{r_i^3}{b}\right]^{1/3}$$

(F-44)

This indicates that the maximum value of r_p is

$$r_{p,max} = \left(1+\frac{1}{b}\right)^{1/3}R$$

(F-45)

Substitution of the above expression for r_i into the previously derived expression for the reaction rate produces the final expression

$$\frac{dr_p}{dt} = \frac{c_\gamma\left(1-x_{\Sigma,b}''\right)}{\dfrac{\rho''' r_p^2}{kE(Th)\left[(1+b)R^3 - br_p^3\right]^{2/3}\rho''} + \dfrac{\rho''' r_p(r_p - r_i)}{\rho'' D_{e,A}''\left[(1+b)R^3 - br_p^3\right]^{1/3}} + \dfrac{2c_\gamma\left(1-x_{\Sigma,b}''\right)r_p}{Sh_A D_{e,A}'''}}$$

(F-46)

where

$$E(Th) = \frac{3\tanh\left(\dfrac{mr_i}{3}\right)}{mr_i} = \frac{3\tanh\left(\dfrac{m\left((1+b)R^3 - br_p^3\right)^{1/3}}{3}\right)}{m\left((1+b)R^3 - br_p^3\right)^{1/3}}$$

(F-47)

This expression has (in principle) a single dependent variable (r_p), which is related to the reaction rate through the previously derived expression

217

$$-r_A = 4\pi \frac{n_p}{V} \rho^{III} x^{III}_{A,b} r_p^2 \frac{dr_p}{dt}$$

(F-48)

This is a reasonably fundamental expression, subject mainly to the assumptions that the overall volume of the system does not change (consistent with observations), that the amount of calcium hydroxide within the shell and the fly ash particle is negligible compared to that in the matrix (initially strictly true and generally true except as the amount of calcium hydroxide approaches zero), and that the parameters are properly used to describe transport and kinetics (transport coefficients dependence on composition has been ignored, for example).

Closed form solutions to this differential equation are difficult to find. However, some limiting forms are instructive. The first simplifying assumption is that the effectiveness factor is unity or, equivalently, that the kinetic rate constant is a global constant based on the fly ash particle external surface area (r_i). The second assumption deals with the time-dependent portions of the first (kinetic), second (shell resistance) and third (matrix and boundary) terms in the denominator. These portions are

$$\frac{r_p^2}{r_i^2} = \frac{r_p^2}{\left[(1+b)R^3 - br_p^3\right]^{2/3}} = \left\{ \frac{x^2}{\left[1+b*\left(1-x^3\right)\right]^{2/3}} \right\}$$

(F-49)

$$\frac{(r_p - r_i)}{r_i} r_p = \frac{r_p^2}{r_i} - r_p = \frac{r_p^2}{\left[(1+b)R^3 - br_p^3\right]^{1/3}} - r_p = R\left\{ \frac{x^2}{\left[1+b*\left(1-x^3\right)\right]^{1/3}} - x \right\}$$

(F-50)

218

$$r_p = R\{x\}$$

<div align="right">(F-51)</div>

where

$$x \equiv \frac{r_p}{R}$$

<div align="right">(F-52)</div>
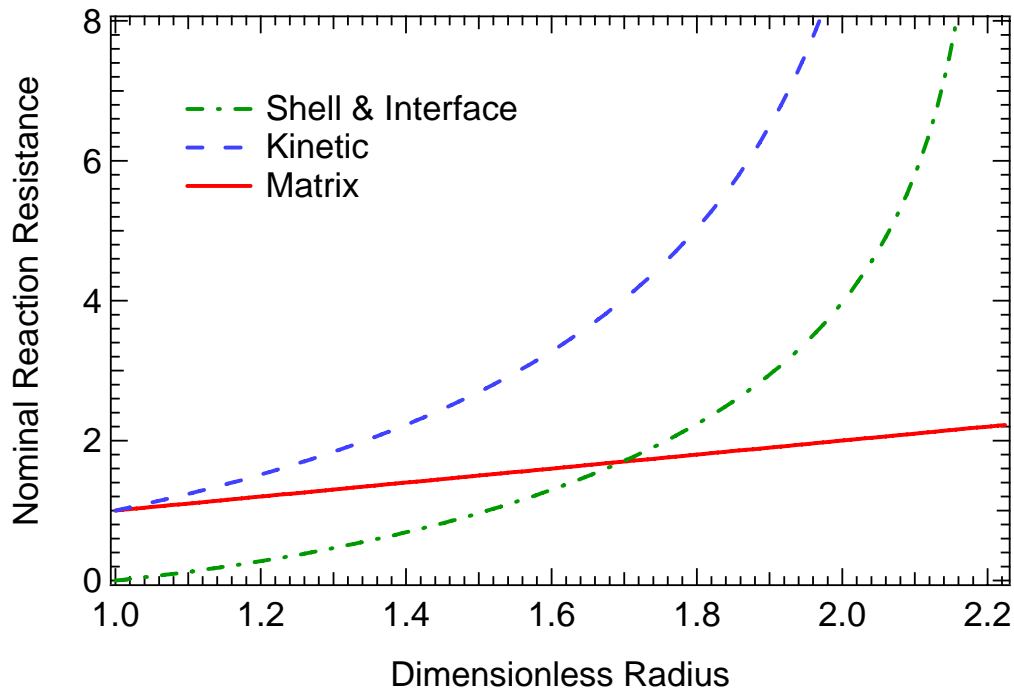
Figure F-2 Changes in resistances with the matrix, shell, and kinetics during reaction [These normalized data assume b = 0.1. The progression is from an unreacted (abcissa=1) to a fully reacted particle. Both the kinetic and the shell/interface resistances approach infinity as the reaction extent approaches unity.]

Over the valid domain for x in the dimensionless functions in curly brackets, which is from unity to $\left(1+\dfrac{1}{b}\right)^{1/3}$, the functions ranges from unity, zero, and unity, respectively, at their initial values to a singular point ($+\infty$) for the first two expressions and x for the final function at the final value. If there is excess calcium hydroxide, the

functions span this entire domain of x. If there is excess fly ash, the functions never reach the maximum value of *x*. These functions appear and show the extent of reaction increases (non-linearly) with increasing dimensionless radius. The complete (quantitative) dependencies in the model are proportional to these lines, with proportionality constants that depend on transport coefficients, physical properties, etc., as indicated in the equation. However, this graph illustrates how any individual dependence and the relative dependencies changes with particle size, and hence time. For example, matrix film resistance becomes increasingly less important as reaction proceeds.

$$\frac{d\,r_p}{dt} = \frac{\left(1 - x_{\Sigma,b}^{II}\right)}{\dfrac{4\pi\rho^{III}}{kE(Th)c_\gamma \dfrac{V}{n_p}\rho_i^{II}}r_p^2 + \dfrac{\rho^{III}(r_p - r_i)}{Sh_A c_\gamma \rho^{II} D_{e,A}^{II} r_i}r_p + \dfrac{2\left(1 - x_{\Sigma,b}^{II}\right)}{Sh_A D_{e,A}^{III}}r_p}$$

$$\frac{d\,r_p^3}{dt} = \frac{3c_\gamma\left(1 - x_{\Sigma,b}^{II}\right)}{\dfrac{\rho^{III}}{kE(Th)\rho^{II}\left[(1+b)R^3 - br_p^3\right]^{2/3}} + \dfrac{\rho^{III}}{\rho^{II}D_{e,A}^{II}}\left\{\dfrac{1}{\left[(1+b)R^3 - br_p^3\right]^{1/3}} - \dfrac{1}{r_p}\right\} + \dfrac{2c_\gamma\left(1 - x_{\Sigma,b}^{II}\right)}{Sh_A D_{e,A}^{III}r_p}}$$

(F-53)

The reaction rate relates to the time-dependent diameter change as follows (previously derived)

$$-r_A = 4\pi\frac{n_p}{V}\rho^{III}x_{A,b}^{III}r_p^2\frac{dr_p}{dt}$$

$$= \frac{4\pi\dfrac{n_p}{V}x_{A,b}^{III}c_\gamma\left(1 - x_{\Sigma,b}^{II}\right)}{\dfrac{1}{kE(Th)\rho^{II}\left[(1+b)R^3 - br_p^3\right]^{2/3}} + \dfrac{1}{\rho^{II}D_{e,A}^{II}}\left\{\dfrac{1}{\left[(1+b)R^3 - br_p^3\right]^{1/3}} - \dfrac{1}{r_p}\right\} + \dfrac{2c_\gamma\left(1 - x_{\Sigma,b}^{II}\right)}{Sh_A D_{e,A}^{III}\rho^{III}r_p}}$$

(F-54)

An analytical, explicit solution to the diameter equation would allow the reaction rate equation to be written in terms of time only. However, both equations are difficult to solve analytically. They could be solved numerically with appropriate estimates of their parameters.

In principal, the dataset generated in this project could be used to determine the unknown parameters, either by numerically solving the equation and using the solution to fit the data (the statistically preferred method), or by differentiating the data and fitting the results to the differential equation (more convenient, but statistically problematic). The primary unknown parameters include two solid-solid diffusion coefficients and a kinetic rate constant. Secondary unknown parameters – those for which reasonable estimates could be made from sources other than the data – include the activity parameter (about 1), two densities (about 2500 kg/m^3), and the mass fraction of non-hydroxide in the shell (SEM images could provide an estimate, which is typically about 0.8). There are over 150 data points for each type of fly ash, more than enough to determine the primary and even secondary unknown parameters from a degree-of-freedom standpoint. In practice, these parameters are too closely related to make meaningful estimates. For example, the temperature dependence of the solid-solid diffusion coefficients generally has an Arrhenius-type dependence identical in form and similar in effective activation energy to that of the kinetic constant. Finally, although this work generated a large dataset, determining values for these closely related parameters with acceptable statistical precision will require large data sets and higher precision.

Despite the difficulties in determining precise parameters, some indication of the equation behavior can be developed. Since the kinetic resistance approaches infinity as

the reaction approaches completion, these equations result in a reaction rate prediction that asymptotically approaches zero. This is a consequence of the first-order kinetic assumption. The shell resistance also approaches infinity if there is an excess of calcium hydroxide, since the particle inner diameter approaches zero and the shell eventually becomes infinitely thick relative to this diameter. If there is excess fly ash, the shell resistance increases to a finite value with increasing extent of reaction. The external matrix diffusion resistance increases with increasing extent of reaction but remains finite.

3 Particle- and Convection-based Model

The previous model assumes, among other things, that the material does not swell or shrink and therefore conserves both mass and volume locally. All mass transfer occurs through diffusion in the previous model. However, it is possible to drive mass fluxes without swelling by inducing pressure gradients. This model assumes that the matrix does not swell but that the pressure induced by the growing shell of products forces reactants through the pores in the shell and that transport is dominated by this pressure-induced convection. Flow through the pores in this model obeys Darcy's law. A conceptual diagram appears below which is similar in many ways to that of the last model except that the silicate products appear as spokes of a wheel, in a manner in which they sometimes appear in SEM images and commonly are illustrated in the literature. The flow through the porous layer in this model obeys Darcy's law, that is

$$Q_A = -\frac{\kappa A_x \Delta p}{\mu L}$$

(F-55)

222

where Q_a represents the volumetric flow [vol/time], κ is the permeability [], A_x is the cross-sectional area perpendicular to the flow, Δp is the pressure difference across the distance L, and μ is the fluid viscosity. In terms of volumetric fluxes and gradients, this becomes

$$\vec{q}_A = -\frac{\kappa}{\mu}\vec{\nabla}p$$

(F-56)

where q is the volumetric flow per unit cross-sectional area (volumetric flux). The remainder of this model is one-dimensional and the vector notation is no longer maintained.

Returning to the volume balance of the previous section,

$$-(1+b)\frac{d\left(\rho^{III}V_A x_A^{III}\right)}{x_A^{III}\rho^{III}dt} = \frac{d\left(\rho^{II}V_{Si8} x_{Si8}^{II}\right)}{x_{Si8}^{II}\rho^{II}dt}$$

$$-(1+b)\frac{\dfrac{V}{n_p}r_A}{x_A^{III}\rho^{III}} = -q_A 4\pi r_p^2 = -\frac{\kappa}{\mu}\nabla p 4\pi r_p^2 = \frac{d\left[\dfrac{4}{3}\pi\left(r_p^3 - r_i^3\right)\right]}{dt}$$

$$\nabla p = -(1+b)\frac{\mu\dfrac{V}{n_p}r_A}{4\pi\kappa x_A^{III}\rho^{III}r_p^2}$$

(F-57)
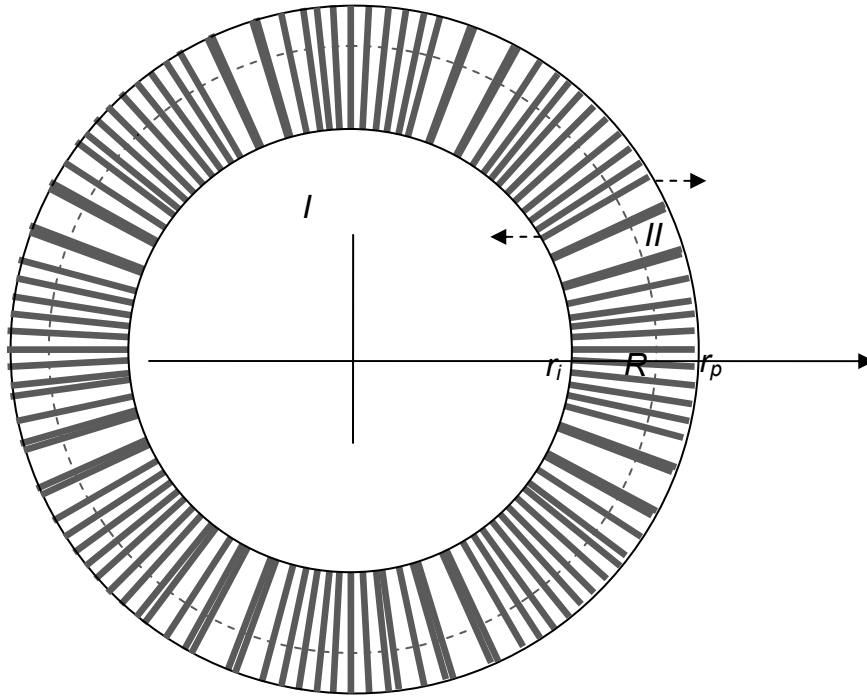
Figure F-3 Schematic diagram of reacting ash particle in concrete/Ca(OH)$_2$ for the convective model.

If all materials are incompressible, this model leads to the non-intuitive result that neither the matrix nor the shell resistances affect the reaction rate, since the expansion of the shell layer quantitatively forces the reactants to the reaction front, r_i. It also suggest that the macromolecular reaction products in the shell will orient themselves along the flow paths to minimize flow resistance and that the outer edge of the shell may be more highly concentrated in Ca than the bulk of the matrix due to the force of the expanding particle forcing water from the expansion front, r_p (and, in reality, compacting it). The effects of viscosity and permeability influence the pressure gradient, but if all materials are incompressible, they do not influence the flow or reaction rates.

This model ultimately results in a much simpler expression for the reaction rate than the previous model. The derivation follows that of the previous model precisely

except (a) there are no mass transfer resistances in the shell or bulk layer, and (b) the activity parameter is assumed unity since there is no phase change at the outer shell surface, just flow of material and two non-chemically-interacting phases.

The derivation of an equation to describe the outer radius begins with the same definition of reaction rate as used previously (first-order in calcium hydroxide, zero order in fly ash),

$$-r_A \equiv -\frac{d(\bar{\rho}\bar{x}_A)}{dt} = -\bar{\rho}\frac{d\bar{x}_A}{dt} = A_{ex}kE(Th)\rho_{A,i}'' = A_{ex}\rho_i''kE(Th)x_{A,i}'' = 4\pi r_i^2 \frac{n_p}{V}\rho_i''kE(Th)x_{A,i}''$$

$$-r_A \equiv -\frac{d(\bar{\rho}\bar{x}_A)}{dt} = 4\pi r_i^2 \frac{n_p}{V}\rho_i''kE(Th)x_{A,i}''$$

(F-58)

The consumption of calcium hydroxide, as indicated by the product of the particle concentration, the rate of volume increase of the outer shell layer, and the density of calcium hydroxide in the matrix, must equal the reaction rate.

$$-r_A = \frac{n_p}{V}\rho'''x_{A,b}'''\frac{d}{dt}\left(\frac{4}{3}\pi r_p^3\right) = 4\pi\frac{n_p}{V}\rho'''x_{A,b}'''r_p^2\frac{dr_p}{dt} = 4\pi r_i^2 \rho_i''\frac{n_p}{V}kE(Th)x_{A,i}''$$

(F-59)

The same relationships between the inner and outer shell radii exist in this model as in the previous model, and they are used without rederivation here. Also, the shell mass fraction of calcium hydroxide should be that in the matrix diluted by the mass fraction of silicate (and anything else) in the shell, as was also previously derived (assuming an activity factor of unity). These substitutions lead to

$$\rho^{III} x_{A,b}^{III} r_p^2 \frac{dr_p}{dt} = r_i^2 \rho_i^{II} kE(Th) x_{A,i}^{II} = \left[(1+b)R^3 - br_p^3\right]^{2/3} \rho_i^{II} kE(Th)\left(1 - x_{\Sigma,b}^{II}\right) x_{A,b}^{III}$$

$$\frac{dr_p}{dt} = \frac{\left[(1+b)R^3 - br_p^3\right]^{2/3} \rho_i^{II} kE(Th)\left(1 - x_{\Sigma,b}^{II}\right)}{\rho^{III} r_p^2}$$

(F-60)

Ignoring the dependence of the efficiency factor on r_i, which is justified if the efficiency factor is unity and the kinetic rate coefficient is a global, external surface area quantity, an analytical solution to this equation is

$$r_p = \left(\begin{array}{c} R^3 + \dfrac{kE(Th)\rho^{II}\left(1-x_{\Sigma,b}^{II}\right)t}{\left(\rho^{III}\right)^3} \times \\[2mm] \left\{3R^2\left(\rho^{III}\right)^2 - bkE(Th)\rho^{II}\left(1-x_{\Sigma,b}^{II}\right)t\left[3R\rho^{III} - bkE(Th)\rho^{II}\left(1-x_{\Sigma,b}^{II}\right)t\right]\right\} \end{array} \right)^{1/3}$$

$$r_p^3 - R^3 = kE(Th)\rho^{II}\left(1-x_{\Sigma,b}^{II}\right)t \times$$

$$\left\{\frac{3R^2}{\rho^{III}} - \frac{bkE(Th)\rho^{II}\left(1-x_{\Sigma,b}^{II}\right)t}{\left(\rho^{III}\right)^2}\left[3R - \frac{bkE(Th)\rho^{II}\left(1-x_{\Sigma,b}^{II}\right)t}{\rho^{III}}\right]\right\}$$

(F-61)

where the efficiency factor is retained since this solution assumes only that it is constant with respect to time, not that it is necessarily unity. As previously shown,

$$r_{p,max} = \left(1 + \frac{1}{b}\right)^{1/3} R$$

(F-62)

The maximum time for this reaction is when $r_p = r_{p,max}$, which occurs at

$$t(r_p = r_{p,max}) = \frac{R\rho'''}{bkE(Th)\rho''\left(1 - x_{\Sigma,b}''\right)}$$

(F-63)

This is a characteristic time that conveniently scales the equation. A dimensionless time, τ, defined as the ratio of time to this quantity and which can also be thought of as dimensionless reaction rate coefficient renders a far simpler form of the r_p equation as follows

$$\tau \equiv \frac{bkE(Th)\left(1 - x_{\Sigma,b}''\right)\rho'' t}{R\rho'''}$$

(F-64)

$$r_p^3 - R^3 = \frac{R^3}{b}\left[3\tau - \tau^2(3 - \tau)\right]$$

(F-65)

$$r_p = R\left\{1 + \frac{1}{b}\left[3\tau - \tau^2(3 - \tau)\right]\right\}^{1/3}$$

(F-66)

so, the complete specification for the diameter is

$$r_p = \begin{cases} R\left[1 + \dfrac{3\tau - \tau^2(3 - \tau)}{b}\right]^{1/3} & 0 < t < \dfrac{R\rho'''}{bkE(Th)\rho''\left(1 - x_{\Sigma,b}''\right)} \ or \ 0 < \tau < 1 \\[4mm] R\left(1 + \dfrac{1}{b}\right)^{1/3} & t \geq \dfrac{R\rho'''}{bkE(Th)\rho''\left(1 - x_{\Sigma,b}''\right)} \ or \ \tau \geq 1 \end{cases}$$

(F-67)

These equations correspond to conditions where fly ash particle size, r_i, ranges from R to zero, that is, when calcium hydroxide is in excess or stoichiometrically

balanced with fly ash. If fly ash is in excess, the reaction stops and r_p stops changing prior to the time limits indicated above. This issue will be formally discussed after deriving an expression for the overall conversion of calcium hydroxide.

The following figure illustrates the time-dependent portion of these functions, $\left(3\tau - \tau^2(3-\tau)\right)^{1/3}$, and shows that it approaches unity rapidly at first and then more slowly. The change in rate is, in this case, associated with the decreasing surface area of the fly ash particle. Specifically, it reflects neither diffusion nor first-order kinetics affects. The lack of diffusion effects is clear. There are no diffusion limitations in this convective model. Traditional first-order kinetics expressions asymptotically approach full conversion because the reactant (calcium hydroxide) concentration approaches zero and the rate is proportional to this reactant concentration. In this model, however, the concentration of calcium hydroxide in the matrix does not change – just the relative amounts of matrix and shell change. Therefore, the approach to unity in this model is not asymptotic; the value is identically unity at a dimensionless time of unity. At longer times, the value is constant at unity. In these ways, the predictions seen here and those for overall conversion discussed later differ fundamentally from predictions that are superficially similar in the context of the purely kinetics and the diffusion models discussed earlier. The dimensionless radius will reach unity (fully reacted particle) if stoichiometric or excess calcium hydroxide exists in the mixture. If excess fly ash exists, the dimensionless radius becomes constant at some value less than unity. This function, including its derivative, (actually the derivative of the cube of the function) plays a prominent role in the reaction rate analysis to be discussed next.
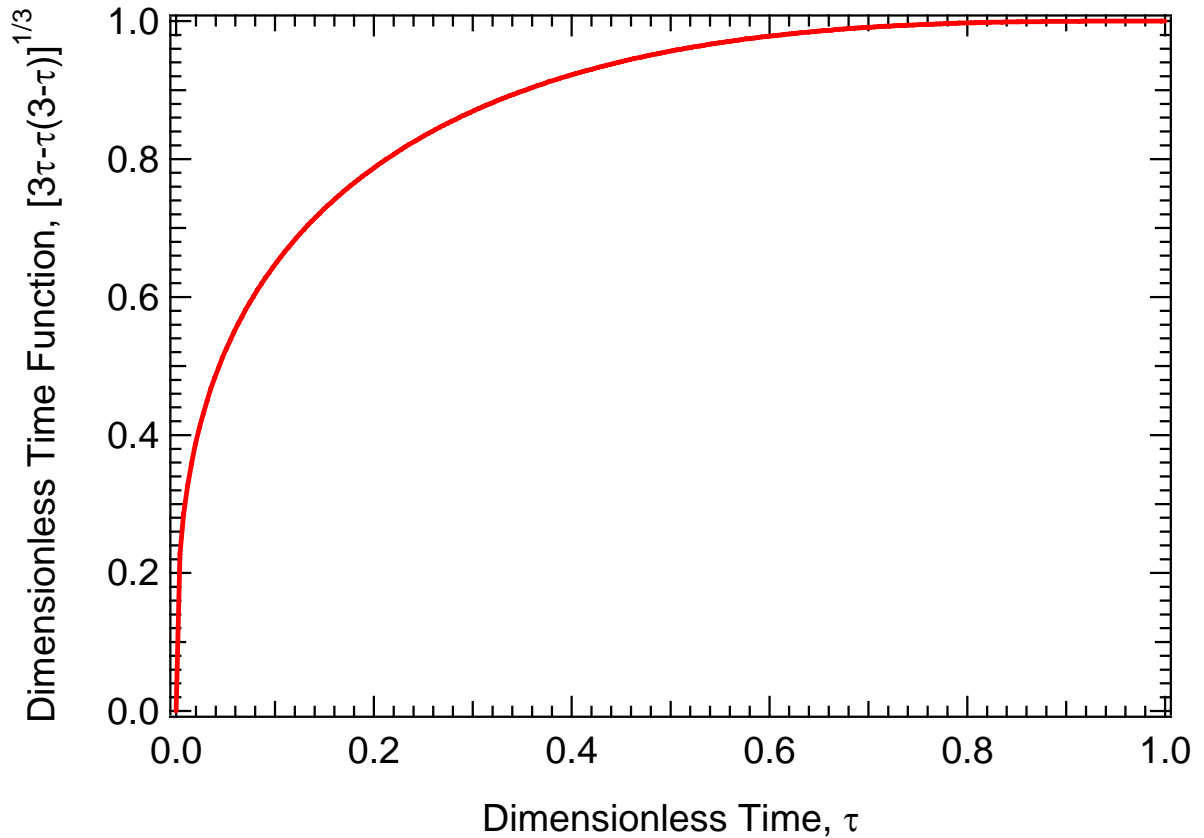
Figure F-4 Development of time-dependent portion of the particle radius equation, $\left(3\tau - \tau^2(3-\tau)\right)^{1/3}$ **on less time**

$$\tau \equiv \frac{bkE(Th)\left(1 - x_{\Sigma,b}^{\prime\prime}\right)\rho^{\prime\prime}t}{R\rho^{\prime\prime\prime}}$$

(F-68)

Particle diameters are not directly measured, nor have methods been established that can do so with precision. SEM-based measurements of cross sections, for example, randomly slice particles, making it very difficult to determine the original diameter or the reacted core diameter. There are methods of converting randomly selected cross sections into original diameters, but they are not precise, especially in the cases of irregular shapes or broad size distributions. However, the consumption of calcium hydroxide can and has

been quantified in this work. The next step is to use these diameter equations to develop a model for the rate of calcium hydroxide consumption.

The rate of calcium hydroxide mass loss is related to the diameter change through the previously derived volume balance

$$-\frac{V}{n_p}r_A = 4\pi\rho^{III}x_{A,b}^{III}r_p^2\frac{d\,r_p}{dt} = \frac{4\pi\rho^{III}x_{A,b}^{III}}{3}\frac{d\,r_p^3}{dt} = \frac{4\pi\rho^{III}x_{A,b}^{III}}{3}\frac{d\left(r_p^3 - R^3\right)}{dt}$$

(F-69)

$$\frac{d\left(r_p^3 - R^3\right)}{dt} = \frac{R^3}{b}\frac{d}{dt}\left\{\left[3\tau - \tau^2\left(3-\tau\right)\right]\right\}\frac{d\tau}{dt}$$

$$= \frac{3R^3}{b}\left(\tau - 1\right)^2\frac{bkE(Th)\left(1 - x_{\Sigma,b}^{II}\right)\rho^{II}}{R\rho^{III}}$$

$$r_A \equiv \frac{d}{dt}\left(\overline{\rho}\overline{x}_A\right) = -\frac{n_p}{V}4\pi R^2 x_{A,b}^{III}kE(Th)\left(1 - x_{\Sigma,b}^{II}\right)\rho^{II}\left(\tau - 1\right)^2$$

$$\overline{x}_A(t) = \overline{x}_A^0 - \frac{n_p}{V}\frac{4\pi R^2 kE(Th)\left(1 - x_{\Sigma,b}^{II}\right)\rho^{II}x_{A,b}^{III}t}{\overline{\rho}}\times$$

$$\left\{1 - \frac{bkE(Th)\left(1 - x_{\Sigma,b}^{II}\right)\rho^{II}t}{\rho^{III}R} + \frac{1}{3}\left[\frac{bkE(Th)\left(1 - x_{\Sigma,b}^{II}\right)\rho^{II}t}{\rho^{III}R}\right]^2\right\}$$

$$= \overline{x}_A^0 - \frac{n_p}{V}\frac{4\pi R^3\rho^{III}}{b\overline{\rho}}x_{A,b}^{III}\tau\left(1 - \tau + \frac{1}{3}\tau^2\right)$$

(F-70)

The dimensionless/scaled equations produce an expression for the time-dependent overall mass fraction of calcium hydroxide that is expressible in both dimensionless and primitive/original forms. The most significant assumptions in this analytical form include

230

(a) that the efficiency factor is constant, (b) that the material and kinetic properties (densities, compositions of each region, stoichiometric ratio b, and reaction rate constants) are constant – which implies constant-temperature conditions, and (c) that the mass of reactant inside the shell is negligible.

Where the last form of the equation more clearly indicates the functional dependence on particle concentration (linear) and initial calcium hydroxide concentration (constant offset). The dependencies on initial size, reaction rate constant, and time are complex but are completely expressed in the dimensionless time, τ. This portion of the solution applies only for dimensionless times from zero to one. At times greater than one, the average concentration is constant, so the complete solution is

$$
\overline{x}_A(t) =
\begin{cases}
\overline{x}_A^0 - \dfrac{n_p}{V}\dfrac{4\pi R^2 kE(Th)\left(1-x_{\Sigma,b}^{II}\right)\rho^{II} x_{A,b}^{III} t}{\overline{\rho}} \times \\[2ex]
\quad \left\{ 1 - \dfrac{bkE(Th)\left(1-x_{\Sigma,b}^{II}\right)\rho^{II} t}{\rho^{III} R} + \dfrac{1}{3}\left[\dfrac{bkE(Th)\left(1-x_{\Sigma,b}^{II}\right)\rho^{II} t}{\rho^{III} R}\right]^2 \right\} \\[2ex]
\quad if \left(0 \le t \le \dfrac{\rho^{III} R}{bkE(Th)\left(1-x_{\Sigma,b}^{II}\right)\rho^{II}} \right) \\[2ex]
\overline{x}_A^0 - \dfrac{n_p}{V}\dfrac{4\pi R^3 \rho^{III} x_{A,b}^{III}}{3b\overline{\rho}} \\[2ex]
\quad if \left(t > \dfrac{\rho^{III} R}{bkE(Th)\left(1-x_{\Sigma,b}^{II}\right)\rho^{II}} \right)
\end{cases}
$$

$$
\overline{x}_A(t) =
\begin{cases}
\overline{x}_A^0 - \dfrac{n_p}{V}\dfrac{4\pi R^3 \rho^{III}}{b\overline{\rho}} x_{A,b}^{III}\tau\left(1-\tau+\dfrac{1}{3}\tau^2\right) & 0 \le \tau \le 1 \\[2ex]
\overline{x}_A^0 - \dfrac{n_p}{V}\dfrac{4\pi R^3 \rho^{III} x_{A,b}^{III}}{3b\overline{\rho}} & \tau > 1
\end{cases}
\tag{F-71}
$$

This derivation prevents fly ash concentration from becoming negative by setting zero as a lower bound on r_i. However, the derivation has not yet specifically enforced overall mass conservation for calcium hydroxide, that is, has not explicitly required that calcium hydroxide mass fraction be a non-negative number. The equations above predict eventual negative calcium hydroxide concentrations if fly ash is in stoichiometric excess. Stoichiometric excess fly ash in this model results from having more potential to react calcium hydroxide than the amount of calcium hydroxide in the mixture, which occurs whenever the following inequality is met,

$$\overline{x}_A^0 \overline{\rho} < \frac{n_p}{V} \frac{4}{3b} \pi R^3 \rho^{III} x_{A,b}^{III} \tag{F-72}$$

where the left side represents the overall concentration of calcium hydroxide present in the mixture and the right side represents the calcium hydroxide concentration that could potentially react with the fly ash.

Formal expressions for the times at which the calcium hydroxide concentration reaches zero when it is limiting are

$$\tau_{max,CaOH\ limiting} = 1 - \frac{\left[\left(\frac{n_p}{V} R^3 \rho^{III} x_A^{III} \right)^2 \left(4 \frac{n_p}{V} \pi R^3 \rho^{III} x_A^{III} - 3b\overline{\rho}\overline{x}_A^0 \right) \right]^{1/3}}{2^{2/3} \frac{n_p}{V} \pi^{1/3} R^3 \rho^{III} x_A^{III}} \tag{F-73}$$

and

$$t_{max,CaOHlimiting} = \frac{R\rho^{III}}{bkE(Th)\left(1-x_{\Sigma,b}^{II}\right)\rho^{II}} - \frac{\left[\left(\frac{n_p}{V}R^3\rho^{III}x_A^{III}\right)^2\left(4\frac{n_p}{V}\pi R^3\rho^{III}x_A^{III}-3b\overline{\rho}\overline{x}_A^0\right)\right]^{1/3}}{2^{2/3}\frac{n_p}{V}\pi^{1/3}R^2x_A^{III}bkE(Th)\left(1-x_{\Sigma,b}^{II}\right)\rho^{II}}$$ (F-74)

In terms of the extent of reaction, the time-dependent portion of the composition equations become

$$\alpha \equiv 1 - \frac{\overline{x}_A}{\overline{x}_A^0} = \frac{\overline{x}_A^0 - \overline{x}_A}{\overline{x}_A^0} = \frac{n_p}{V}\frac{4\pi R^3\rho^{III}x_{A,b}^{III}}{\overline{\rho}\overline{x}_A^0 b}\tau\left(1-\tau+\frac{1}{3}\tau^2\right)$$

$$= \frac{n_p}{V}\frac{4\pi R^2 kE(Th)\left(1-x_{\Sigma,b}^{II}\right)\rho^{II}x_{A,b}^{III}t}{\overline{\rho}\overline{x}_A^0}\left\{1-\frac{bkE(Th)\left(1-x_{\Sigma,b}^{II}\right)\rho^{II}t}{\rho^{III}R}+\frac{1}{3}\left[\frac{bkE(Th)\left(1-x_{\Sigma,b}^{II}\right)\rho^{II}t}{\rho^{III}R}\right]^2\right\}$$ (F-75)

Figure F-5 illustrates the time-dependent portion of the normalized reaction extent, $\frac{V}{n_p}\frac{3\overline{x}_A^0 b\overline{\rho}}{4\pi R^3\rho^{III}x_{A,b}^{III}}\alpha$ as a function of dimensionless time. This indicates that the normalized reaction extent reaches (non-asymptotically) an ultimate value at a dimensionless time of 1. Depending on the relative amounts of fly ash and calcium hydroxide, the ultimate conversion may be as high as unity. It plateaus either at unity if fly ash is in stoichiometric excess or at some value less than unity if calcium hydroxide is in stoichiometric excess.

An expression for the pressure gradient at the matrix-shell interface (at r_p) as a function of time results from substituting the time-dependent expressions for the radius and the reaction rate into the previously derived expression for pressure gradient based on Darcy's law, as shown below. The expressions include a dimensioned and a

dimensionless expression for pressure gradient. The latter also appears in Figure F-, which illustrates a high initial gradient followed by a more measured approach to the ultimate value of zero as the reaction rate approaches zero. Although the initial dimensionless pressure gradient may appear to approach infinity, it is identically unity on this normalized plot. The pressure gradient is even higher (though the pressure is lower) at the fly-ash-shell interface (r_i), approaching infinity as the particle size approaches zero. The primary interest in the pressure gradient is its potential for forming microfractures in the matrix, which will be proportional to the pressure gradient at r_p.
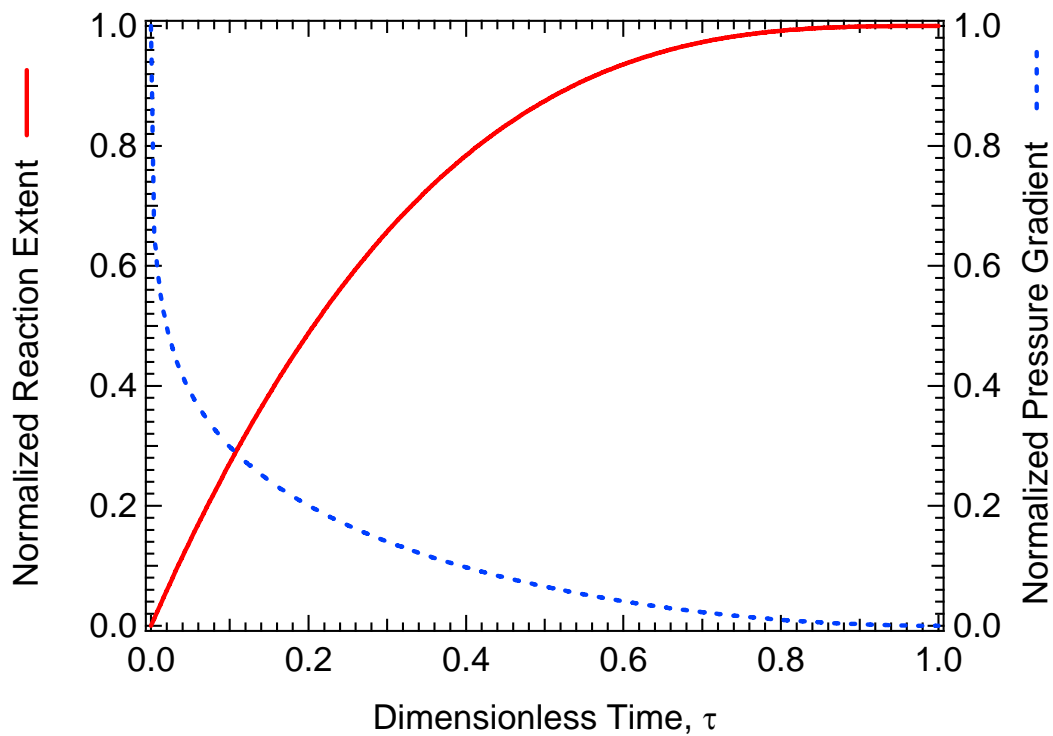

Figure F-5 Change in normalized reaction extent and pressure gradient at the shell outer radius (r_p) with dimensionless time predicted by the convective model.

$$\nabla p = \frac{-(1+b)\mu \dfrac{V}{n_p} r_A}{4\pi\kappa x_A^{III} \rho^{III} r_p^2} = \frac{-(1+b)\mu k E(Th)\left(1-x_{\Sigma,b}''\right)\rho''(\tau-1)^2}{\kappa\rho^{III}\left\{1+\dfrac{1}{b}\left[3\tau-\tau^2(3-\tau)\right]\right\}^{2/3}}$$

(F-76)

$$\frac{\kappa\rho^{III}\nabla p}{-(1+b)\mu k E(Th)\left(1-x_{\Sigma,b}''\right)\rho''} = \frac{(\tau-1)^2}{\left\{1+\dfrac{1}{b}\left[3\tau-\tau^2(3-\tau)\right]\right\}^{2/3}}$$

(F-77)

4. Kinetics for Polydisperse Fly Ash Mixtures

The above derivation presumes a single fly ash particle size, that is, that fly ash is monodisperse. Generally, fly ash sizes range considerably, that is, fly ash in real applications is polydisperse. Accommodating polydisperse fly ash alters the above equations slightly. Specifically, the equation for normalized reaction extent becomes

$$\alpha \equiv 1 - \frac{\overline{x}_A}{\overline{x}_A^0} = \frac{\overline{x}_A^0 - \overline{x}_A}{\overline{x}_A^0} = \sum_{i=1}^{\infty}\left[\left(\frac{n_p}{V}\right)_i \frac{4\pi R_i^3 \rho^{III} x_{A,b}^{III}}{\overline{\rho}\,\overline{x}_A^0 b_i}\tau_i\left(1-\tau_i+\frac{1}{3}\tau_i^2\right)\right] = \sum_{i=1}^{\infty}\alpha_i$$

(F-78)

where

$$\tau_i = \frac{b_i k_i E_i(Th_i)\left(1-x_{\Sigma,b}''\right)\rho'' t}{\rho^{III} R_i}$$

(F-79)

Fly ash composition and properties vary, sometimes markedly, with size. This leads to all of the *i*-subscripted parameters in the above equation also varying with size. However, determining so many size-dependent parameters may only be able to be done reliably with a series of experiments on monodisperse samples. This, however, compromises the greater objective of determining the impact of fly ash in practical applications since the polydisperse nature of fly ash strongly influences the ultimate material strength beyond the sum of the contributions from monodispersions. That is, polydispersions commonly include small particles in interstitial sites between large particles. This nonlinearly adds to the strength of the material beyond the chemical bonding contributions of the particles themselves. Experiments with polydispersions are ultimately more realistic, but analyzing such data is only tractable if the size-dependence of some of the parameters is neglected. Specifically, a more tractable approach is

$$\alpha \equiv 1 - \frac{\overline{x}_A}{\overline{x}_A^0} = \frac{\overline{x}_A^0 - \overline{x}_A}{\overline{x}_A^0} = \sum_{i=1}^{\infty} \left[\left(\frac{n_p}{V} \right)_i \frac{4\pi R_i^3 \rho^{III} x_{A,b}^{III}}{\overline{\rho} \overline{x}_A^0 \overline{b}} \overline{\tau}_i \left(1 - \overline{\tau}_i + \frac{1}{3} \overline{\tau}_i^2 \right) \right] = \sum_{i=1}^{\infty} \alpha_i \qquad \text{(F-80)}$$

Where

$$\overline{\tau}_i = \frac{\overline{b} \, \overline{k} \, \overline{E} \, (Th_i)(1 - x_{\Sigma,b}^{II}) \rho^{II} t}{\rho^{III} R_i} \qquad \text{(F-81)}$$